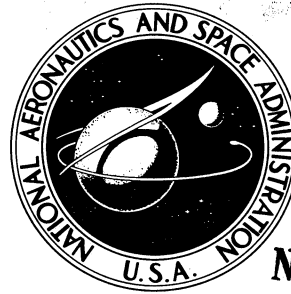


336

210p.

NASA TECHNICAL NOTE



(NASA TN D-1893)

N 64 10 932 *
CODE-1

NASA TN D-1893

A WIND-TUNNEL INVESTIGATION OF GROUND-WIND LOADS ON AXISYMMETRIC LAUNCH VEHICLES

*by Donald A. Buell, George B. McCullough,
and William J. Steinmetz*

*Washington, NASA, Oct. 1963
reg. OTS: \$9.50*

*NASA Ames Research Center
Moffett Field, California*

TECHNICAL NOTE D-1893

A WIND-TUNNEL INVESTIGATION OF GROUND-WIND
LOADS ON AXISYMMETRIC LAUNCH VEHICLES

By Donald A. Buell, George B. McCullough,
and William J. Steinmetz

Ames Research Center
Moffett Field, California

NATIONAL AERONAUTICS AND SPACE ADMINISTRATION

TABLE OF CONTENTS

	<u>Page</u>
SUMMARY.	1
INTRODUCTION	1
NOTATION	2
MODELS	5
INSTRUMENTATION.	6
MEASUREMENTS	7
Test Methods	8
Test Variables	9
Calibrations	9
Data Reduction	10
RESULTS AND DISCUSSION	10
Dynamic Response Moments	11
Steady-State Forces and Moments.	19
Oil-Flow Pictures.	20
Steady-State Pressures	21
Fluctuating Pressures.	22
CONCLUDING REMARKS	28
APPENDIX	30
REFERENCES	35
TABLE I.	36
TABLE II	37
FIGURES.	39

A WIND-TUNNEL INVESTIGATION OF GROUND-WIND

LOADS ON AXISYMMETRIC LAUNCH VEHICLES

By Donald A. Buell, George B. McCullough,
and William J. Steinmetz

SUMMARY

Wind-tunnel tests were made of a family of models representing launch vehicles on the launching pad. Model characteristics which were varied included fineness ratio, stage diameter ratio, scale, frequency, mass, damping, surface roughness, and payload shape. Steady ground winds were simulated at Reynolds numbers up to 10 million based on the diameter of the upper stage. Measurements were made of the dynamic and steady-state bending moments, the steady-state forces, and the fluctuating and steady-state pressures acting on the models. A limited number of flow studies and wake surveys were also made. A large body of dynamic and steady-state response data is presented to show the amplitude and statistical nature of the induced loads. Spectral and cross-spectral analyses of the aerodynamic input, response, and wake pressures are also presented.

Large lateral response at some particular wind speed was usually associated with nose shapes of medium bluntness and with surface roughness near the nose. Conduits on the exterior surface also produced large lateral responses, and in a few instances, large lateral oscillations, believed to be self-excited, were encountered on models with slender noses.

INTRODUCTION

The effect of wind on long slender bodies has been observed and speculated upon for many years, and references to Aeolian tones (i.e., sounds generated by wind action on cylindrical objects) can be found in ancient writings. In more recent times, a closely related phenomenon has exhibited itself in the galloping of electrical transmission lines, the oscillations of long suspension bridges, and the swaying of tall smokestacks in a direction perpendicular to the wind. In some cases these structures have failed because of the violence of the wind-induced oscillations. Wind-induced loads concern designers of launch vehicles who attempt to keep structural weight to a minimum. The wind-induced forces, both steady and oscillatory, are almost wholly the result of flow separation from the sides of the launch vehicle. This complex flow has been investigated for several launch vehicles but there is no firm foundation for predicting the air loads on a previously untested shape. Furthermore, most data have been obtained at Reynolds numbers much lower than those on a large missile in any appreciable breeze.

The oscillatory air loads on two-dimensional cylinders have received much attention. In the low Reynolds number flow regime the flow separation results in the periodic shedding of vortices from alternate sides of the cylinder (ref. 1). At supercritical Reynolds numbers (greater than about 500,000) the existence of periodicity is uncertain. The more typical observation has been that the aerodynamic input to a two-dimensional cylinder is random with no characteristic frequency (ref. 2), although reference 3 reports a characteristic frequency in the wake of a two-dimensional cylinder at Reynolds numbers above 3.5 million. It has not been demonstrated whether any of these concepts apply to three-dimensional structures.

An early wind-tunnel investigation of the Titan missile (ref. 4) has shown that the magnitude of the lateral dynamic response was influenced by several factors, chiefly the shape of the nose of the vehicle. Other related factors were surface roughness and protuberances, such as external conduits, and, of course, the dynamic response is affected by structural properties, such as stiffness, mass, and damping. The complicated relationship among these factors indicated that a systematic study of the design variables was needed to assess their importance and effects; therefore, the investigation reported herein was devised.

Models resembling launch vehicles were tested at Reynolds numbers up to 10 million in the Ames 12-Foot Pressure Wind Tunnel. Response stresses were measured on a large number of model configurations to determine which shape factors led to large oscillations. Pressures were measured to determine the axial distribution of the exciting forces on interesting configurations. These measurements were supplemented by statistical analyses of response moments, by spectral analyses of the pressures, and by oil flow studies.

Steady-state loads and pressures were also measured on the various configurations. Such data are necessary not only for calculating average stresses but also for estimating gust loads due to normal wind-velocity variations. It is usually assumed (as in ref. 5) that a knowledge of the steady-state drag loads coupled with a knowledge of gust spectra is sufficient for predicting dragwise oscillations.

The investigation reported herein is of limited use to designers because of the simplified nature of the models. The purpose of the report is, rather, to provide a guide to further research.

NOTATION

The models of this investigation simulate vehicles that are standing vertically on the launch pad prior to firing. The wind (and drag) direction is 90° from the axis of symmetry. The pitching moment acts in a plane which is parallel to the wind direction and passes through the axis of symmetry. The lateral forces and moments act in a plane which is perpendicular to the wind direction and passes through the axis of symmetry. The center of moments is the intersection of the tunnel floor fairing with the axis of symmetry as shown in figure 1. Positive forces and moments are aft and to the right of an observer looking up-wind. Many of the geometrical parameters are illustrated in figure 1.

C_C	steady-state lateral force coefficient, $\frac{\text{mean lateral force}}{qA}$
C_D	steady-state drag coefficient, $\frac{\text{mean drag}}{qA}$
C_l	steady-state lateral bending-moment coefficient, $\frac{\text{mean lateral bending moment}}{qAy_A}$
$C_{l,d}$	dynamic lateral bending-moment coefficient, $\frac{(M_l)_{\max}}{qAL} Nr \sqrt{\xi_l \frac{V}{fD}}$
C_m	steady-state dragwise bending-moment coefficient, $\frac{\text{mean dragwise bending moment}}{qAy_A}$
$C_{m,d}$	dynamic dragwise bending-moment coefficient, $\frac{(M_m)_{\max}}{qAL} Nr \sqrt{\xi_m \frac{V}{fD}}$
P	steady-state pressure coefficient, $\frac{p - p_\infty}{q}$
A	frontal area of model exposed to wind, sq ft
C	absolute value of cross power spectrum of inputs corresponding to X and Y
D	diameter of upper stage, ft unless otherwise noted
d	diameter of lower stage, ft
f	frequency of first cantilever mode in lateral direction, cps
L	total length of model exposed to wind, ft
L_1	length of lower stage, ft
L_2	length of upper stage, ft
L_n	length of nose, ft
L_T	length of roughness tapes, ft
M	generalized mass, $\int_0^L \phi^2 m dy$, slugs
$(M_l)_{\text{ampl}}$	amplitude of dynamic lateral bending moment in first cantilever mode
$(M_l)_{\max}$	maximum dynamic lateral bending moment in first cantilever mode
$(M_m)_{\max}$	maximum dynamic dragwise bending moment in first cantilever mode
$\sqrt{M_l^2}$	rms value of dynamic lateral bending moment
m	mass per unit length, slugs/ft

N	number related to structural characteristics of model, $\frac{\int_0^1 \varphi^2_m d\left(\frac{y}{L}\right)}{\int_0^1 \varphi_m \frac{y}{L} d\left(\frac{y}{L}\right)}$
p	local static pressure, psf
p_∞	free-stream static pressure, psf
q	free-stream dynamic pressure, psf
R	free-stream Reynolds number, $\frac{\rho V D}{\mu}$
r	"generalized" fineness ratio, $\frac{1}{\int_0^1 \varphi \frac{x}{L} d\left(\frac{y}{L}\right)}$
V	free-stream velocity, fps
w_1	local deflection of the model oscillating in first cantilever mode, ft
X	power-spectral value of input at upper pressure-measuring station, or at source otherwise specified
x	local diameter, ft
Y	power-spectral value of input at lower pressure-measuring station, or at source otherwise specified
y	axial distance from moment center to model station, ft
y_A	axial distance from moment center to center of area A, ft
z	nominal value of $\frac{(M_l)_{\text{ampl}}}{\sqrt{M_l^2}}$
ζ_l	ratio of damping to critical damping in first cantilever mode, lateral direction
ζ_m	ratio of damping to critical damping in first cantilever mode, dragwise direction
θ	angle from upstream stagnation line to point of pressure measurement on model
μ	free-stream air viscosity, slugs/ft sec
ρ	free-stream air density, slugs/cu ft
φ	normalized mode shape, $\frac{w_1}{\xi_1}$, of first cantilever mode

- ϕ (in spectral analyses) phase angle of C, zero when inputs are in phase, positive when input corresponding to X leads input corresponding to Y
- ξ_1 tip deflection of model oscillating in first cantilever mode, ft

MODELS

All parts of the generalized models were made of steel, and were either machined from solid stock or from commercially available tubes with bulkheads welded in the ends. Each of the four base sections had a flange at the bottom end so that it could be bolted to a 4-inch-thick steel plate rigidly attached to the shell of the wind tunnel. Two of the bases were nominally 14 inches in diameter, and the other two were nominally 8 inches in diameter. One base of each set was made from 1/2-inch-thick wall tubing, and the other base from 1/10-inch-thick wall tubing. They are referred to as the "stiff" and the "flexible" bases, respectively. The internal diameters of the stiff bases were increased for a short distance near the bottom to provide greater strain gage sensitivity than would have been the case if the wall thickness were uniform.

A variety of upper sections could be bolted to any of the bases to produce models of constant diameter or models which necked down to a second stage of smaller diameter. Heavy (solid) or light (tubular) upper sections could be used. A typical model assembly is shown in figure 1. This drawing depicts the 14-inch stiff base with the 10-inch heavy upper section. A photograph of this configuration (with roughness tapes to be mentioned later) is shown in figure 2. Photographs of the various modules are shown in figure 3. In all, there were 17 modules from which more than 20 basic models could have been assembled, although not all possible combinations were used because of unrealistic structural properties. The lengths and diameters of the modules are listed in table I. It should be noted that the bottom 3-1/4 inches of the base sections covered by the tunnel fairing is included in the tabulated values.

A variety of nose shapes or payloads could be attached to the top of the various models. These noses were made of wood, aluminum, or a combination of both. The noses were attached to a metal plate which, in turn, was attached to the upper section with a central stud. Drawings of some of the more complex noses are shown in figure 4. The other noses were simpler geometric shapes which will be described as the data are presented. Photographs of some of these noses are shown in figure 5.

In addition to the generalized models, data are also presented from tests of a model with a tapered upper stage (fig. 6). This model was supplied by The Martin Company, Baltimore, Maryland, and was machined from solid magnesium. The model was made in sections with threaded connections. The base of the model was bolted to a large steel center piece which was supported by four steel circular bars arranged horizontally and spaced 90° apart like spokes radiating from the hub of a wheel. The outer ends of the bars were pressed into steel blocks bolted to the 4-inch steel plate in the wind tunnel. The radial bars provided the spring for the model which was otherwise rigid. Two sets of bars were provided

to furnish two degrees of stiffness. During preliminary calibration, the model was found to have very low and nonlinear values of damping. To increase the damping and to make it less variable with bending moment, vibration isolators were installed between the flexible steel bars and the base plate.

The modular models were machined by ordinary methods and lightly sanded. No attempt was made to attain a polished finish except for the two heavy 10-inch sections which were given a ground finish during the course of testing.

Surface roughness was simulated by 1/2-inch-wide strips of cellulose tape. The strips were applied axially every $22\text{--}1/2^\circ$ over the front half of the upper sections of the models as shown in figure 2, and are referred to as "tapes."

INSTRUMENTATION

The principal instrumentation consisted of four strain-gage bridges. On the generalized models the gages were installed on the inside of the base tube about 4 inches above the bottom end. The gages were arranged in pairs on the streamwise and lateral meridians so as to be sensitive to streamwise and lateral bending. The manner of connection cancelled any axial lifting force. The thin-wall bases had a second set of gages installed higher up in the tubes. The strain-gage pairs for the model with the tapered upper stage were installed on opposite arms of the flexible support spider and were sufficiently sensitive to give accurate results in the subcritical Reynolds number range.

A 20-kilocycle carrier-amplifier unit was used to power the bridges and to amplify the output signals. The output signal was fed to three separate recording devices: a recording oscillograph, a magnetic tape recorder, and a digital readout apparatus which computed the mean square, arithmetic mean, and peak output signals.

With the tunnel running, the output signals from the strain gages in the base of the models consisted of a fluctuating voltage which varied randomly in amplitude with an approximately sinusoidal wave form. The recording oscillograph and magnetic tape recorder provided continuous records of the voltage for later analysis. The digital readout apparatus converted the fluctuating voltage to the desired outputs through circuits of high impedance. The mean square circuitry consisted essentially of a heater in series with a capacitor. A thermocouple next to the heater produced an output voltage proportional to the square of the fluctuating input voltage. The averaging circuit consisted of a capacitive-resistive network, and the peak circuit consisted of a rectifier and a capacitor provided with a shorting button to erase the "memory" of the capacitor. The output voltages (three for the lateral and three for the dragwise bending moment) were connected to light-beam galvanometers with automatic followers which printed a digital reading when a "print" button was pressed. The necessary calibration factors relating the digital readings to bending moment at the base of the model were obtained by pulling on the model with known forces. The time constant of the circuitry was long enough that there was little, if any, change in the mean during a data sample. The mean square moments for a given test velocity were

obtained by averaging the values printed throughout the time interval of the data sample. The peak was obtained from the maximum value printed during the time interval.

Instrumented disks, such as shown in figure 7, were used to measure fluctuating pressures acting on the surface of the models. Each disk contained 12 transducers spaced as follows: $\pm 15^\circ$, $\pm 45^\circ$, $\pm 75^\circ$, $\pm 105^\circ$, $\pm 135^\circ$, and $\pm 165^\circ$ from the upstream stagnation line. The transducers at $\pm 15^\circ$ and $\pm 165^\circ$, however, were inoperative because of damage incurred during installation. The transducers were mounted with their 1/2-inch-diameter diaphragms flush with the outer surface of the disk. (This resulted in flat spots in the otherwise cylindrical surface.) A short distance below each transducer was an orifice which was connected through a long length of tubing to the reference pressure side of the transducer and to a liquid-in-glass manometer. Each transducer was powered by its own adjustable d.c. power supply and the applied voltage was adjusted to provide the same ratio of signal to pressure on all transducers. The transducer signals were combined into one output which represented the spatially averaged pressure difference between opposite sides of the model. It is assumed that this was nearly the same average which would have been obtained by a large number of transducers having equal spacing in the streamwise direction. Disks of the proper diameter could be inserted between any two modules (stations A, F, J, or K) or could be stacked next to each other, but only two disks could be used at one time. A photograph of a modular model with disks installed at stations A and F is shown in figure 8. (This photograph also shows a portion of the pressure measuring rake and a friction damping device to be described later.) The transducers were calibrated against a liquid manometer. The output signal of each disk was recorded on magnetic tape and on an oscillograph. Connections were also available for recording the output from any individual transducer.

The distribution of static pressure at other axial stations along the length of the upper stage was obtained from pressure orifices installed in six circumferential rows in the 10-inch light center and upper modules as shown in figure 7. Also shown in figure 7 is a sketch of the rake used for measuring pressure fluctuations in the wake.

The rake was attached to the ceiling of the wind tunnel and could be moved longitudinally along the tunnel axis. Electrical pressure transducers were located in each of the five tubes of the rake. For some tests the transducers were arranged to respond to the difference in static pressure on opposite sides of the probe. The orifices leading to this transducer were 3.5 diameters downstream from the nose of the probe. For other tests the transducers were arranged to respond to the difference between local total pressure and a reference pressure.

MEASUREMENTS

The following four types of measurements were made during the course of the investigation:

1. Dynamic bending-moment measurements.
2. Steady-state force and bending-moment measurements.
3. Oil flow studies.
4. Dynamic and steady-state pressure measurements on the models and in the wakes.

Dynamic response data were obtained for all model configurations, but the other types of data were obtained for selected model configurations only.

Test Methods

The response data were obtained with the digital readout and recording equipment described previously. The data samples were approximately 60 seconds long. During this interval the digital readout was printed ten times. It was found that the digitally recorded peak values, adjusted to include only the oscillatory portion, were low compared to the peak-to-peak values measured on the oscillograms. A calibration factor was determined and applied to the digital peak values to bring them into agreement with the oscillograph values. As the testing proceeded, the oscillograph and tape recorder were used more selectively.

The manner of making a test run was to start with a low value of tunnel dynamic pressure, say 20 pounds per square foot, and take data samples at successively increased values of dynamic pressure until visual observation of the monitoring oscilloscopes indicated that the design bending moment was being approached. The test run was then terminated. The maximum dynamic pressure of the tests was 570 pounds per square foot.

The steady-state force measurements were made with the model mounted on the six-component wind-tunnel balance system. Dynamic response data were not obtained with the model mounted on the balance because of the flexibility of the system. Readings of the balance system were printed out for successively increased values of tunnel dynamic pressure.

A light-weight automotive lubricating oil in which a fluorescing power had been stirred was used in the oil flow studies. A thin coating of the mixture was smeared on the model by hand. The model was illuminated with ultraviolet light from high-intensity mercury arc lamps filtered to remove most of the visible light. The model was photographed with a remotely controlled 35 mm camera. The wind tunnel was run at each of several speeds until the oil flow pattern became stabilized; then the photograph was taken.

In another series of tests, pressures were measured on the model and in the wake at several test velocities and for various rake positions. The fluctuating-pressure data were recorded on magnetic tape for later spectral analysis. Steady-state pressure readings were recorded on photographs of multiple-tube manometers. Base bending moments were also obtained in these tests, for purposes of comparison with the more extensive data obtained on the models without transducers and orifices.

Test Variables

Reynolds number was a principal test variable. Variations in Reynolds number were obtained by changing model size, wind-tunnel density, and wind-tunnel velocity. Tests were made with densities up to 4.7 atmospheres, and the maximum Reynolds number obtained was 10 million. The maximum Mach number was limited to 0.3 to eliminate major compressibility effects.

The other variables included surface roughness, payload shape, damping, mass, natural bending frequency, fineness ratio, and stage-diameter ratio. All of these variables were interdependent to some extent, although the first three could each be adjusted with negligible changes in the other variables. For some tests roughness up to 0.00057 of the diameter was added to the upper stage. Roughness on the lower stage was expected to be less important, and nose roughness was not considered a likely variable at the time these tests were made. The lateral damping ζ_l was increased to values as high as 0.1060 by a simple friction damper consisting of two sliding metal plates connected between the model and the tunnel wall as shown in figure 8.

Some variables could not be adjusted independently, and their effects could be evaluated only on circumstantial evidence involving large adjustments in various combinations. Structural parameters had the following extremes: lateral damping ζ_l (without friction) 0.0020 to 0.0350, dragwise damping ζ_m from 0.0006 to 0.0038, generalized mass M from 1.4 to 25.7 slugs, and frequency f from 10 to 49 cycles per second. Maximum and minimum values of the geometrical variables are: $d = 0.703$ or 1.158 feet; $D = 0.438$ to 1.158 feet; $L/D = 5.5$ to 16.6 ; $D/d = 3/5$, $3/4$, and 1 ; $L_2/L_1 = 0$ to 0.73 .

Calibrations

To determine the mode shapes and structural damping the models were shaken in the lateral and in the streamwise planes with an electromagnetic shaker while no air flowed in the wind tunnel.

Mode shape.- The mode shapes of the model were computed from the outputs of accelerometers temporarily attached to the model at five axial stations. The first cantilever mode shapes of the modular models with the hemisphere nose are shown in figure 9. (The nose had little effect on the mode shape.) In general, these mode shapes resemble the first mode shape of a uniform cantilevered beam. It is recognized that the mode shape ϕ does not reach zero at the floor level, particularly in the case of the large stiff-base models. The implication here is that the 2-ton base plate and parts of the wind tunnel are moving and should really be included in the generalized mass. Fortunately, the displacement of the base plate is small, and hence the generalized mass is not greatly affected. It is estimated that the generalized mass and the dynamic response coefficients are 10 to 20 percent smaller than the true value in the worst cases.

Damping.- To determine the model damping the decay of the bending moment was recorded after the shaker power had been cut. The first-mode structural damping

of typical models is shown in figure 10. The damping parameter ζ is the ratio of damping to critical damping. The solid portions of the curves are values measured from decay records, and the dashed portions are averages or extrapolations required for reducing the data. The limitation in maximum bending moment resulted from limitations in shaker amplitude or power. The damping curves are roughly similar in shape, tending to rise rapidly at first, then to level off at nearly constant value with increasing bending moment. The models with a large amount of artificial damping (figs. 10(d) and 10(e)) had typical friction-type damping which decreased as bending moment increased.

Several irregularities in the damping characteristics deserve comment. At particular frequencies, models such as model A, light, in figure 10(a), interacted with remote parts of the wind tunnel to produce irregular decays. These characteristics were not repeatable and were averaged out as indicated by the dashed fairing. Other unknown errors were caused by the damping inherent in the shaker and by the damping due to an open hatch in the top of the test section. The former error is known to be insignificant except for the small, light models, and it is believed that the latter error affected only one frequency, 49 cycles per second, which coincides with that of model E in figure 10(c).

Data Reduction

The reduction of the dynamic response data to coefficient form is explained in the appendix. The equations of motion normally used for relating input to response do not make allowance for nonlinear damping characteristics such as were measured on the models. Therefore, it was considered appropriate to apply the damping values in an approximate and convenient fashion. Except where the variation of damping with bending moment was excessive, as with the artificial damper, one average value was used for each model in each direction of motion. This procedure resulted in possible errors of 15 percent in the dynamic-moment coefficients for the lateral direction and 30 percent in those for the drag direction.

The form of the coefficients for the steady-state forces, moments, and pressures is conventional. The statistical analyses of the response and the spectral analyses of the fluctuating pressures are explained at some length in the Results and Discussion.

Corrections computed by the method of reference 6 were applied to the measured dynamic pressure and to the drag forces to account for blockage of the models and wakes. The correction increased the velocity by amounts up to 2-1/2 percent and reduced the drag by 1 percent.

RESULTS AND DISCUSSION

The main body of the data presented herein consists of bending-moment measurements. A sample oscillogram of the bending moments measured at the base of the models is shown in figure 11. The amplitude of the oscillatory response in both dragwise and lateral directions is random, but the response occurs

essentially at the natural cantilever frequency of the model and support system. A difference normally existed between the drag frequency and the lateral frequency of the models because the wind tunnel is stiffer in the dragwise direction than in the lateral direction. Occasionally, a model was tested which had a large lateral response and for which the dragwise frequency changed to that in the lateral direction; however this was the exception rather than the rule. The higher frequencies of the second cantilever mode are barely discernible in figure 11. On the models of this investigation, the second-mode moments were usually small in comparison to those in the first mode.

A steady-state drag moment (i.e., a mean other than zero) is apparent in figure 11, and a steady-state moment was also often present in the lateral direction. Since the steady-state loads are not necessarily extrapolated to full-scale values by the same factor as the oscillatory loads, the two types of loading must be separated and considered individually. This procedure is necessary also for the determination of moments at any other location on the model, since the two types of loading produce different moment distributions. To define the moment distributions for the steady-state case, additional measurements were made of the aerodynamic forces acting on the models. The oscillatory moment distributions are sufficiently defined by a knowledge of the mode shapes and mass distributions, since the oscillatory aerodynamic forces are normally much smaller than the inertial forces. The gages near the top of the flexible bases provided data with which to check this assertion. It was found that, for any given model, the ratio of oscillatory moments at this upper station to those at the base was always within 15 percent of the same value in the lateral direction and within 30 percent in the drag direction.

The force and moment data are presented in the following groups:

- Dynamic response moments
- Steady-state forces and bending moments

The remainder of the data are concerned with the input to the models rather than with the resulting loads. These data are presented as follows:

- Oil flow pictures
- Steady-state pressures
- Fluctuating pressures

Dynamic Response Moments

Attempts have been made repeatedly to generalize upon the characteristics of response moments, and one of the primary aims of this investigation was to determine the propriety of such generalizations for ground-wind loads. In presentation of data, it is useful to derive coefficients or "similarity" parameters which represent the aerodynamic input in order to apply the data to full-scale vehicles. In the derivation of the dynamic bending-moment coefficient (see appendix) used in presenting the response data, the following assumptions were made:

(1) The input is independent of the response.

(2) The power spectrum (energy) of the input is flat and equal to the spectral value at the natural frequency of the system.

(3) The damping of the system is small ($\zeta \ll 1$).

One of the primary objectives of the investigation is to evaluate the assumptions used in the derivation of the dynamic-moment coefficients. If the assumptions are valid, the data in coefficient form should be invariant for a range of model structural parameters.

Since it has been assumed that the excitation is random, another important variable is the size of the sample (i.e., the number of cycles). For example, the maximum load encountered in a one minute sample would probably be exceeded in a 100 minute sample. Hence, it is obvious that comparisons of various configurations, based on the coefficient discussed above, should consider only data samples of equal size.

If one wishes to extrapolate data from one sample size to another, for a given vehicle, it is necessary to consider the statistical distribution of the data. In this regard, it is convenient to assume (in addition to the assumptions made above) that:

(4) The excitation random process is both stationary and ergodic.

Freely interpreted, this means that averages over the space domain (many samples) and over the time domain (one sample) are equal and invariant.

(5) The excitation follows a Gaussian (normal) probability distribution.

With these five assumptions, it is shown in reference 7 that the response will be Gaussian with a Rayleigh distributed amplitude.

A good measure of the variability of a random variable is the standard deviation which, for zero mean, is the rms of the variable. If the Rayleigh probability distribution were an adequate description of the response, a measurement of the rms for a given sample would be sufficient to predict the maximum response for any sample size. Specifically, the Rayleigh distribution predicts that the amplitude of the oscillations will be less than or equal to three times the rms with a 98.9-percent confidence level. A very limited statistical investigation is included in the presentation of dynamic response moments.

Interpretation of dynamic-moment characteristics.- Typical response data for one configuration are shown in figure 12. The coefficient $C_{l,d}$ represents the aerodynamic input, as do conventional aerodynamic coefficients, and the input was evaluated indirectly by measuring the response and the structural parameters of the system. The response characteristic upon which $C_{l,d}$ is based is the maximum value of the dynamic lateral moments over a one minute data sample. The rms was not considered appropriate for this purpose since it is of little value without knowledge of the statistical distribution. It should be noted that sample length should have been varied with the frequency of the model being investigated since sample size is identical with the number of cycles included in the record. However, as will be discussed later, the one minute (fixed time) sample gives results which are a good approximation to those which would be obtained in samples of a fixed number of cycles.

The second parameter presented in the ensuing series of figures is the ratio of the maximum value of the dynamic lateral moments in the entire data sample to the rms value. This ratio gives some indication of the statistical distribution of the data. For example, a sinusoidal distribution would have a ratio approximately equal to 1.4, whereas, for a Rayleigh distributed response amplitude, this ratio would be near 3. In general, data have been omitted where instrumentation error became significant.

The coefficients and ratio are plotted as functions of the basic scaling parameter V/fD , which is the reciprocal of the reduced frequency. Since the frequency f and the diameter D are constant for any given model or for any simulated vehicle, increasing values of V/fD represent increasing wind speeds.

Another parameter used in conjunction with the response data is $f_0 D^2$. This is a convenient scaling parameter because it is fixed for a given vehicle. Duplication of $f_0 D^2$ and V/fD assures the duplication of Reynolds number if the viscosity, μ , is considered to be invariant, since $R = (f_0 D^2 / \mu)(V/fD)$. For the data presented here, $R = 2.6 \times 10^6 (f_0 D^2)(V/fD)$. (The values of $f_0 D^2$ shown in the figures are sometimes approximate and may vary by as much as 3 in the last digit.) As an example, the model of figure 12 might simulate a vehicle having an upper stage diameter of 8.7 feet and a natural frequency of 1/2 cycle per second. The simulated velocity for such a vehicle would be 4.35 times V/fD in feet per second. One of the purposes of this accumulation of data is to find whether it is necessary and/or sufficient to duplicate these parameters on various models in order to define values of the moment coefficients. Figure 13 illustrates the relationship between the dynamic moment coefficient, bending moment, and V/fD . Note that large values of $C_{l,d}$ at small values of V/fD may not represent large bending moments.

The different symbols shown in figures 12(a) and (b) represent tests of the same model conducted at various times during the investigation. The lateral moment coefficients for the model without roughness (fig. 12(a)) fall in a broad band, the upper and lower boundaries of which are indicated by the solid- and dashed-line fairings. The coefficients for the model with tapes (fig. 12(b)) also exhibit scatter, but the percentage scatter is generally smaller than that without roughness. Even though the repeatability is poor, it is clear that the effects of small roughness additions are extremely large. It is reasoned, therefore, that the poor repeatability may be due to small changes in surface condition due to model changes or to fine particle accumulation during the tests. The greater emphasis is henceforth given to the reasonably well-defined upper limit of the broad band of moment coefficients. In considering the importance of the data scatter, it should be kept in mind that these dynamic moments make up only a part of the resultant moment on the vehicle.

A definite peak in the curve of moment coefficient versus V/fD apparent in figure 12(b) indicates that the spectrum of the input is not flat, thus violating one of the assumptions in the derivation of the coefficient. However, the ratio of maximum to rms moments remains near 3, so the input could have followed a normal probability distribution. This figure is typical of certain blunt nose shapes and indicates the difficulty in generalizing on the type of input to these models.

Figure 12(c) shows another characteristic which is typical of many sets of data. The test was terminated because the nominal strength of the model was exceeded. It is conjectured in all such cases that a stronger model would have permitted passing through the peak and that the coefficients would have decreased at higher values of V/fD .

Response data for models with hemisphere nose. - Data for the family of models with the hemisphere nose are shown in figures 14 to 17. Each plot is a collection of results for models having widely varying structural characteristics. Separate plots are used to show data for various values of $f\rho D^2$, tape thickness, ratio of stage diameters, and fineness ratio, all of which affect the aerodynamic profile. Summary plots showing the effects of these parameters on $C_{l,d}$ are presented in figure 18. The summary plots compare only the upper portions (solid-line fairings) of the data bands. A coefficient for dynamic dragwise moments is presented in figures 14, 15, and 17. The dragwise-moment data are not presented for all configurations because the instrumentation which recorded the moment maximums was not properly calibrated for the early tests. No summaries are presented for the dragwise-moment coefficients since they rarely exceed a value of 1.

Variations in the structural parameters - frequency, mass, and damping - and in model size were not considered to have important effects on the moment coefficients. Such an assessment is based on two factors. First, the effects of the structural parameters and model size are inconsistent and small in comparison with the effects of surface roughness and nose shape, which will be shown in later figures. Second, the differences between results for various models are no larger than the differences shown for one model from various tests in figure 12. It is recognized that an orderly step-by-step variation in each structural parameter was not achieved. However, since the range in values for each parameter was quite large, it is expected that important effects of frequency, mass, or damping would have become clearly evident in figures 14 to 17.

The effects of increasing $f\rho D^2$ (or Reynolds number) are summarized in the first three parts of figure 18. For the constant diameter models without roughness, the moment coefficients had a monotonic increase both with V/fD and with $f\rho D^2$. As the upper stage diameter was decreased on the models without roughness (figs. 18(b) and (c)) the moment coefficients were increased at the lower values of V/fD and $f\rho D^2$. Minor peaks in the curves were thought to be discernible for the model with the smallest ratio of diameters. At the lowest value of $f\rho D^2$ (0.01 in fig. 18(c)), a different type of characteristic appeared; for these data the Reynolds number falls below the "critical" value of 500,000 as V/fD decreases. It is likely that a subcritical type of vortex shedding caused the large increase in moment coefficient. At this low Reynolds number it is, in reality, inappropriate to use the moment coefficient shown since it is based on assumptions which are incompatible with the expected type of input. Also, the strain gages were not sufficiently sensitive to give good resolution at these low speeds.

The moment coefficients for the models with tapes had large peaks at certain values of V/fD . For the models of figure 18(b) the peaks moved progressively to lower values of V/fD as $f\rho D^2$ was increased, thus causing a large change in $C_{l,d}$ at certain values of V/fD . A minimum V/fD for the peaks appears to be about 11 or 12. The same trend was true for the constant diameter models but the

lower values of $f\rho D^2$ were not investigated. Figure 18(c) shows most of the peaks occurring at a V/fD of approximately 11 despite low values of $f\rho D^2$. This situation may be the result of using tapes which were thicker in relation to the upper stage diameter than were used on the models previously discussed. The data at the lowest $f\rho D^2$ are again probably too low in Reynolds number to be appropriate for the comparison. In summary, it is shown that Reynolds number can have large effects on the lateral moment coefficients under certain conditions of roughness and nose shape. Roughness on the models with hemisphere noses can result in values of $C_{l,d}$ well above 10 at values of V/fD slightly more than 10.

Other effects, shown in figures 18(d) and 18(e), are small. These are the effects of stage-diameter ratio and fineness ratio. In these comparisons the form of the moment coefficient is important. The assumptions regarding the distribution of the input forces were influenced in part by the desire to make the moment coefficients for models with different fineness ratios approximately equal. In this respect the development of the moment coefficient used herein was empirical.

Response data for models with cone-cylinder nose.- The dynamic response data for the models with the cone-cylinder nose are shown in figures 19 to 22 with summary plots in figure 23. In most of the cases investigated, the lateral dynamic response with this nose shape was much less than that with the hemisphere nose. The spread between moment coefficients from different tests and different models was also generally less with the cone-cylinder nose than with the hemisphere nose.

An important exception to these generalizations was encountered with the constant-diameter models at V/fD of 5. In figure 19(c) it can be seen that a sharp peak in $C_{l,d}$ was reached with one of the smooth models (Reynolds number almost 3 million). The type of input to this model was unusual since the ratio of maximum to rms moments decreased to 1.7; that is, the response had a nearly constant amplitude. Some evidence of the peak also appeared at a lower $f\rho D^2$ (fig. 19(b)) and at a smaller fineness ratio (fig. 20(a)). It disappeared, however, when tapes were added or the test conditions were otherwise altered. Data for a number of models for which this region of V/fD was investigated are not shown because they had relatively small bending moments. Often, in these cases, values of $C_{m,d}$ are shown, indicating that lateral moments were also measured but were insignificant.

The possibility of a self-excited phenomenon exists for the unusual response peak shown in figure 19(c); that is, it is possible that there was an interaction between the response and the input that increased the input forces as the response increased. In such situations the structural damping and generalized mass would be expected to have a greater influence than is attributed to them in formulating $C_{l,d}$. A similar situation has occasionally been encountered with models of specific missiles when certain combinations of conduits and umbilical towers were present. In such cases, the model motion tends to attain a constant amplitude over extended periods of time and thus can usually be differentiated from the more typical random response. Some further evidence of the self-excited phenomenon is presented in the section on fluctuating pressures.

The comparisons of the lateral moment coefficients in figure 23 show rather small effects of changing $f\rho D^2$ or adding roughness except for the situation just discussed. It is interesting to note that the presence of the cone-cylinder nose caused the effect of roughness to be beneficial for most test conditions. With the tapes and the cone-cylinder nose, the effect of increasing $f\rho D^2$ was also usually beneficial. In contrast to the results for the hemisphere nose (fig. 18), the values of $C_{l,d}$ for the roughened models with the cone-cylinder nose did not exceed 3 except at the smallest value of $f\rho D^2$ investigated.

The effect of stage-diameter ratio, shown in figure 23(d), is not large in comparison to some of the other effects. The range of fineness ratio was too small to establish an effect of this variable.

Response data for models with the blunted-cone nose.- A limited number of tests were made of models with a blunted-cone nose, and the results are shown in figures 24 to 26. It was presumed that the effective bluntness of this nose would lie between that of the hemisphere and the cone-cylinder nose. If the lateral moment coefficients are compared with those in previous figures at comparable values of V/fD , $f\rho D^2$, and tape thickness, it will be found that the results for the blunted-cone nose do tend to fall between those for the previously discussed models.

It is evident that the shape of the moment-coefficient curves for the blunted-cone models differs considerably from previous curves. In general, the moment coefficients have values near those for the hemisphere models until some critical V/fD is reached. At this point the coefficients fall off toward the values corresponding to the cone-cylinder models.

Figures 24(b) and (d) include data for a model in which a lower stage cluster was crudely simulated. The cluster consisted of 8 circular-arc segments of wood with a radius of $0.161D$ attached to the outside of the basic model. The segments extended $0.084D$ outward from the surface and from $0.038L$ to $0.500L$ above the tunnel floor. The cluster caused some increase in the moments on the smooth model and had little effect on the taped model.

It should be noted that the investigation of roughness was confined to the upper stage. Recent unpublished data have indicated that roughness on the conical portion of a nose might be beneficial. More information on this point is desirable.

Response data for the flat-faced model.- The flat-faced model was investigated as a limiting case for blunt nose shapes. Coefficients for the model, shown in figure 27, were generally low by comparison with the hemisphere-nose models previously discussed.

Response data for the model with the tapered upper stage.- Characteristics of this model are shown in figure 28. The general level of the lateral moment coefficients was low. In figures 28(a) and (c), however, large values of $C_{l,d}$ were measured for V/fD near 5. This value corresponds to the Strouhal number at which vortices are discharged from a two-dimensional circular cylinder at subcritical Reynolds numbers, and the Reynolds numbers were in fact subcritical in

this region. It is again noted that these moment coefficients are actually inappropriate for subcritical test conditions and are only included to show trends.

Comparison of various parts of figure 28 will show that the addition of tape to the model generally had only minor effects on the moment coefficients. The tapes were added to the tapered section rather than to the constant diameter section, so a direct comparison of tape effects with previous models is not possible. It may be noted that, on the average, the ratios of maximum to rms moments are higher than was true with other models. The reason for this cannot be determined from the available data. It has been suggested that the higher ratios may be due to the nonlinearities in the model support system that were introduced by the vibration isolators used to increase damping.

Effects of miscellaneous nose shapes and model additions on the lateral response data. - The ensuing figures present lateral moment characteristics for a variety of model modifications. There are insufficient data for any one configuration to establish generally repeatable trends. As a consequence, the broadband type of fairing has been abandoned. It should be remembered that only gross effects are significant. Structural parameters for all the models in any one set of comparisons are approximately equal. Where duplicate tests of the same model have been made, only that set of results is shown which was obtained nearest in time to the compared results (i.e., those results for which the model surface and other test conditions were least likely to have changed).

The effect of nose shape is shown in figure 29. The nose shapes investigated included families of ellipses, cones, and cone-cylinder combinations at moderate values of $f\rho D^2$. With tapes on the models, the noses of medium bluntness (ellipses and cones with $L_n/D = 0.5$ and the double-cone nose) are uniform in causing large moment coefficients at some velocity. Also, the removal of the tapes generally decreased the coefficients on these models. The model with the cone-cylinder nose was uniform in having comparatively small coefficients. It would, of course, be desirable to isolate the portion of the cone-cylinder nose which is most helpful in reducing the lateral response. However, figure 29(d) shows that neither a cylinder by itself nor conical sections, such as exist on the double-cone nose, are sufficient to keep the response small.

The effect of a small spoiler mounted at the tip of the double-cone nose and of the blunted-cone nose is shown in figures 30 and 31. The spoiler was a small section of angle mounted with its 1-inch high by 3-inch wide face normal to the wind. Throughout most of the range of V/fD , the spoiler reduced the lateral dynamic moments. It was apparently more effective on the blunter of the noses, the double-cone nose.

The effect of surface finish on a model with the hemisphere nose is shown in figure 32. For these tests the upper stage was given a ground finish which was appreciably smoother than the normal machined and sanded surface. There was very little difference between the lateral responses of the model with either degree of surface finish.

The effects of tape thickness and tape length on two models are shown in figures 33 and 34. In these tests the top end of the tape was always at the base

of the nose. It is only at the low values of $f\rho D^2$ (fig. 33(b)) that increasing tape thickness causes distinctly larger lateral response. Figure 34 shows that increasing the tape length by a factor of more than 2 had a rather small effect on the lateral response.

The effect of number 280 carborundum granules applied to the upper stage of the blunt-nosed model is shown in figure 35. The granules were applied to various areas symmetrically disposed on opposite sides of the model. It can be seen that the most pronounced effect on the lateral response was caused by roughness covering the areas between 45° and 90° measured from the upstream stagnation line. A comparison of figures 35(a) and (b) shows that the model had somewhat smaller moment coefficients with grit strips than with solid areas of grit on the upstream side. The most critical region for roughness effects appeared to be 45° from the wind direction. Figure 30(b) gives moment coefficients for tape strips on the model comparable to that of figure 35(b).

The effect of circular-arc conduits simulated by wooden slats symmetrically disposed on opposite sides of an upper stage is shown in figure 36. For the model with the double-cone nose and without tapes, conduits $67-1/2^\circ$ from the wind direction produced the largest lateral response for $f\rho D^2 = 0.09$. The effects of conduits at $67-1/2^\circ$ for other values of $f\rho D^2$, and also on a model with the cone-cylinder nose, are shown in figure 36(b). The effect of conduits resembles that of tapes from the standpoint that peaks in the coefficient curves are produced, and these peaks occur at lower values of V/fD as $f\rho D^2$ is increased. The conduits, however, caused higher response moments with the cone-cylinder nose than had been measured previously. It is apparent that conduits can cause large changes in the lateral response, and only a very limited amount of information on their effects is presented here.

As previously mentioned, a friction device was attached between the model and the tunnel wall in an attempt to introduce damping without altering the other structural parameters of the model. The coefficients, presented in figure 37, show little effect of the added damping or of the external attachments (on the lower half of the models). Unfortunately, the added damping is small at the larger bending moments.

Statistical analysis of response. - Some knowledge of the statistical distribution of the response data had been gained by comparison of maximum and rms values. Data corresponding to extreme values of the ratio of maximum to rms values were selected and analyzed to determine their distributions. Figure 38 shows the proportion of times that selected values of $(M_l)_{\text{ampl}}/\sqrt{M_l^2}$ were exceeded as well as the Rayleigh probability distribution in the form:

$$\text{Prob} \left[\frac{(M_l)_{\text{ampl}}}{\sqrt{M_l^2}} \right] > z = e^{-(1/2)z^2}$$

where $(M_l)_{\text{ampl}}$ is the amplitude and $\sqrt{M_l^2}$ is the rms of the dynamic lateral bending moment for the one minute data sample. If the response were a sine wave, the only possible value of $(M_l)_{\text{ampl}}/\sqrt{M_l^2}$ would be 1.4. Indeed, it may be seen in figure 38 that for one configuration analyzed, the response distribution is

very nearly sinusoidal. This cone-cylinder model was discussed in regard to figure 19(c). The distribution for the model with the tapered upper stage also strays significantly from that of the bulk of the data. For this model, the largest $(M_l)_{\text{amp}}/\sqrt{M_l^2}$ attained was 4.73 in a sample consisting of 1,512 cycles.

The sample size for each configuration analyzed may be obtained by computing the reciprocal of the proportion of times the maximum bending moment amplitude was exceeded. It can be seen that an increase in sample size by a factor of 2 or 3 for any one configuration would not change appreciably the maximum load to be expected.

It would seem from the data presented that expected maximum loads computed from the Rayleigh distribution could differ significantly in some cases from the actual maximum loads.

Steady-State Forces and Moments

Typical steady-state drag and dragwise-moment data for the generalized models, with and without tape, and with different noses are shown in figure 39. The drag data were obtained from wind-tunnel balance measurements, whereas the moment data were obtained from both balance and strain-gage measurements. The drag coefficient was minimum at a Reynolds number of 1.2 million. The different noses had no significant effect on drag, but the addition of tape to the upper stage slightly increased the drag coefficient.

The dragwise-moment data (fig. 39(b)) have a variation with Reynolds number similar to that of the drag data. This indicates that the center of pressure was close to the center of area because the distance from the base to the center of area was taken as the length dimension in the denominator of the moment coefficient. The agreement between the wind-tunnel balance measurements (considered to be the more accurate) and the strain-gage measurements was generally good. Force and moment data from the wind-tunnel balance system were not obtained on other configurations. It is assumed that the steady-state moments measured in conjunction with the dynamic tests are sufficiently accurate to establish the moment characteristics. The steady-state moment coefficients in succeeding figures have been computed from strain-gage measurements.

The effect of conduits on the steady-state dragwise moments of a modular model is shown in figure 40. Circular-arc slats were attached to the upper stage in pairs at three angular positions on either side of the front stagnation line. The largest increase in drag and dragwise moment was produced with the slats at $22-1/2^\circ$. Very little effect was shown with the slats in the $67-1/2^\circ$ position, which had been the more critical position for the dynamic response of the model without tapes (fig. 36). The "low pressure data" referred to here and in subsequent figures are measurements made with a reduced air density in the wind tunnel. The chief significance of the low-pressure data is that it was obtained at higher dynamic pressures than other data at the same Reynolds number and thus provided larger and presumably more accurate gage outputs at low Reynolds numbers.

The effect of fineness ratio on the dragwise- and lateral-moment coefficients of the modular models with the hemisphere and the cone-cylinder nose is shown in figure 41. There does not appear to be any consistent effect of fineness ratio within the range tested. Such differences as do exist might be attributed to differences in surface finish of the models. The variation with Reynolds number of the lateral moments was erratic for even the smoothest cylindrical models investigated.

The effect of stage diameter ratio on the steady-state moments of the modular models is shown in figure 42. No distinct trends are observable except for a tendency for the model with the smallest upper stage diameter to have the largest dragwise-moment coefficients.

Oil-Flow Pictures

Photographs of fluorescent oil on the surface of the models were taken as described in Test Methods, and examples, typical of most test conditions, are shown in figures 44 and 45. The air flow is from left to right in each photograph. The straight bright bands that run the length of the model (fig. 44(a), for example) are direct reflections of the illumination sources. The irregular bright line just to the right of the reflections is an accumulation of oil near the line of flow separation. The oil to the right of this separation line had been blown upstream while that to the left had been blown downstream until the oil to the left of the separation line had been reduced to a very thin layer. Stabilization of the oil pattern took less than a minute. The typical separation line on the smooth models such as the one shown in figure 44(a) was irregular, with its shape depending on the thickness and evenness of the initial oil coating. The separation line terminated at what looked like vortical motion at the base of the hemisphere nose, well downstream of the maximum width.

Figure 44(b) shows that the addition of tapes straightened out the separation line and moved it forward except near the nose. The straightening is attributed to a more uniform transition of the air flow upstream of the separation, because the roughness added by the oil itself was relatively small compared to that of the tapes. For purposes of orientation it may be noted that the rear-most strip of tape is located 90° from the upstream side of the model.

A change of nose shapes from the hemisphere to the cone-cylinder did not change the character of the separation line except near the nose. Figure 44(c) shows the separation line extending up onto the nose, well above the constant diameter section of the upper stage. It is believed that this vertical extension of flow separation onto the nose is one of the important characteristics which differentiates the models of small response from those of large response.

Close-ups of the region just below the noses are shown in figure 45. This part of the model has the largest moment arm and also has a significant amount of area for the pressures to act upon. With the hemisphere nose (figs. 45(a) and (b)), the fine smooth filaments of oil around the vortex center give evidence of an energetic flow downstream of the separation line. With the cone-cylinder nose (figs. 45(c) and (d)) the oil is relatively stagnant downstream of the separation

line. The appearance of the oil behind the separation line on the hemisphere suggests that energy is transferred from the flow about the nose to the separated-flow region. The hemisphere nose was therefore tested in conjunction with a streamwise plate which was intended to isolate the flow around the nose from that around the cylindrical part of the model. A photograph of this arrangement in figure 45(e) shows that the oil movements behind the flow separation line were much more sluggish with the plate. The lateral response was low for this configuration.

It may be reasoned that separation along a nose isolates the separated region behind the upper stage from the free stream much as does the plate. The conical noses probably vary in their effectiveness as oscillation suppressors in relation to the amount of separation induced along the length of the nose. The separation is in turn a function of cone angle, tip shape, roughness, Reynolds number, etc. The small tip spoiler which was discussed with the dynamic response data was probably effective because it tripped a flow separation that extended over much of the nose.

In general, it would appear that a nose shape which allows a smooth flow of air into the low-pressure region behind a cylindrical section of the model induces the largest oscillatory loads on the model.

Steady-State Pressures

The distributions of steady-state surface pressures on the upper stage of one of the models with various noses are shown in figures 46 and 47. The first figure presents data for the clean model, and the second figure presents data for the model with tapes. Dots on the sketches represent orifices at which the pressures were measured. Measurements were not made on both sides of the model except at stations midway between the ends of the cylindrical modules.

Important effects of nose shape on the steady-state pressures were confined to the upper one or two stations. The solid fairing in figures 46 and 47 applies to data for the hemisphere nose, for which the oscillatory loads were large. The dashed fairing signifies data for the cone-cylinder nose, for which the oscillatory loads were generally small. At the uppermost station (figs. 46(a) and 47(a)) the hemisphere nose had the more negative pressures. A horizontal plate under the hemisphere nose made the pressures more positive than those near the cone-cylinder nose (figs. 46(a) and (b)). This increase in pressure coincided with a reduction in dynamic response. The results for the blunted-cone nose were similar to those for the cone-cylinder nose.

A comparison of figures 46(a) and 47(a) shows that the effect of nose shape on the steady-state pressures was more pronounced without the tapes than with them. In contrast, the effect of nose shape on the dynamic moments was greater with the tapes. It must be concluded, therefore, that the steady-state pressures and the dynamic loads are not functionally related.

A rather large effect of roughness can be ascertained from a comparison of the data at various stations with and without tapes. At such locations as

station G (figs. 46(e) and 47(e)) the added roughness of the tapes made the pressures more positive over much of the periphery. At station E (figs. 46(d) and 47(d)) the parting line between the upper stage modules, 1.7 inches below the orifices, imparted enough roughness to the flow to give nearly the same pressure levels as were measured on the taped model, even though the joint was carefully assembled under considerable compression. Thus, rather minute amounts of roughness alter the steady-state pressures and the resulting steady-state loads.

Fluctuating Pressures

Dynamic data presented in previous sections have been concerned with measurements of the response of the models to simulated ground winds. It would seem possible to determine the aerodynamic loading which produced the response by measuring the pressure fluctuations from point to point on the surface of the structure. Such an approach, however, has two distinct disadvantages from the experimental point of view. First, for the data to be meaningful, there must be a large number of pressure transducers on the surface of the model. The multiplicity of transducers leads to data-recording complications because the outputs of the individual transducers should be recorded simultaneously so that the phase relation of the pressure fluctuations can be determined. (Pressure-fluctuation data without phase information are of little value.) Secondly, the presence of the transducers on the model introduces surface roughness. It has already been shown by the response data that the effects of intentionally applied surface roughness are significant; hence, it is obvious that unintentional but unavoidable surface roughness could also have a significant effect on the pressure fluctuations which caused the response.

The pressure-measuring system chosen for the present investigation was, therefore, a compromise; it utilized too few pressure transducers to define the total pressure input to the model, but sufficed to describe the amplitude and phase relationship between integrated pressure distributions at several axial stations of interest. The flush-mounted transducers described in the Models section were connected to give one output for a station. This output represented a spatially averaged pressure fluctuation acting laterally to the model at the axial station of the transducers. The outputs of two transducer stations were recorded simultaneously.

Method of analysis. - The fluctuating aerodynamic input to a typical model is known to contain a wide range of frequencies with a nonuniform distribution of energy across the spectrum. Because of its small damping, a typical launch vehicle responds primarily at its natural bending frequency. The magnitude of the response depends on the energy content of the input spectrum at or near the natural frequency of the model and on the phase relations of the inputs at various points on the model. If most of the energy of the input were concentrated near a natural frequency of the model, and if the pressures were everywhere in phase, the resulting resonance could be catastrophic. It is important, therefore, to determine the energy content and phase relations of the input as a function of frequency. In the present case this was done with electronic equipment capable of yielding power spectra and cross power spectra from data recorded on magnetic tape. The power spectra were obtained, in essence, by feeding the fluctuating

signal to a band-pass filter whose center frequency was swept through the range of frequencies of interest. The voltage output of the filter was squared, averaged, and recorded by a graphic recorder as a function of the center frequency of the band-pass filter. To obtain the phase relationship between two signals representing pressure fluctuations at different stations, the cross power spectrum was obtained. In this case, instead of the signal at one station being squared, the component of the signal at station 1 which is in phase with the signal at station 2 is multiplied by the signal at station 2. The average of this product is the cospectrum and gives a measure of the in-phase energy common to stations 1 and 2. Similarly, the out-of-phase component is multiplied by the signal at station 2 to yield the quadspectrum. The cross power spectrum is the vectorial sum of both spectra. The angle between the resultant and the cospectrum is the average phase angle between the two inputs. A discussion of power spectra and cross power spectra can be found in the literature (e.g., ref. 8). The application of cross power spectra to the problem at hand has been considered by several investigators (e.g., refs. 9 and 10).

In the present investigation the signals from the pressure transducers in the model, from the bending moment gages, and from the pressure transducers in the rake were recorded on magnetic tape and later analyzed on electronic analog equipment by means of circuitry devised by Mr. Robert Munoz of Ames Research Center. The recorded signals from two of the sources were transcribed to a 20-second tape loop so that a given piece of data could be scanned repeatedly. The actual system used a two-phase sweeping oscillator which produced two signals of high stability and accuracy, 90° out of phase from each other. The two reference signals were heterodyned with the two input signals, giving in each case a signal of high frequency and one of low frequency. The higher frequencies were eliminated by filters with zero center frequency. This principle of operation permitted the use of filters of nearly identical characteristics for both inputs, and introduced only small errors in the analysis process. Gradual sweeping of the frequency of the reference signals through the frequencies of interest produced power spectra and cross power spectra with a constant band width. The band width was about 3.8 cycles per second. The coordinates of the power spectra plots were not made dimensionless because of the large amount of additional effort required.

Figure 48 shows power spectra, X and Y, for two inputs of 1/2 volt rms at 25 cycles per second, inserted on the magnetic tape for calibration purposes, at the time of the tests. The finite width of the curves results from the analyzer characteristics. Thus, the analyzer was not capable of distinguishing between two nearly equal frequencies in the same input but had the advantage of improving the statistical quality of the measurement. (See ref. 8.) The discontinuity visible near the peak was caused by the magnetic splice in the tape loop. Although not readily visible in the figure, discontinuities also exist near 20 and 30 cycles per second for the same reason, and give an idea of how often the analyzer returned to the start of the data sample.

The magnitude of the cross power spectrum, C, is also shown. Because both signals were supplied by the same oscillator, the cross power spectrum shows the maximum possible correlation, \sqrt{XY} . In the usual terminology, the coherence is said to be 1. The phase angle (not recorded in this example) was 0. An example

of relatively uncorrelated inputs was provided by two commercial oscillators which were set by dial to 25 cycles per second. For this example the value of C was only 0.1 of \sqrt{XY} , and the phase angle varied rapidly.

Interpretation of pressure measurements on a model. - Figure 49 presents the first of a series of analyzer results for pressures measured on the models. For example, X is the power spectrum of the pressures measured just beneath the model nose. The voltages used in the analysis have been converted to pressure units and the result has been divided by the band width (3.8 cps) of the analyzer. The abscissa is the frequency being analyzed. It is shown in figure 49 that most of the energy of the lateral pressure fluctuations for $R = 2.7$ million and $V = 96$ feet per second is concentrated below 15 cycles per second. The cross spectrum at 10 cycles per second, for example, reaches 3, or about half of \sqrt{XY} , indicating that the fluctuations are rather strongly interrelated. However, the phase angle is roughly -150° , meaning that the two fluctuations almost oppose each other, and little model motion in the first cantilever mode would be anticipated from these two inputs. Also, this value of C is small compared to values that will be shown for other configurations and test conditions, so that a relatively small model motion would be expected even if ϕ were 0. The resolver on the analyzer had a limit of $\pm 200^\circ$, so a phase angle of -150° means either that the signal for Y leads X by 150° or lags X by 210° . No significance can be attached to variations in the spectral values such as those in Y from 4 to 8, because their cyclical nature indicates that the value depends on which part of the data sample is being analyzed; that is, the time constant of the averaging circuit was too small to give the spectral value for the entire data sample.

To be meaningful the test velocities and frequencies shown in figure 49 and ensuing figures should be related to full-scale values. The simulated full-scale velocity in feet per second is approximately

$$\frac{R}{10^6} \times \frac{156}{D_{\text{full scale}}}$$

For example, the simulated velocity for an 8.7-foot-diameter vehicle varies from about 48 to 104 feet per second in figure 49. The only frequencies of interest in each analysis would be those near the frequency which simulates the natural frequency of the full-scale vehicle. This frequency of interest is approximately $(f_p D^2) \times (V/R)_{\text{model}} \times 3 \times 10^6$, where $f_p D^2$ is the simulated parameter previously used in the response plots. For the example of a full-scale vehicle in which $D = 8.7$ feet and $f = 1/2$ cycle per second, the frequency of interest in figure 49 would be approximately 10 cycles per second. A larger vehicle would have a smaller simulated velocity and a higher frequency of interest in the analyses.

Lateral-pressure spectra near hemisphere nose. - Figure 49 compares power spectra of the pressures measured just beneath the hemisphere nose and of pressures measured about 2 diameters lower on the model. In these and subsequent figures the reader is cautioned to note the ordinate scales because they differ greatly from figure to figure. Although the larger energies are shown to exist at the lower frequencies, they are generally accompanied by phase angles which are not conducive to motion in the first cantilever mode. The phase angle has a nearly linear relation with frequency for this configuration, with the lower

station pressures apparently leading the upper station pressures at the low frequencies. The cross spectra have nearly the same variation with frequency as the power spectra of the upper station pressures. Thus a correlation between pressures at the two stations seems to be influenced by the energy of the fluctuation near the upper station.

As might be expected, the spectral values increase approximately with the square of the dynamic pressure q . It can be noted that there is no apparent increase in energy at 23 cycles per second, the natural frequency of the model. This is another indication that the input to this configuration is not affected by the response.

Figures 50 and 51 compare power spectra of pressures for the model with roughness. Figure 50 concerns tests at a reduced wind-tunnel density, and the frequencies of interest for a specific vehicle would be higher here than in figure 51. At the lowest Reynolds number (2.2 million), the spectra resemble those of the model without tapes. At any higher Reynolds number, however, the pressure fluctuations at the lower station became insignificant by comparison to those at the upper station, and the presentation of cross spectra and phase angle is no longer meaningful.

The roughness caused a very large increase in the energy of the pressure fluctuations at the upper station over a very limited range of frequencies. For example, at a Reynolds number of 5.2 million and a velocity of 193 feet per second (fig. 51(a)) the spectra reach values about 20 times as high as without roughness (fig. 49(b)), and the fluctuations are concentrated at a higher frequency. At the same time the roughness reduced spectral values for the pressures at the lower station by a factor of almost 10 (figs. 49(b) and 51(b)). The clearly predominant frequency at the upper station (figs. 50 and 51(a)) varies almost linearly with velocity. The reduced frequency of the pressure fluctuations is roughly 0.1 with little dependence on Reynolds number. This predominant frequency can also be seen in the spectra of the lower station pressures at a greatly reduced level. In the one situation where the energy is concentrated at the upper station and where phase angle is shown (fig. 50(a)), it can be seen that the lower station pressure fluctuations apparently led the upper station pressure fluctuations near the predominant frequencies.

It is instructive to compare the response of the roughened hemisphere-nose configuration with the pressures measured just under its nose. Figure 52 shows this comparison for the reduced wind-tunnel density, at which the predominant input frequency was sometimes below the model frequency and sometimes above. In this series the maximum spectral value for the response increases from about 8 to 1,250 (when the predominant frequency of pressure fluctuation equals the model frequency) and then decreases to about 100. At a Reynolds number of 3.1 million, the response spectrum exhibits two peaks; one at the input frequency of 18 cycles per second and one at the natural frequency of 23 cycles per second. This response at other than the natural frequency of the system attests to the strength of the pressure fluctuations near the nose, while it is also evident that enough random type inputs were present somewhere on the model to excite it at its natural frequency. The really large responses occurred when the fluctuations near the nose coincided with the natural frequency of the model.

A comparison of pressure spectra is made in figure 53 for the case in which a horizontal plate was placed immediately below the hemisphere nose. The purpose of the plate was to isolate the air flow around the nose from that around the constant diameter section. Comparing the spectra with those in figures 49(b), 51(a), and 51(b), one can see that the plate did indeed decrease the spectral values by factors up to 200. The most spectacular decreases were on the roughened model nearest the nose, and the smallest decreases were on the roughened model at the lower station.

The spectra of pressures measured only $1/8$ of a diameter apart, just beneath the hemisphere nose, are shown in figure 54. A comparison of X in figure 54 with that in figures 49(b) and 51(a) shows that the presence of the transducers themselves increased the pressure fluctuations on the smooth model but slightly decreased those on the roughened model. That is, the transducers added a roughness less than that of the tapes but still of considerable magnitude, as had been anticipated. Figure 54 also shows larger fluctuations at the lower station. Rake measurements will be presented subsequently that also indicate the fluctuations increased with distance from the nose for a limited distance. As would be expected, the cross spectra for the adjoining pressure stations were large compared to the individual power spectra, and the phase angle was essentially zero.

Lateral-pressure spectra near cone-cylinder nose. - Spectra of the pressure fluctuations just under the cone-cylinder nose and about 2 diameters lower on the model are presented in figure 55. In contrast to the values for the hemisphere nose, the spectral values were generally small, so fewer data are presented. A comparison with figure 49(b) shows that at a Reynolds number of 5.2 million, the model with the cone-cylinder nose has maximum spectral values about $1/10$ of those for the hemisphere nose at both upper and lower stations. The cross spectral values for the cone-cylinder nose are even smaller in proportion and were generally too small and erratic for the analyzer resolver to compute an accurate phase angle. The spectral values are approximately the same as those for the hemisphere nose with separator plate (fig. 53).

Figure 56 shows spectra of the pressures with roughness on the model. As was true with the hemisphere nose, the lower station pressure fluctuations were decreased and the upper station pressure fluctuations were increased by the roughness (figs. 55 and 56) but to a rather small degree. More important, the cross spectra were reduced to essentially zero by the roughness.

Lateral-pressure spectra near blunted-cone nose. - Spectra of the pressures measured at the same stations as for previous figures are presented in figure 57, for the model with the blunted-cone nose. This nose might be described as of intermediate bluntness when compared to the hemisphere and cone-cylinder nose and in some respects its behavior confirms this description. The spectral values for the upper station fall in between values for the other noses, but the lower station has pressure fluctuations of less magnitude than either of the other configurations. The cross spectra are very small. The peak in the power spectrum of the upper station pressures at a Reynolds number of 5.1 million is of particular interest because it coincides with the natural frequency of the model.

The interdependence between input and response is further demonstrated in figure 58, where the spectra of input and response are shown for the blunted-cone configuration at the higher Reynolds numbers. This is the only case analyzed

where an interaction between pressures and motion appeared to exist. In the discussion of the oil-flow pictures, it was proposed that flow separation from the cone-cylinder nose keeps the free stream from feeding energy into the pressure fluctuations behind the cylindrical part; whereas the hemisphere nose does not accomplish this. It seems likely that the blunted-cone nose promotes separation except under certain combinations of Reynolds number and model motion.

This configuration produced another unexpected trend when roughness was applied, as shown in figure 59. The "self-excited" peak disappeared and a high frequency fluctuation appeared near the nose at the highest Reynolds number. It may be recalled that the higher frequencies would be more applicable to the larger vehicles.

Lateral-pressure spectra near base of upper stage.- Figure 60 compares spectra of the pressures near the center of the upper stage and at the base of the upper stage. Various nose configurations are considered; the effect of roughness is shown only for the hemisphere nose, since roughness generally reduced the fluctuations at both stations. All of the spectra shown are small relative to those obtained near the hemisphere nose, and the cross spectra are very nearly zero. The two peaks in the lower station spectra of figure 60(b) are an interesting variation from measurements farther up on the model and indicate another three-dimensional effect in the flow around the transition between stages.

Spectra of pressures on both sides of the transition are presented in figure 61 for a representative configuration. The cross spectra were negligible and are not presented. Roughness on the upper stage had little effect on the lower stage pressures. The same double peak mentioned earlier can be seen in the spectra for the upper stage pressures when no roughness is present.

Spectra of pressures from individual pressure transducers.- Pressures measured by each transducer were also recorded for some test conditions, but no provision was made to record the readings simultaneously. Consequently, no cross spectra could be computed. Figure 62 shows spectra of the pressures measured near each of three nose shapes. In these and all other measurements near the nose, the maximum pressure fluctuations occurred at the measuring location 105° from the wind direction.

Spectra for the pressures two diameters below the blunted-cone nose are shown in figure 63. Here the maximum fluctuations are at the location 75° from the wind direction.

Spectra of pressures in the model wake.- The correlation of pressures measured at the static orifices of the rake tubes with those measured on the model will be considered next. Two cases are shown in figure 64, one involving large fluctuations on the model and the other involving relatively small fluctuations. The spectra shown for the model pressures do not compare precisely with those shown earlier (figs. 51(a) and 56) possibly because of the presence of the rake tube or possibly because of small differences in surface roughness on the model. It is clear, however, that the wake pressures near the nose exhibit characteristics similar to those of the pressures upstream on the model. A great deal of trouble was experienced in restraining rake vibration which was so severe that

the wires to the rake transducers were repeatedly broken. It is strongly suspected that the electrical connections to the rake transducer were reversed in the test of the hemisphere-nose model so that the 180° phase angle shown is in reality zero.

Spectra of the pressures at two locations in the wake are shown in figure 65 for the model configuration involving large fluctuations. A comparison of X for the two rake positions indicates that the pressure fluctuations at the lower position have no predominant frequency. Cross spectra between the wake pressures and the pressures on the model show the strong phase relation that existed between widely separated points of the flow field, despite the presence of random type fluctuations in the lower part of the wake.

A more revealing comparison of wake pressures is shown in figure 66 which presents spectra of the pressures measured at the nose of the rake tubes. With this type of pressure measurement, one reversal in the flow direction from one side of the wake to the other results in a double reversal in the pressure rise on the transducer. Thus, the pressure fluctuation on the model of figure 66(a) has a frequency of 24 cycles per second (fig. 50(b)) but results in a predominant fluctuation frequency of about 48 cycles per second on the rake nose. A peak also appears at 60 cycles per second as a result of inadequate filtering in the instrumentation and should be discounted. The most apparent trend shown in figure 66(a) is the much larger spectral values for the rake tube R4, which was midway between the nose and the center of the upper stage. These results would indicate that the largest pressure fluctuations on the model with the hemisphere nose occurred about one diameter below the nose. In contrast, the cone-cylinder nose had its largest pressure fluctuations near the nose (fig. 66(b)).

Finally, in figure 67, spectra are presented of the pressures measured with the rake only 0.2 inch from the model. These are assumed to approximate the pressures which would be measured on a transducer in the rear of the model. It is again shown that the hemisphere nose produced the larger pressure fluctuations about one diameter below the nose while the cone-cylinder nose produced its larger pressure fluctuations at the base of the nose. The spectral values associated with the two configurations are of course at greatly different levels.

CONCLUDING REMARKS

Tests were made of a family of axisymmetric models resembling launch vehicles. The models had a variety of shapes and a wide range of structural properties. The tests were designed to simulate the effect of steady ground winds on slender vehicles standing vertically on the launching pad. Reynolds numbers up to 10 million were attained. Measurements were made of the dynamic and steady-state bending moments, the steady-state forces, and the fluctuating and steady-state pressures acting on the models. In addition, fluorescing oil flow studies were made.

For nose shapes of medium bluntness, such as a hemisphere, lateral responses were large especially if the upper stage of the model was rough. A limited investigation of a model with conduits attached to the outer surface indicated

that external protuberances also can cause large lateral responses. The fact that the large lateral oscillations appeared at particular Reynolds numbers and reduced frequencies which varied with model configuration indicated that these are important scaling parameters.

Certain assumptions concerning the aerodynamic excitation were examined to determine whether the excitation could be analytically related to the model response. An indication of self-excited motion obtained in a few cases with relatively slender nose shapes precludes the assumption that the input is independent of the response. The assumption that the response was Gaussian was satisfied for most of the data analyzed but significant deviations did occur. In the case of supposed self-excitation, for instance, the response was approximately sinusoidal. For the models tested, it appeared that the assumption could be made that the excitation force is inversely proportional to the average fineness ratio.

The steady-state dragwise loads were increased by surface roughness and by conduits. Other changes in exterior shape caused no discernible trends in the steady-state moment coefficients.

Because of the simplified nature of the models, the data presented herein are not suitable for design purposes. More information on the effect of protuberances, adjacent structures, the damping of the full-scale structure and the effect of gusts must be compiled before rational estimation of ground-wind loads can be made. To date these factors have received little attention.

Ames Research Center

National Aeronautics and Space Administration

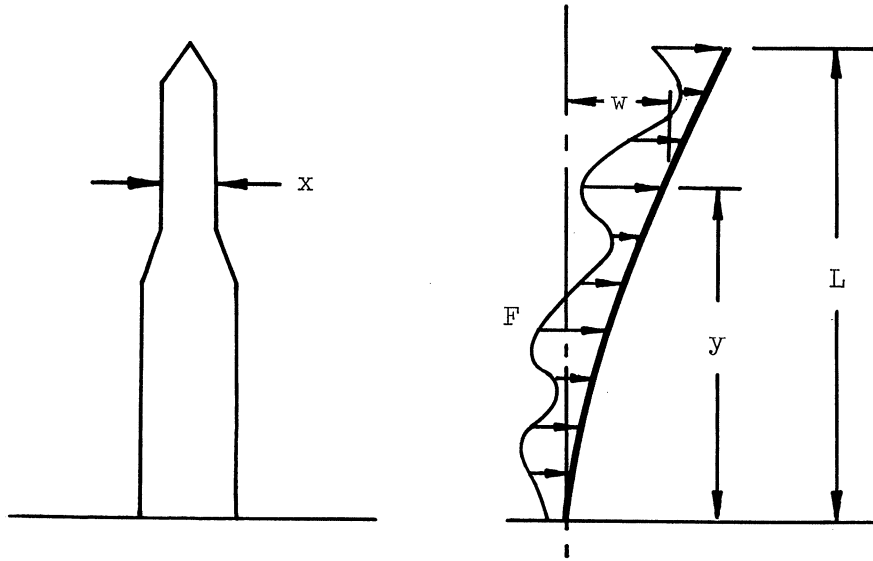
Moffett Field, Calif., July 5, 1963

APPENDIX

DEVELOPMENT OF THE DYNAMIC-MOMENT COEFFICIENTS, $C_{m,d}$ and $C_{l,d}$

The dynamic-moment coefficients are meant, first of all, to indicate the oscillatory input to the models in a form which might be applicable to vehicles with arbitrary structural properties. To derive an expression for the input, it is necessary to make assumptions as to the nature and distribution of the input forces and then to calculate the magnitude of the input from the observed response using the measured structural properties of the models. The rigorous development of the relation between input and response can be very complicated and can obscure the functions of the important variables. So, another consideration in developing the coefficients was to evolve as simplified a form as possible, making approximations consistent with the accuracy of the test results.

The equations of motion applicable to an elastic body can be taken from sources such as reference 11 or 12. Assume the body to be as shown in the sketch:



The deflection, w , of a point on the body is the sum of the deflections in each mode of oscillation and may be separated into functions of time and distance from the origin to facilitate the solution of the equations; that is,

$$w = \sum_{i=1}^{\infty} \varphi_i \xi_i \quad (1)$$

where

ϕ_i mode shape, normalized to 1 at tip, as a function of distance, y , from the origin, in the i th mode of oscillation

ξ_i generalized displacement of the body as a function of time, t , in the i th mode of oscillation

The generalized mass is

$$M_i = \int_L \phi_i^2 m \, dy \quad (2)$$

where m is mass per unit length, and L is total length of the moving mass. The generalized force is

$$\bar{H}_i = \int_L \phi_i F x \, dy \quad (3)$$

where F is external force per unit area. The equation of motion for the body oscillating in the i th mode is

$$M_i \ddot{\xi}_i + 2\zeta_i \omega_i M_i \dot{\xi}_i + \omega_i^2 M_i \xi_i = \bar{H}_i \quad (4)$$

where

$\ddot{\xi}_i$ generalized acceleration

$\dot{\xi}_i$ generalized velocity

ζ_i ratio of damping to critical damping

ω_i undamped natural frequency, $2\pi f_i$

To define the nature of the exciting force F , it is assumed that the force is independent of the response and is random. The data presented elsewhere in the report indicate that these are usually adequate assumptions, although certainly not strictly correct. The pressure data strongly indicate that the force fluctuations of most concern occur in the vicinity of the nose, because the pressure fluctuations can have the greatest amplitude and coherence in this area. Considering the constant-diameter section just below the nose (the only section near the nose having appreciable area on which the pressures can act), one may denote the force per unit area as

$$F_{\text{nose}} = C_F q \quad (5)$$

where C_F is a randomly varying coefficient of force near the nose and q is the free-stream dynamic pressure. This force can also be expressed in terms of its power spectrum, as was done in references 2 and 13 for the two-dimensional case; that is, the mean square force per unit area is

$$\overline{F_{\text{nose}}^2} = \overline{C_F^2} q^2 \int_0^\infty F\left(\frac{nD}{V}\right) d\left(\frac{nD}{V}\right) \quad (6)$$

where $F(nD/V)$ = power spectrum of force near nose, normalized such that

$$\int_0^\infty F\left(\frac{nD}{V}\right) d\left(\frac{nD}{V}\right) = 1$$

with

n frequency of external force

D diameter at base of nose

V free-stream velocity

For vehicles very short compared to their diameters, F_{nose} would presumably be the force per unit area for the entire vehicle. However, it is deduced from the data of this report that for "long" vehicles, the force per unit area averaged over the span would be less than F_{nose} . A convenient way to compensate for this deviation is to divide F_{nose} by the average fineness ratio and consider this to be the force per unit area applicable to the body; that is,

$$F = F_{\text{nose}} \frac{A}{L^2} \quad (7)$$

where A is frontal area. This is obviously not applicable to the two-dimensional case. Neither is it applicable to bending modes higher than the first cantilever mode, since the force was defined empirically from data which are significant only in the first mode. Consequently, the i indicating any mode will be dropped; and the equations henceforth will be applied to the first mode only.

The power spectrum of the generalized force can be derived from equations (3), (6), and (7), and can be combined with the mechanical impedance to give the solution to equation (4) as was done in reference 2. In the symbols of the present report,

$$\overline{\xi^2} = \left(\int_L \varphi x \, dy \right)^2 \left(\frac{A}{L^2} \right)^2 \overline{C_F^2} q^2 \int_0^\infty \frac{F\left(\frac{nD}{V}\right) d\left(\frac{nD}{V}\right)}{M^2 \omega^4 \left| 1 - \left(\frac{2\pi n}{\omega} \right)^2 + 2i\zeta \frac{2\pi n}{\omega} \right|^2} \quad (8)$$

If it is assumed that

$$F\left(\frac{nD}{V}\right) = F\left(\frac{fD}{V}\right) \quad (9)$$

and $\zeta \ll 1$, the deflection can be approximated (as in ref. 2) by

$$\overline{\xi^2} = \left(\frac{1}{r} \right)^2 A^2 \overline{C_F^2} q^2 \frac{\pi}{4} \frac{fD}{V} F\left(\frac{fD}{V}\right) \frac{1}{M^2 \omega^4 \zeta} \quad (10)$$

where

$$\frac{1}{r} = \int_0^1 \varphi \frac{x}{L} d\left(\frac{y}{L}\right) \quad (11)$$

One must resort to experiment to determine $\overline{C_F^2}$, $F(fD/V)$, and the ratio of the maximum expected value, ξ_{\max} , to the rms value $\sqrt{\xi^2}$. It seems logical, then, to combine these strictly empirical factors and the numerical constants into one coefficient. This dynamic input coefficient will be termed $C_{l,d}$ for the lateral direction and $C_{m,d}$ for the dragwise direction. In the lateral direction, then,

$$C_{l,d} = \sqrt{\frac{\xi_{\max}^2}{\xi^2} \overline{C_F^2} \frac{\pi}{4} F\left(\frac{fD}{V}\right)} \quad (12)$$

so that

$$\xi_{\max} = C_{l,d} \left(\frac{1}{r}\right) Aq \sqrt{\frac{fD}{V} \frac{1}{\xi} \frac{1}{M\omega^2}} \quad (13)$$

The deflection can be related to the bending moment at any desired station by experiment or by the mode displacement method (ref. 11). The moment at the base is equal to the inertial loads on each segment, $m\xi\varphi\omega^2$, converted to moments and integrated over the total length of the vehicle. The maximum amplitude of the base bending moment is

$$\begin{aligned} (M_l)_{\max} &= \xi_{\max} \omega^2 \int_L \varphi m y \, dy \\ &= C_{l,d} \left(\frac{1}{r}\right) Aq \sqrt{\frac{fD}{V} \frac{1}{\xi}} L \left[\frac{\int_0^1 \varphi m \frac{y}{L} d\left(\frac{y}{L}\right)}{\int_0^1 \varphi^2 m d\left(\frac{y}{L}\right)} \right] \end{aligned} \quad (14)$$

In this equation it is assumed that the base is at $y = 0$ and that the moving mass is from the base up. It is convenient to replace the expression in brackets by $1/N$. The object of the tests, then, is to measure $(M_l)_{\max}$ and calculate values of the coefficient from

$$C_{l,d} = \frac{(M_l)_{\max}}{qAL} \left[Nr \sqrt{\frac{V}{fD} \xi} \right] \quad (15)$$

It is presumed that these values of $C_{l,d}$ will apply to any vehicle for which reduced frequency, Reynolds number, and the aerodynamic shape near the nose are duplicated.

The part of the expression for $C_{l,d}$ outside the brackets is a typical aerodynamic coefficient. The rest of the expression modifies the coefficient according to the structural properties. The number N would be unity if ϕ were equal to y/L , which is the situation when all the bending takes place at the base. Values of N for the modular models reported herein fell between 0.88 and 1.00, so it is apparent that mass distribution had little effect on the coefficients. The ratio r is a kind of generalized fineness ratio and would be twice the geometrical fineness ratio for a constant-diameter vehicle if $\phi = y/L$. Values of r for the models fell between 11 and 36.

In reference 14 there is developed a form for representing the oscillatory input to a vehicle, and $C_{l,d}$ is equal to $\sqrt{(\pi/4)\phi(S)}$ in that reference if certain substitutions are made. The primary difference results from the assumption made herein that the nose forces predominate. Reference 14 substitutes a mode participation factor, W_n , for the term $1/r$. It also bases reduced frequency fD/V on the first stage diameter instead of the diameter of the base of the nose. Either relation will result in the same full-scale bending moments if it is applied to data for a model geometrically similar to the full-scale vehicle. Differences will arise if the model data are applied to any other configuration. The only expected advantage of using $C_{l,d}$, then, is to have a more logical basis for comparing different geometrical shapes.

Methods of determining the input forces by means of pressure measurements and more exact relations between the input and response are outlined in references 9 and 10.

REFERENCES

1. Roshko, Anatol: On the Development of Turbulent Wakes From Vortex Streets. NACA Rep. 1191, 1954.
2. Fung, Y. C.: Fluctuating Lift and Drag Acting on a Cylinder in a Flow at Supercritical Reynolds Numbers. Jour. Aero/Space Sci., vol. 27, no. 11, Nov. 1960, pp. 801-13.
3. Roshko, Anatol: Experiments on the Flow Past a Circular Cylinder at Very High Reynolds Number. Jour. Fluid Mechanics, vol. 10, pt. 3, May 1961, pp. 345-56.
4. Buell, Donald A., and Kenyon, George C.: The Wind-Induced Loads on a Dynamically Scaled Model of a Large Missile in the Launching Position. NASA TM X-109, 1959.
5. Bohne, Quentin R.: Power Spectral Considerations on the Launch Pad. USAF Geophysics Research Directorate, Air Force Surveys in Geophysics No. 140, Proc. National Symposium on Winds for Aerospace Vehicle Design, vol. I, AFCRL-62-273(I), March 1962.
6. Herriot, John G.: Blockage Corrections for Three-Dimensional-Flow Closed-Throat Wind Tunnels, With Consideration of the Effect of Compressibility. NACA Rep. 995, 1950.
7. Crandall, Stephen H., ed.: Random Vibration. Second ed., Cambridge Technology Press of M.I.T., 1958.
8. Bendat, Julius S., et al.: The Application of Statistics to the Flight Vehicle Vibration Problem. USAF, ASD Tech. Rep. 61-123, Dec. 1961.
9. Fung, Y. C.: The Analysis of Wind-Induced Oscillations of Large and Tall Cylindrical Structures. Tech. Rep. no. STL/TR-60-0000-09134, Space Technology Laboratories, Inc., June 1960.
10. Bohne, Q. R.: Ground Wind-Induced Loads on Launch Vehicles. Boeing, ASD Tech. Doc. Rep. ASD-TDR-62-371, Aug. 1962.
11. Bisplinghoff, Raymond L., Ashley, Holt, and Halfman, Robert L.: Aeroelasticity. Addison-Wesley, Cambridge, Mass., 1955.
12. Fung, Y. C.: An Introduction to the Theory of Aeroelasticity. Galcit Aeronautical Series, John Wiley and Sons, N. Y., 1955.
13. Wood, J. D., and Berry, J. G.: Random Excitation of Missiles Due to Winds. USAF Geophysics Research Directorate, Air Force Surveys in Geophysics no. 140, Proc. National Symposium on Winds for Aerospace Vehicle Design, vol. I, AFCRL-62-273(I), March 1962.
14. Ezra, A. A., and Birnbaum, S.: Design Criteria for Space Vehicles to Resist Wind Induced Oscillations. American Rocket Society Paper 1081-60.

TABLE I. - DIMENSIONS OF MODULES

Name of Module	Diameter, ft	Length, ft
14-inch stiff base	1.158	4.560
14-inch flexible base	1.158	4.560
14-inch light center	1.158	2.062
14-inch heavy top	1.158	1.490
14-inch light top	1.158	1.545
14- to 10-inch transition	---	.989
10-inch heavy center	.874	1.486
10-inch light center	.874	1.567
10-inch heavy top	.874	1.486
10-inch light top	.874	1.583
14- to 8-inch transition ¹	---	1.000
8-inch center ¹	.703	1.531
8-inch heavy top	.703	1.485
8-inch light top	.703	1.567
8-inch stiff base	.703	4.070
8-inch flexible base	.703	4.059
8-inch flat face	.703	3.970
8- to 5-inch transition ¹	---	.625
5-inch top ¹	.438	1.945

¹Transition and adjoining section in one piece

TABLE II.- INDEX OF FIGURES

<u>Number</u>	
1-8	Model sketches and photographs
9	Mode shapes
10	Structural damping
11	Sample oscillogram of base bending moments
	Dynamic-moment characteristics of models:
12	Double-cone nose
13	Applied to hypothetical full-scale vehicles
	Hemisphere nose:
14-15	Upper-stage diameter equal to lower
16	Upper-stage diameter $3/4$ of lower
17	Upper-stage diameter $3/5$ of lower
18	Summary
	Cone-cylinder nose:
19-20	Upper-stage diameter equal to lower
21	Upper-stage diameter $3/4$ of lower
22	Upper-stage diameter $3/5$ of lower
23	Summary
24-26	Blunted-cone nose
27	Flat-face
28	Tapered upper stage
29	Miscellaneous nose shapes
30-31	Spoilers
32-35	Roughness
36	Conduits
37	Friction damper
38	Statistical distributions
	Steady-state force and moment characteristics:
39	Forces and moments
40-43	Moments only
44-45	Oil-flow pictures
46-47	Steady-state pressure characteristics
	Fluctuating pressure and moment spectra:
48	Sinusoidal input
	Pressures at stations near nose:
49-54	Hemisphere nose
55-56	Cone-cylinder nose
57-59	Blunted-cone nose
60-61	Pressures at lower stations
62-63	Pressures at various radial locations
64-67	Pressures in wake

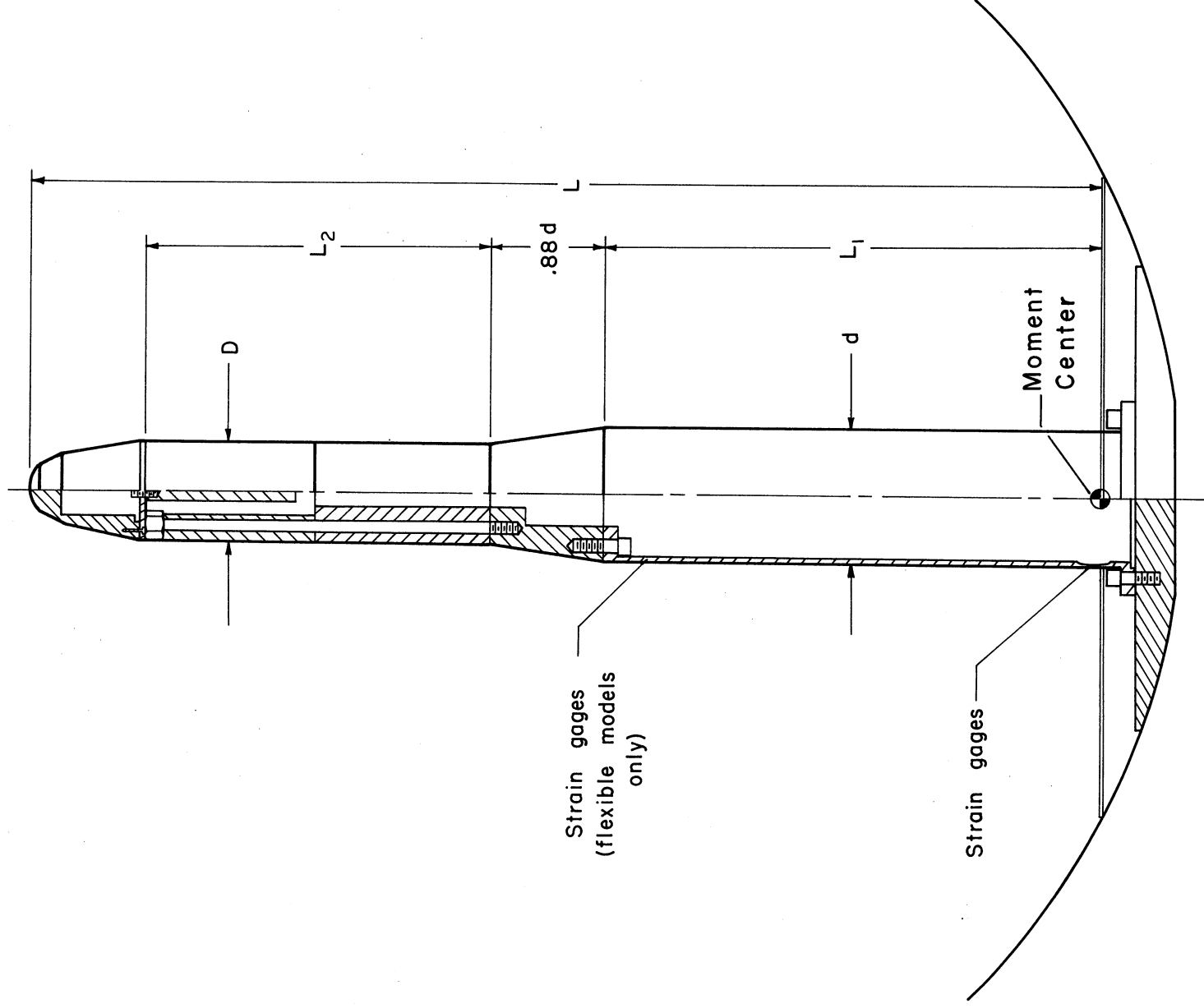
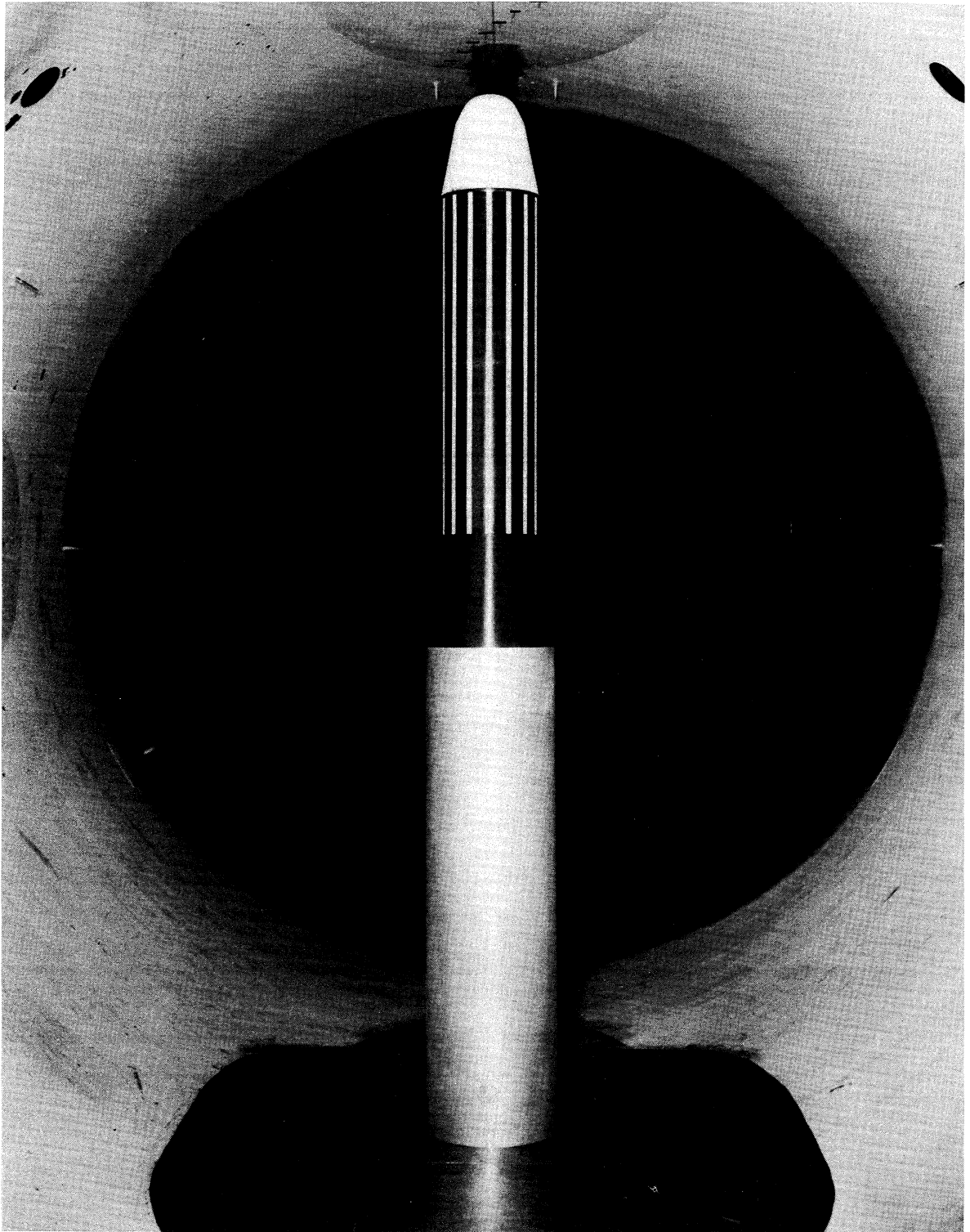
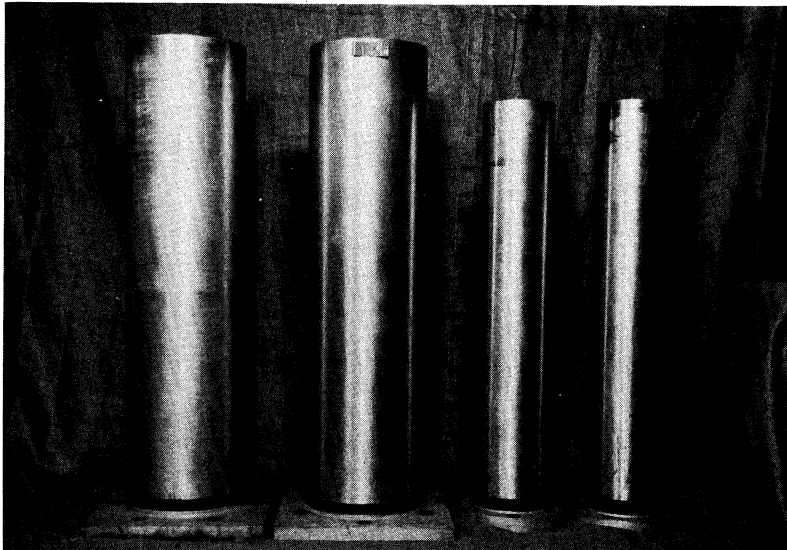


Figure 1.- Sketch of a typical modular model with heavy upper stage.
 Variations in model combinations: $d = 0.703$ or 1.158 feet;
 $D = 0.438$ to 1.158 feet; $L/D = 5.5$ to 16.6 ; $D/d = 3/5, 3/4$, and
 1 ; $L_2/L_1 = 0$ to 0.73 .



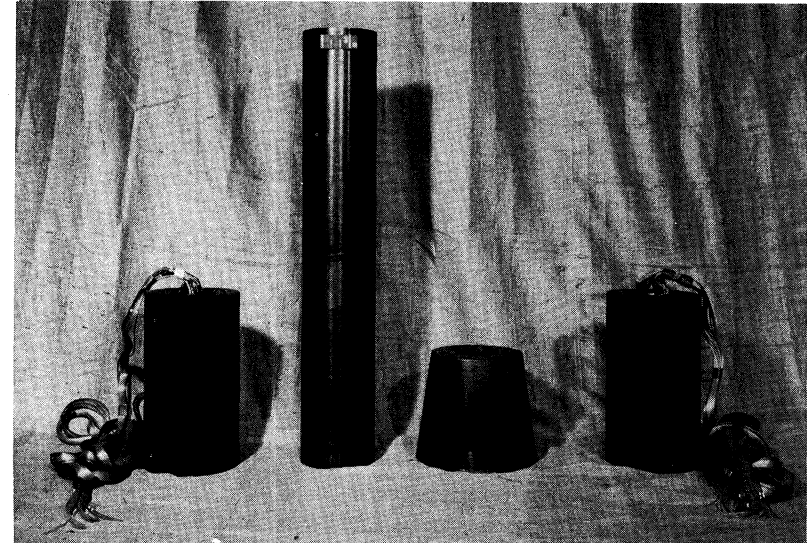
A-26163

Figure 2.- Photograph of a typical model installed in the wind tunnel showing standard roughness strips (tapes every 22.5° on front half).



A-27761

(a) 14-inch and 8-inch bases.



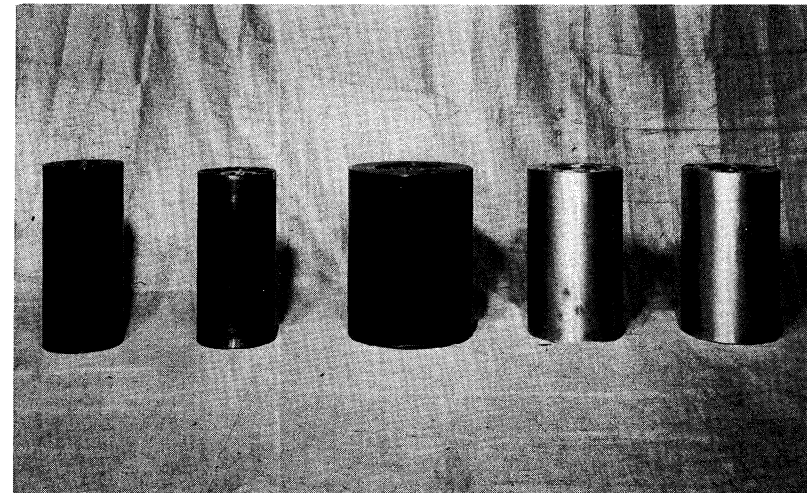
A-27763

(b) 10-inch and 8-inch sections and transition.



A-27762

(c) Transitions and 14-inch sections.



A-27764

(d) 8-inch, 14-inch, and 10-inch sections.

Figure 3.- Photograph of modules making up the models.

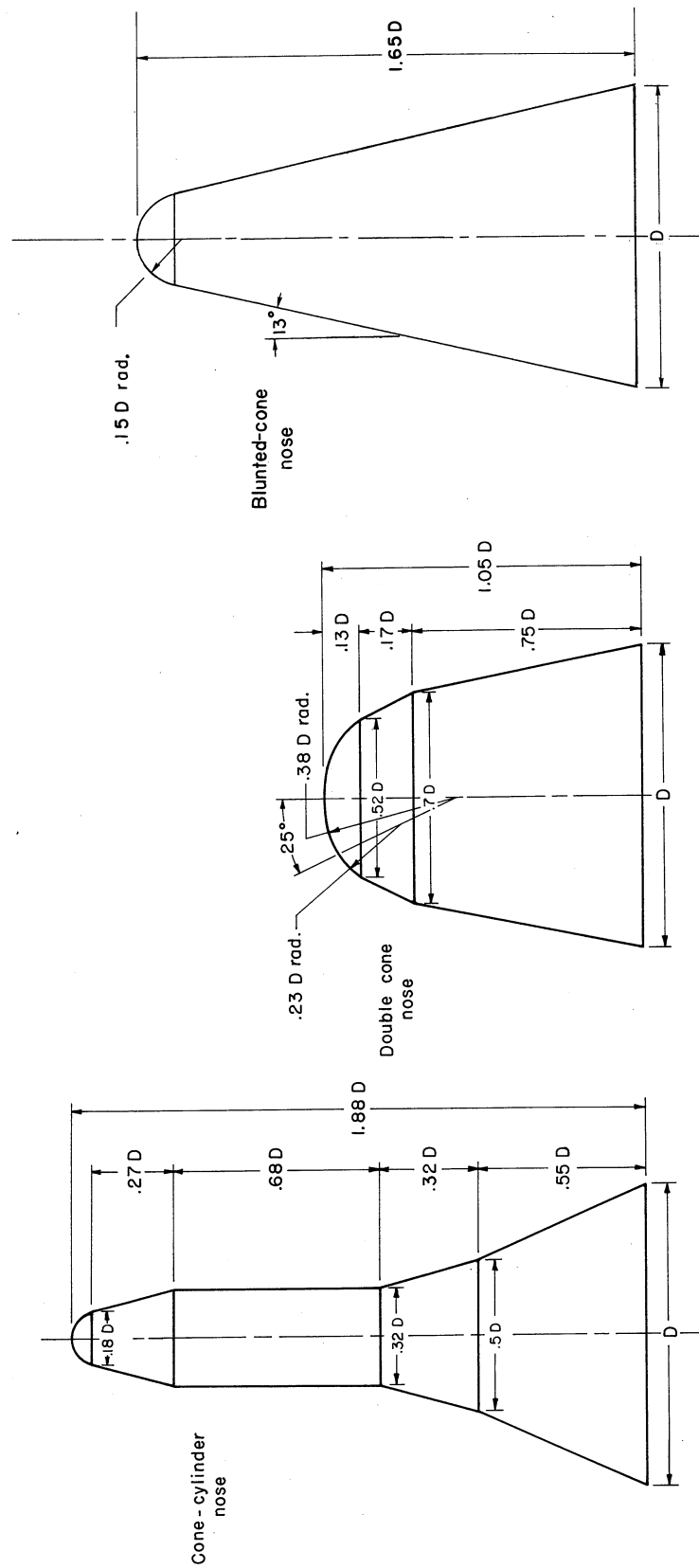


Figure 4.- Geometry of model noses not having simple geometrical forms;
 $D = 0.438, 0.703, 0.874, \text{ or } 1.158 \text{ feet.}$

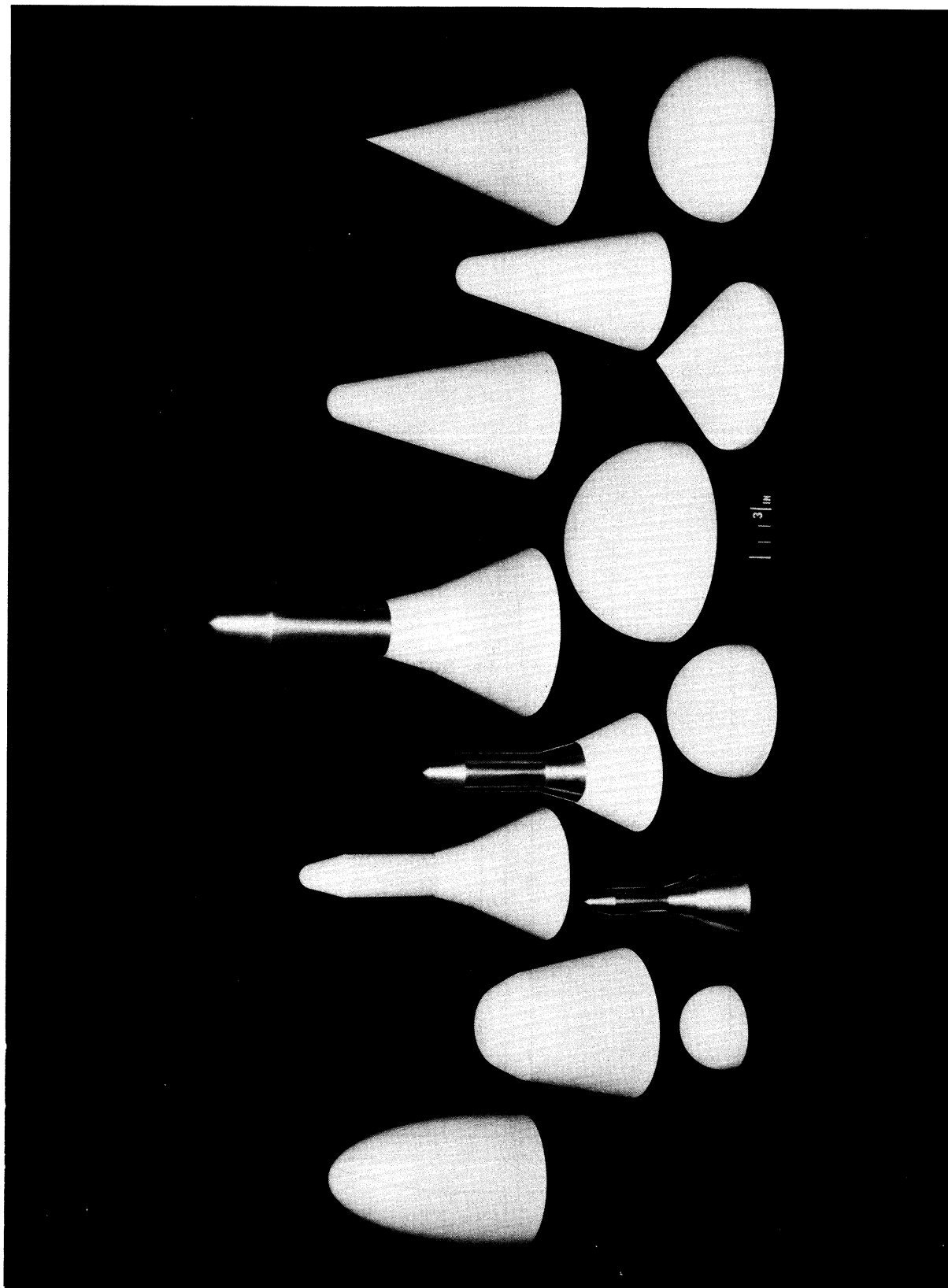
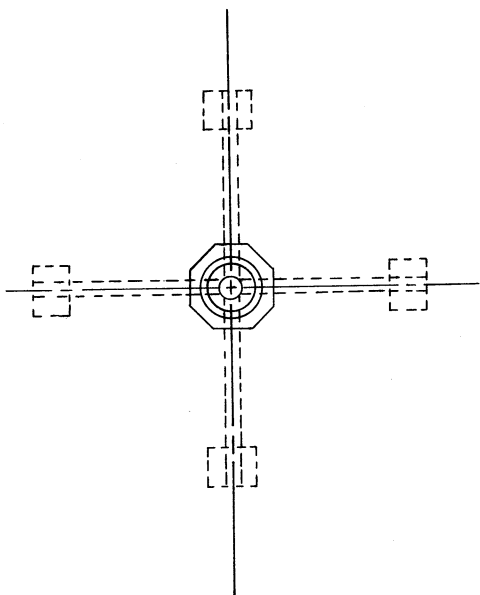


Figure 5.- Some of the model noses tested.

A-27760



All dimensions
in inches

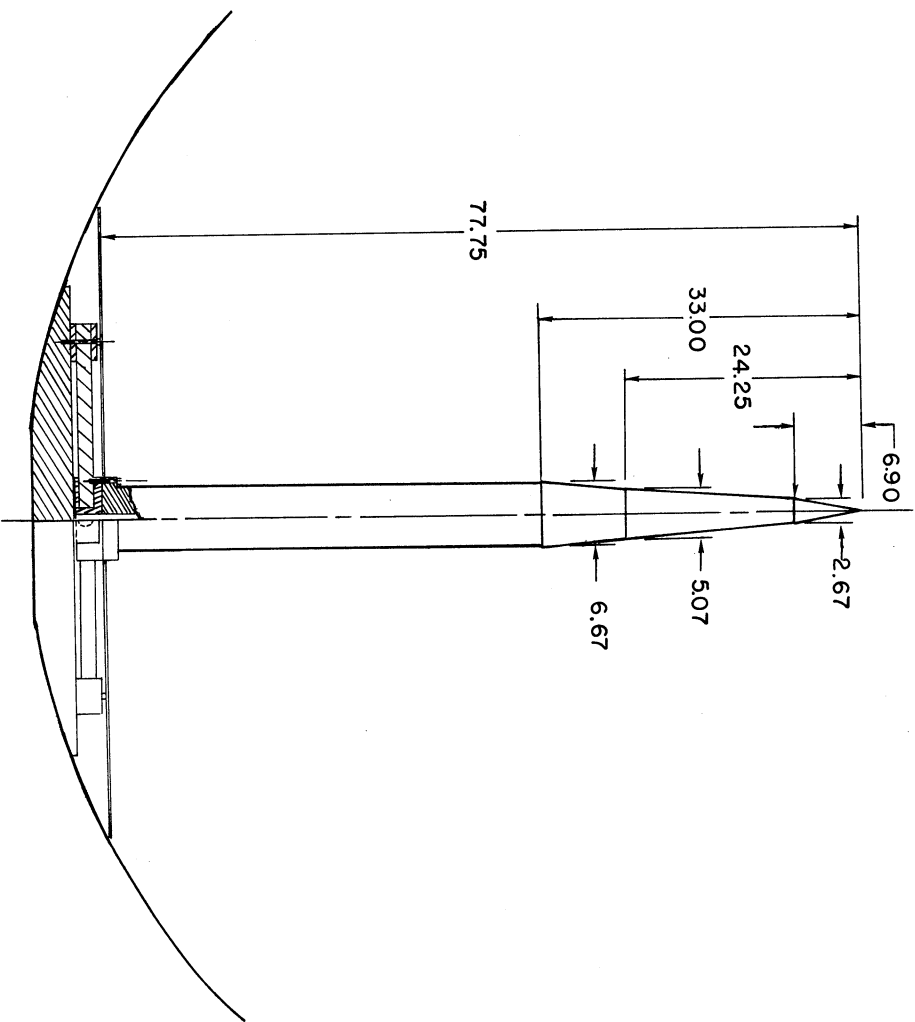
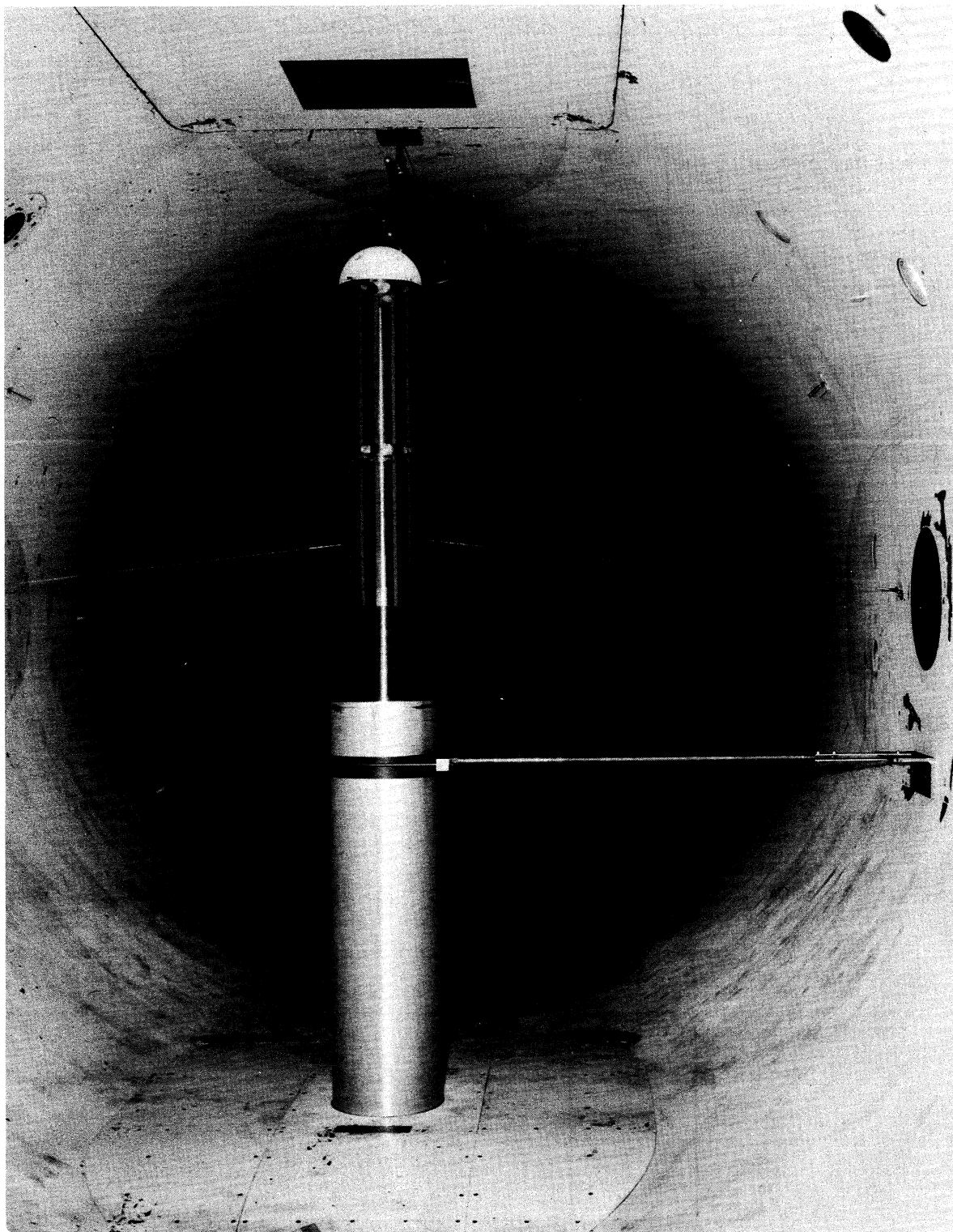
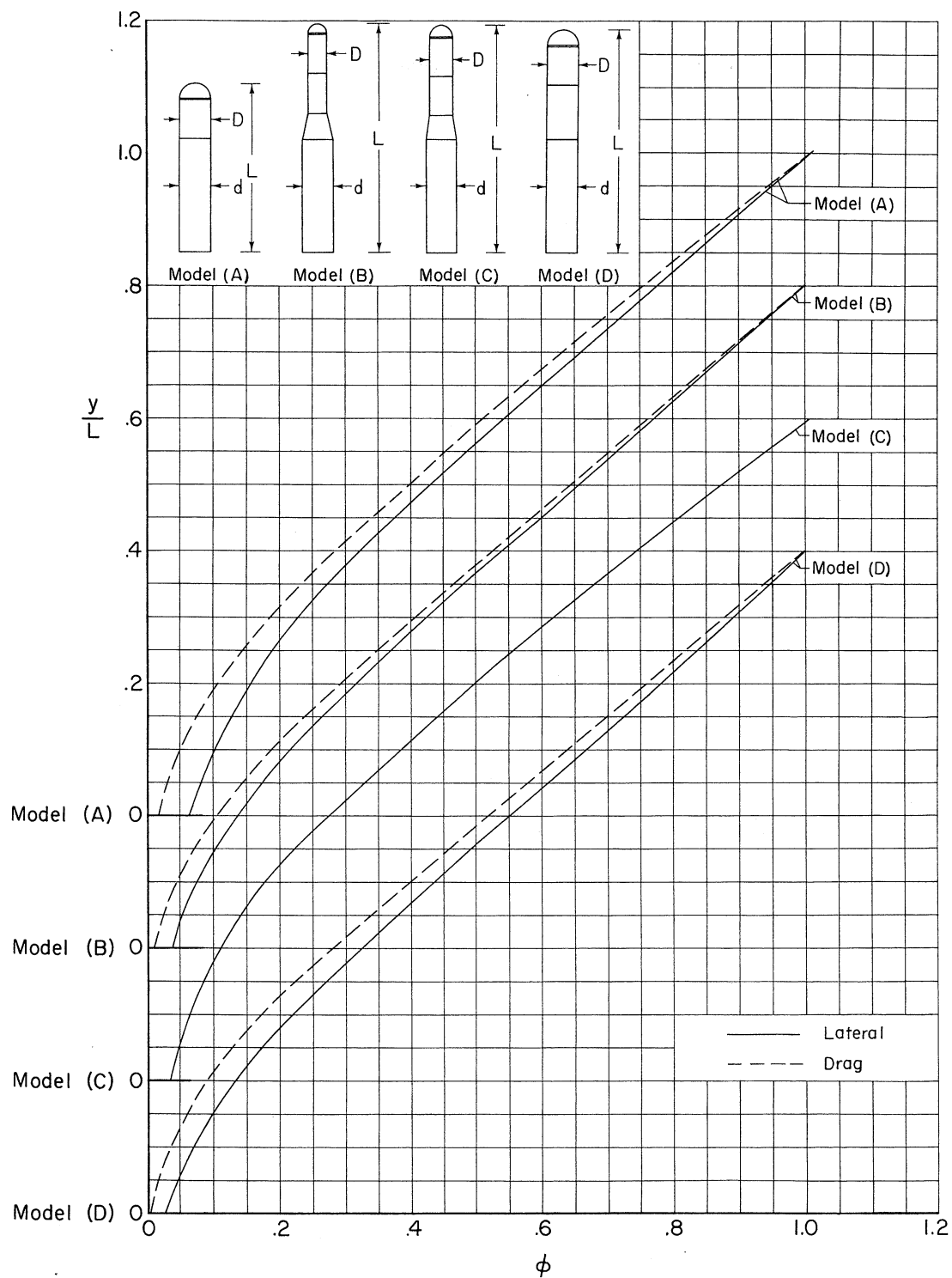


Figure 6.- Geometry of the model with tapered upper stage.



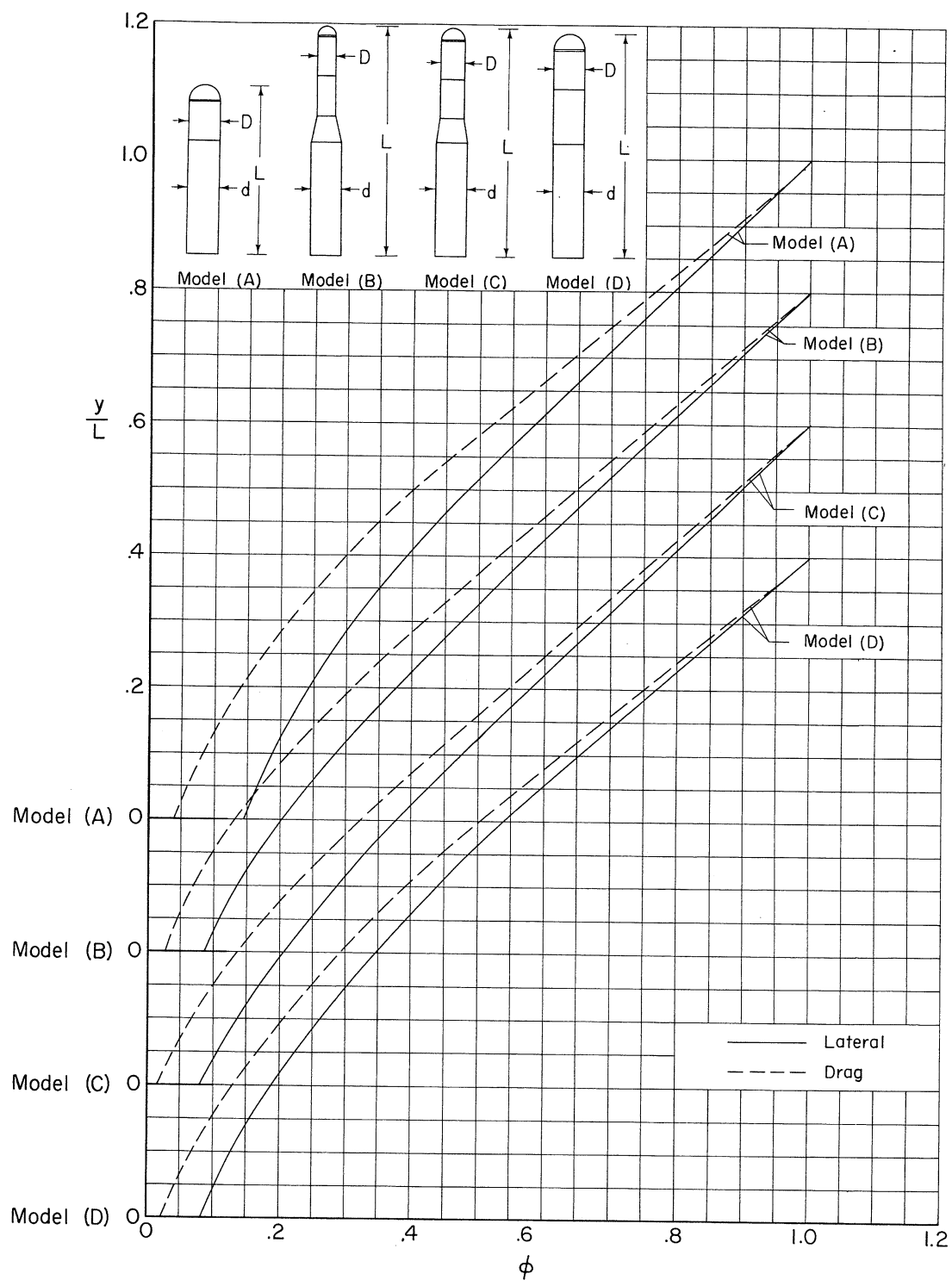
A-27435

Figure 8.- Photograph of a modular model containing pressure transducers and attached to the friction-damping device.



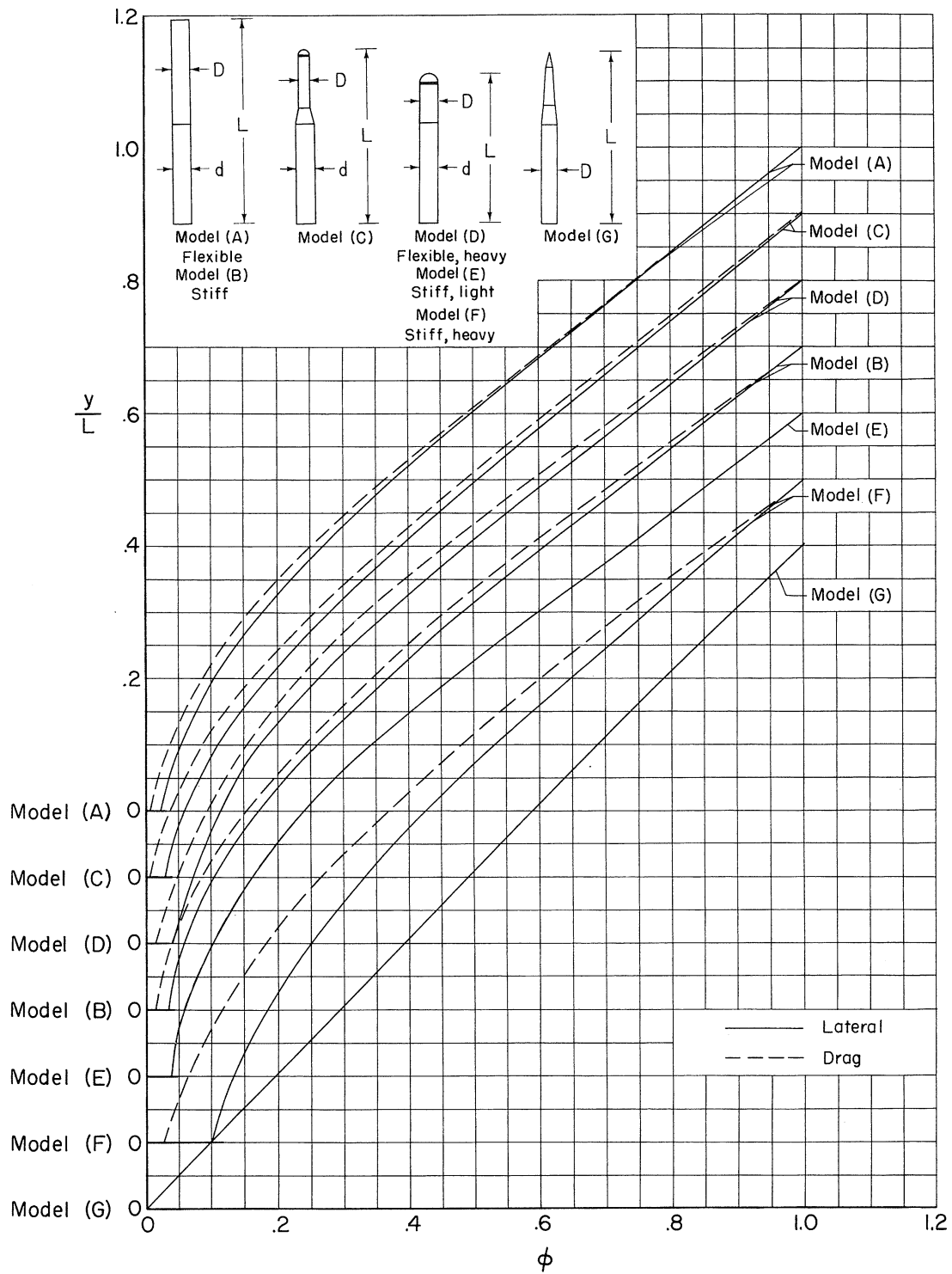
(a) Large flexible-base models, $d = 1.158$ feet.

Figure 9.- First cantilever mode shapes (typical of mode shapes for other nose configurations); $D/d = 3/5$, $3/4$, and 1; L/d from 5.5 to 11.1.



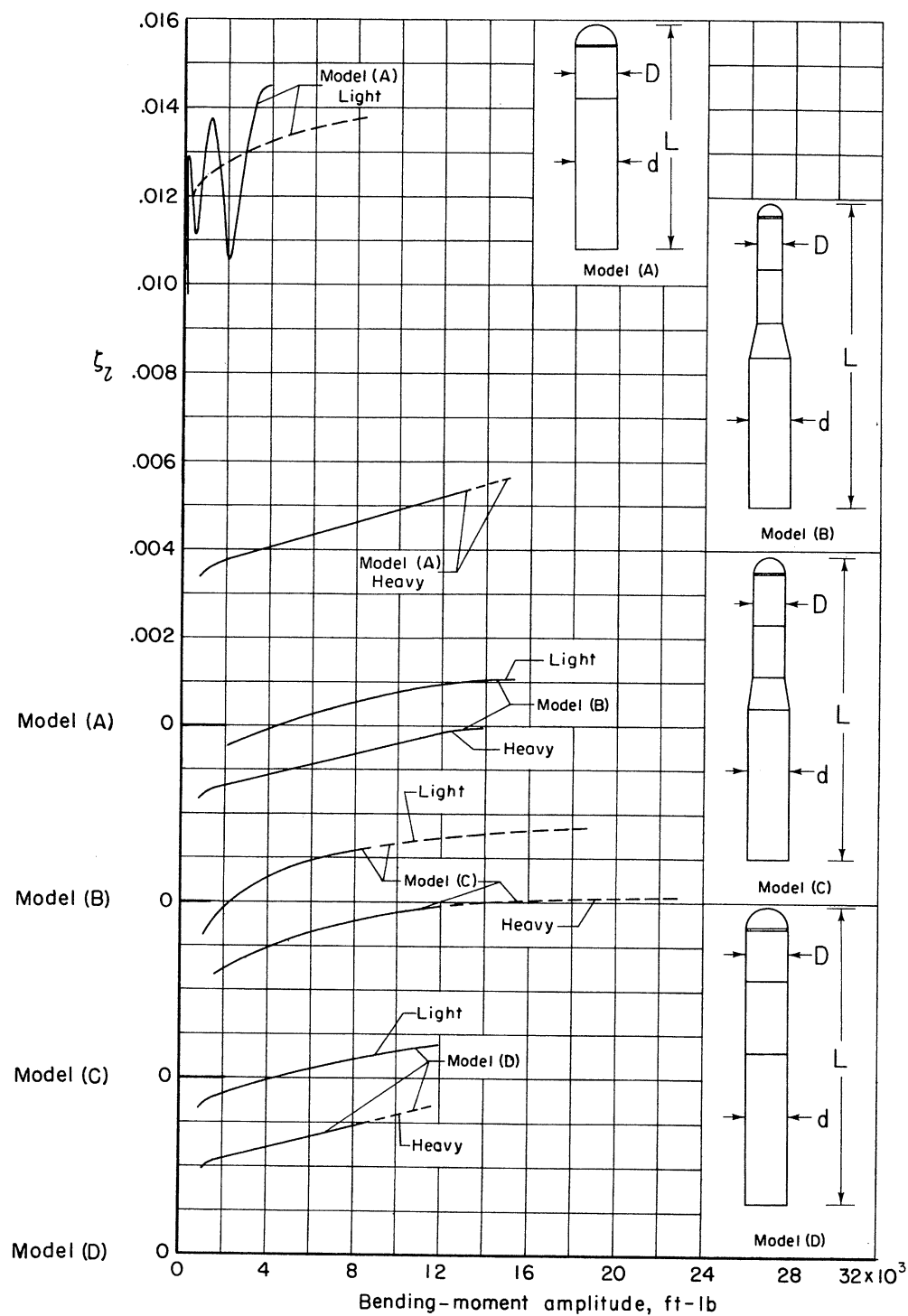
(b) Large stiff-base models; $d = 1.158$ feet.

Figure 9.- Continued.



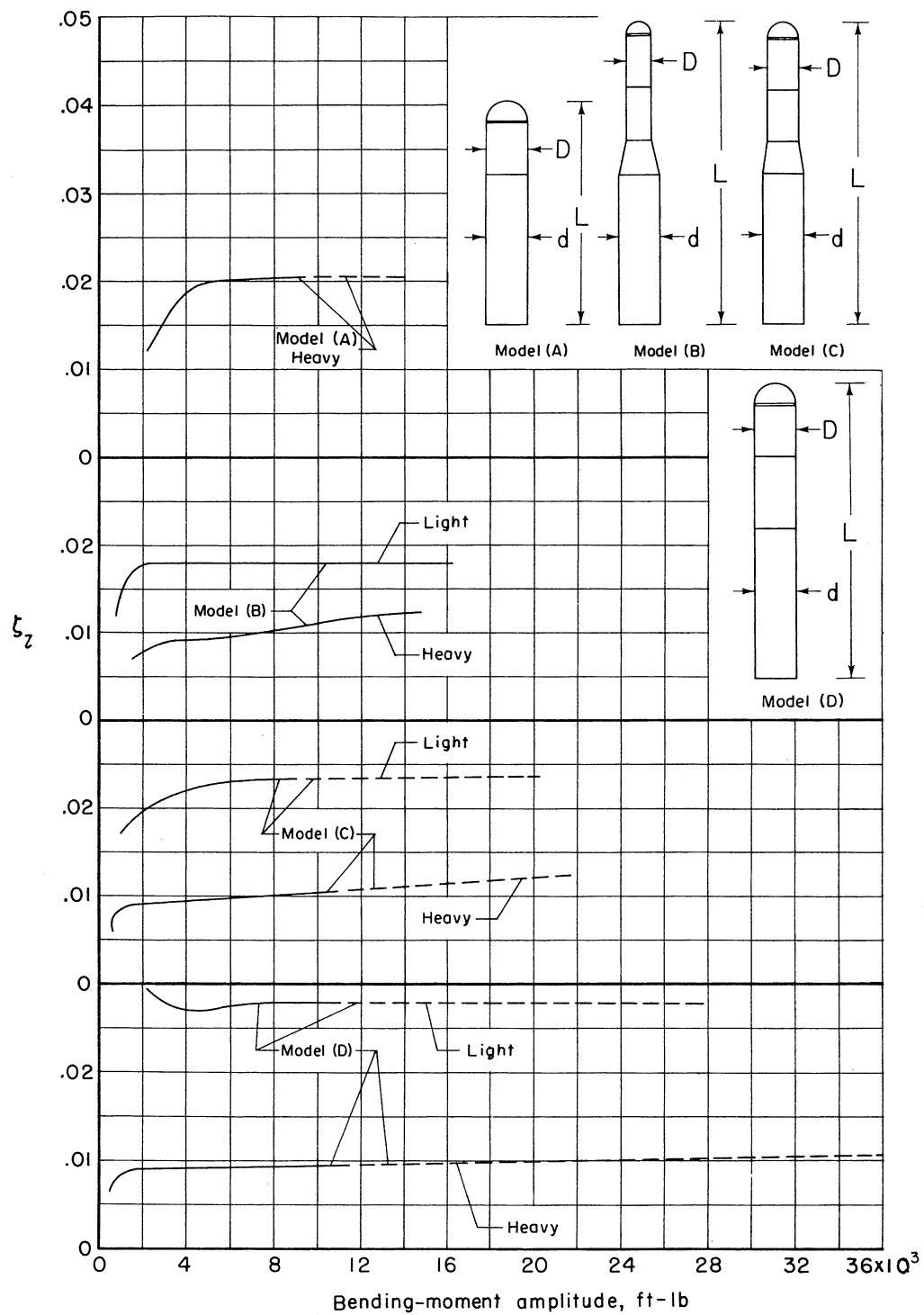
(c) Small-base models; $d = 0.703$ foot.

Figure 9.- Concluded.



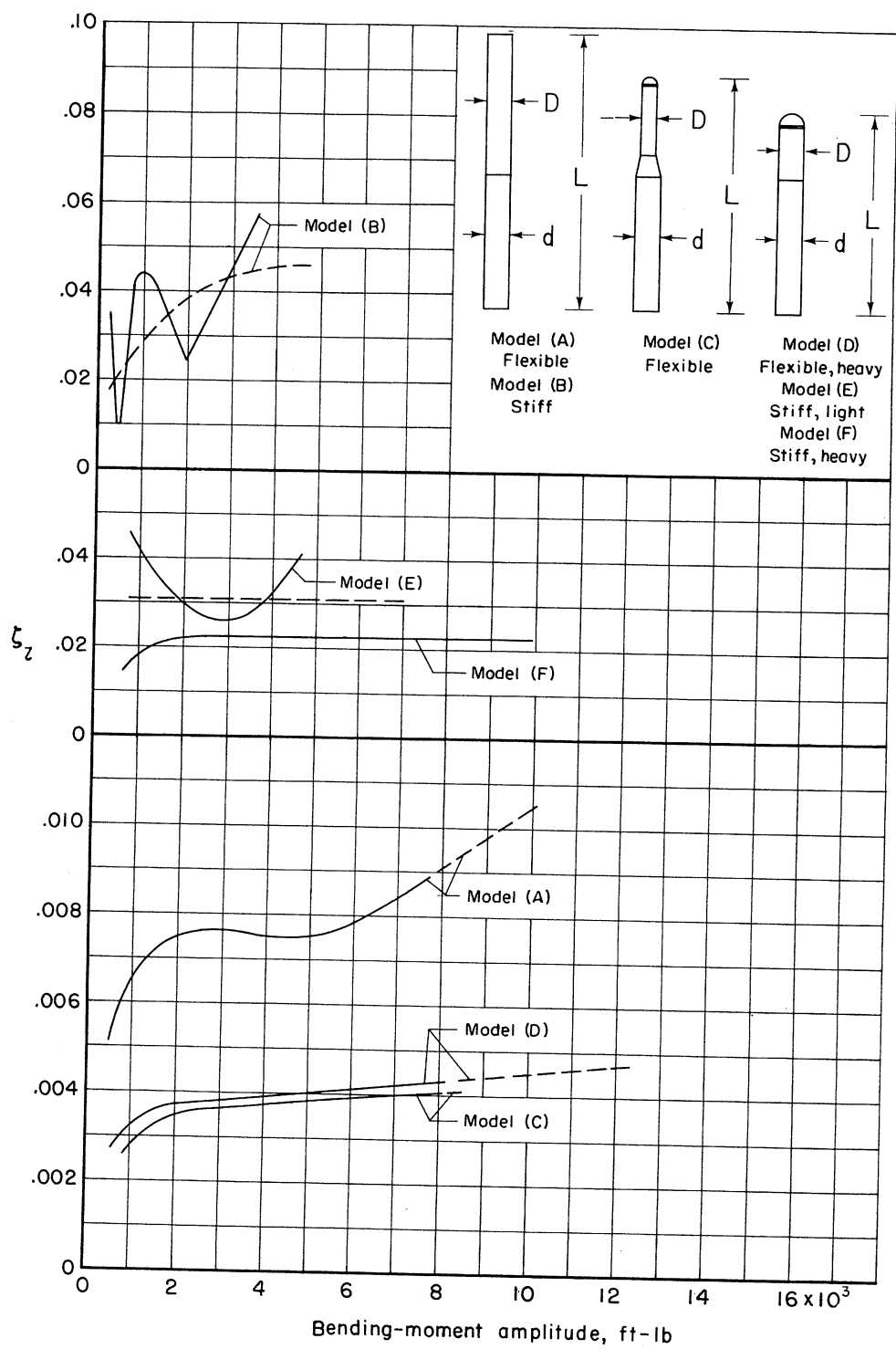
(a) Lateral damping of large flexible-base models; $d = 1.158$ feet.

Figure 10.- First-mode values of the ratio of damping to critical damping (typical of values for other nose configurations); $D/d = 3/5, 3/4$, and 1 ; $L/d = 5.5$ to 11.1 .



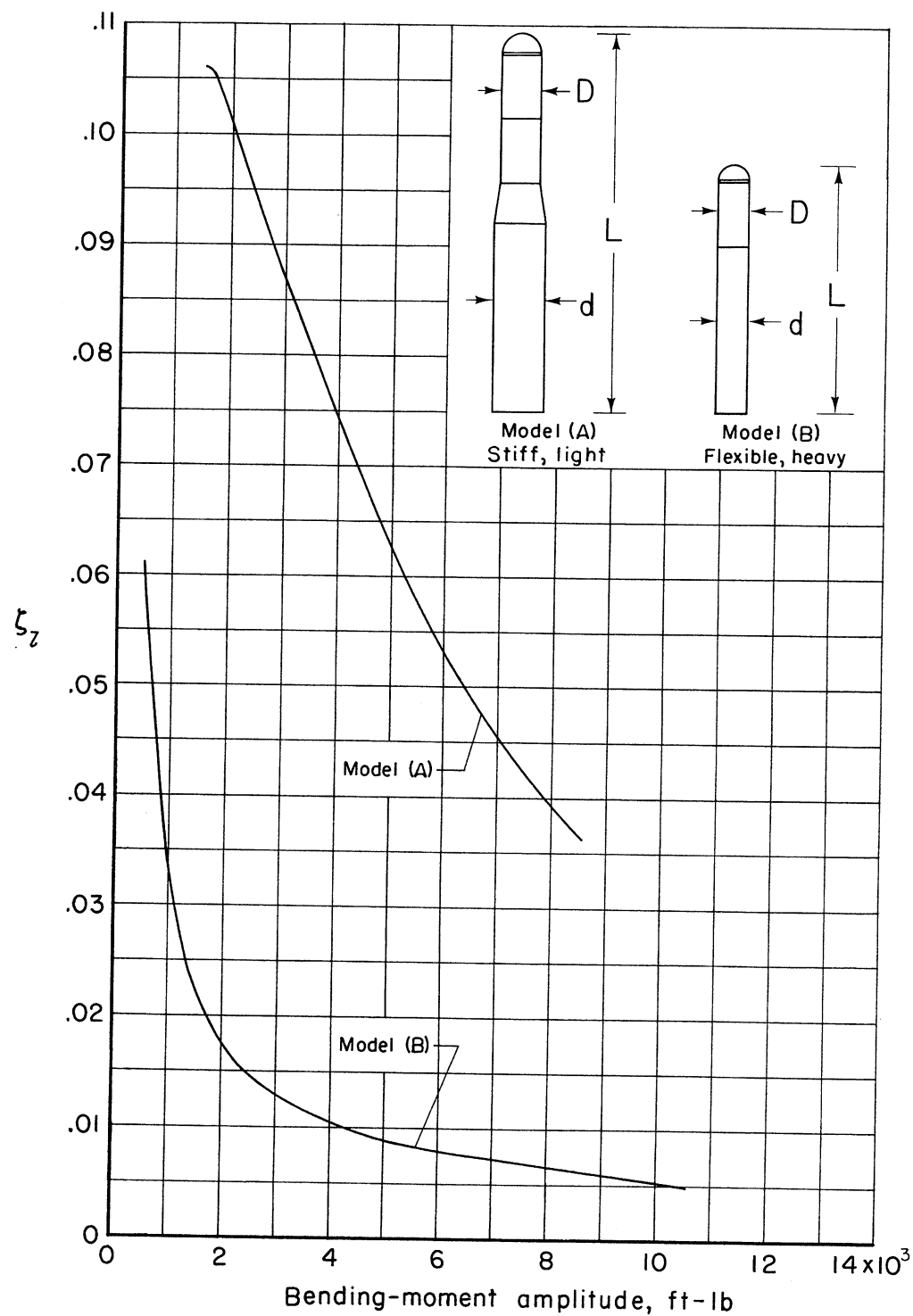
(b) Lateral damping of large stiff-base models; $d = 1.158$ feet.

Figure 10.- Continued.



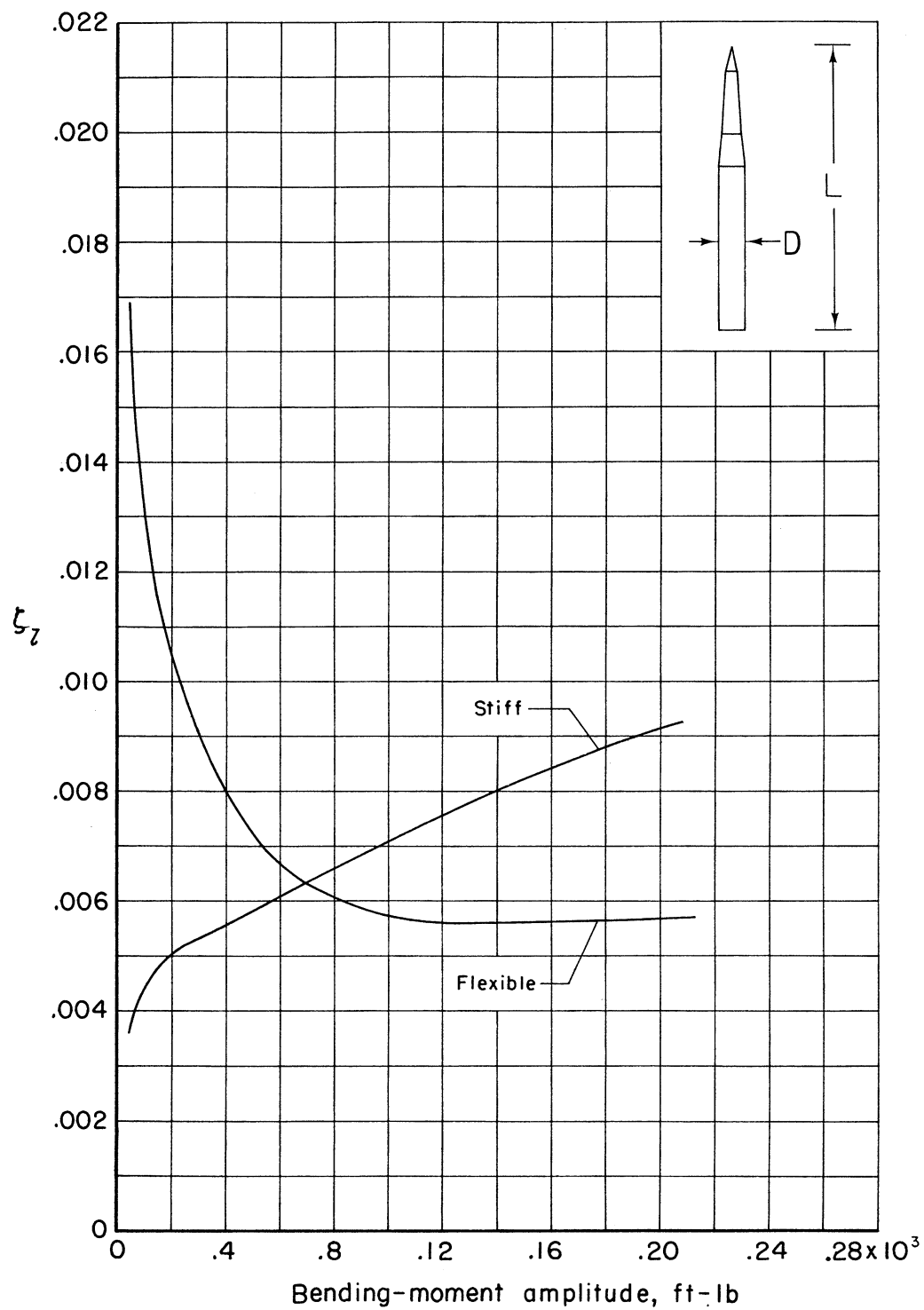
(c) Lateral damping of small-base models; $d = 0.703$ foot.

Figure 10.- Continued.



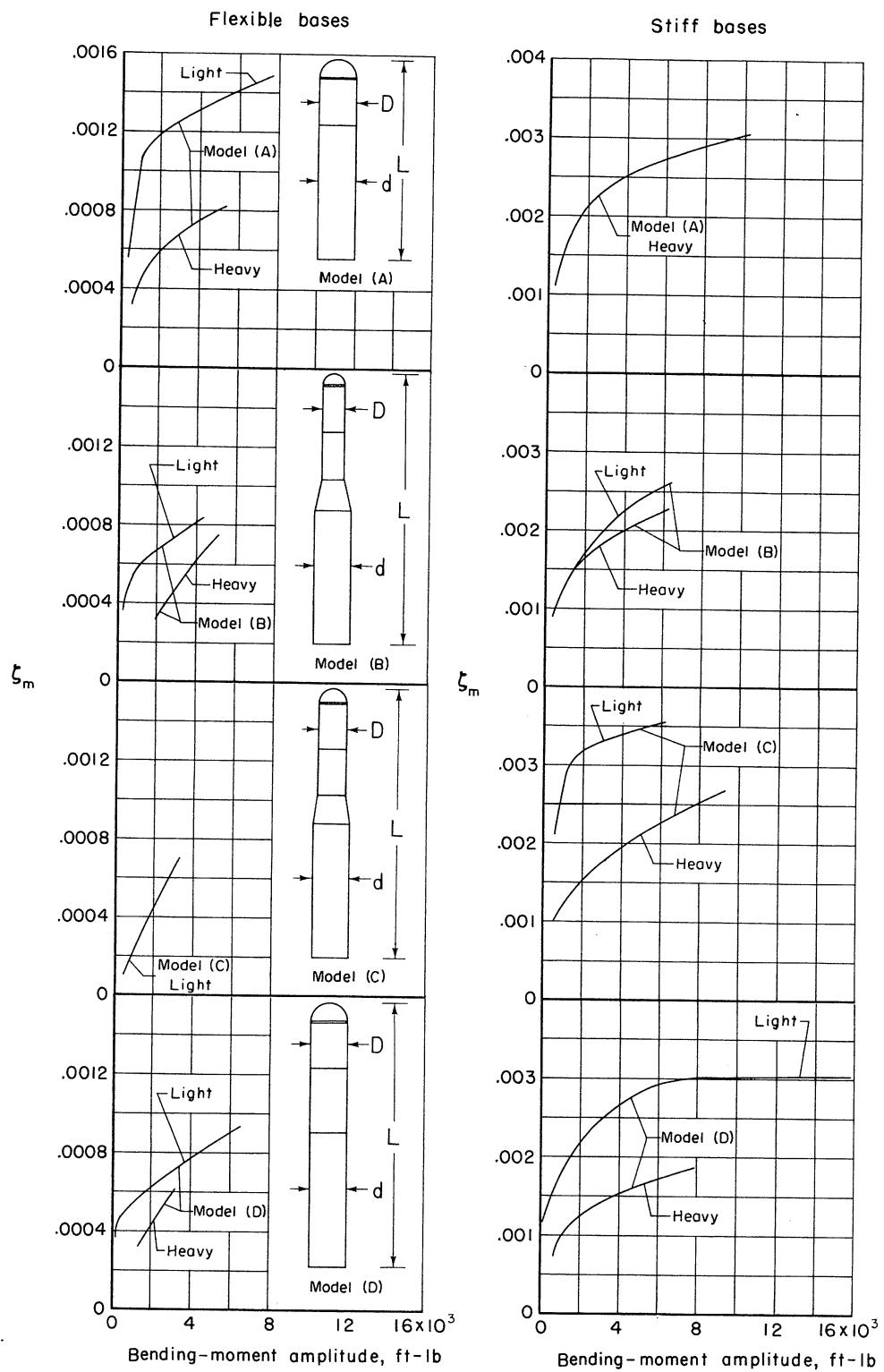
(d) Lateral damping of models with friction damper.

Figure 10.- Continued.



(e) Lateral damping of the model with tapered upper stage (typical of dragwise damping); $D = 0.555$ foot.

Figure 10.- Continued.



(f) Dragwise damping of large-base models; $d = 1.158$ feet.

Figure 10.- Continued.

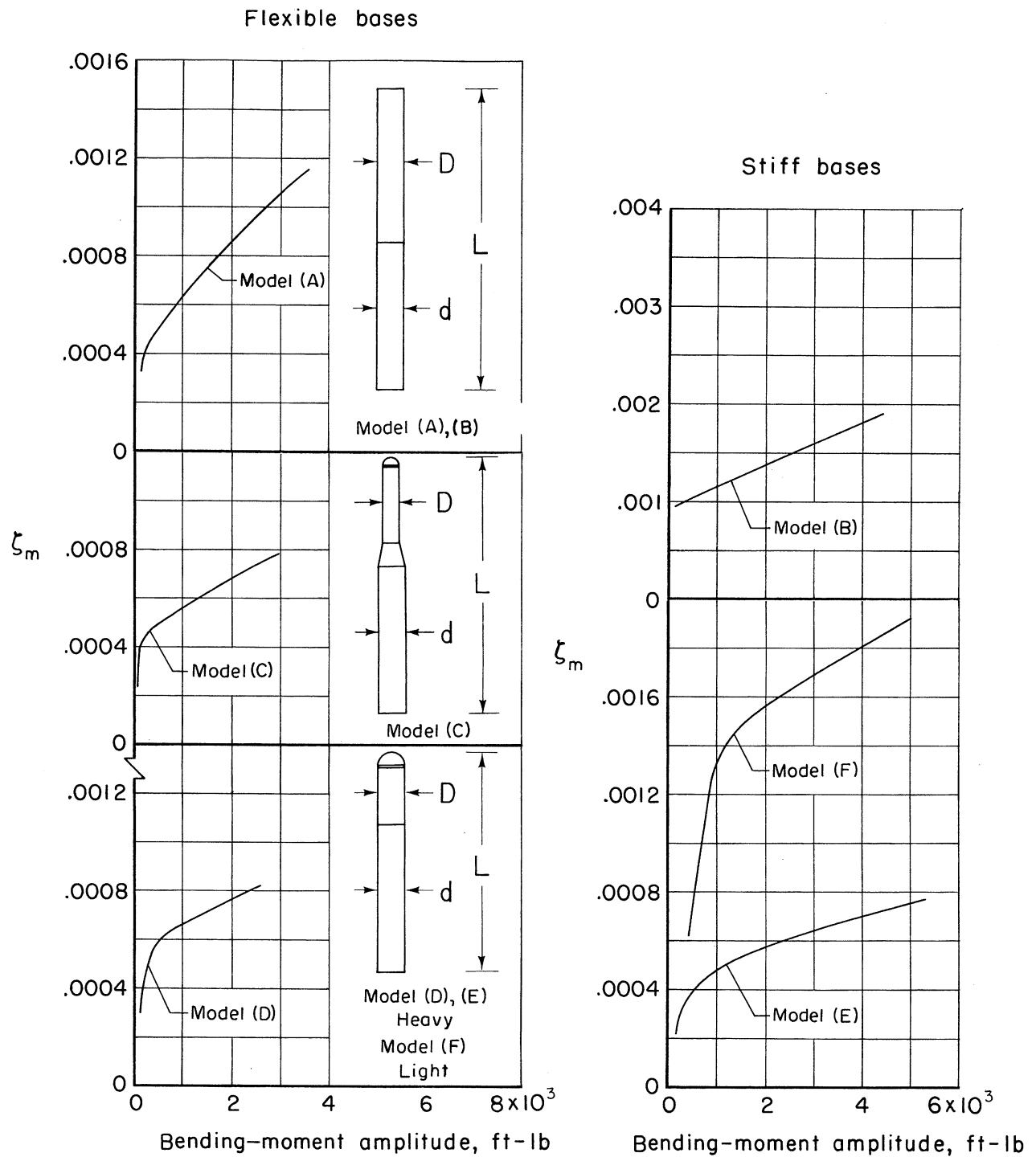


Figure 10.- Concluded.

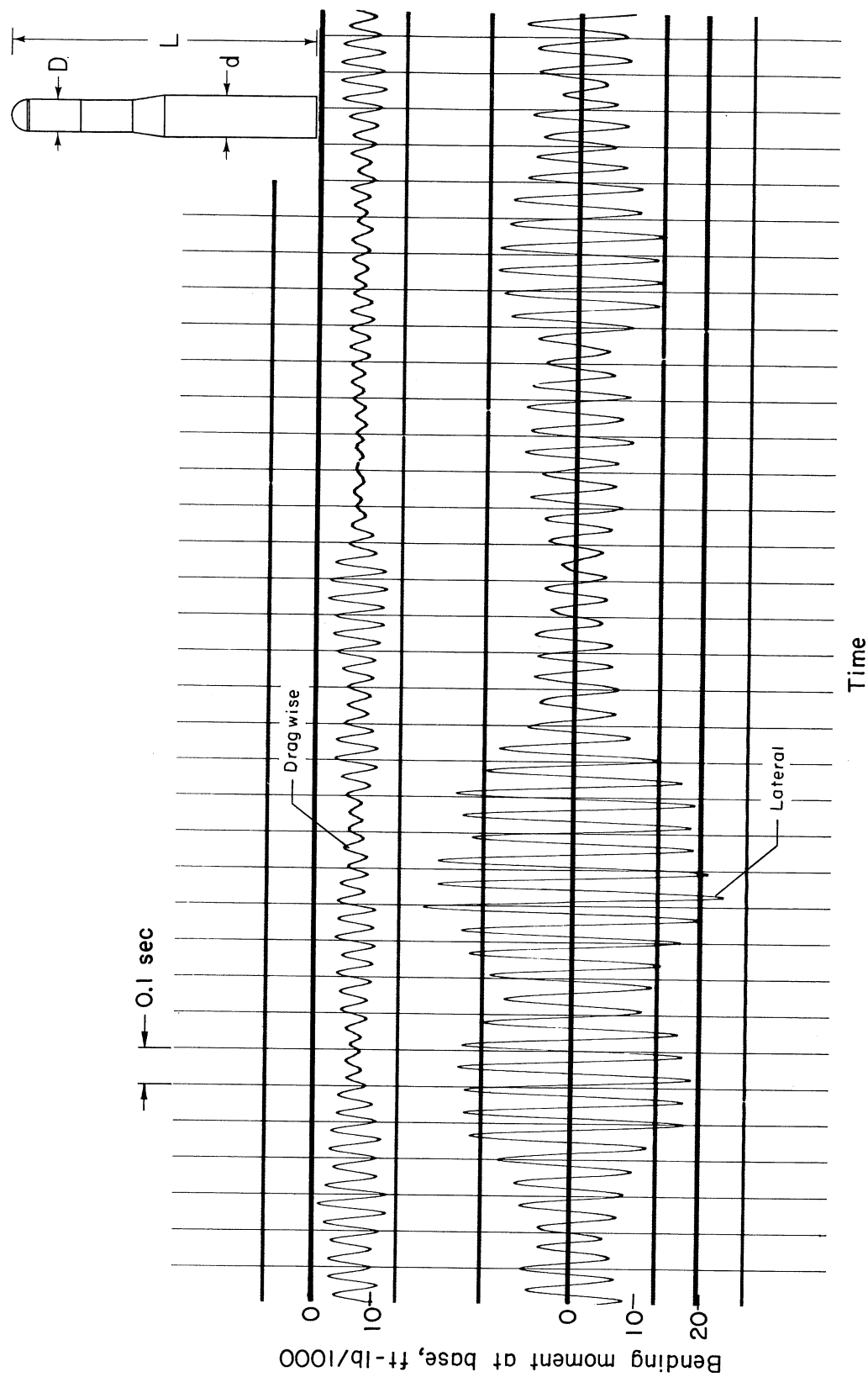
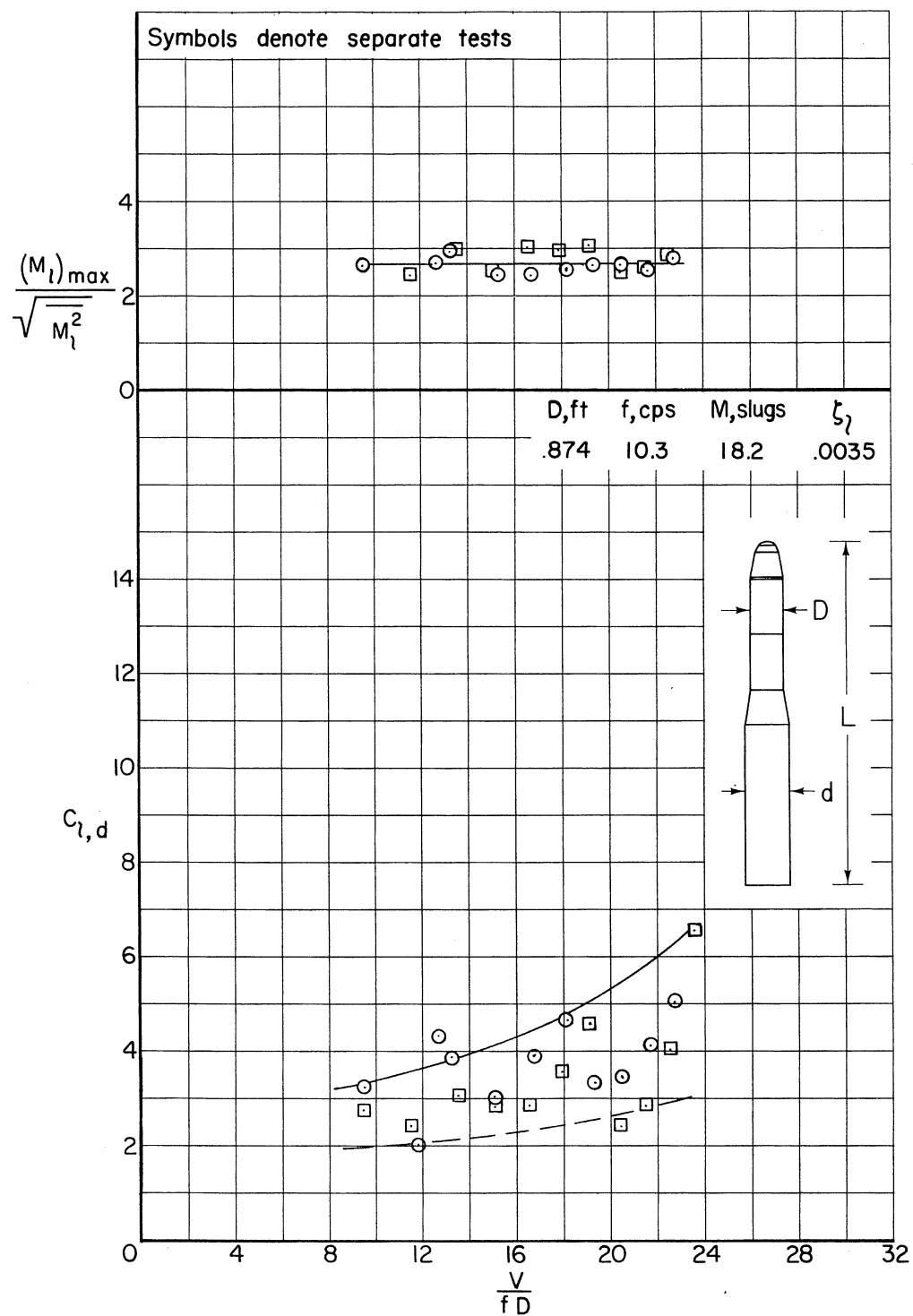
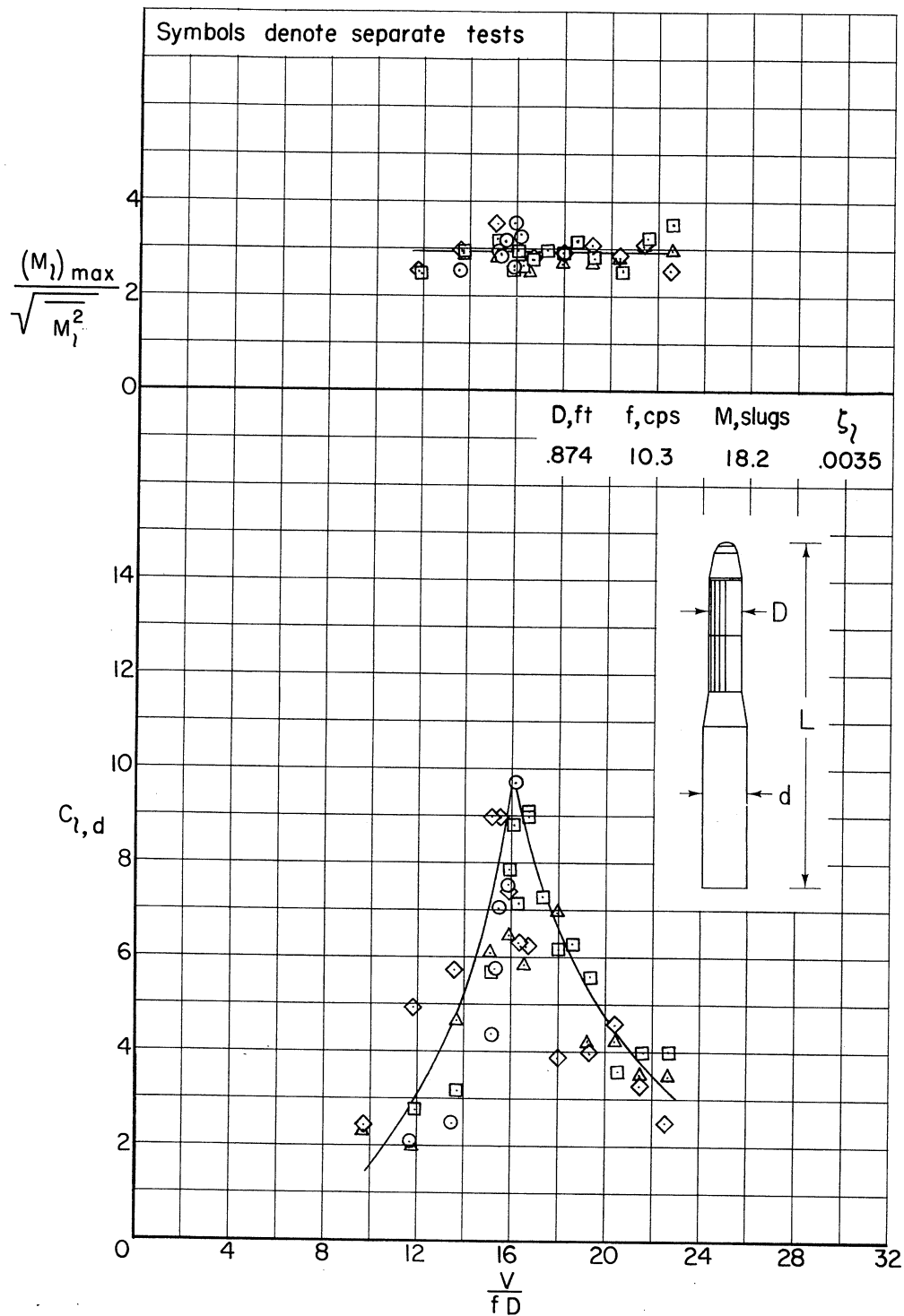


Figure 11.- A sample of the bending moments measured at the base of the models; stiff heavy model; $d = 1.158$ feet; $D/d = 3/4$.



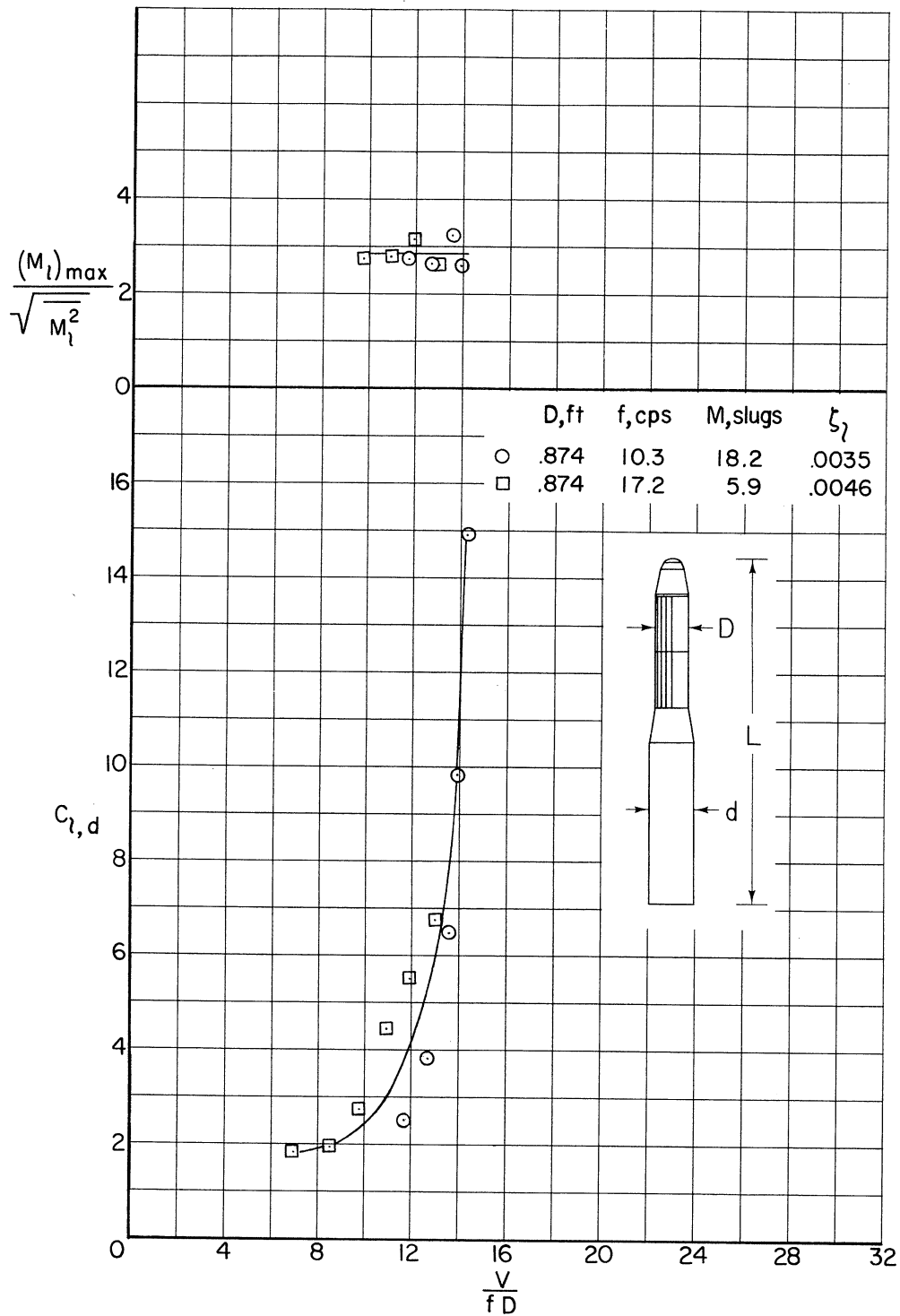
(a) Without roughness.

Figure 12.- Dynamic lateral moment characteristics of models with the double cone nose and two stages; $D/d = 3/4$; $L/D = 10.0$; $f\rho D^2 \cong 0.09$.



(b) With tapes 0.00029D thick.

Figure 12.- Continued.



(c) With tapes 0.00057D thick.

Figure 12.- Concluded.

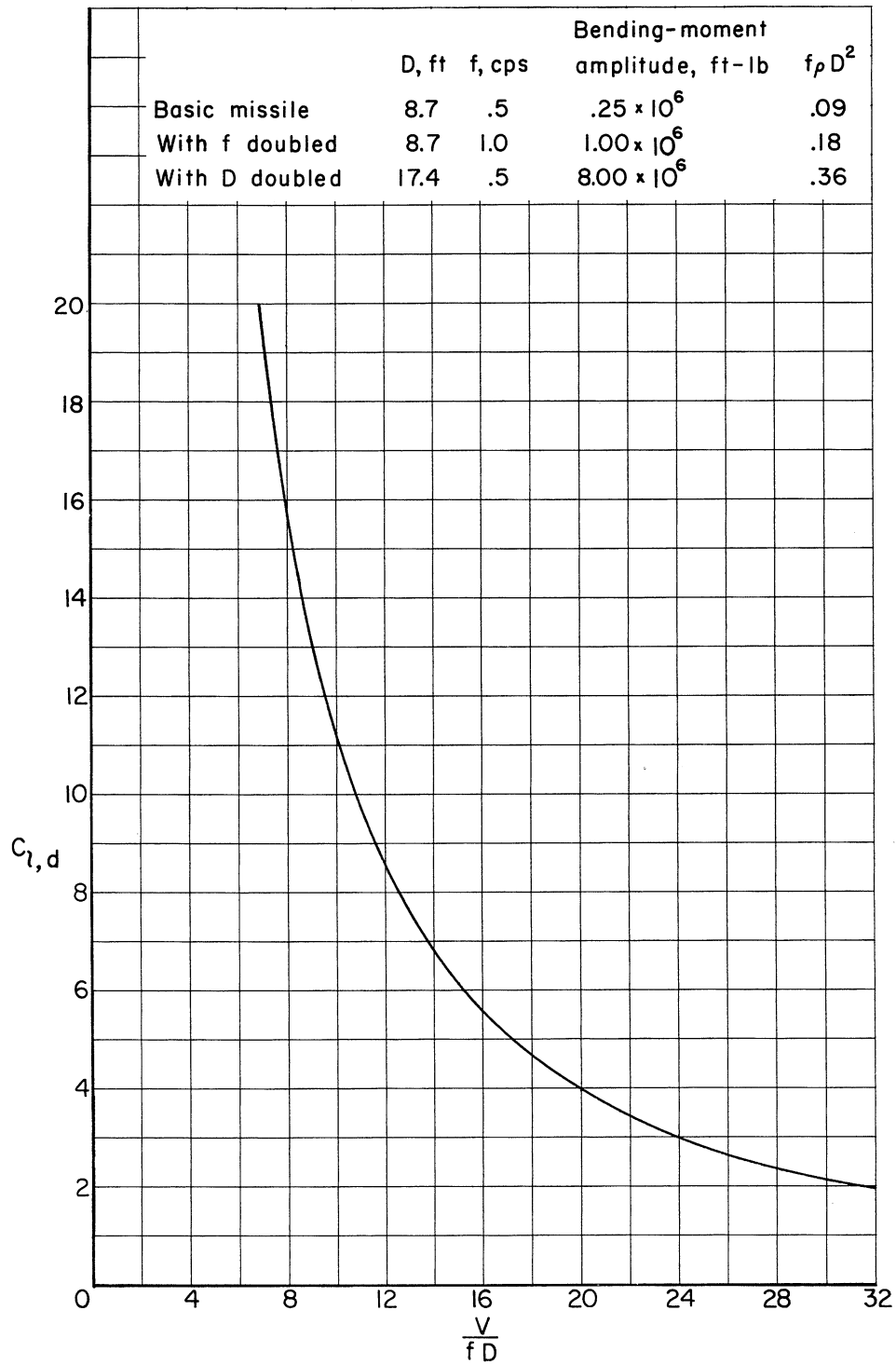
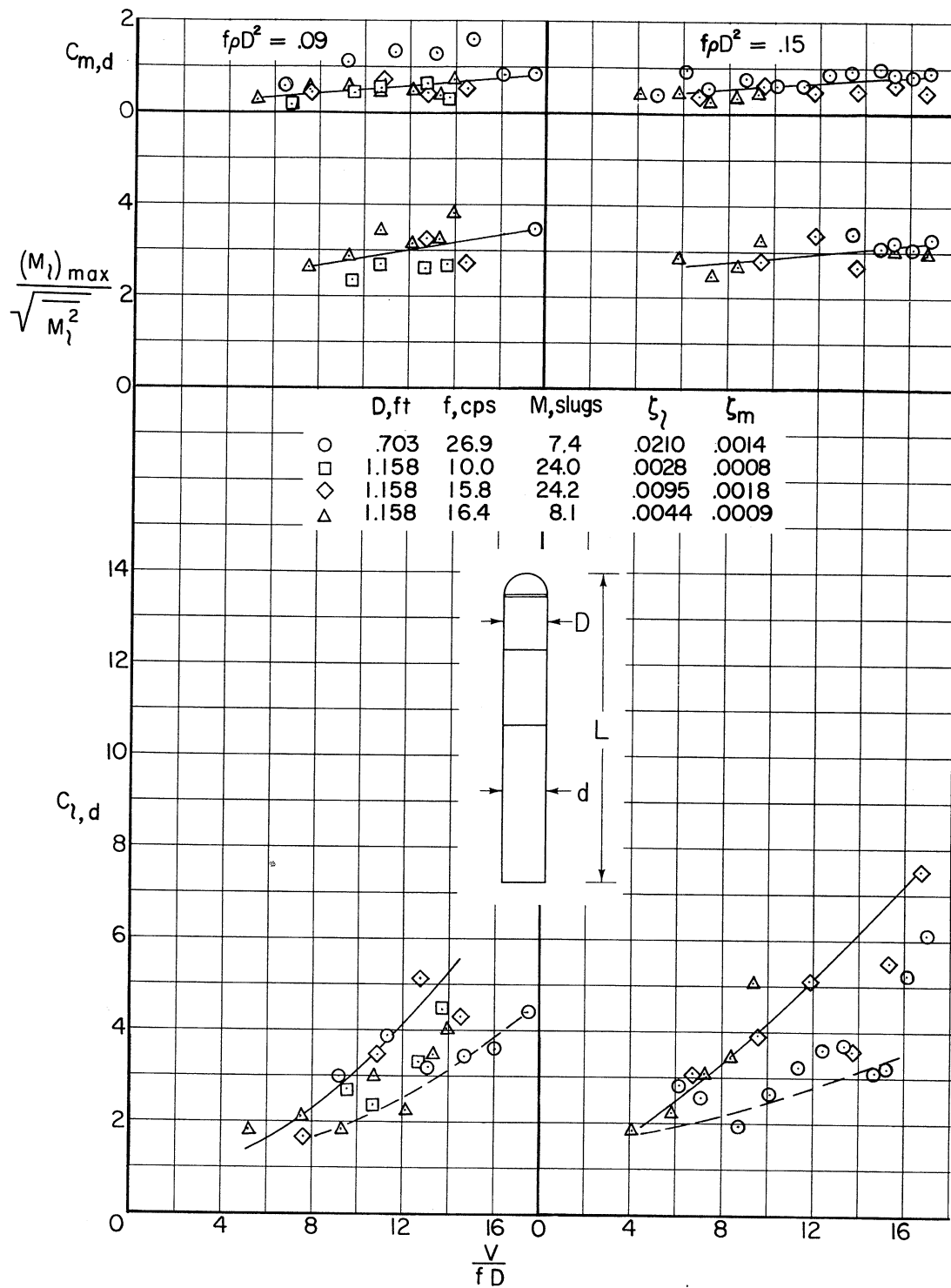
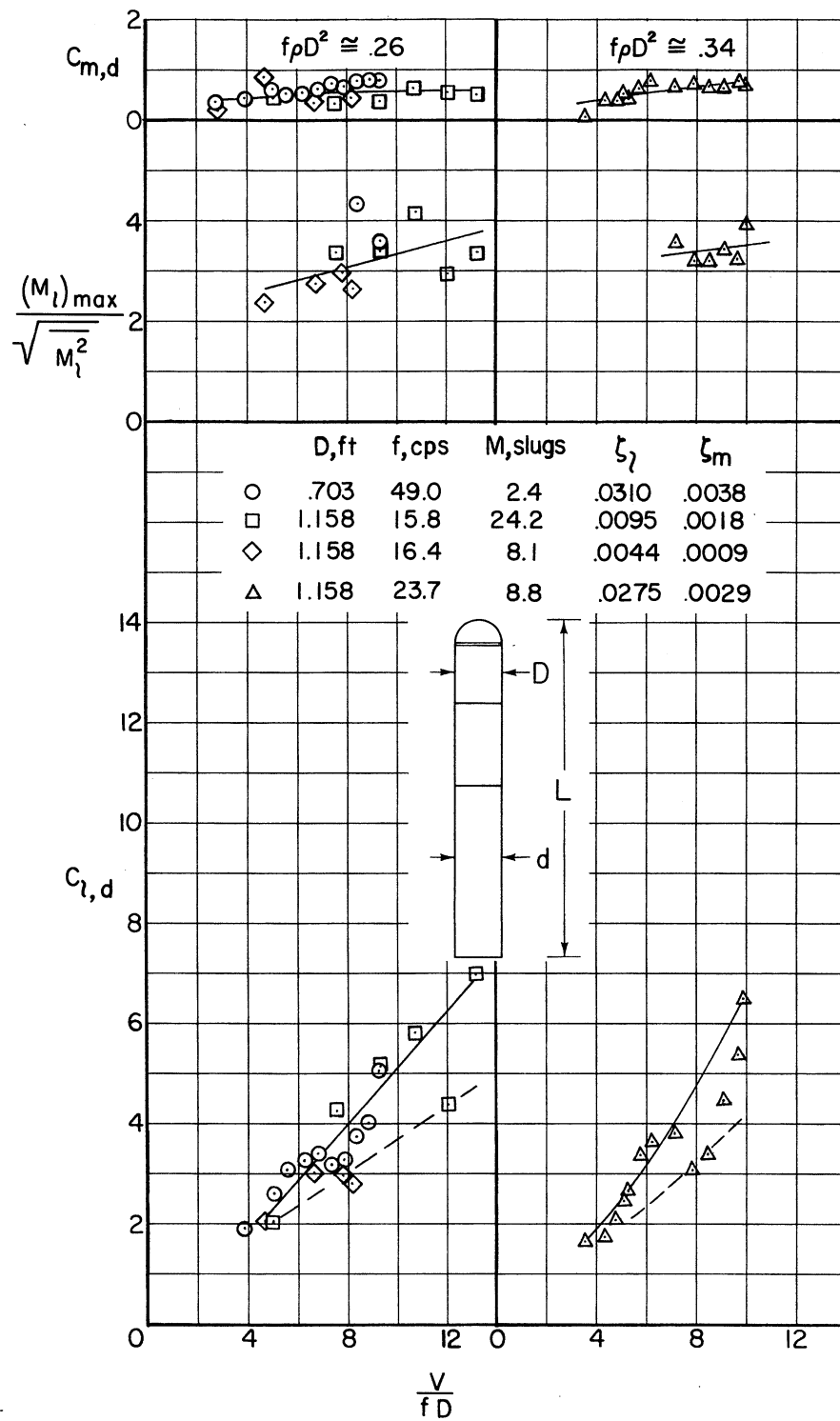


Figure 13.- Variation of dynamic moment coefficient with V/fD for a given oscillatory bending moment on hypothetical missiles; assumed:
 $AL/\rho D^3 = 4 \times 10^4$; $Nr = 20$; $\zeta_l = 0.01$.



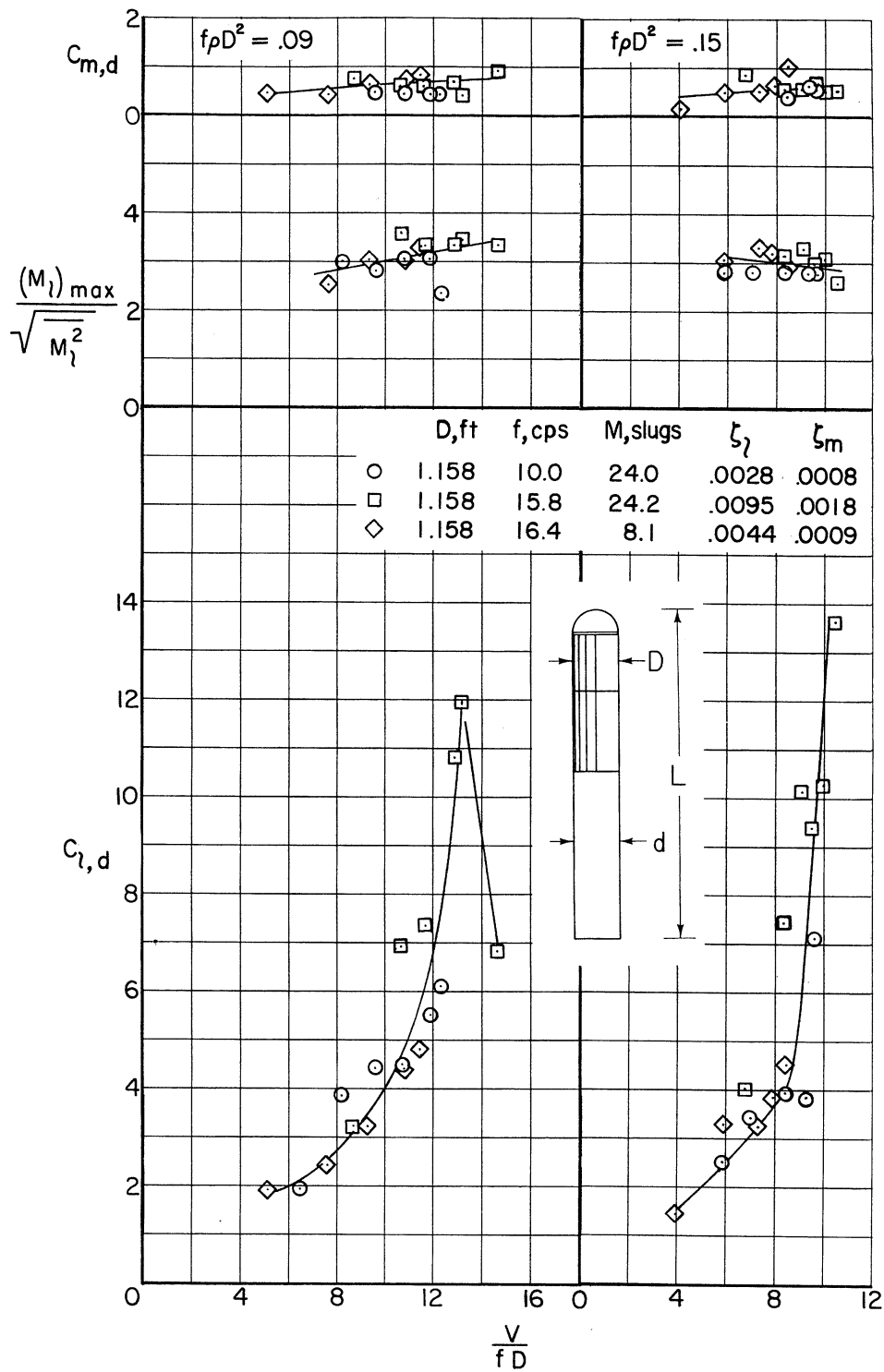
(a) Without roughness; $f\rho D^2 = 0.09, 0.15$.

Figure 14.- Dynamic moment characteristics of models with the hemisphere nose; $D/d = 1$; $L/D = 7.3$ to 8.1 .



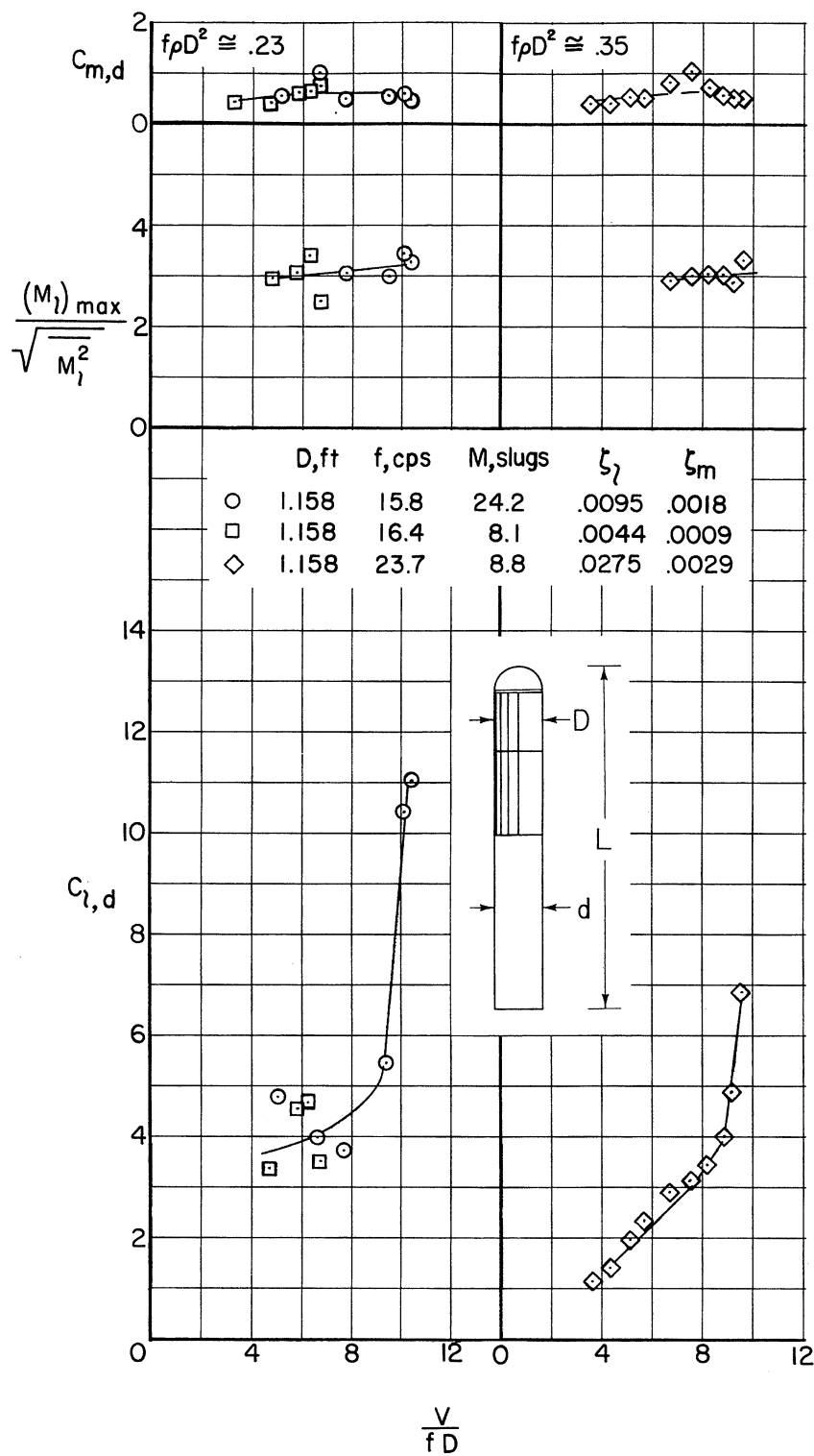
(b) Without roughness; $f\rho D^2 \approx 0.26, 0.34$.

Figure 14.- Continued.



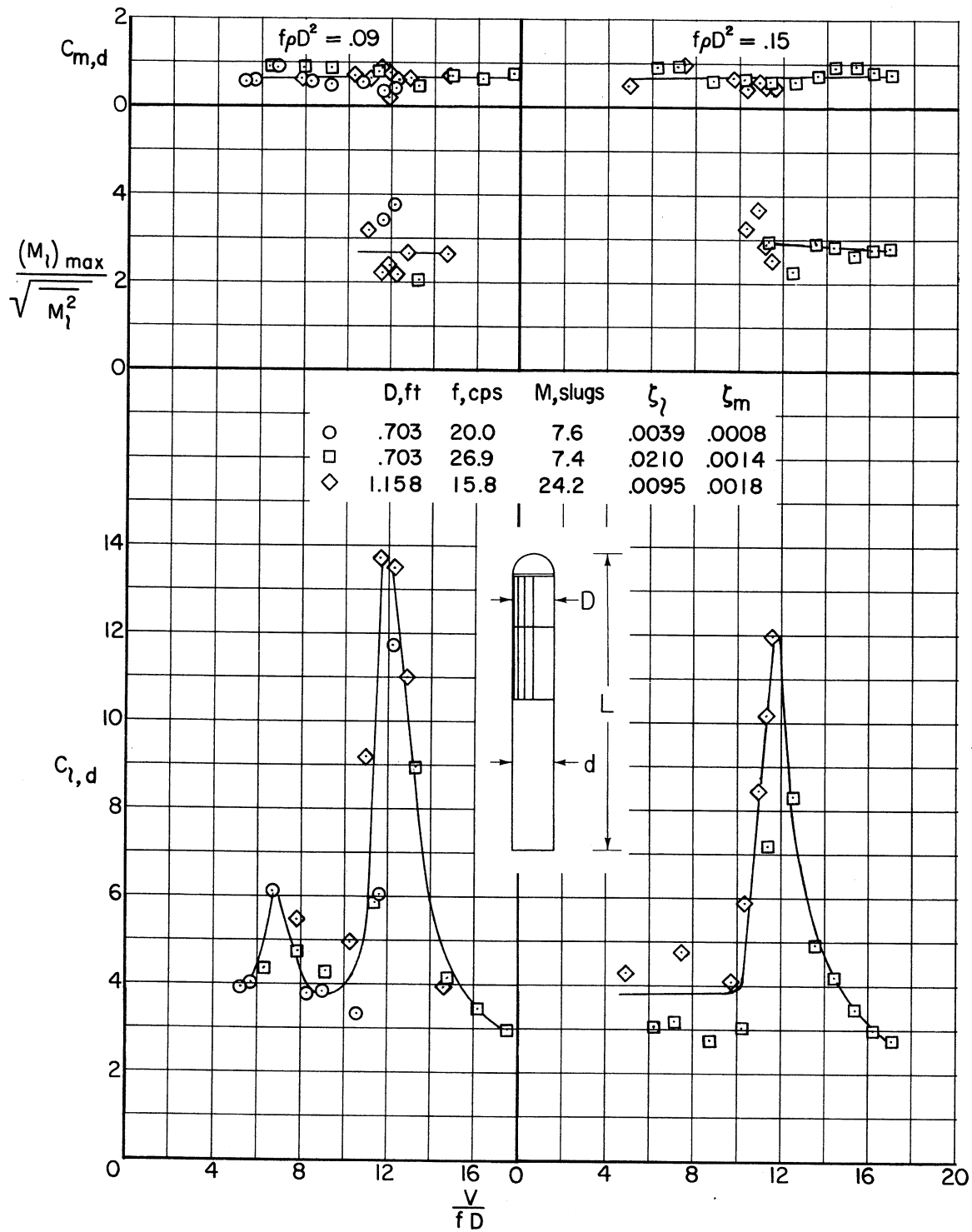
(c) With tapes 0.00022D thick; $f\rho D^2 = 0.09, 0.15$.

Figure 14.- Continued.



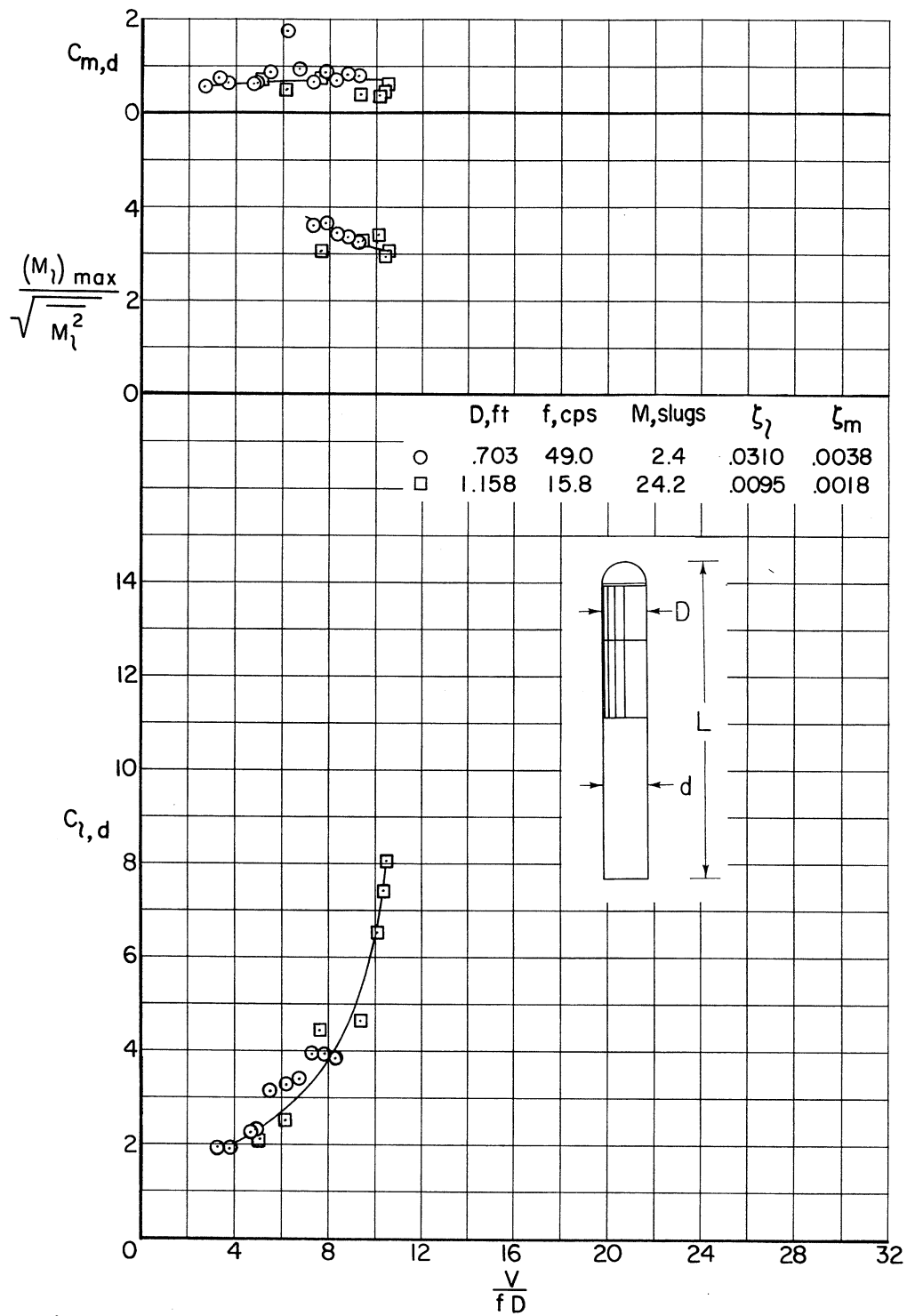
(d) With tapes 0.00022D thick; $f\rho D^2 \approx 0.23, 0.35$.

Figure 14.- Continued.



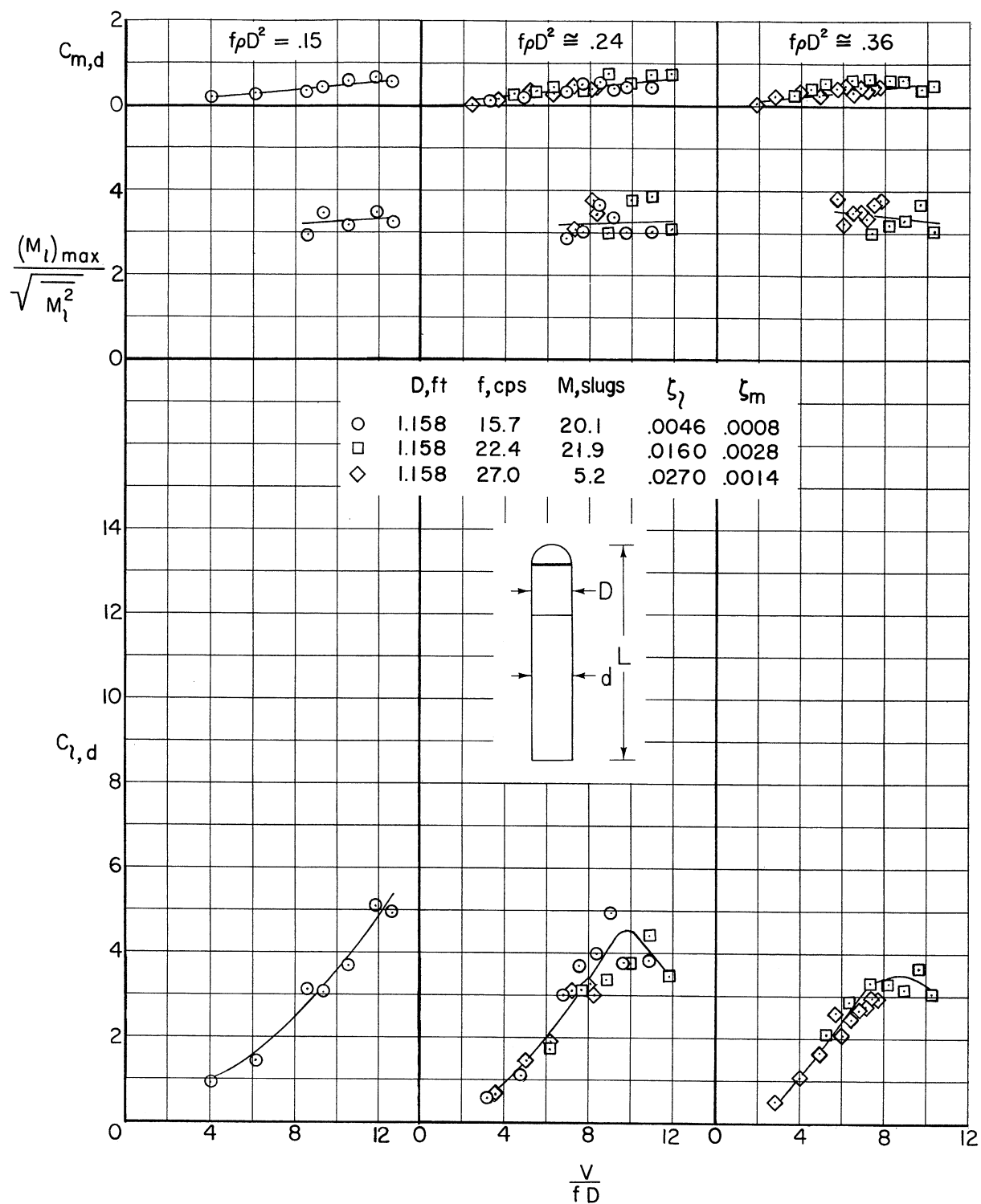
(e) With tapes 0.00036D thick; $f\rho D^2 = 0.09, 0.15$.

Figure 14.- Continued.



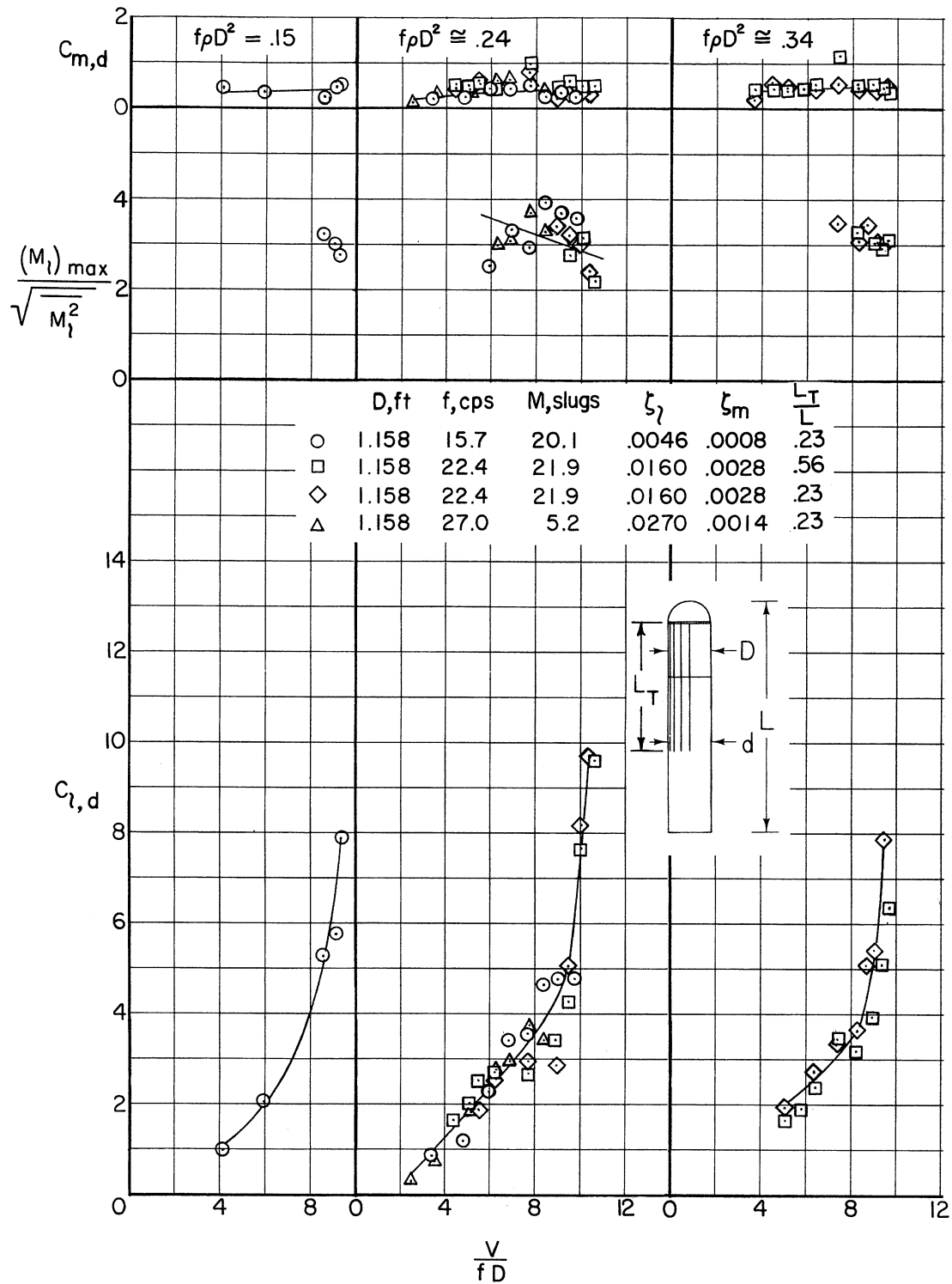
(f) With tapes 0.00036D thick; $f_0 D^2 \approx 0.26$.

Figure 14.- Concluded.



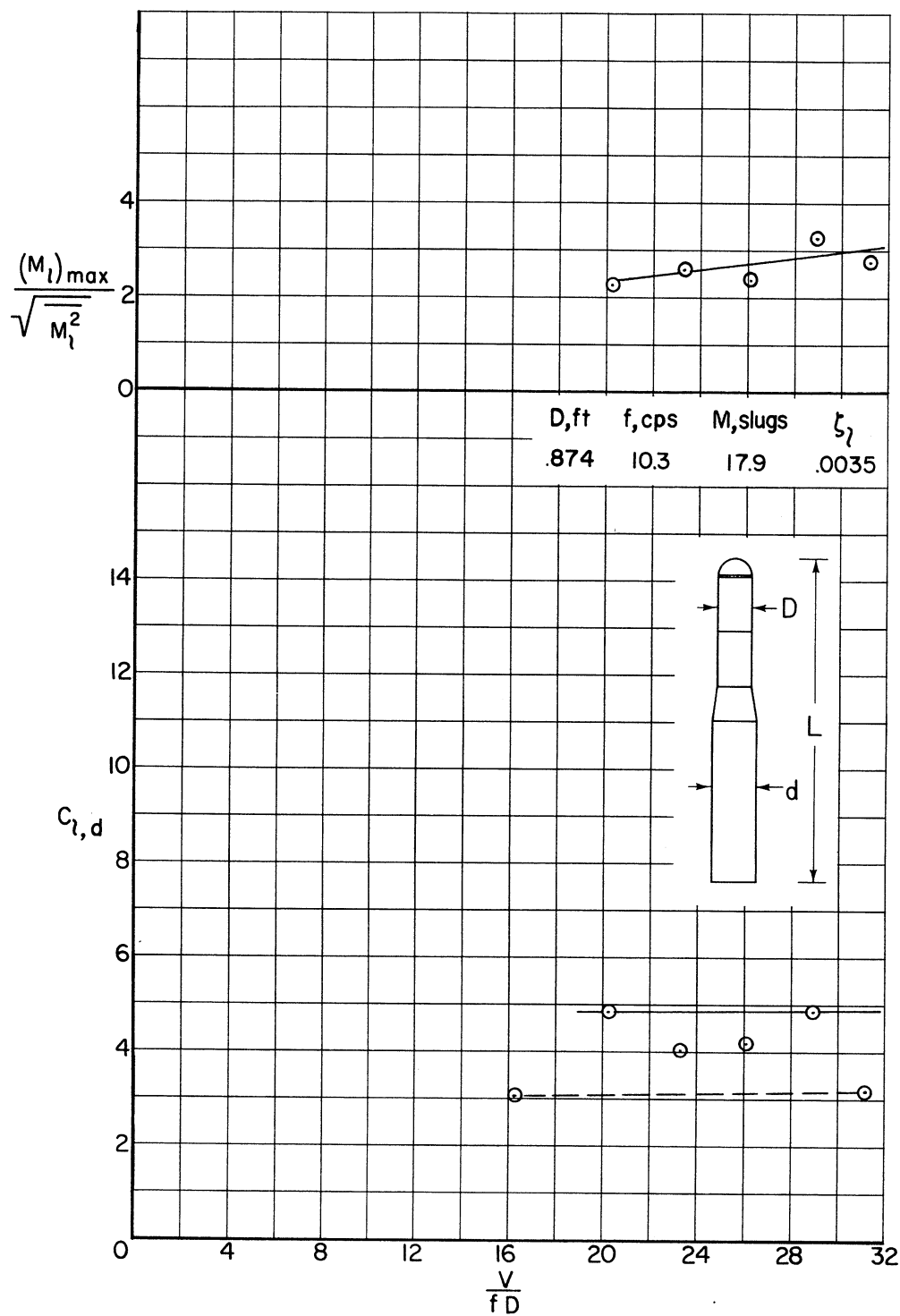
(a) Without roughness.

Figure 15.- Dynamic moment characteristics of models with the hemisphere nose; $D/d = 1$; $L/D = 5.5$



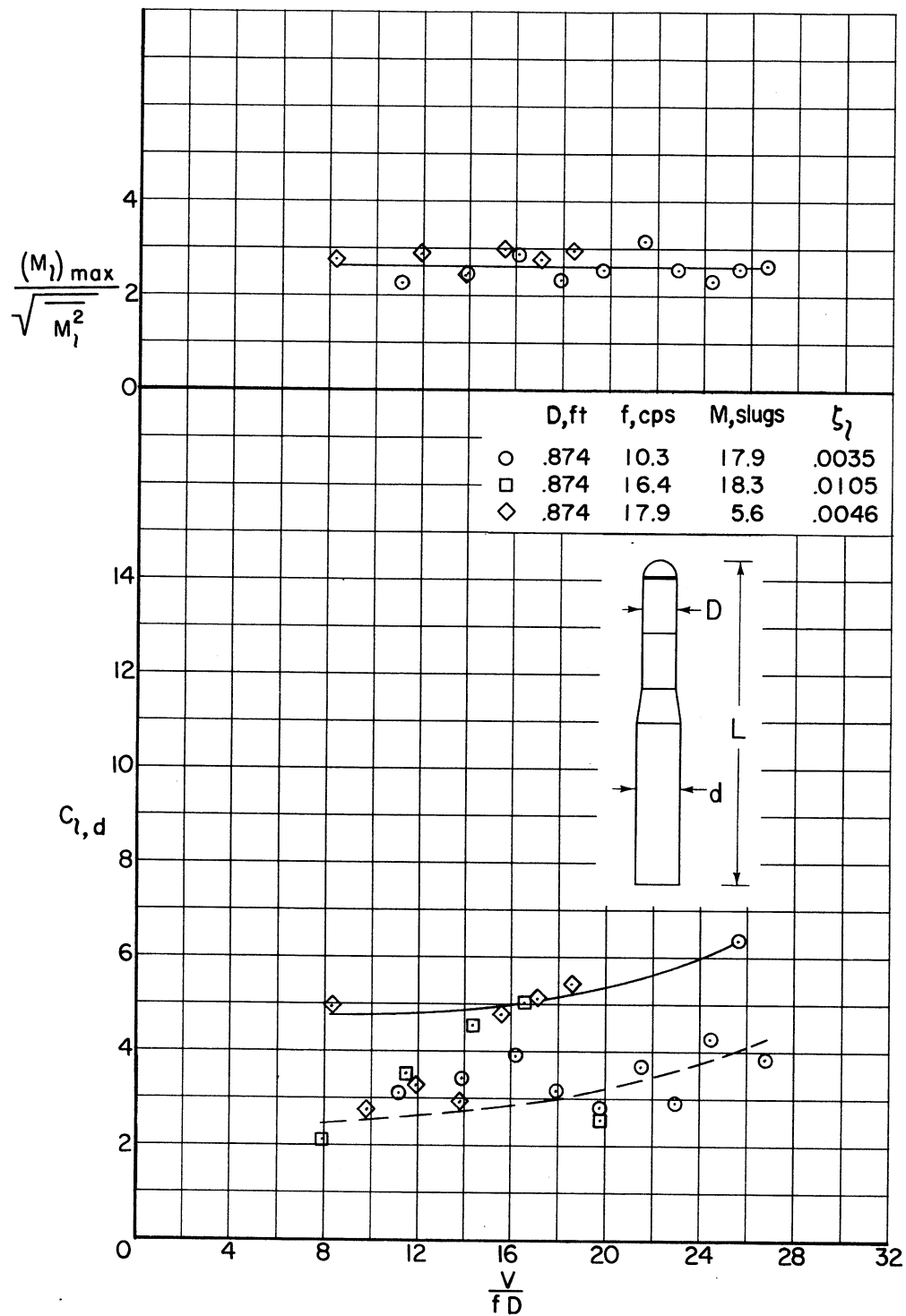
(b) With tapes 0.00022D thick.

Figure 15.- Concluded.



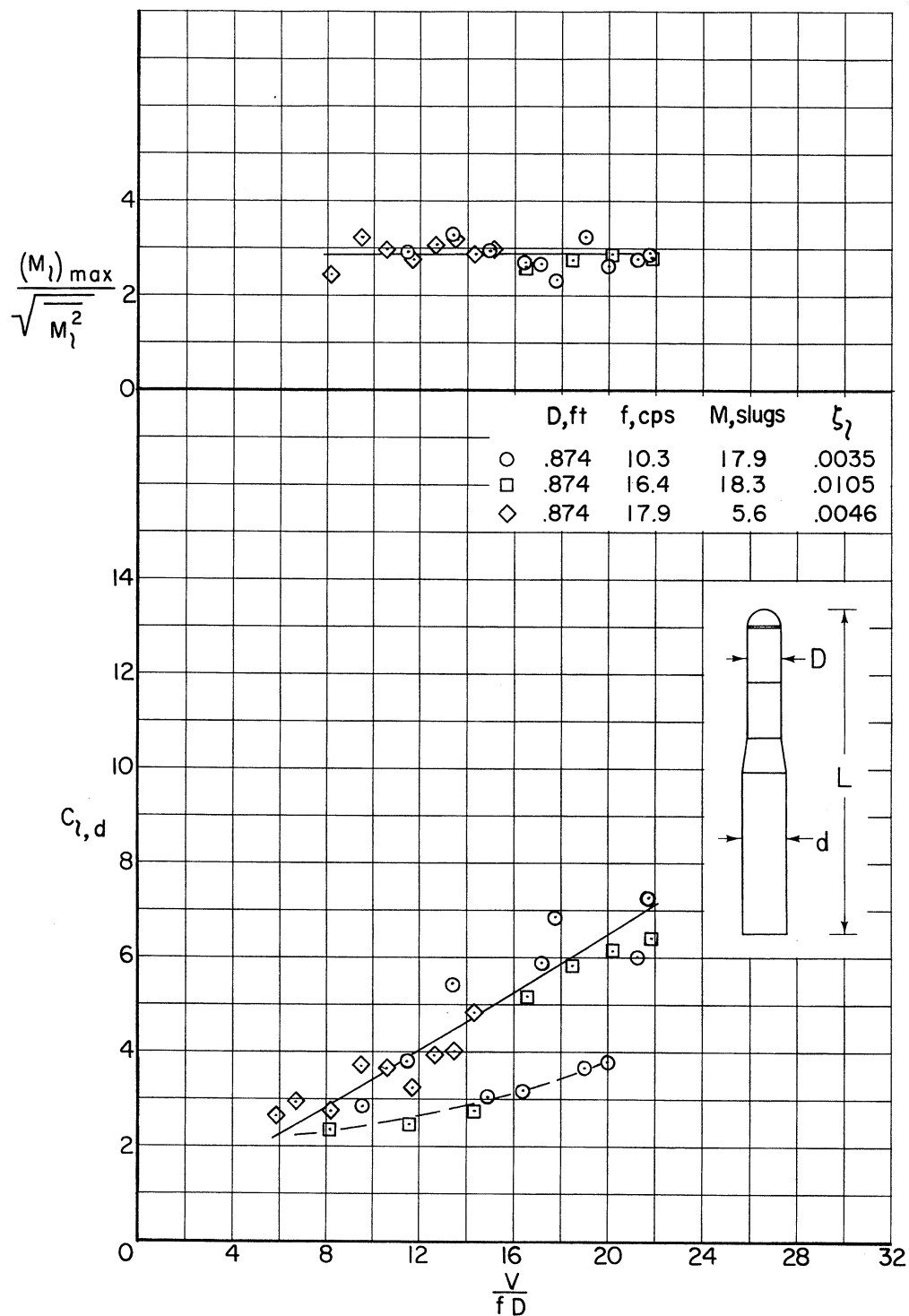
(a) Without roughness; $f_p D^2 = 0.03$.

Figure 16.- Dynamic moment characteristics of models with the hemisphere nose; $D/d = 3/4$; $L/D = 9.5$ to 9.8 .



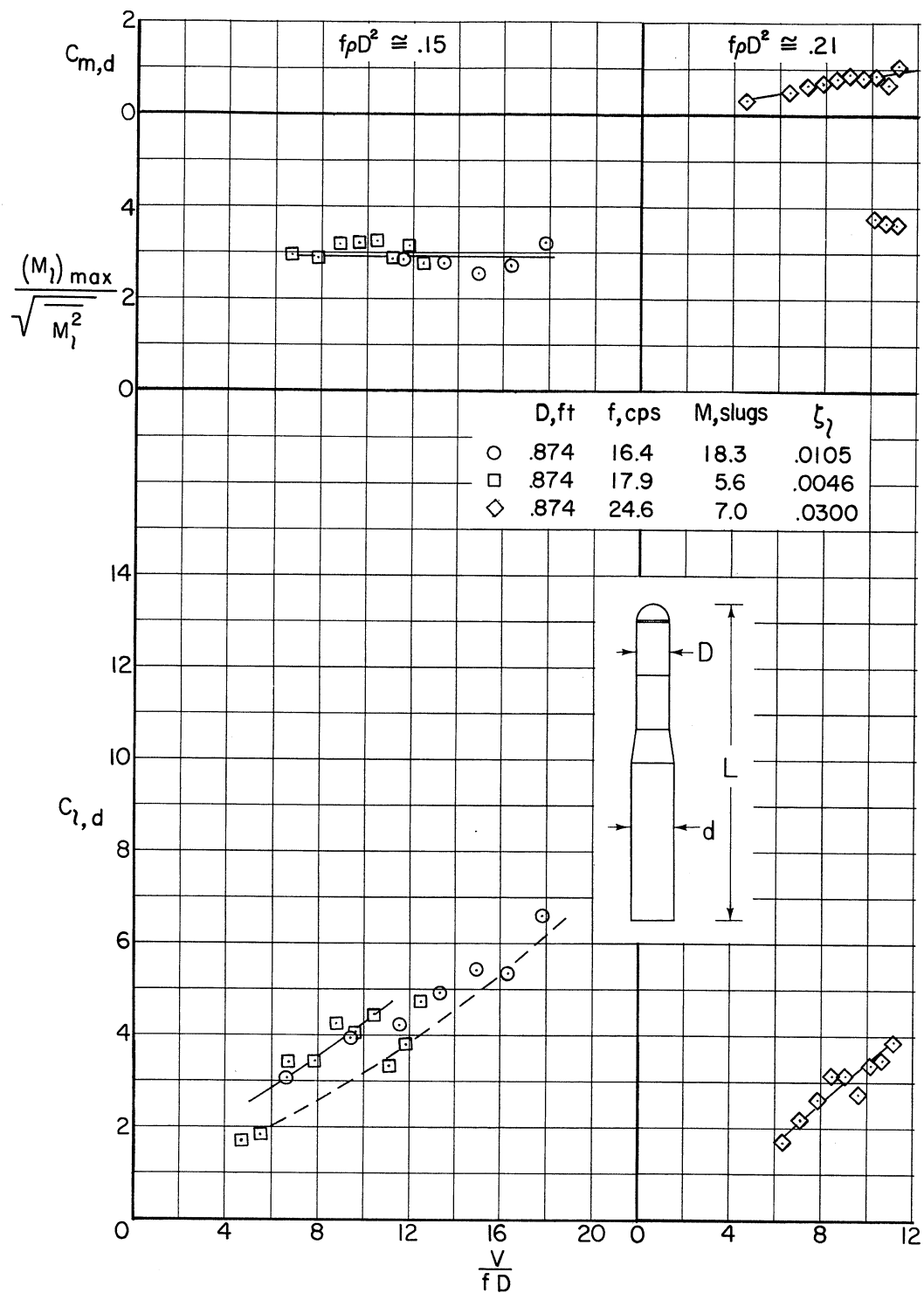
(b) Without roughness; $f_0 D^2 \approx 0.05$.

Figure 16.- Continued.



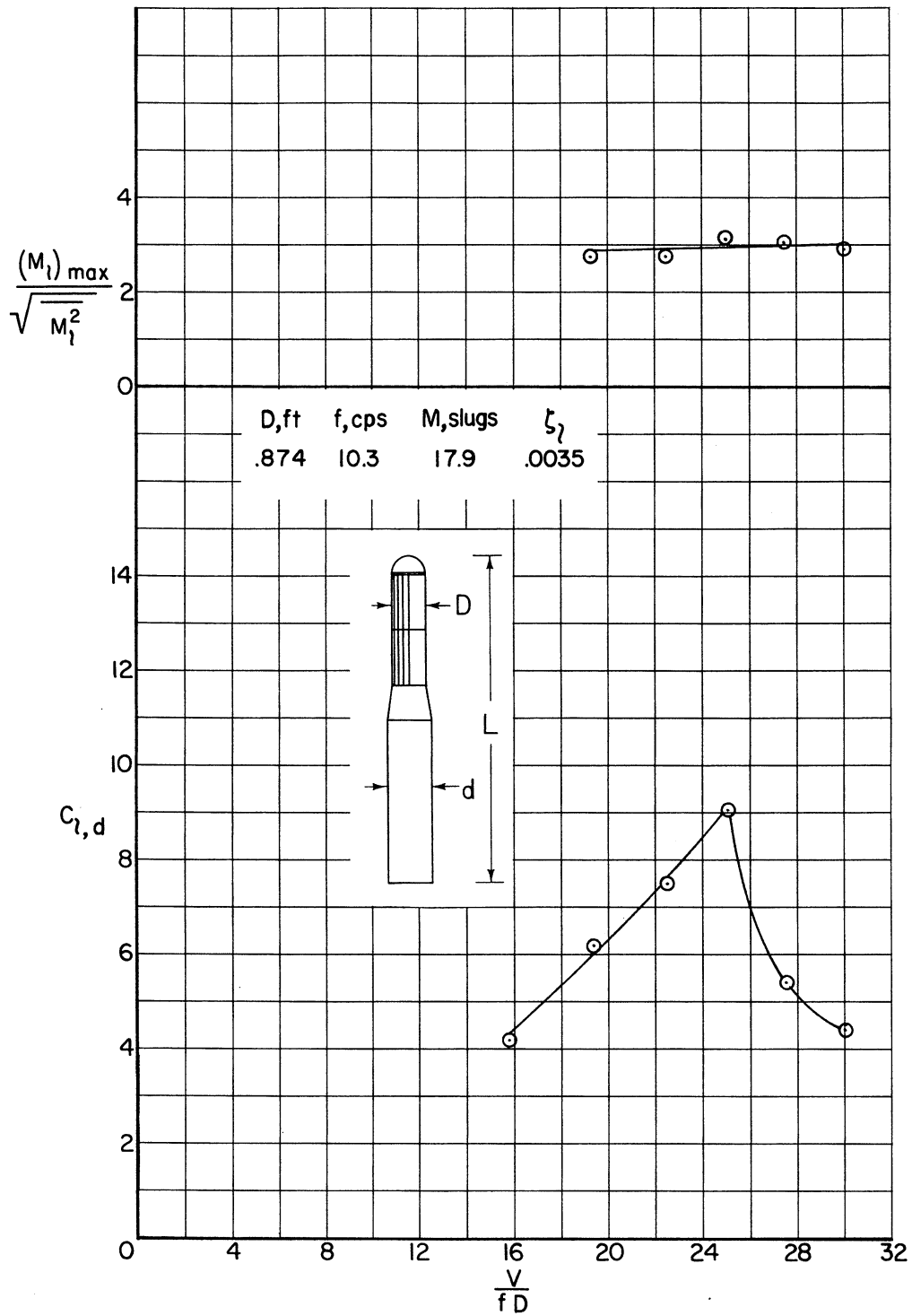
(c) Without roughness; $f_0 D^2 \approx 0.10$.

Figure 16.- Continued.



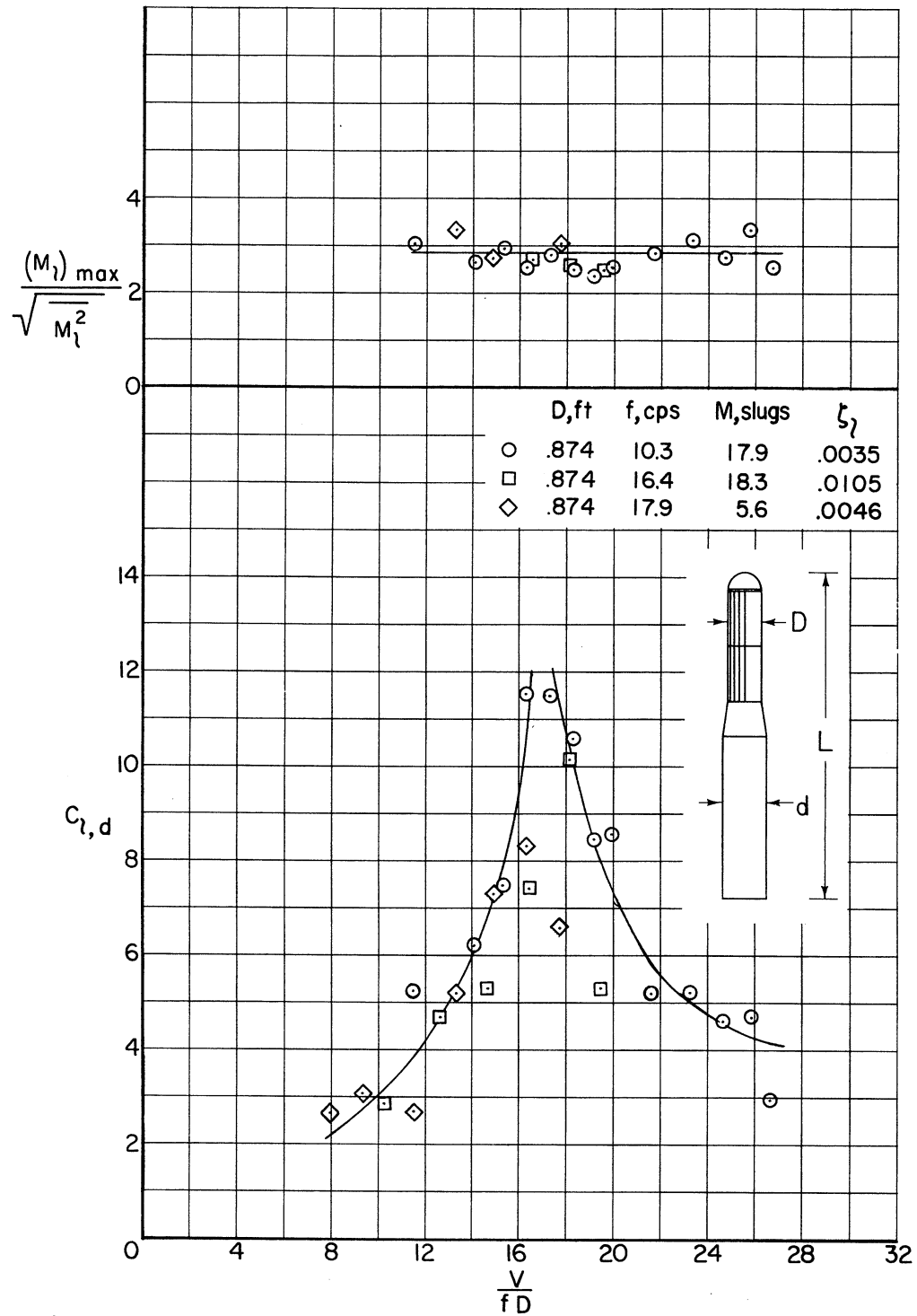
(d) Without roughness; $f\rho D^2 \approx 0.15, 0.21$.

Figure 16.- Continued.



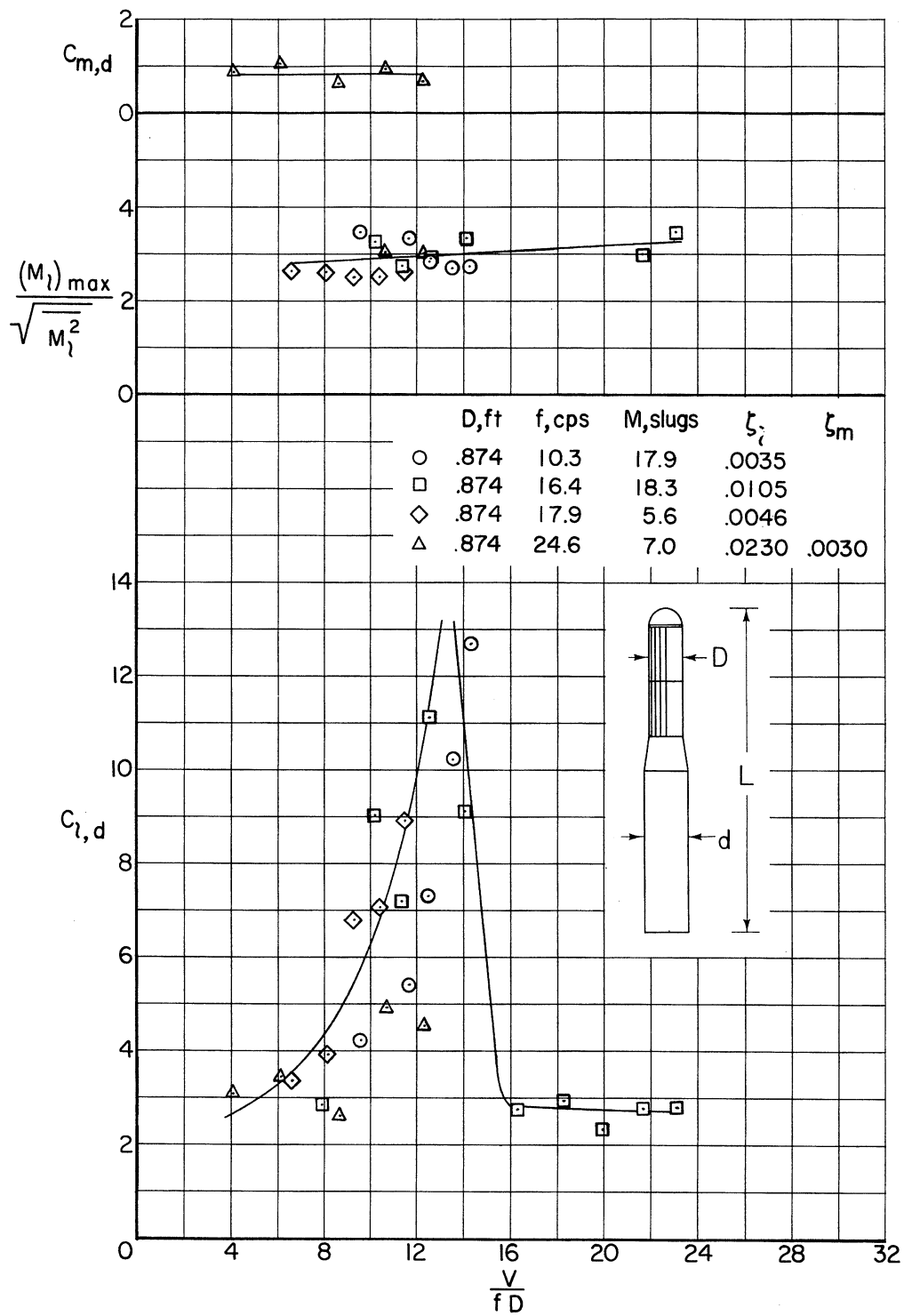
(e) With tapes 0.00029D thick; $f_p D^2 = 0.03$.

Figure 16.- Continued.



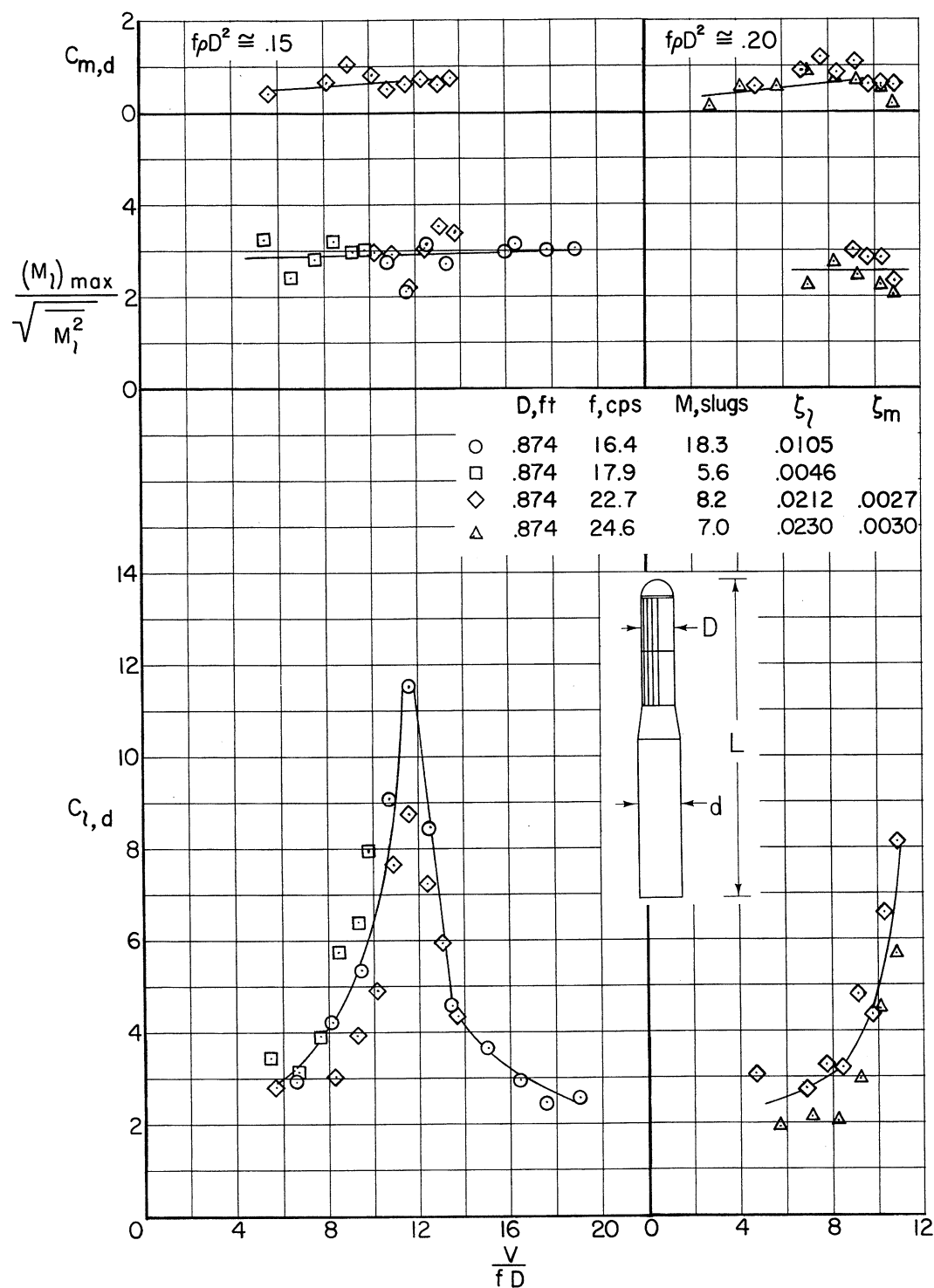
(f) With tapes 0.00029D thick; $f_0 D^2 \approx 0.05$.

Figure 16.- Continued.



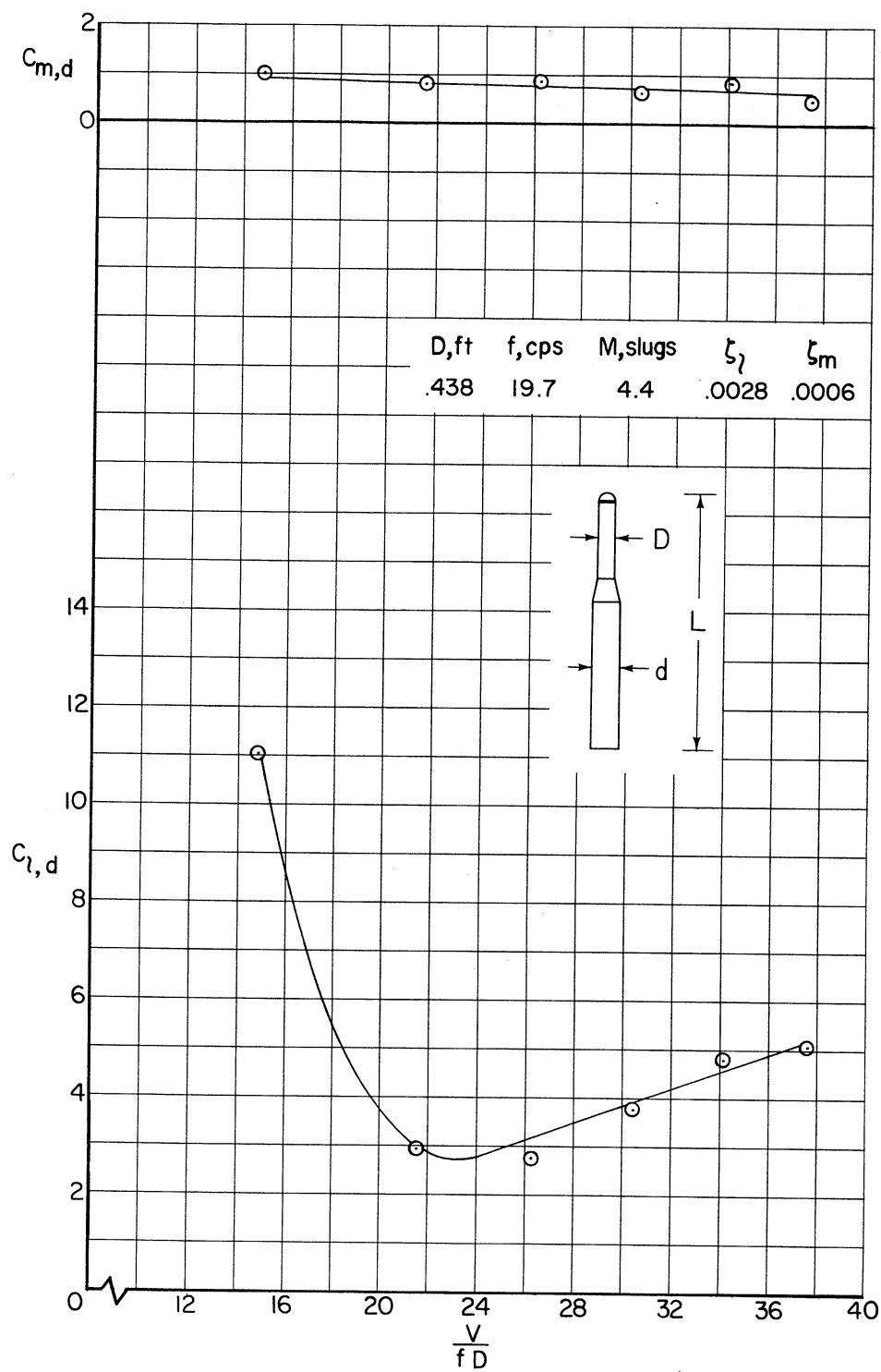
(g) With tapes 0.00029D thick; $f_p D^2 \approx 0.10$.

Figure 16.- Continued.



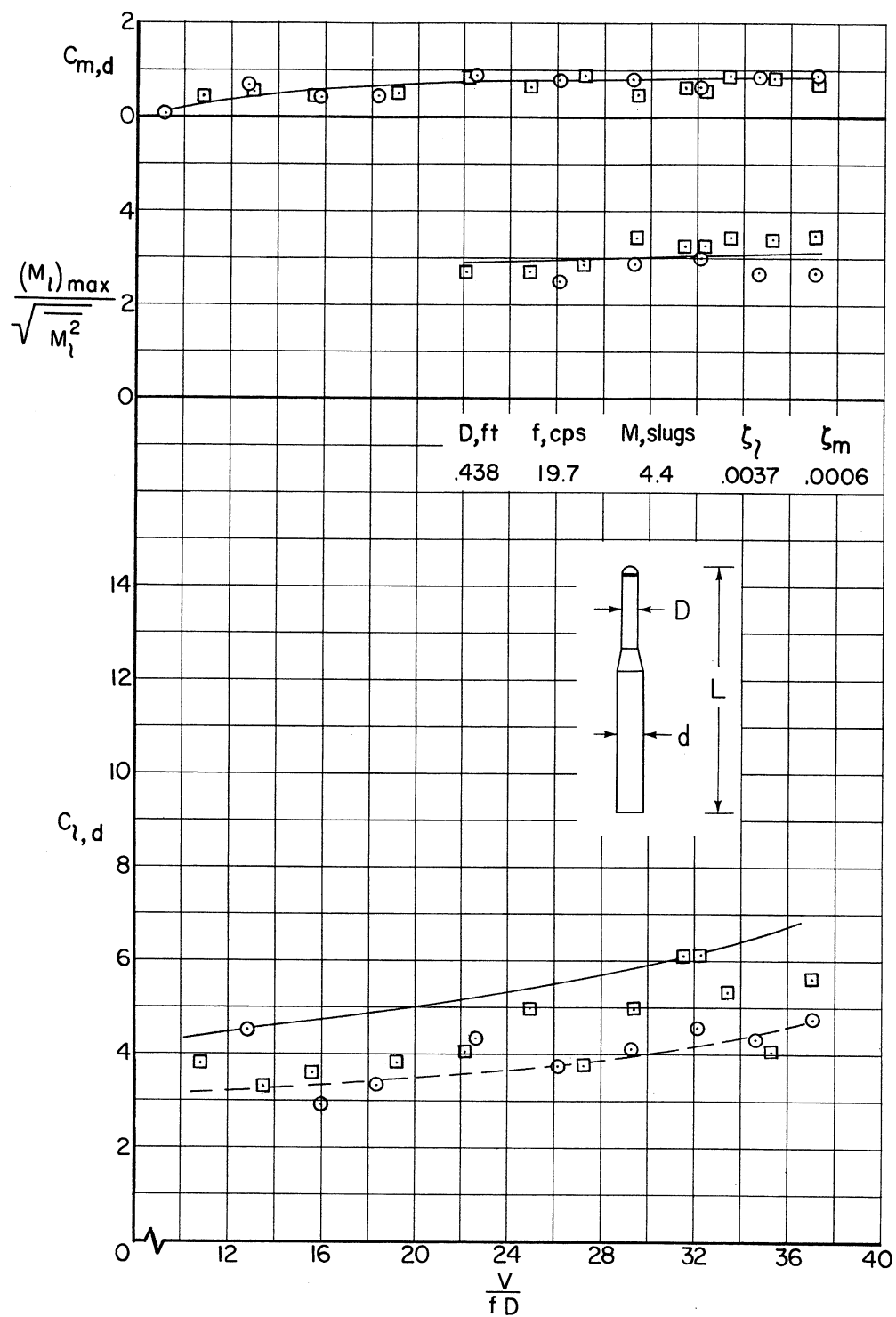
(h) With tapes 0.00029D thick; $f_0 D^2 \approx 0.15, 0.20$.

Figure 16.- Concluded.



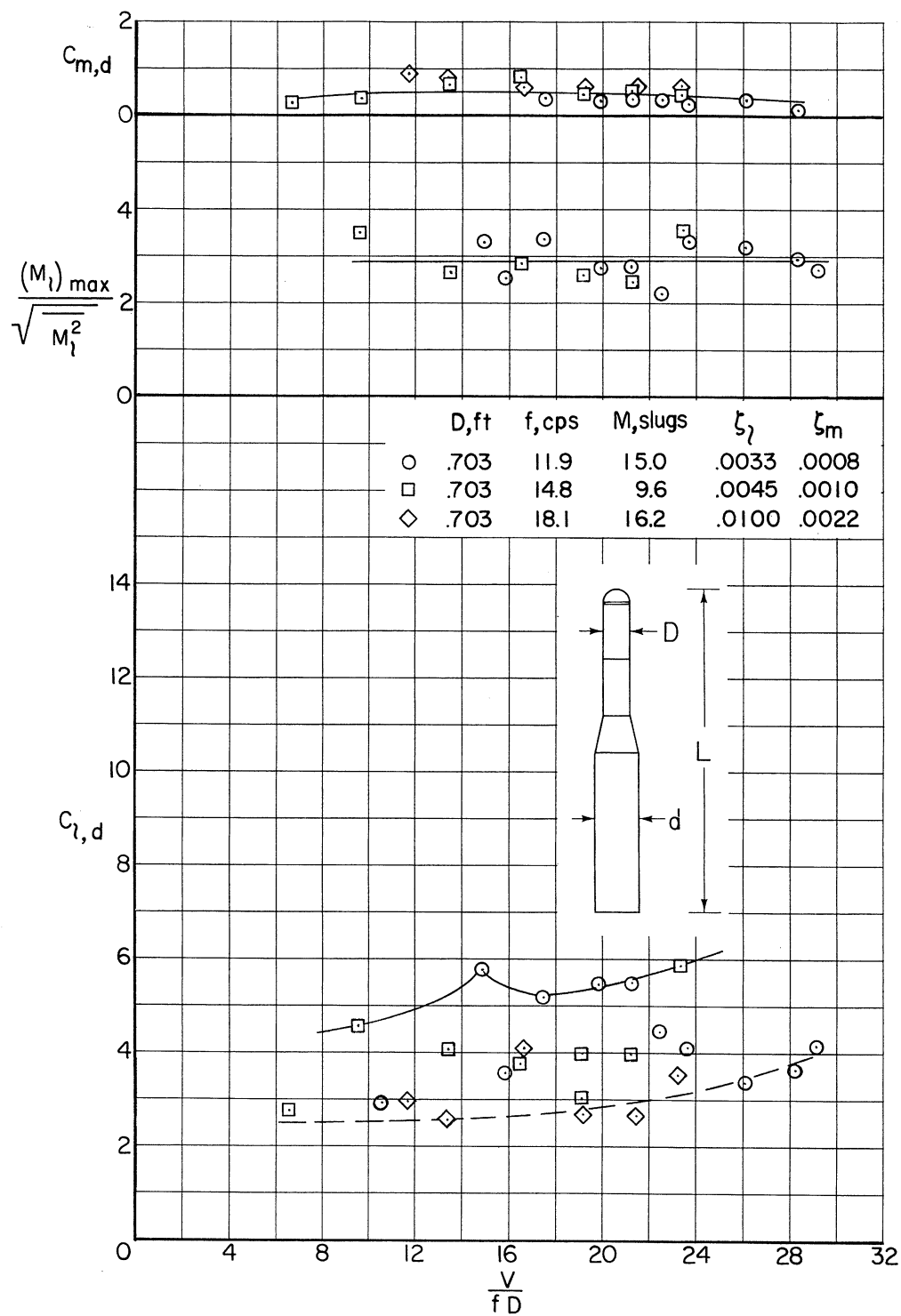
(a) Without roughness; $f_p D^2 = 0.01$.

Figure 17.- Dynamic moment characteristics of models with the hemisphere nose; $D/d = 3/5$; $L/D = 12.4$ to 15.2 .



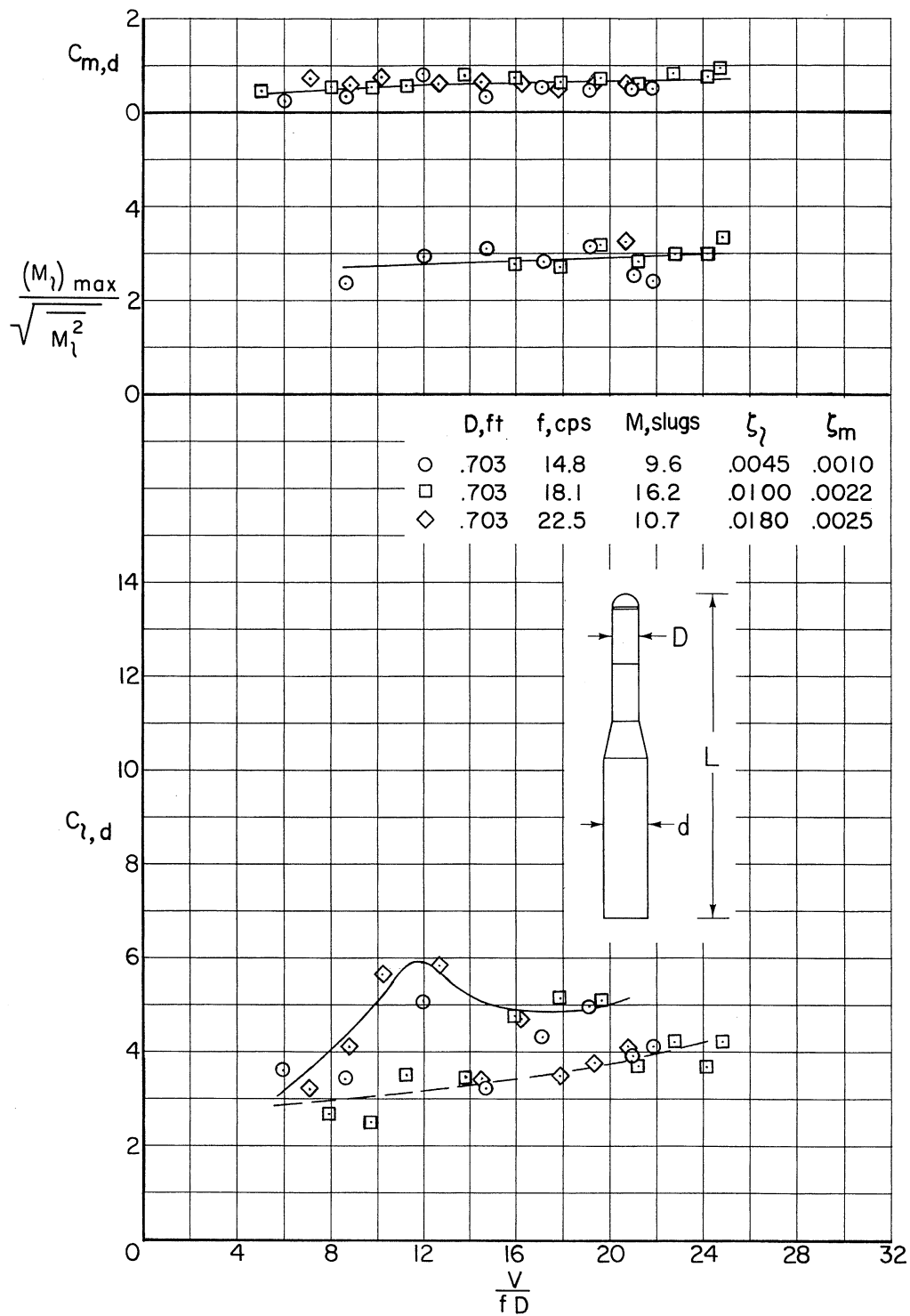
(b) Without roughness; $f_p D^2 = 0.03$ to 0.04 .

Figure 17.- Continued.



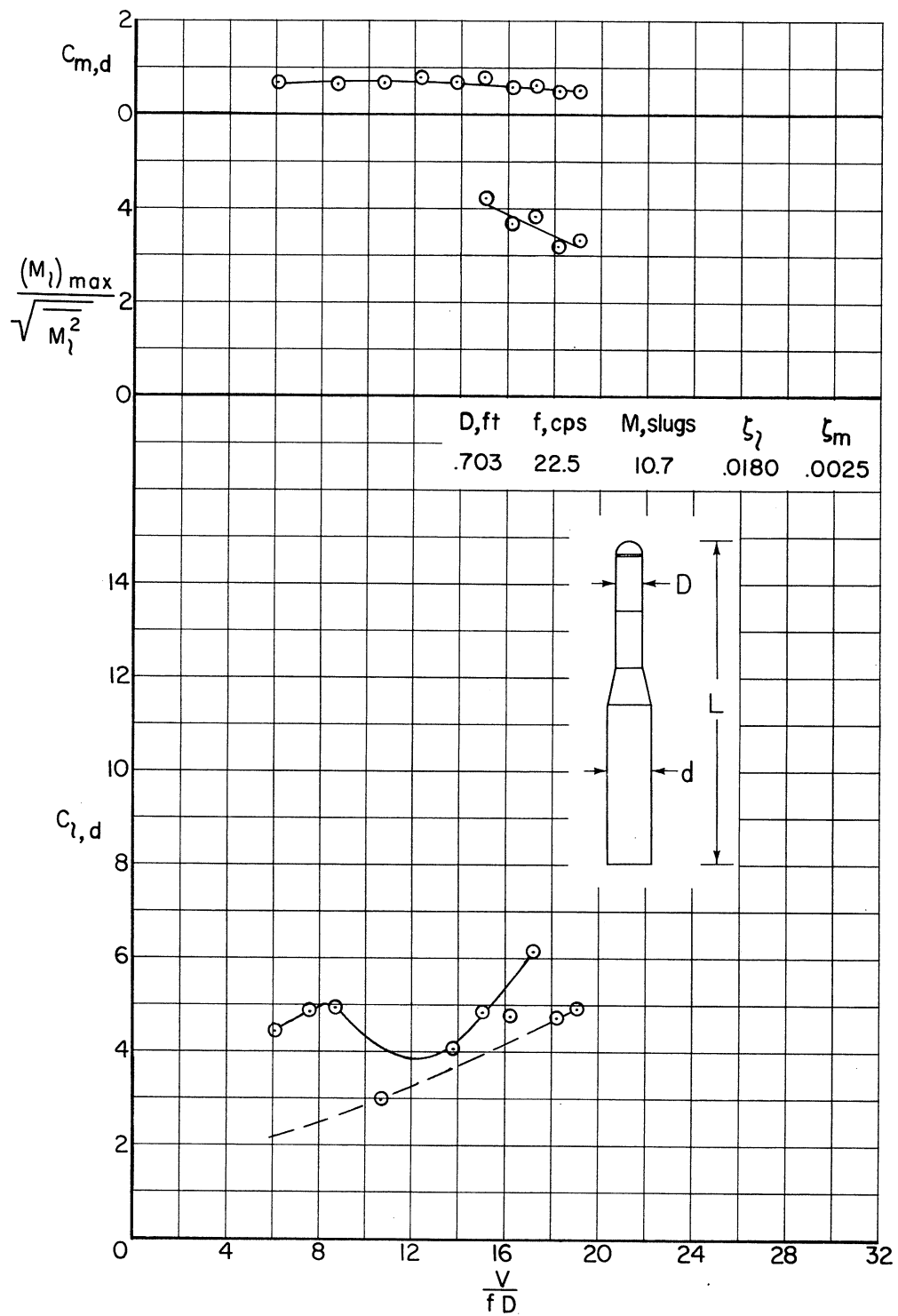
(c) Without roughness; $f_0 D^2 = 0.06$.

Figure 17.- Continued.



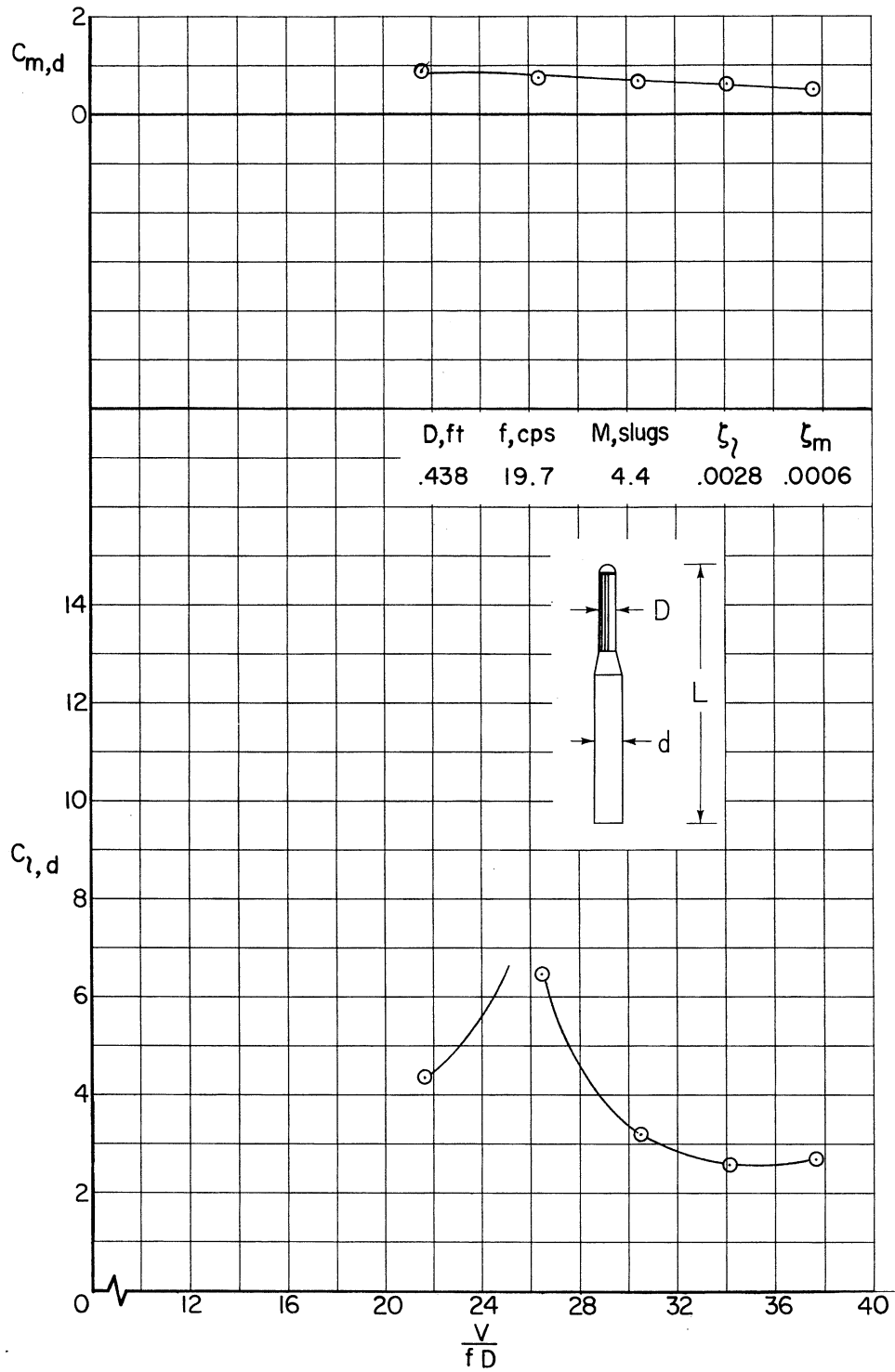
(d) Without roughness; $f_0 D^2 \approx 0.09$.

Figure 17.- Continued.



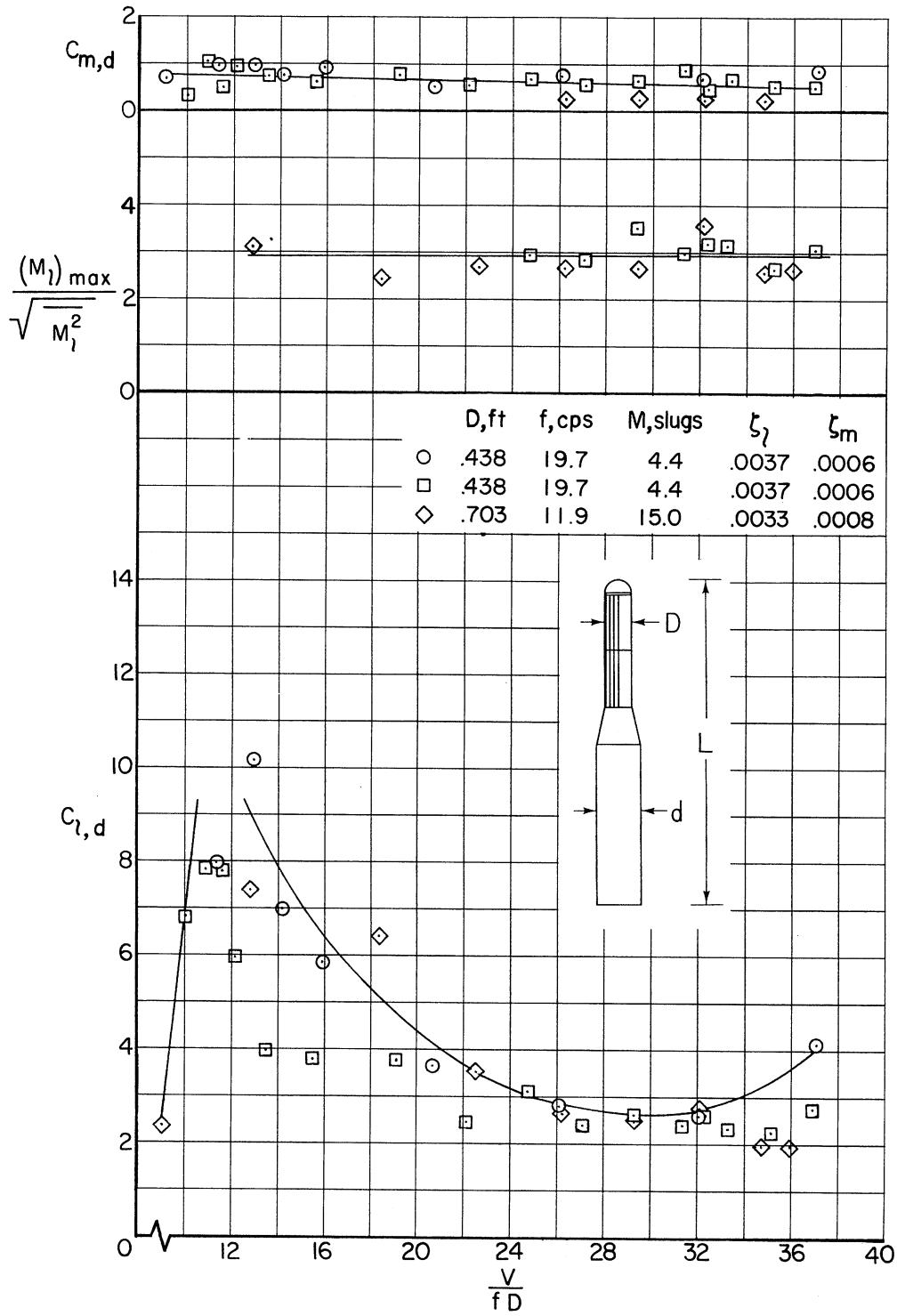
(e) Without roughness; $f_p D^2 \approx 0.12$.

Figure 17.- Continued.



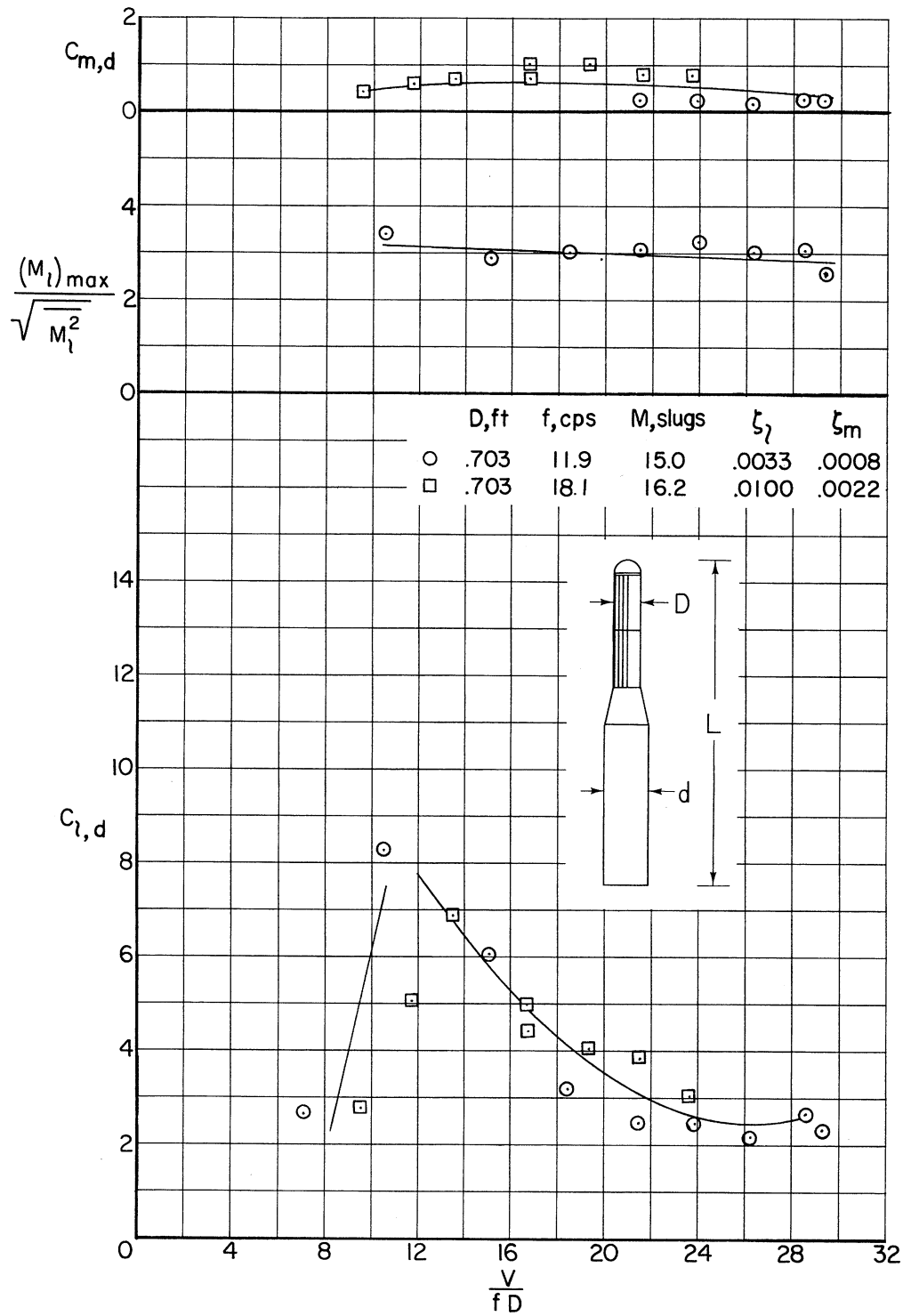
(f) With tapes 0.00057D thick; $f_0 D^2 = 0.01$.

Figure 17.- Continued.



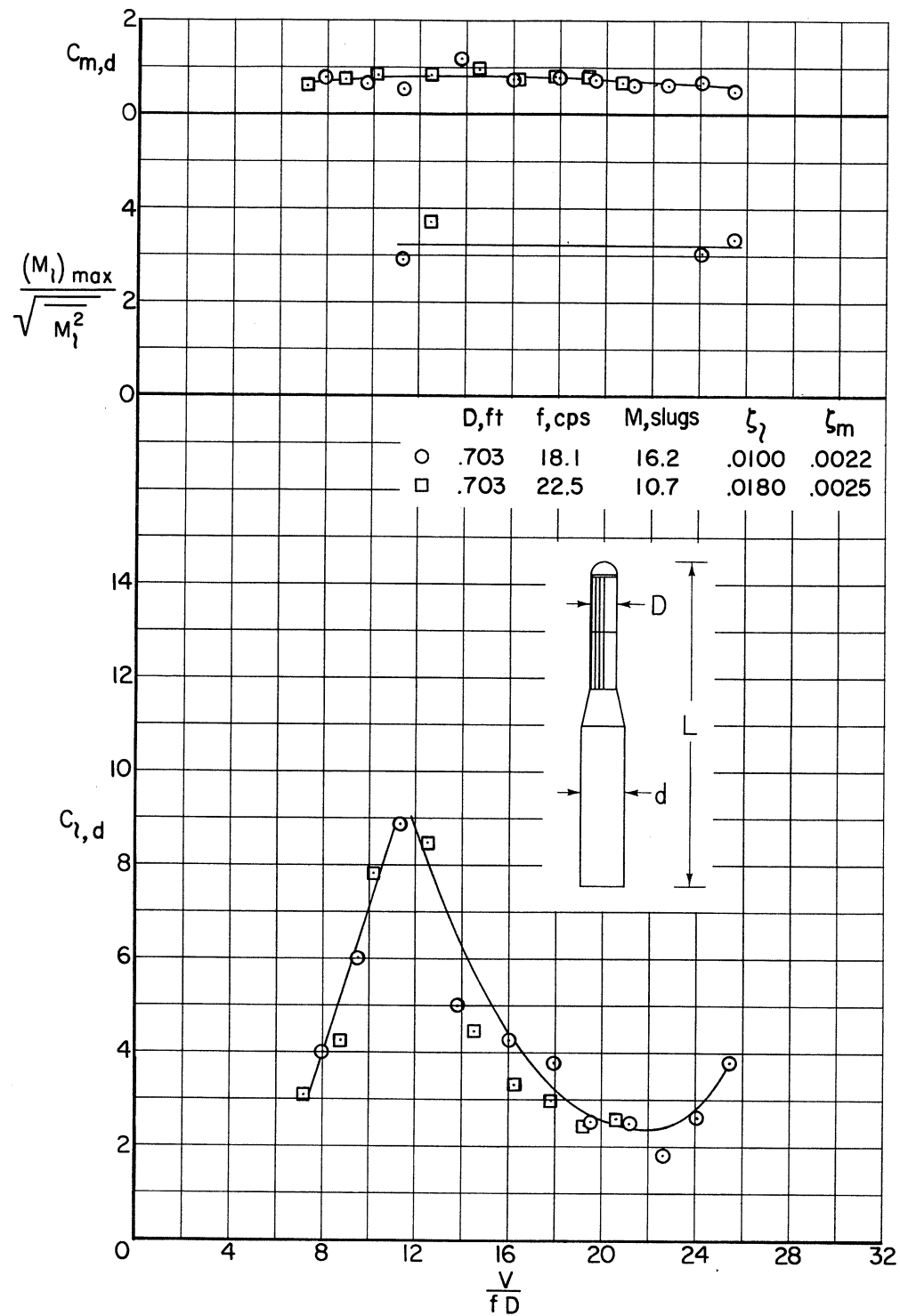
(g) With tapes 0.00036D and 0.00057D thick; $f_0 D^2 = 0.03$ to 0.04.

Figure 17.- Continued.



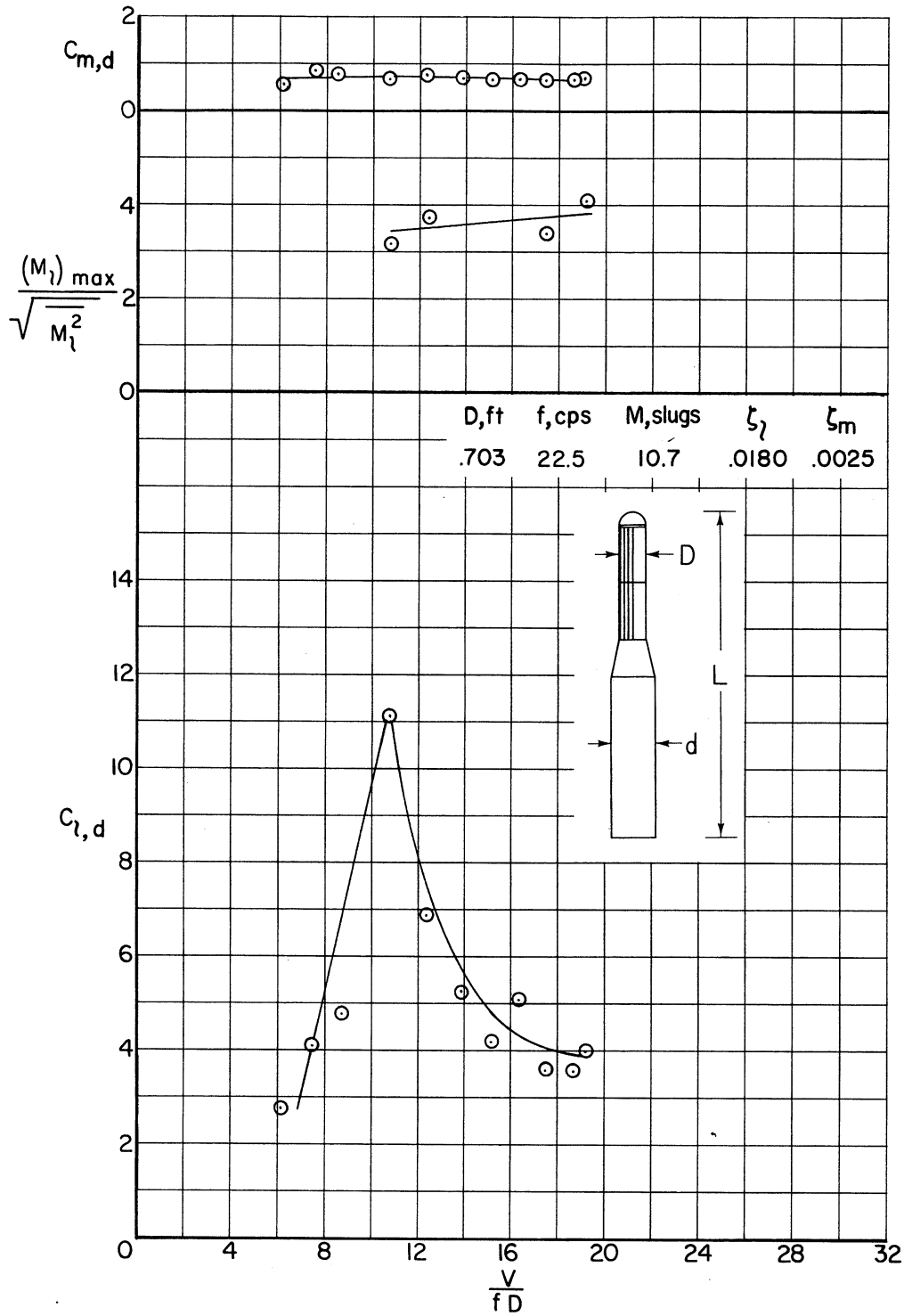
(h) With tapes 0.00036D thick; $f_p D^2 = 0.06$.

Figure 17.- Continued.



(i) With tapes 0.00036D thick; $f_0 D^2 = 0.09$.

Figure 17.- Continued.

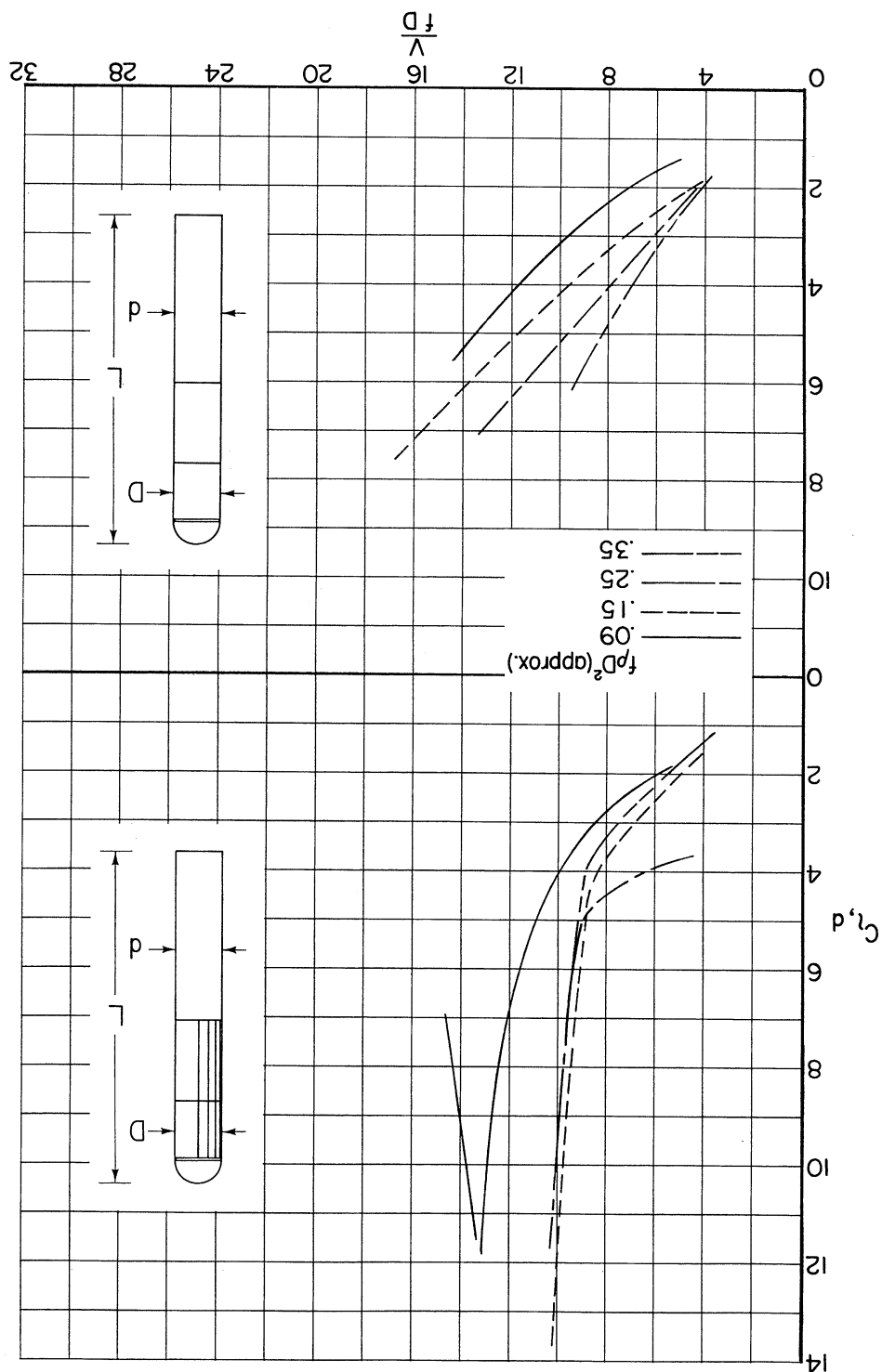


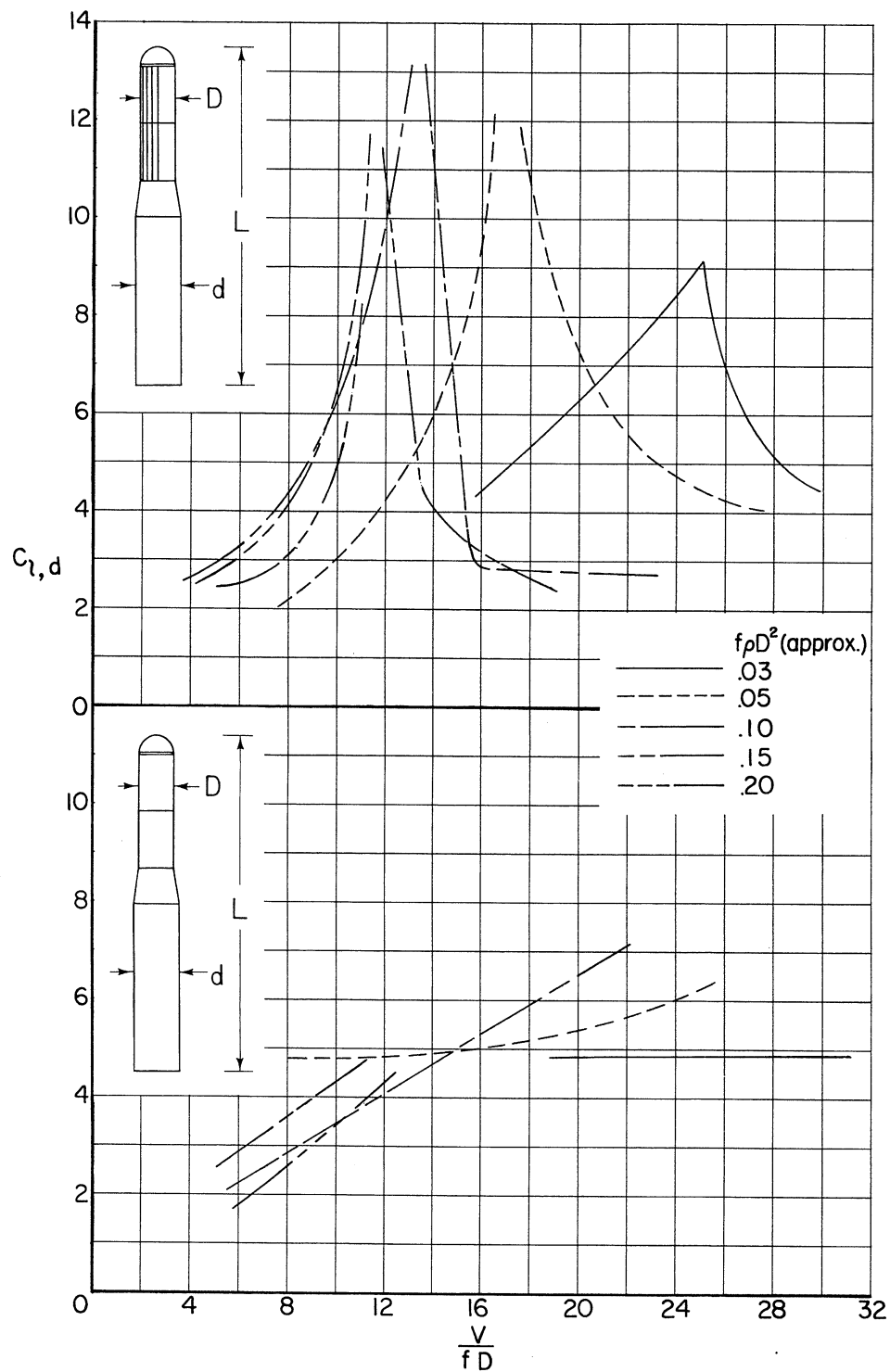
(j) With tapes 0.00036D thick; $f_p D^2 \cong 0.12$.

Figure 17.- Concluded.

Figure 18.- Comparison of dynamic lateral moment characteristics of models with hemisphere nose.

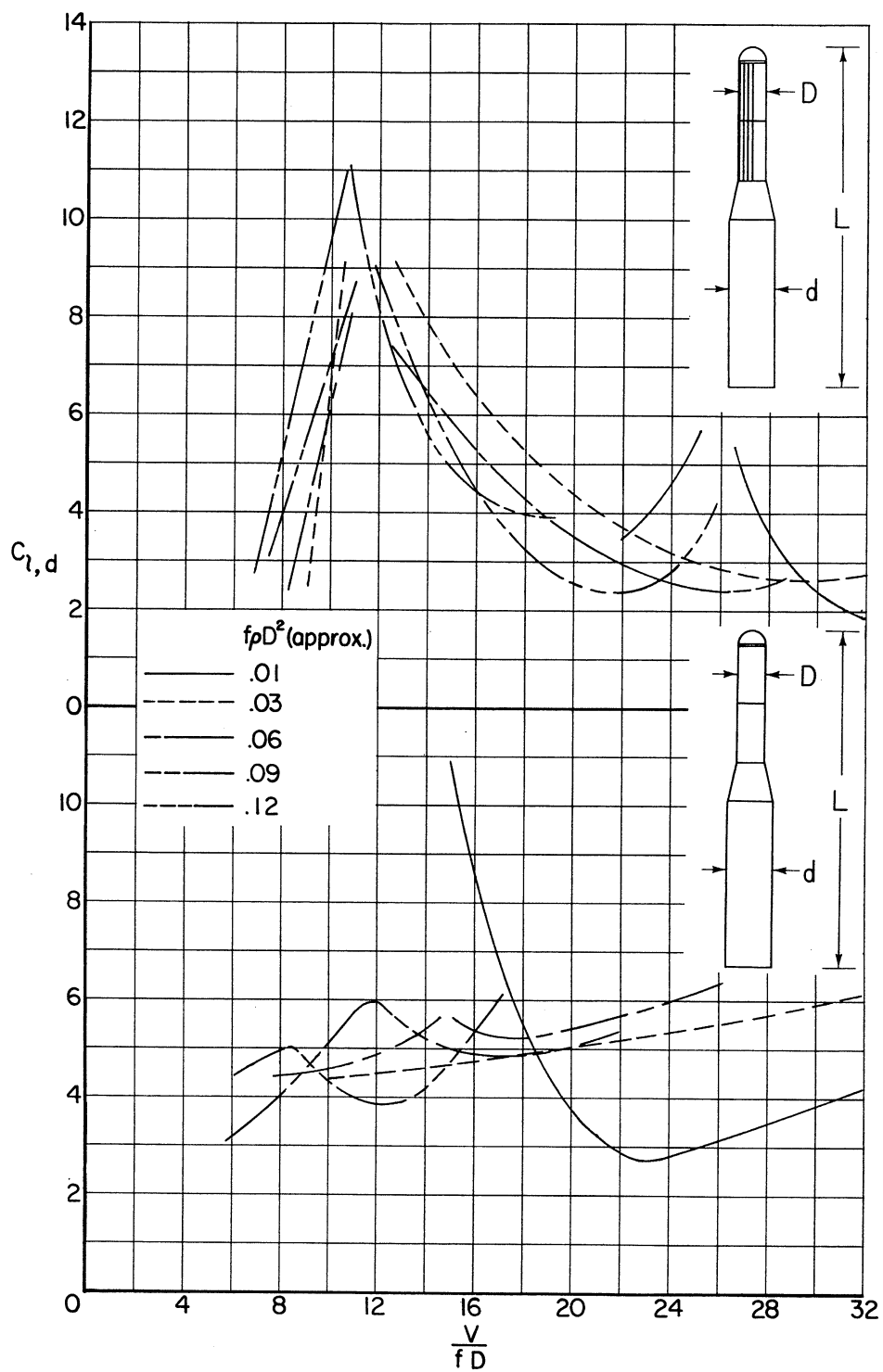
(a) Effect of fD^2 with and without tapes 0.00022D thick; $D/d = 1$.





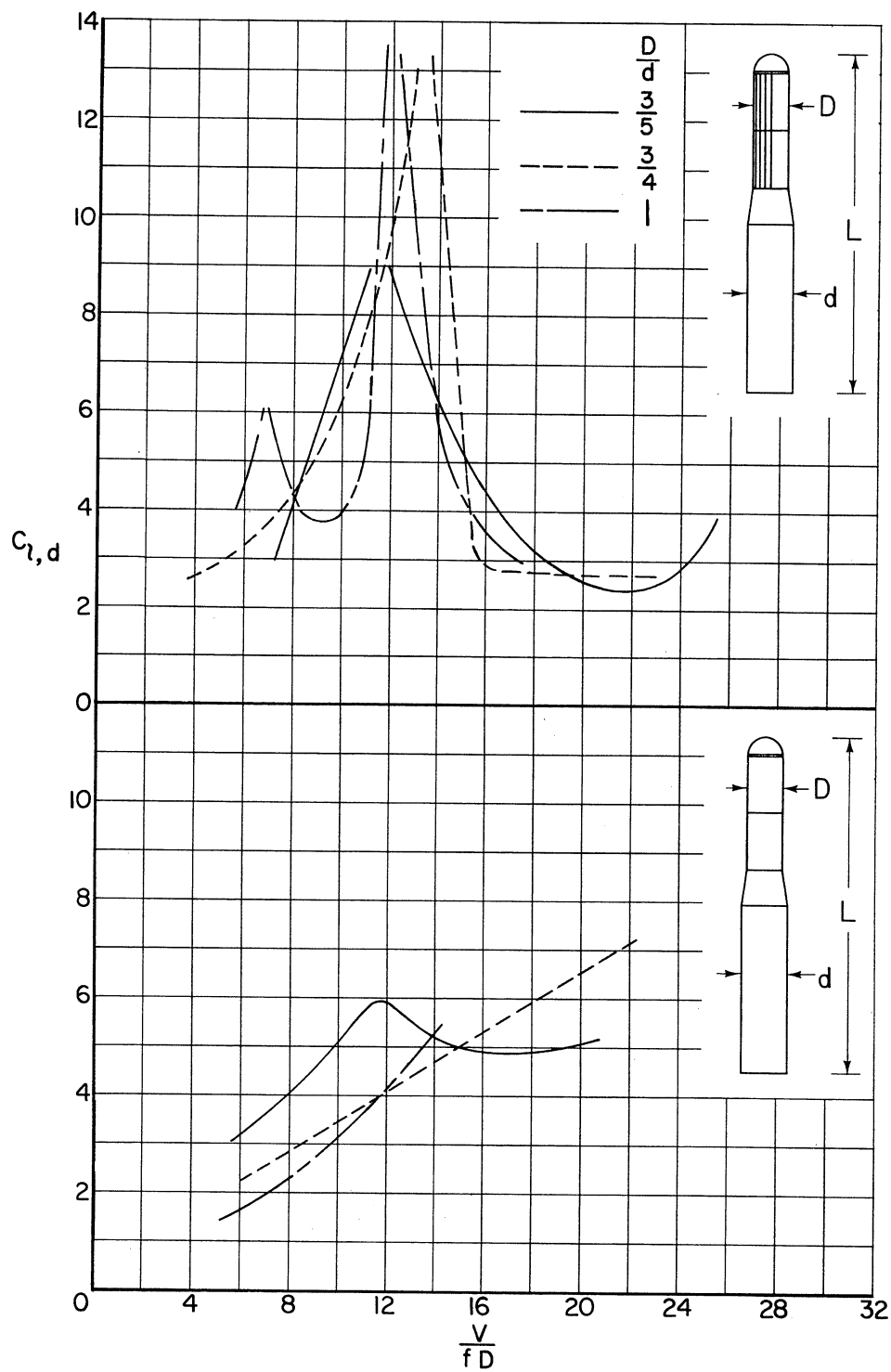
(b) Effect of $f\rho D^2$ with and without tapes 0.00029D thick; $D/d = 3/4$.

Figure 18.- Continued.



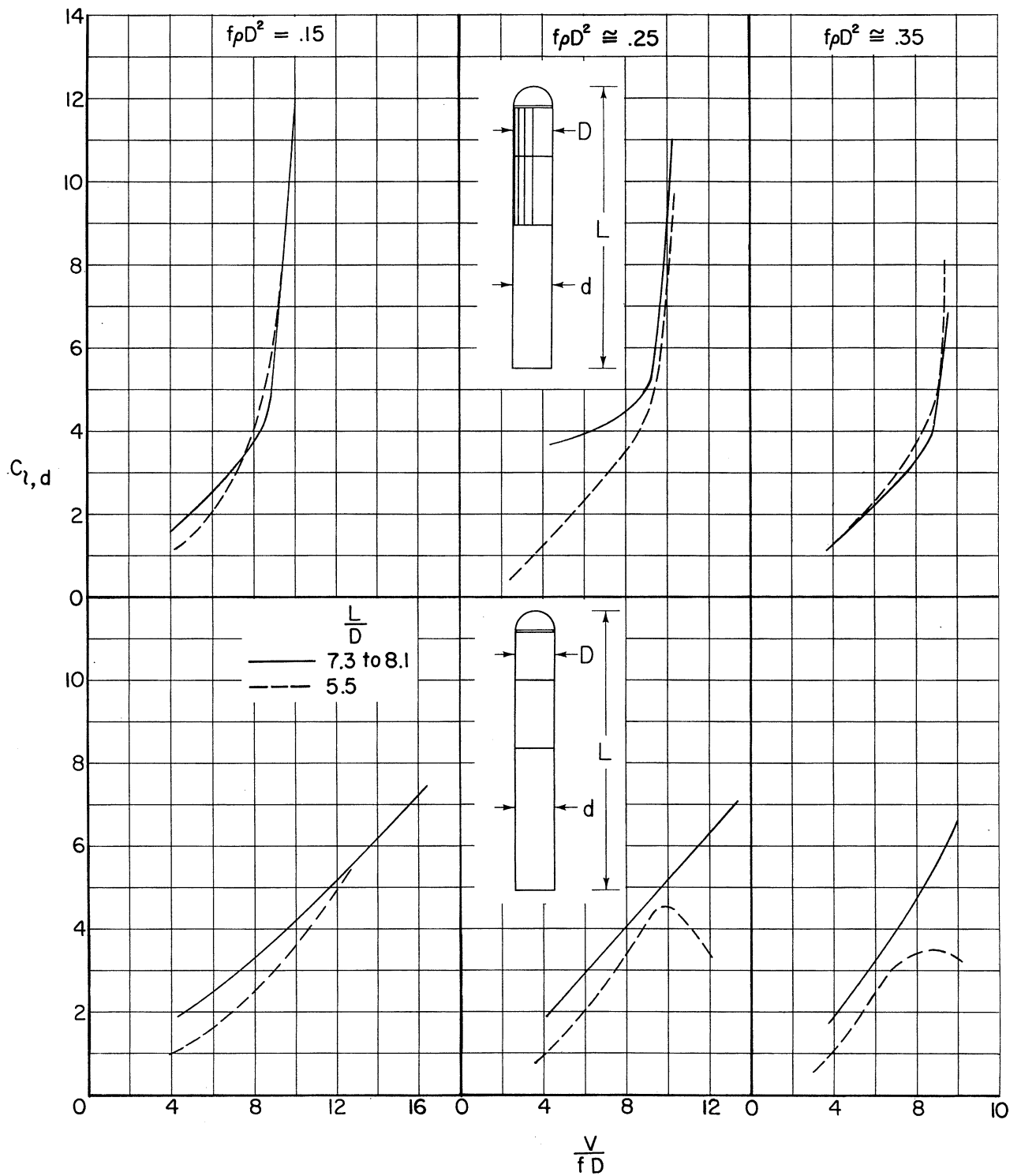
(c) Effect of $f\rho D^2$ with and without tapes 0.00036D to 0.00057D thick;
 $D/d = 3/5$.

Figure 18.- Continued.



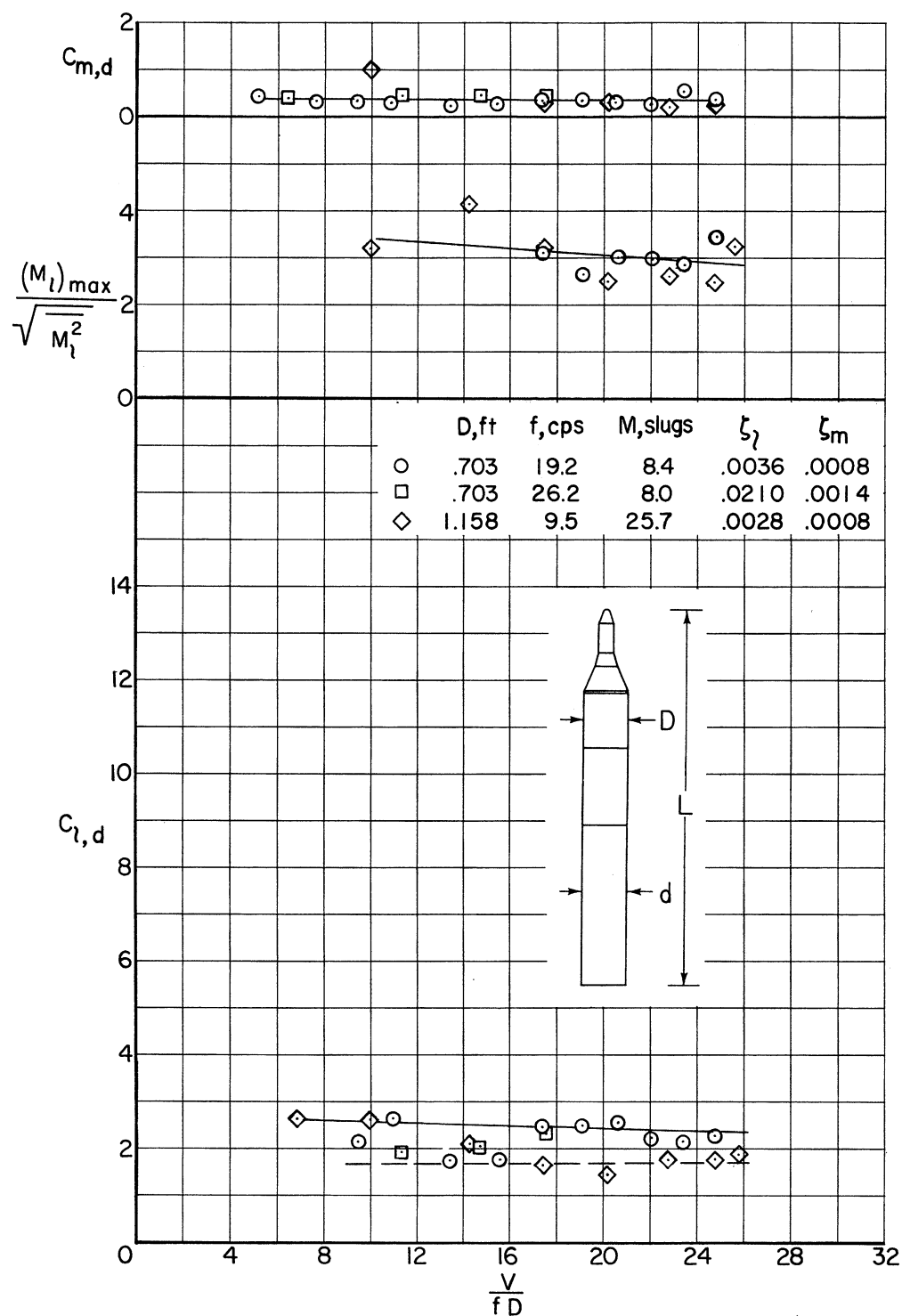
(d) Effect of stage-diameter ratio with and without tapes 0.00029D to 0.00036D thick; $L/d = 7.2$ to 9.5 , $f_p D^2 \approx 0.09$.

Figure 18.- Continued.



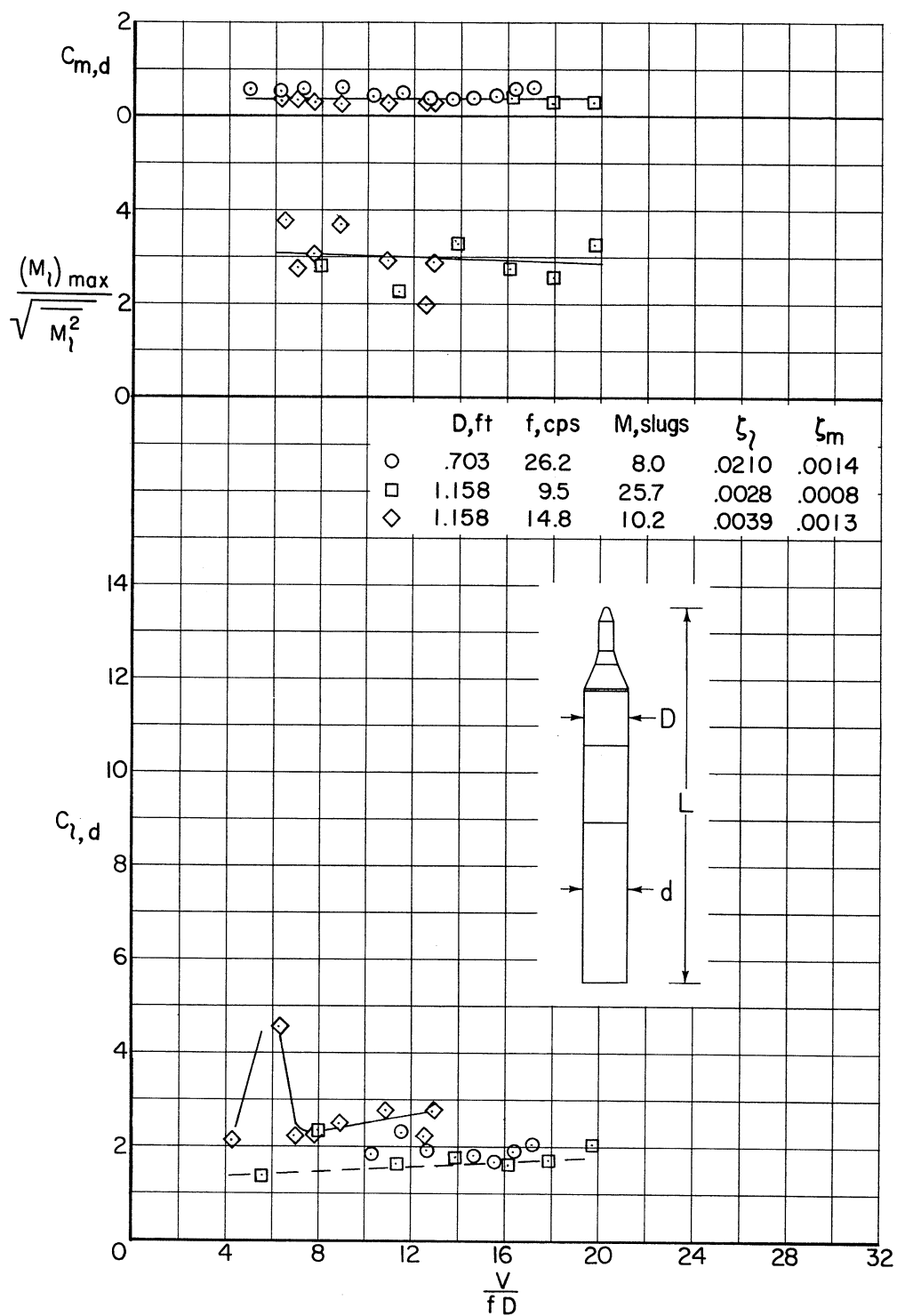
(e) Effect of fineness ratio with and without tapes 0.00022D thick;
 $D/d = 1$.

Figure 18.- Concluded.



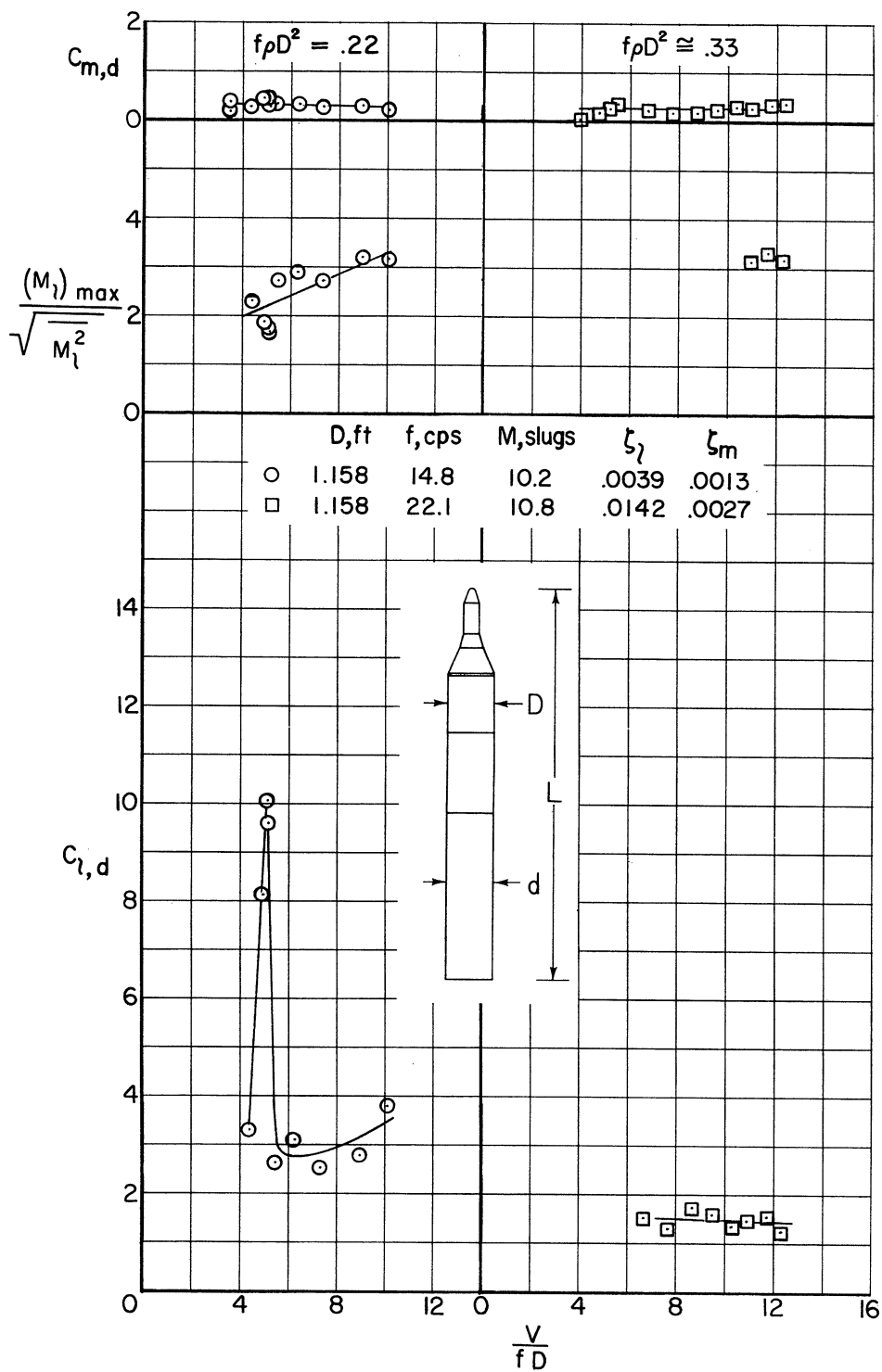
(a) Without roughness; $f_p D^2 = 0.09$.

Figure 19.- Dynamic moment characteristics of models with the cone-cylinder nose; $D/d = 1$; $L/D = 8.6$ to 9.5 .



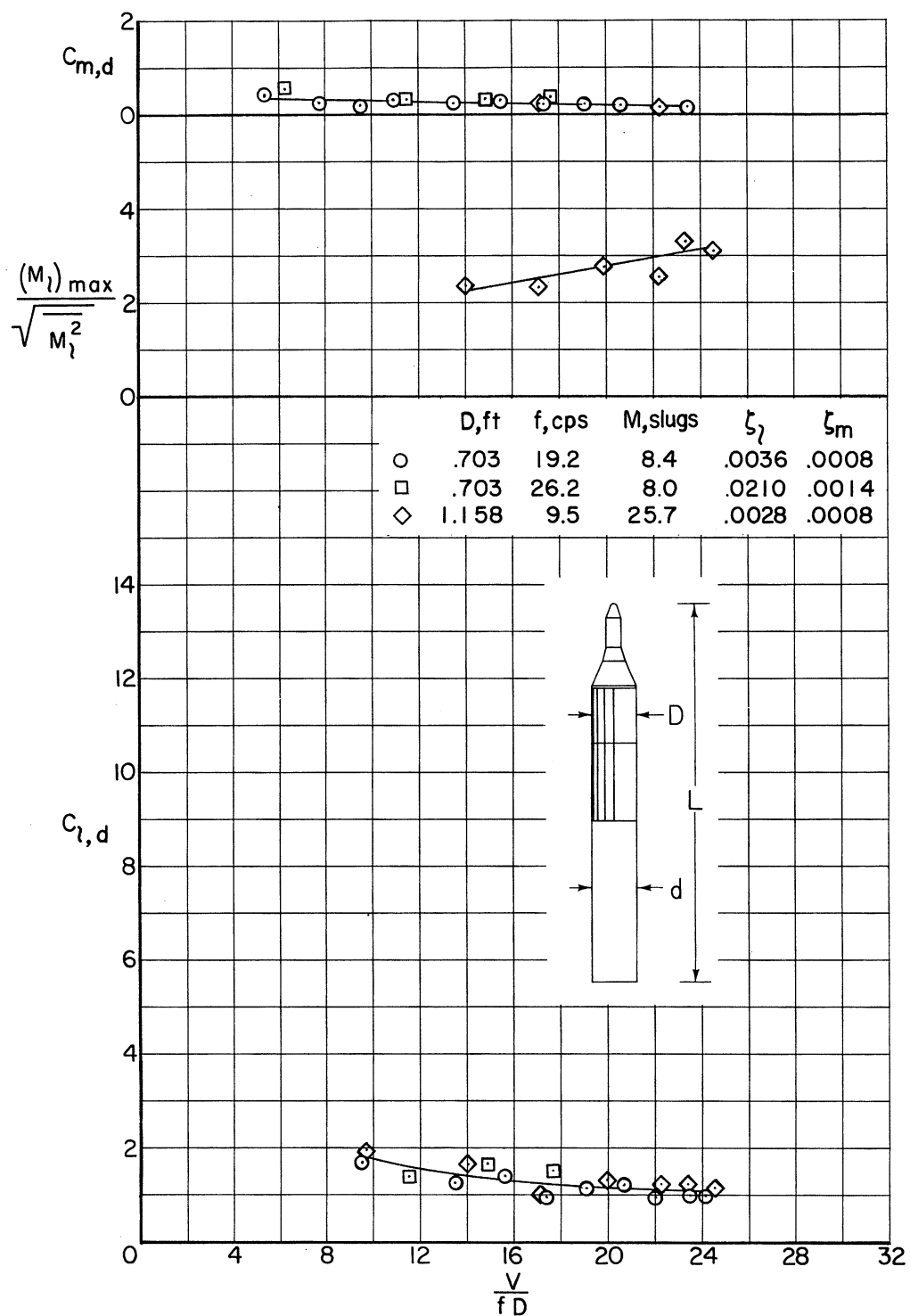
(b) Without roughness; $f_0 D^2 \approx 0.15$.

Figure 19.- Continued.



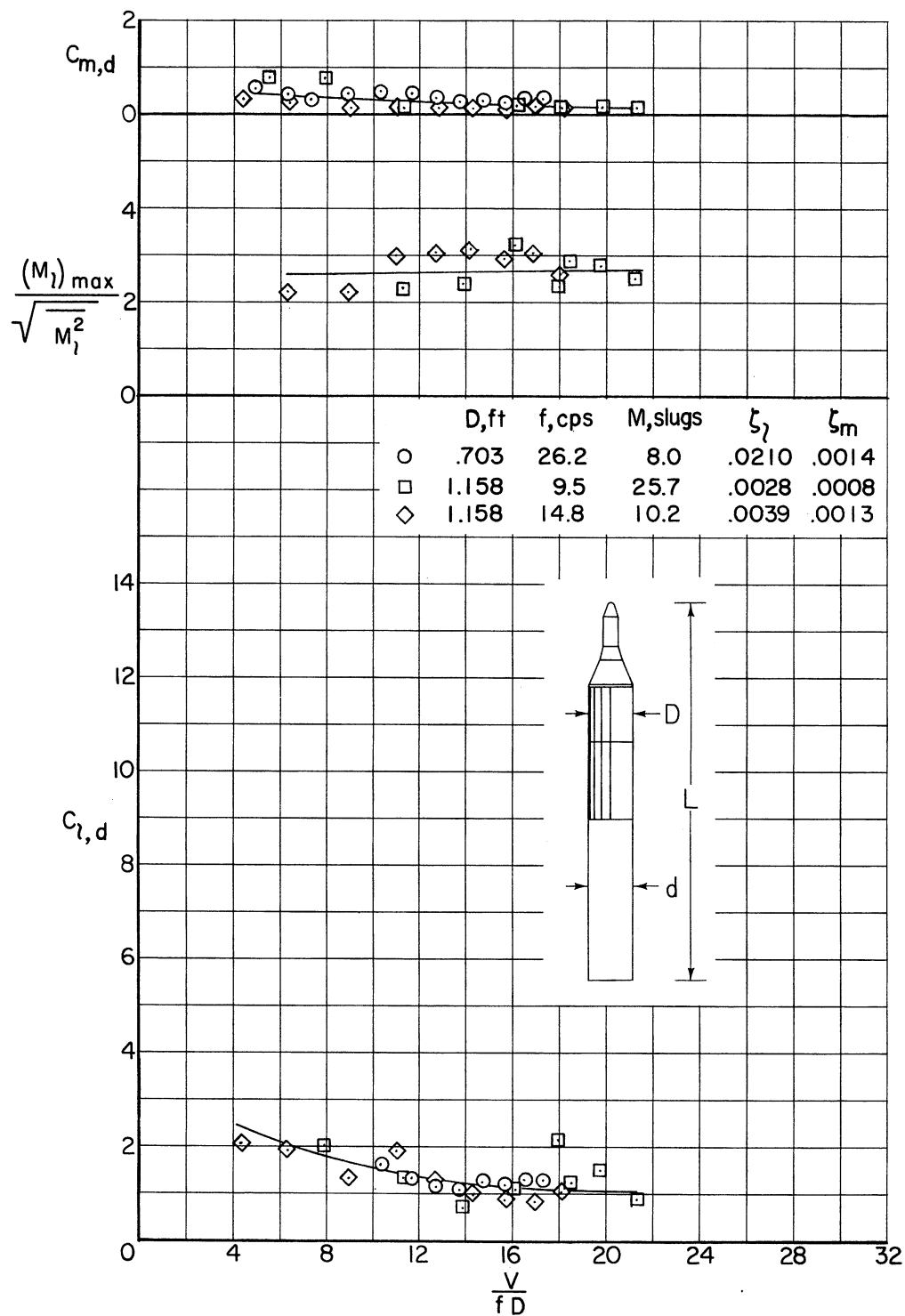
(c) Without roughness; $f\rho D^2 \cong 0.22, 0.33$.

Figure 19.- Continued.



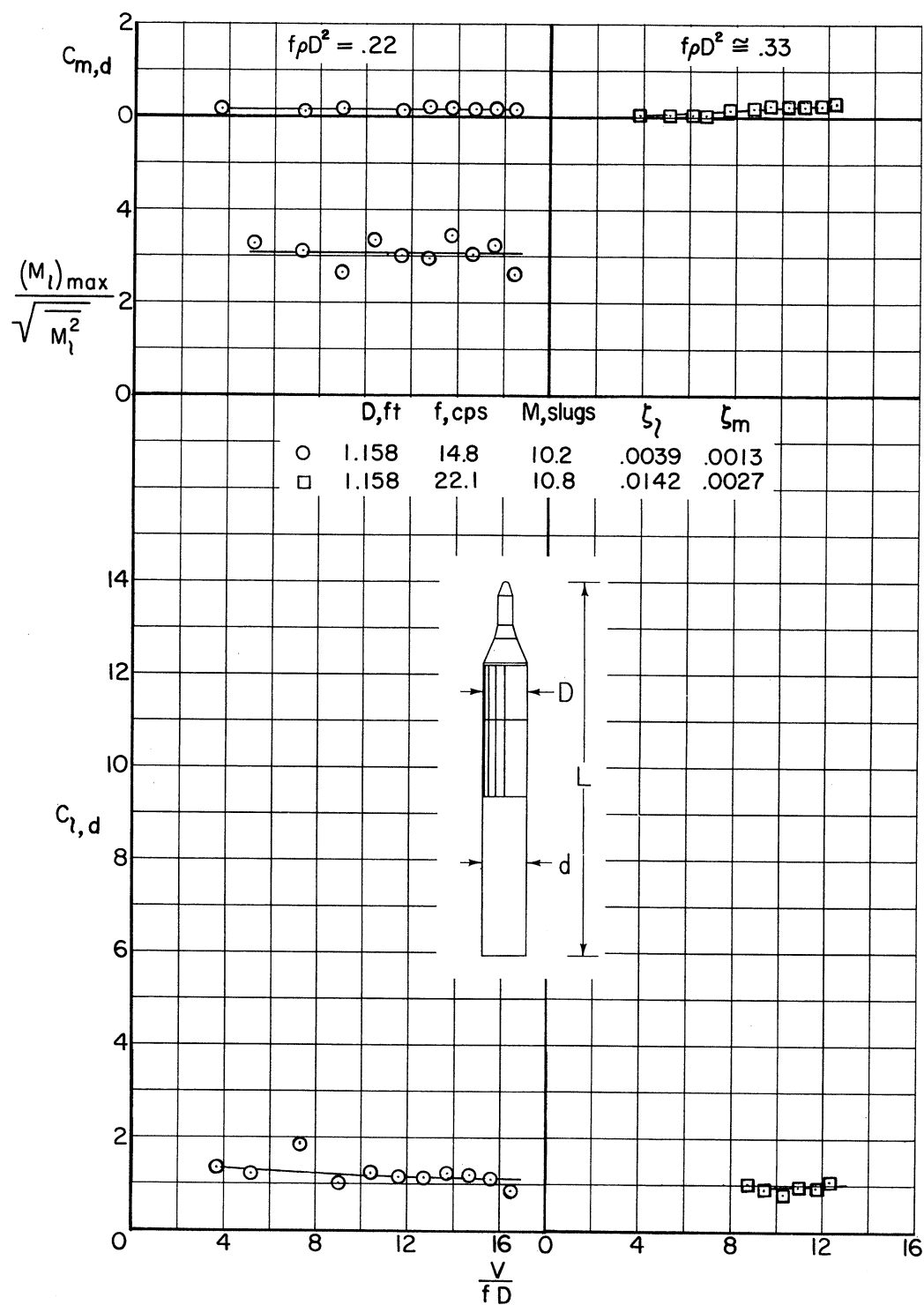
(d) With tapes 0.00022D to 0.00036D thick; $f_p D^2 = 0.09$.

Figure 19.- Continued.



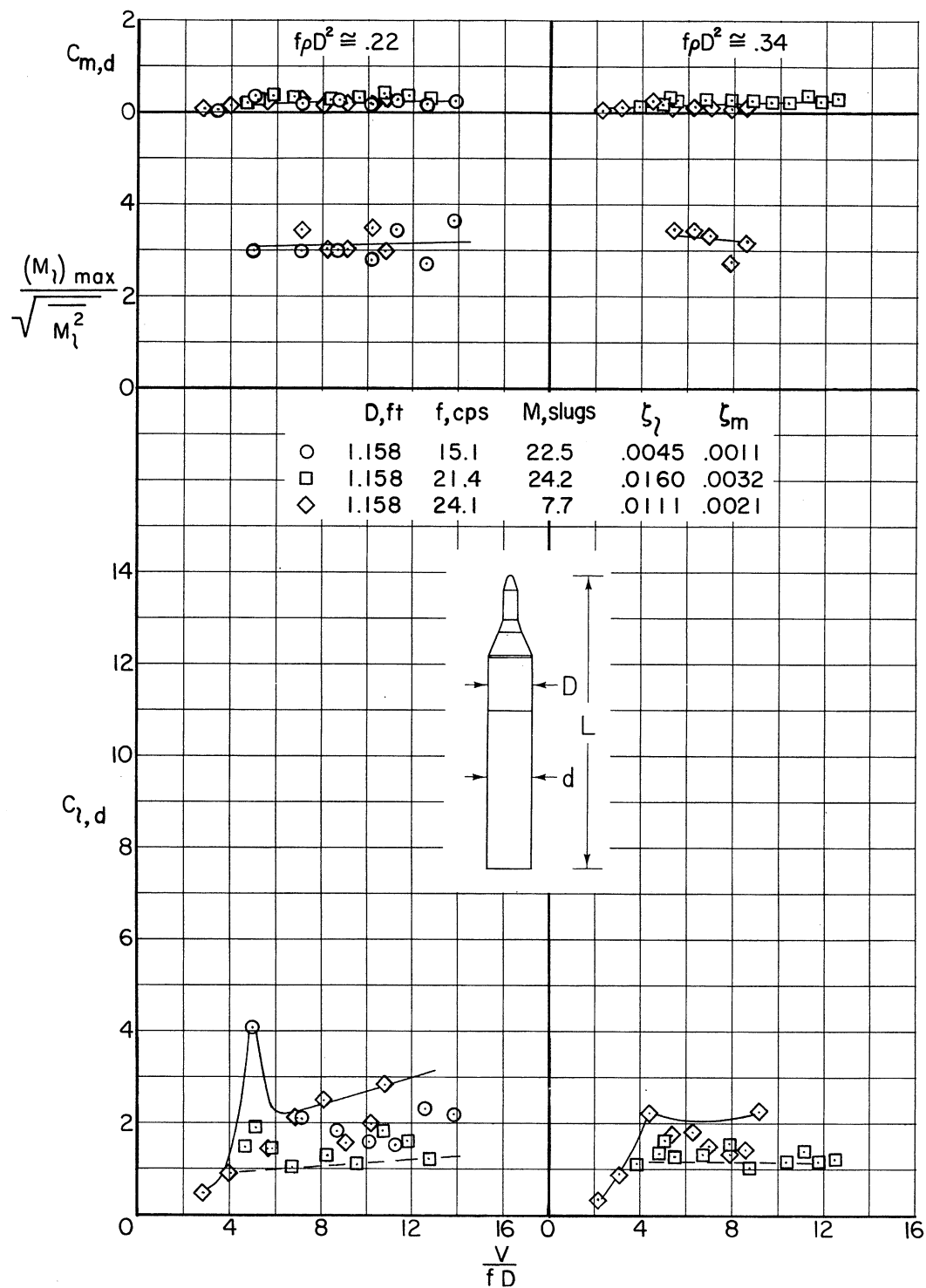
(e) With tapes 0.00022D to 0.00036D thick; $f_p D^2 \approx 0.15$.

Figure 19.- Continued.



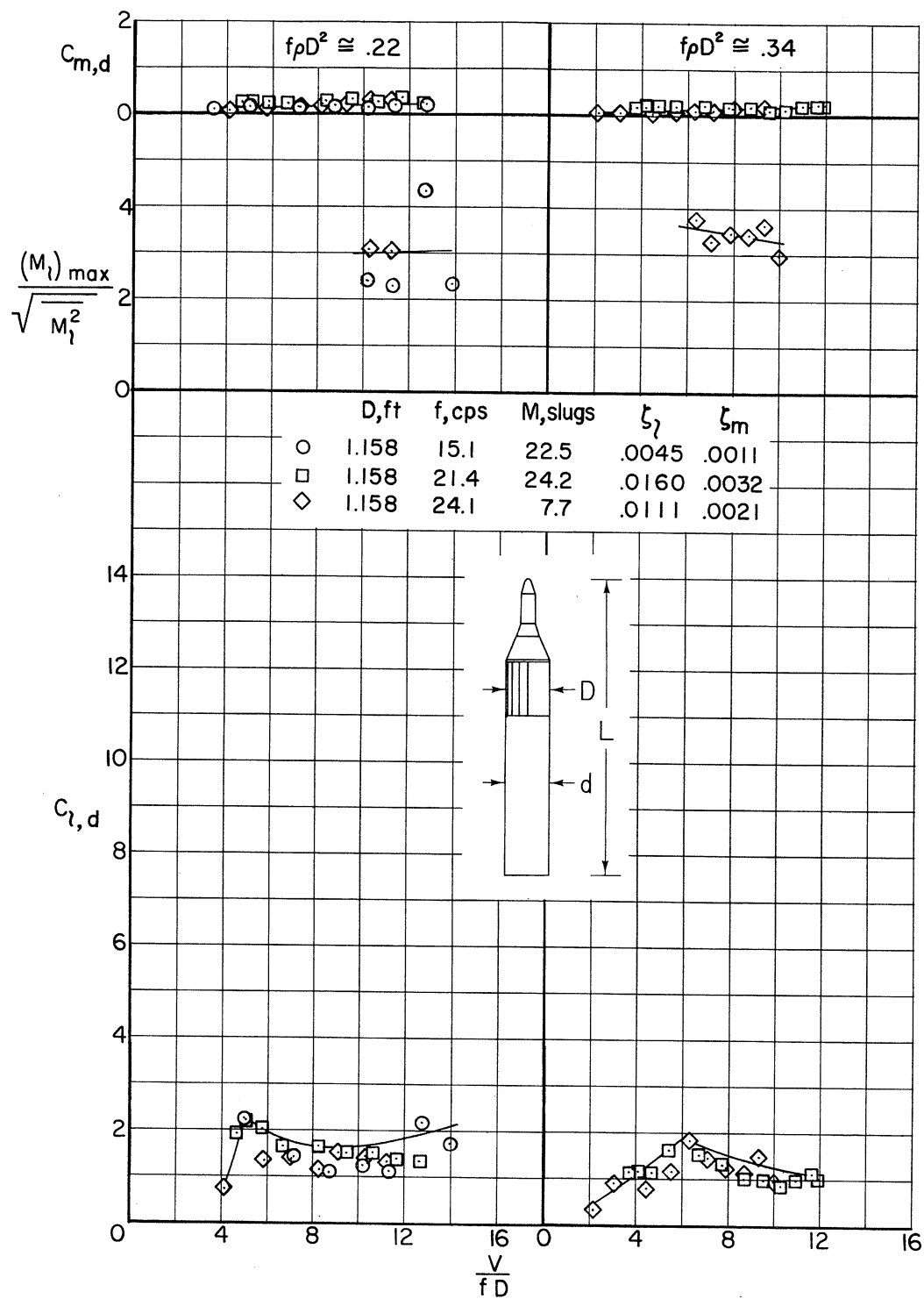
(f) With tapes 0.00022D thick; $f_p D^2 \approx 0.22, 0.33$.

Figure 19.- Concluded.



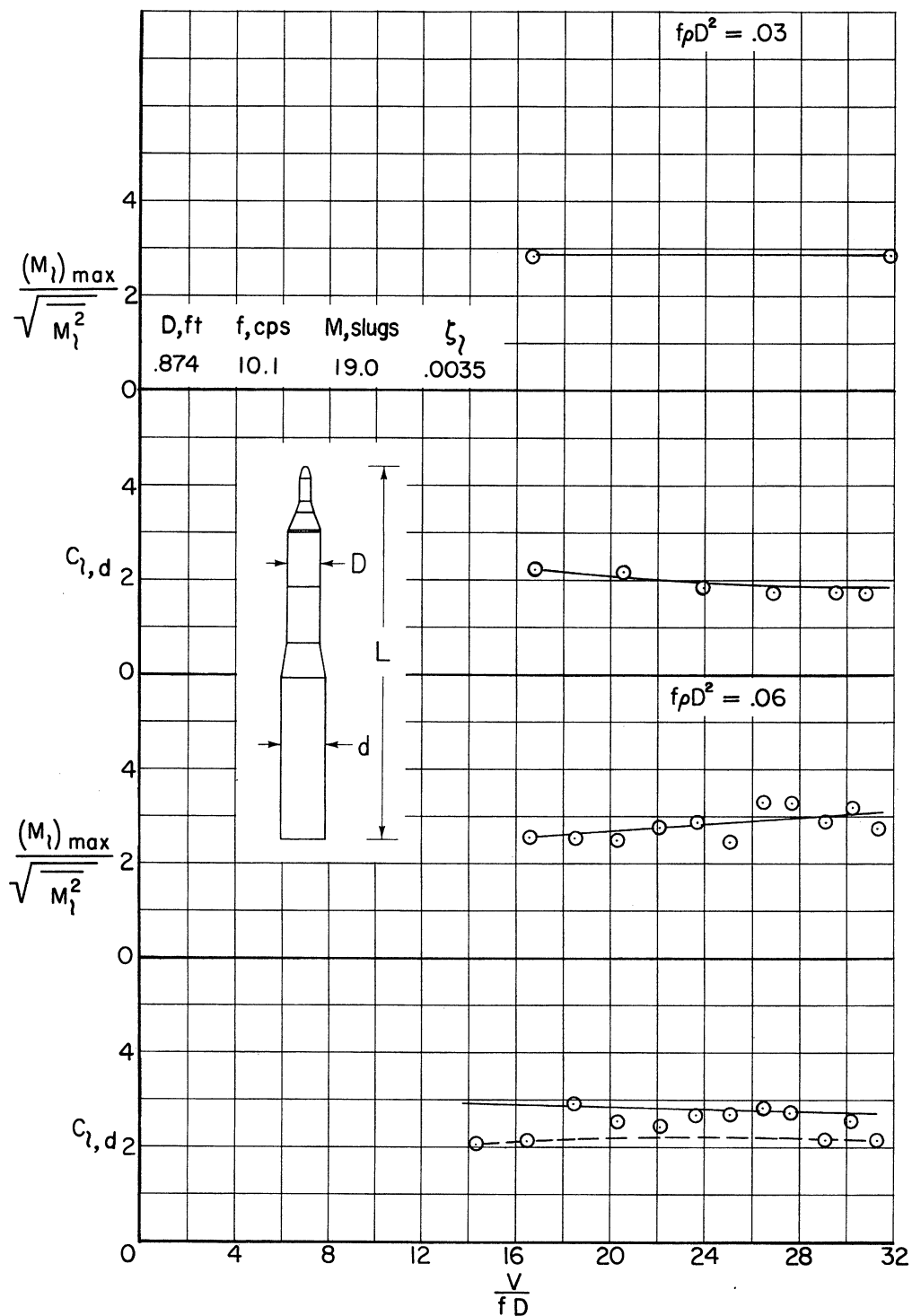
(a) Without roughness.

Figure 20.- Dynamic moment characteristics of models with the cone-cylinder nose; $D/d = 1$; $L/D = 6.9$.



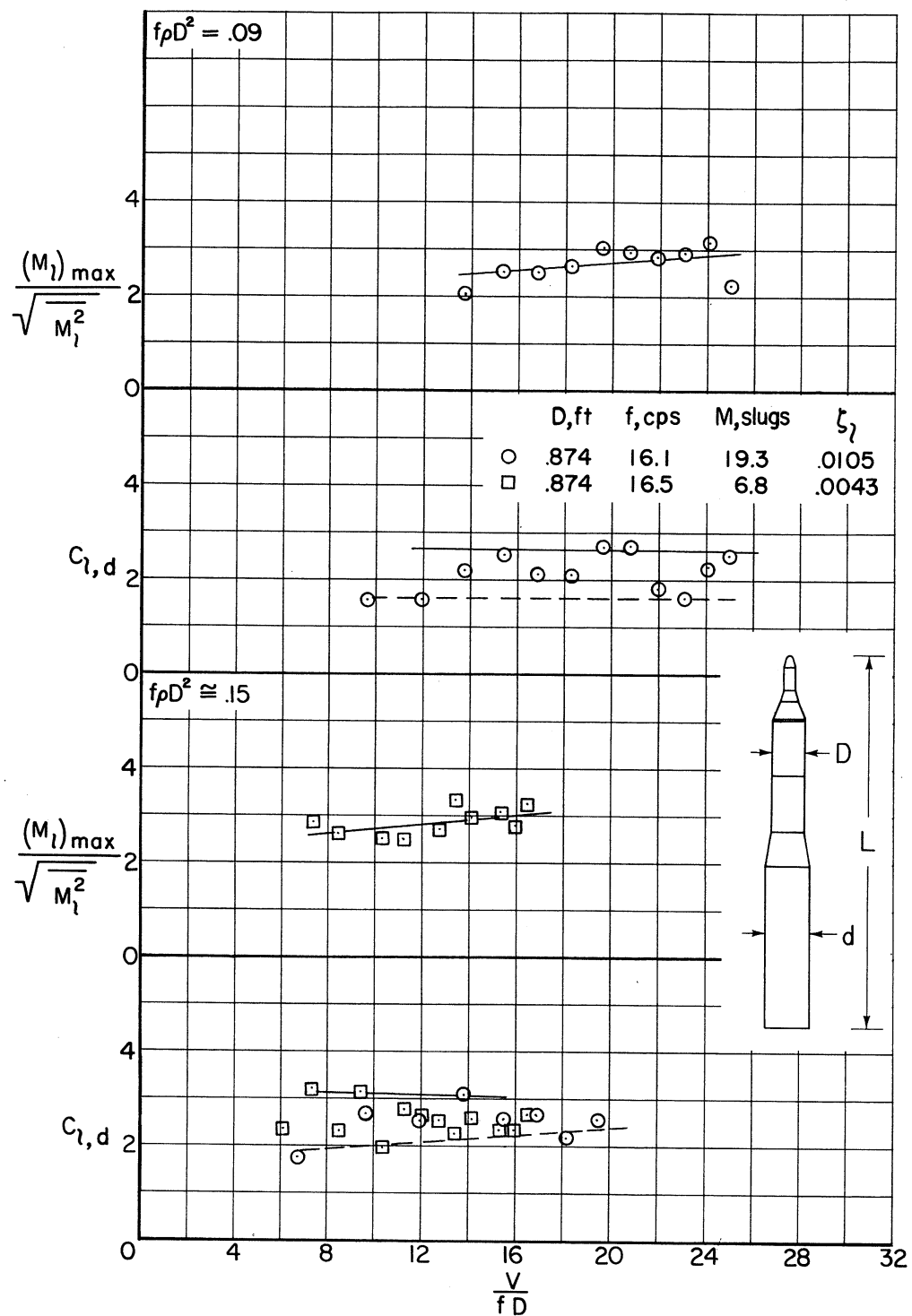
(b) With tapes 0.00022D thick.

Figure 20.- Concluded.



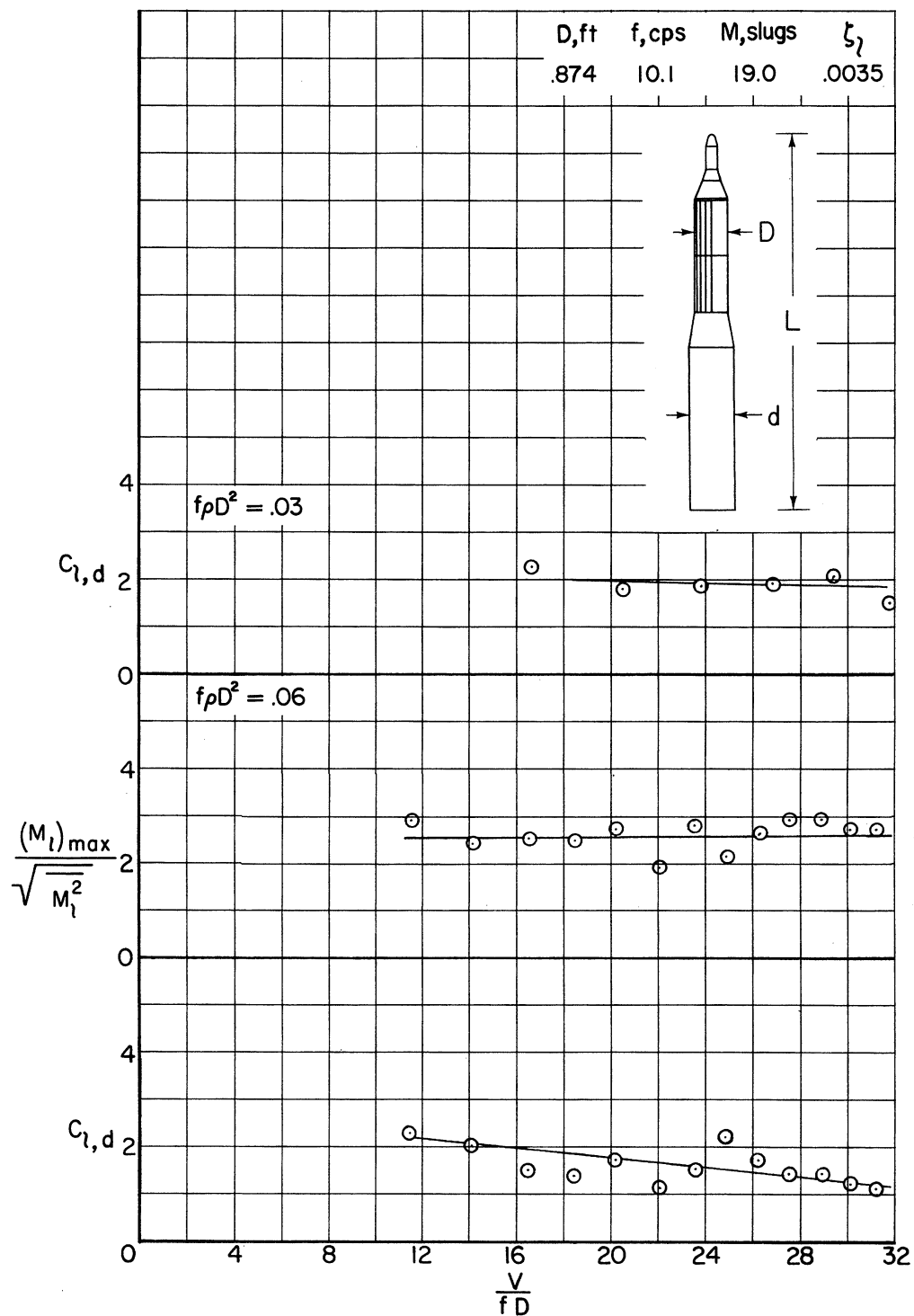
(a) Without roughness; $f_p D^2 = 0.03, 0.06$.

Figure 21.- Dynamic moment characteristics of models with the cone-cylinder nose; $D/d = 3/4$; $L/D = 10.9$.



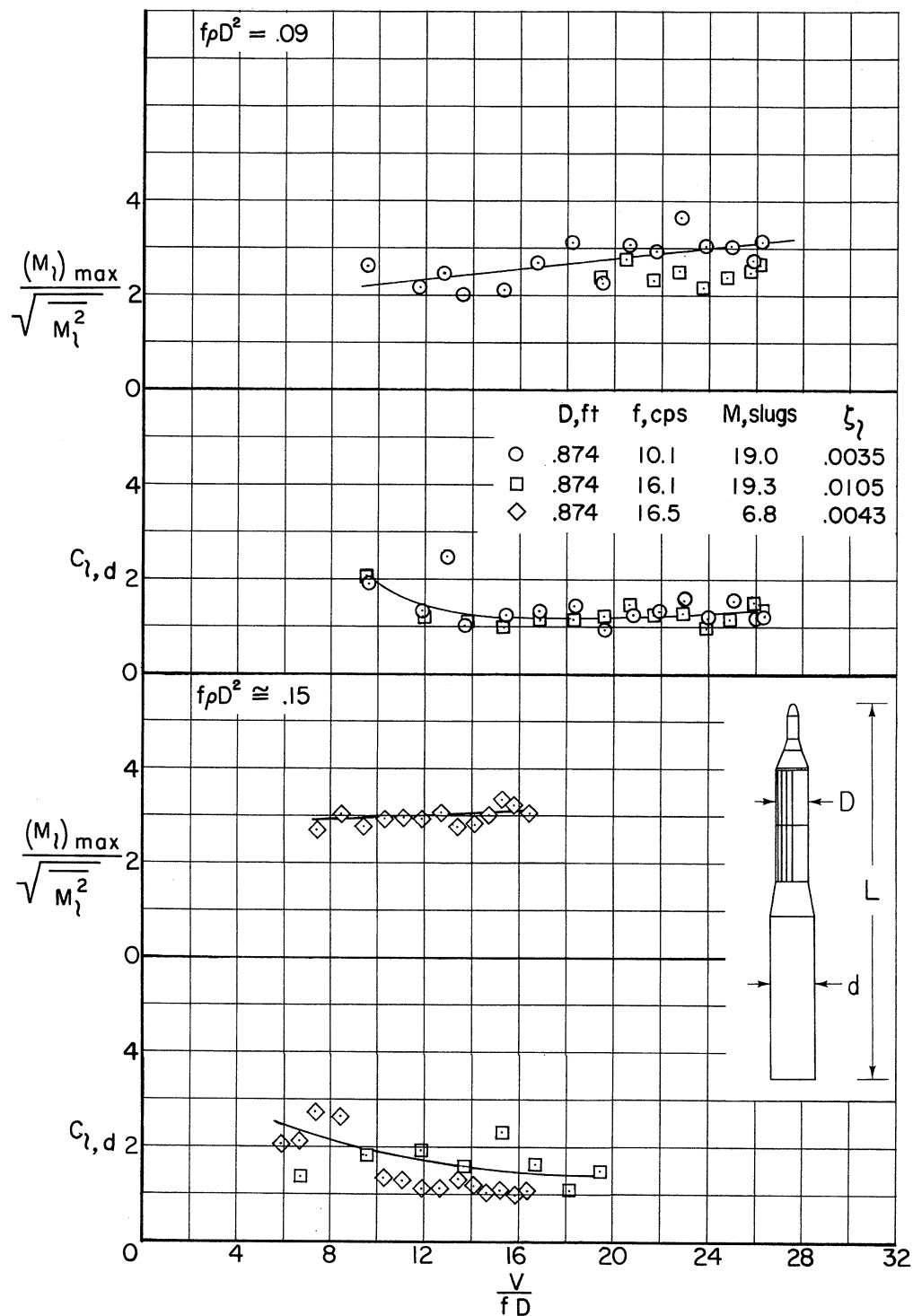
(b) Without roughness; $f\rho D^2 \cong 0.09, 0.15$.

Figure 21.- Continued.



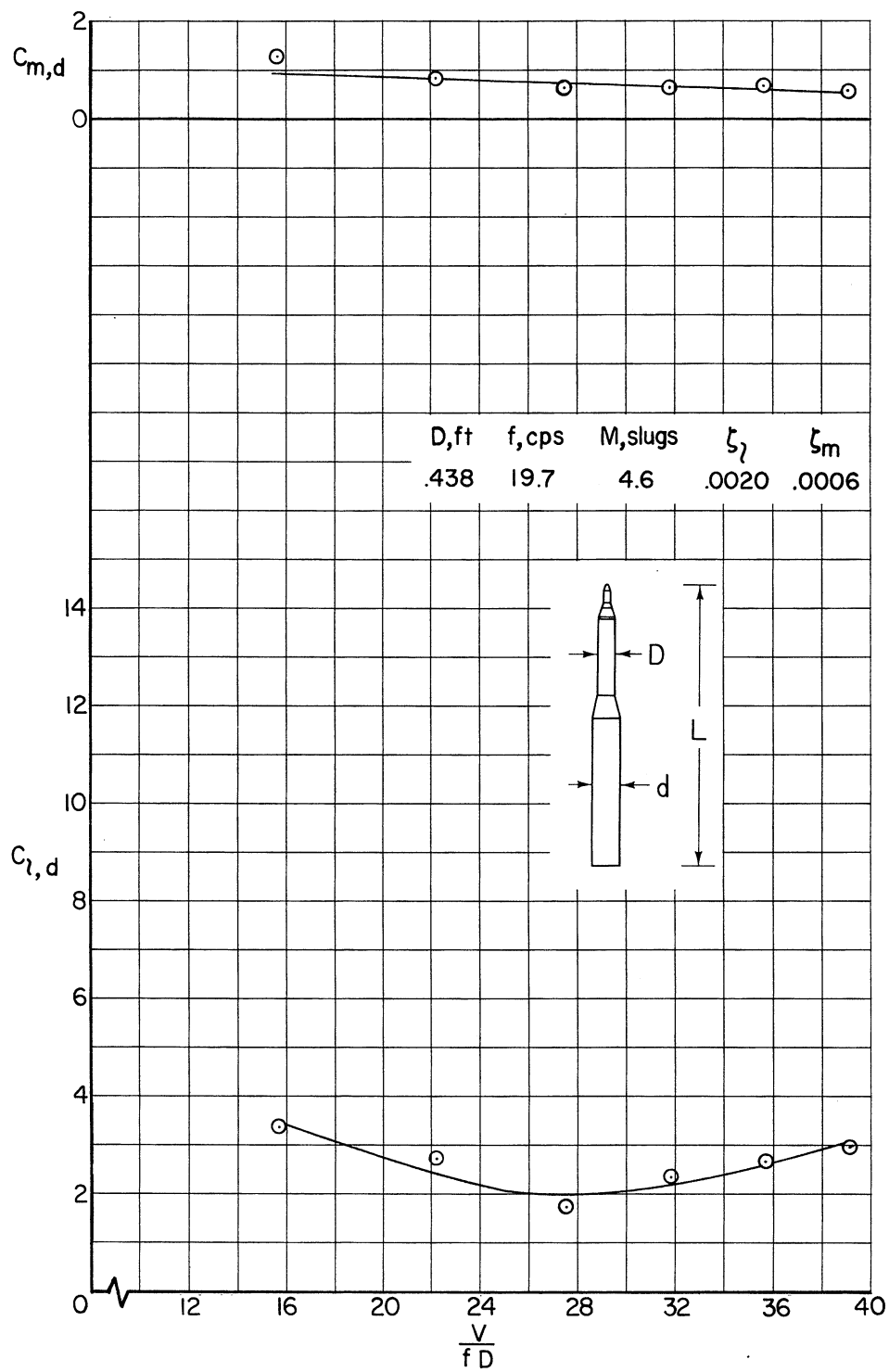
(c) With tapes 0.00029D thick; $f\rho D^2 \approx 0.03, 0.06$.

Figure 21.- Continued.



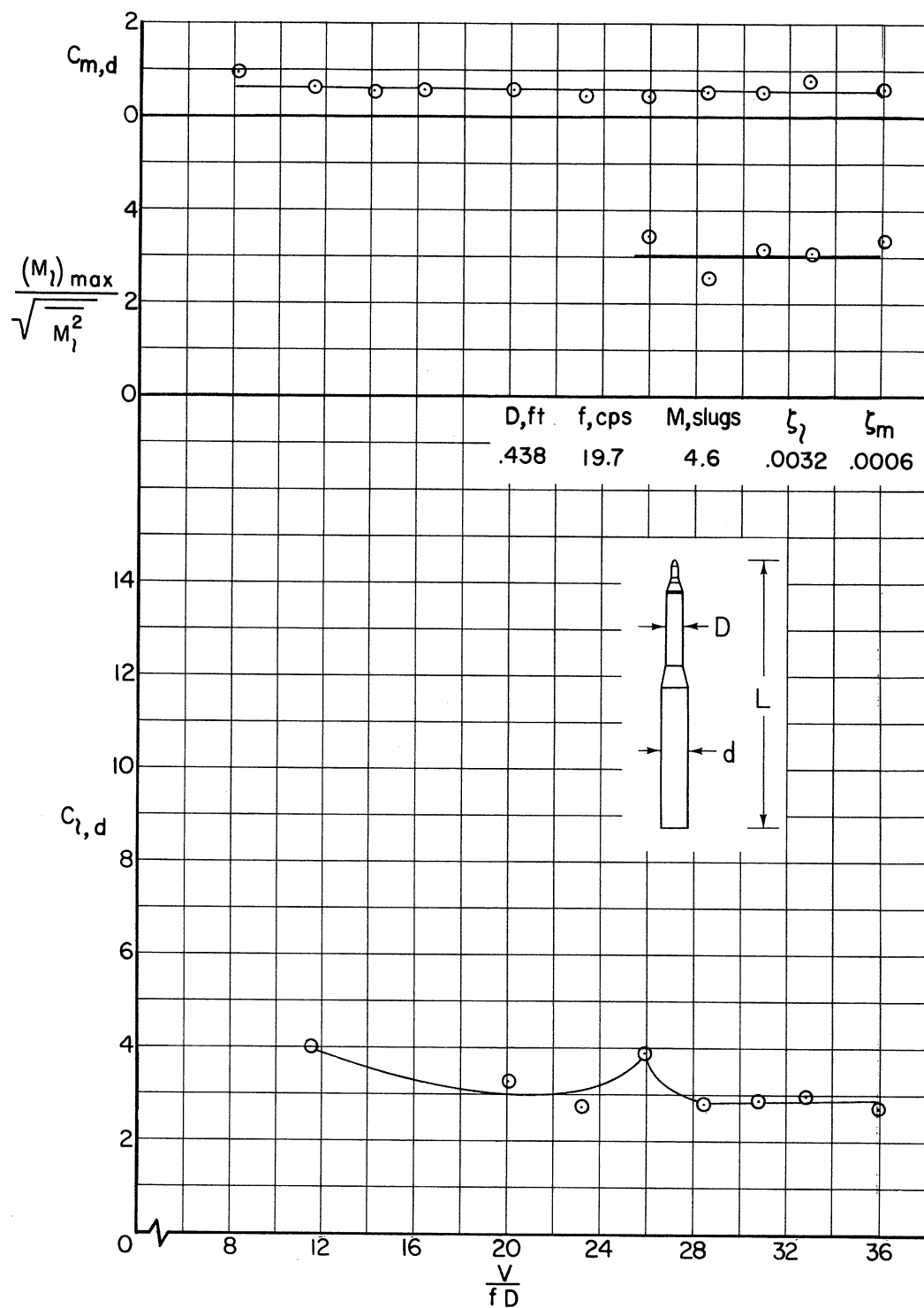
(d) With tapes 0.00029D thick; $f\rho D^2 \cong 0.09, 0.15$.

Figure 21.- Concluded.



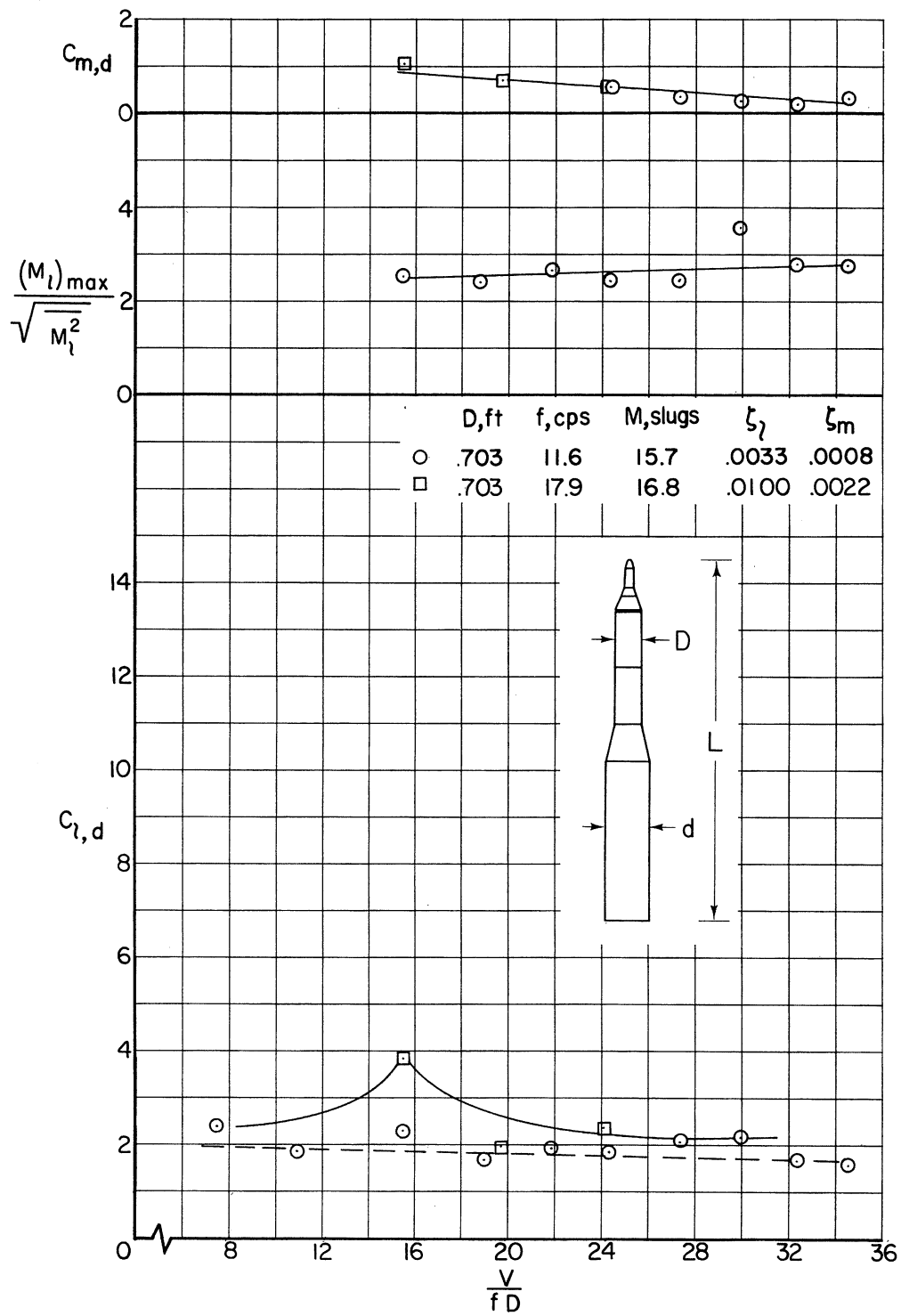
(a) Without roughness; $f\rho D^2 = 0.01$.

Figure 22.- Dynamic moment characteristics of models with the cone-cylinder nose; $D/d = 3/5$; $L/D = 13.8$ to 16.6 .



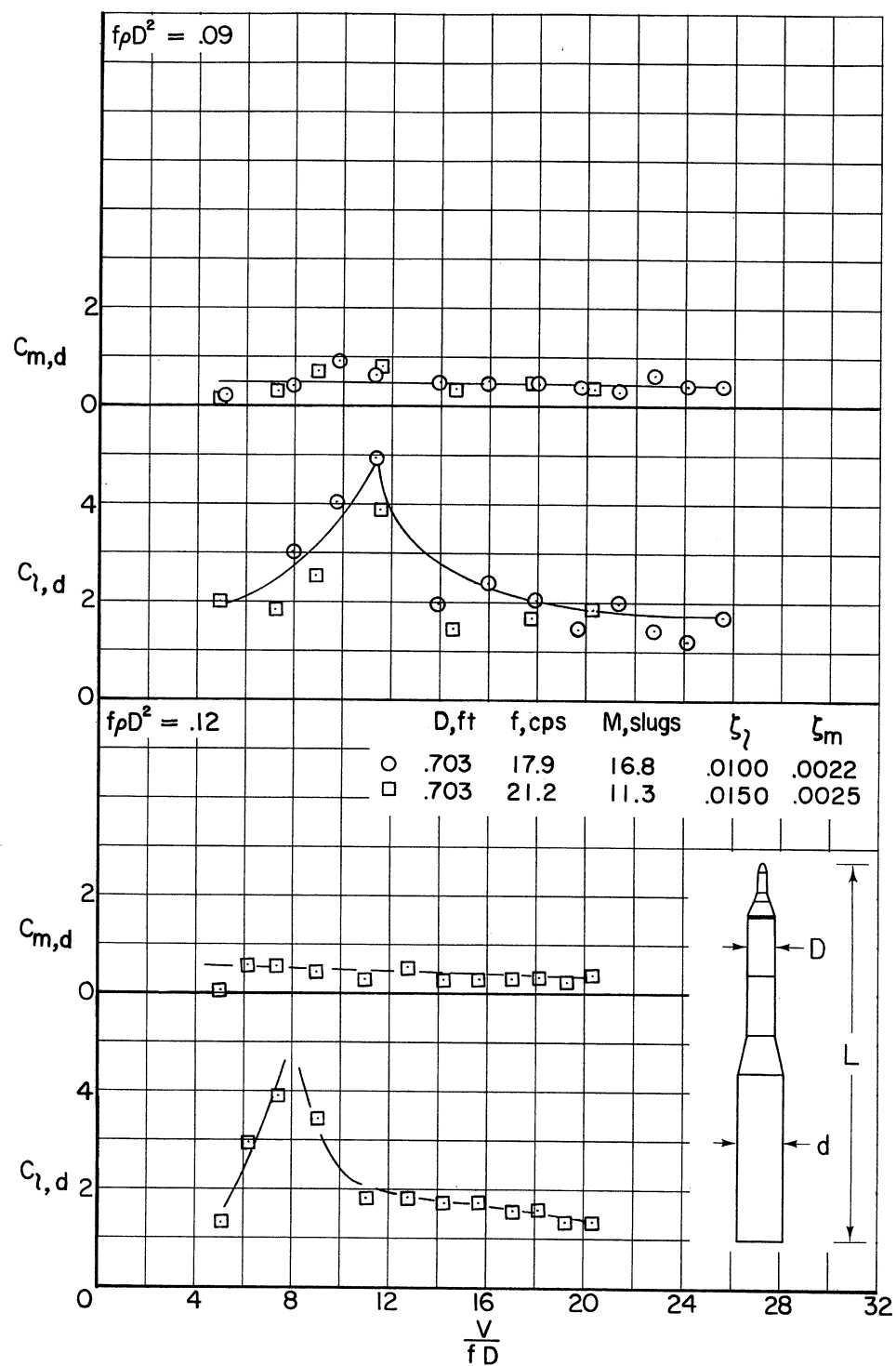
(b) Without roughness; $f\rho D^2 = 0.04$.

Figure 22.- Continued.



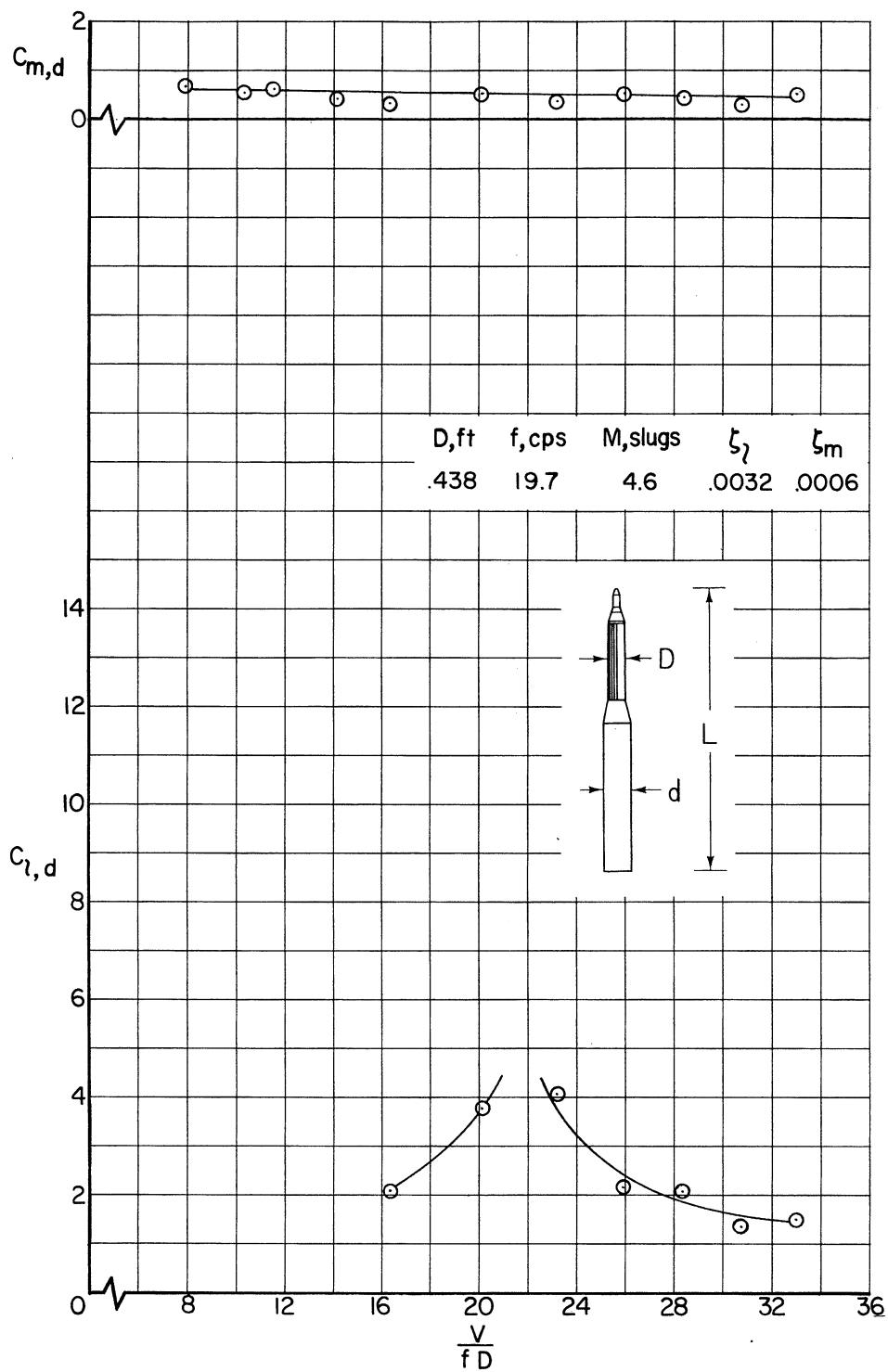
(c) Without roughness; $f\rho D^2 = 0.06$.

Figure 22.- Continued.



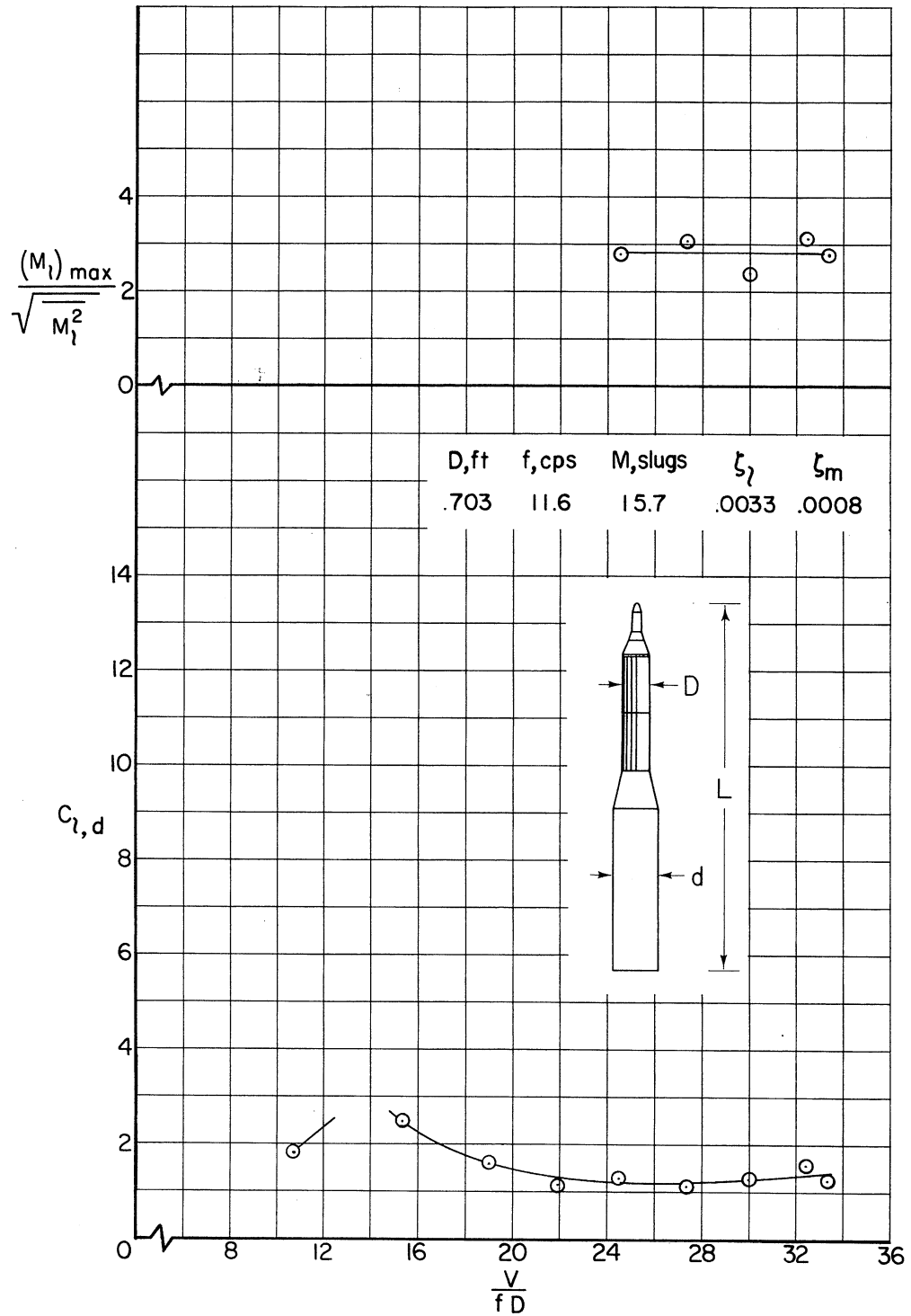
(d) Without roughness; $f\rho D^2 = 0.09, 0.12$.

Figure 22.- Continued.



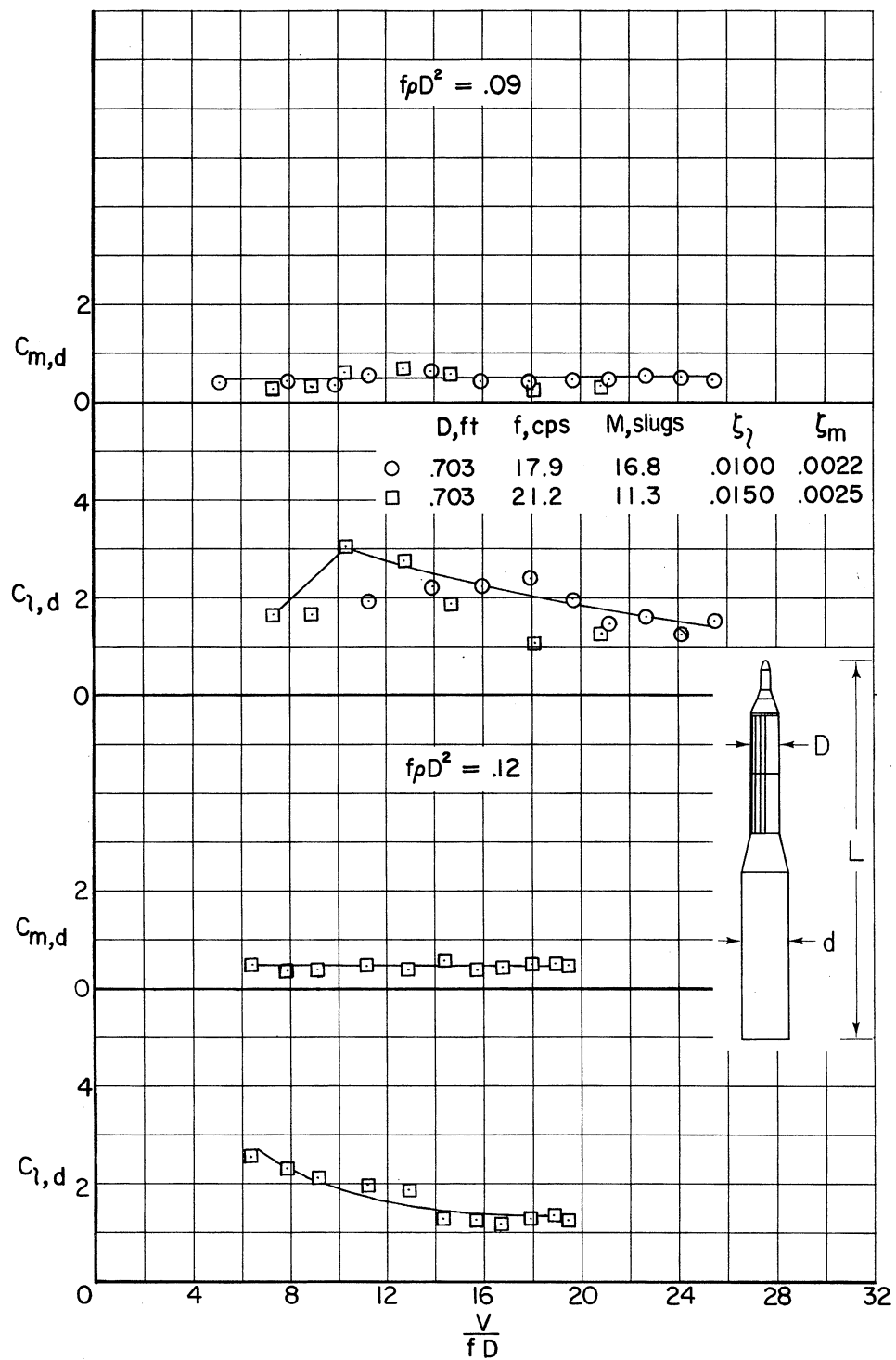
(e) With tapes 0.00057D thick; $f_0 D^2 = 0.04$.

Figure 22.- Continued.



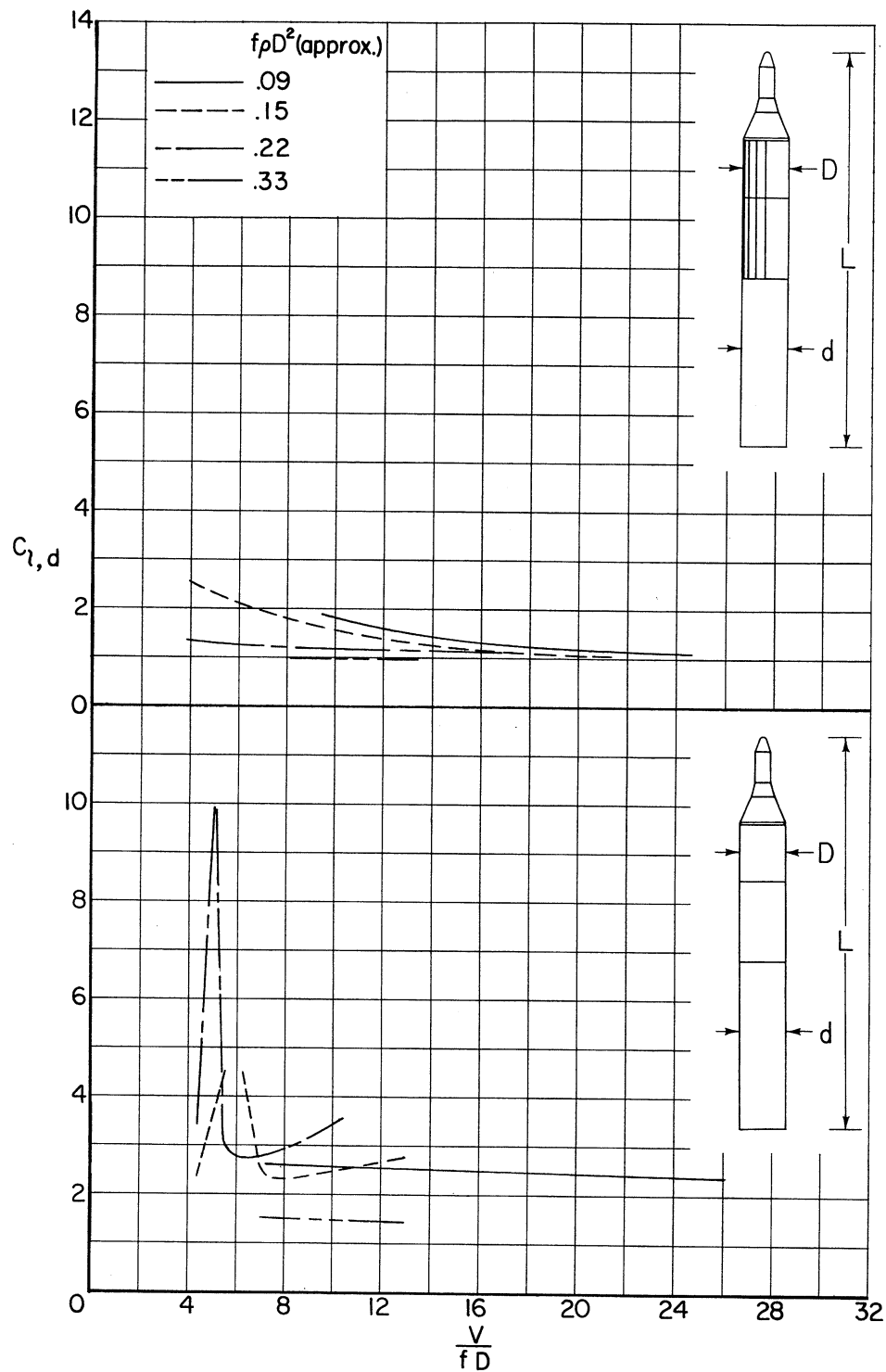
(f) With tapes 0.00036D thick; $f_0 D^2 = 0.06$.

Figure 22.- Continued.



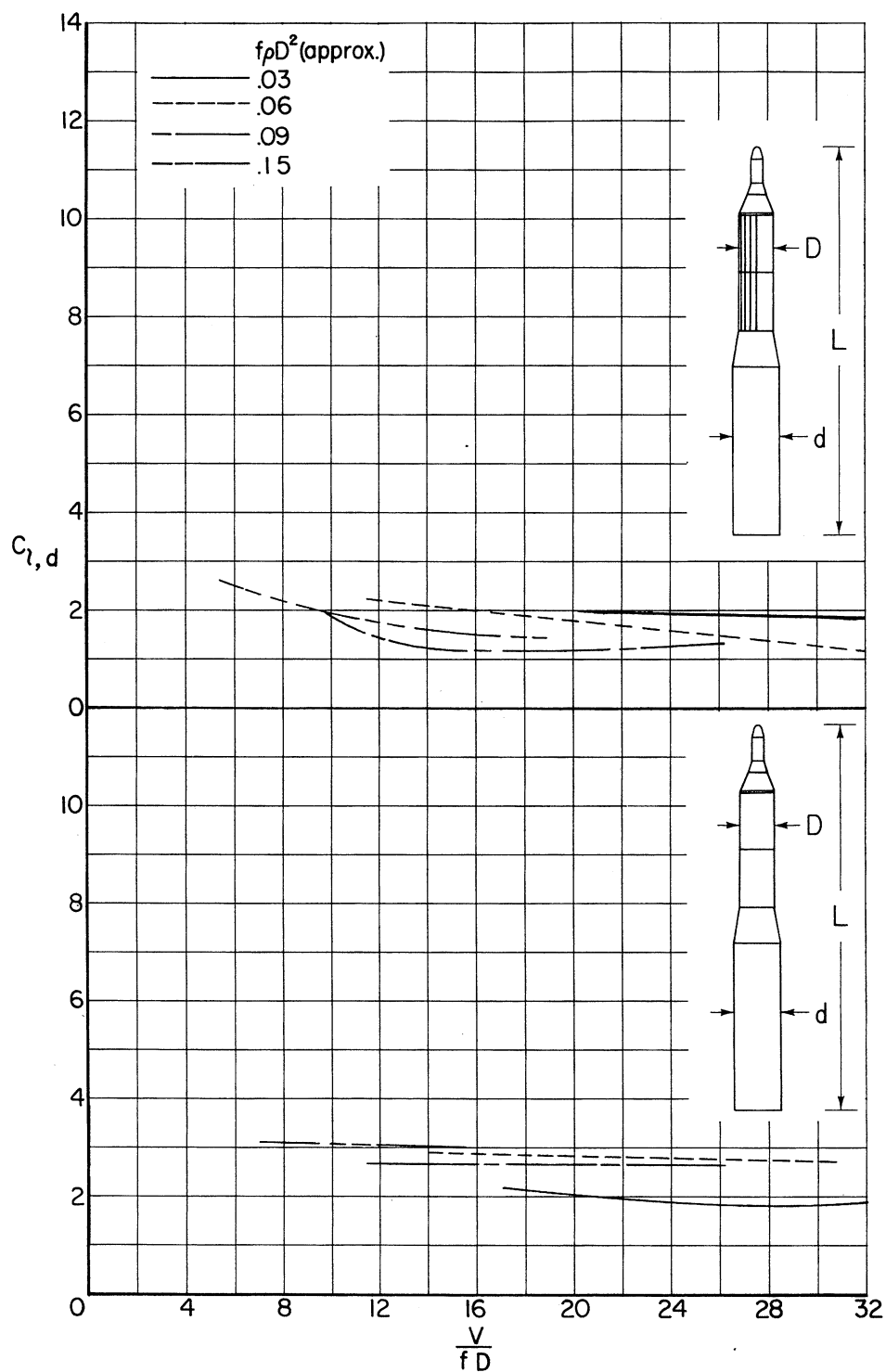
(g) With tapes 0.00036D thick; $f\rho D^2 = 0.09, 0.12$.

Figure 22.- Concluded.



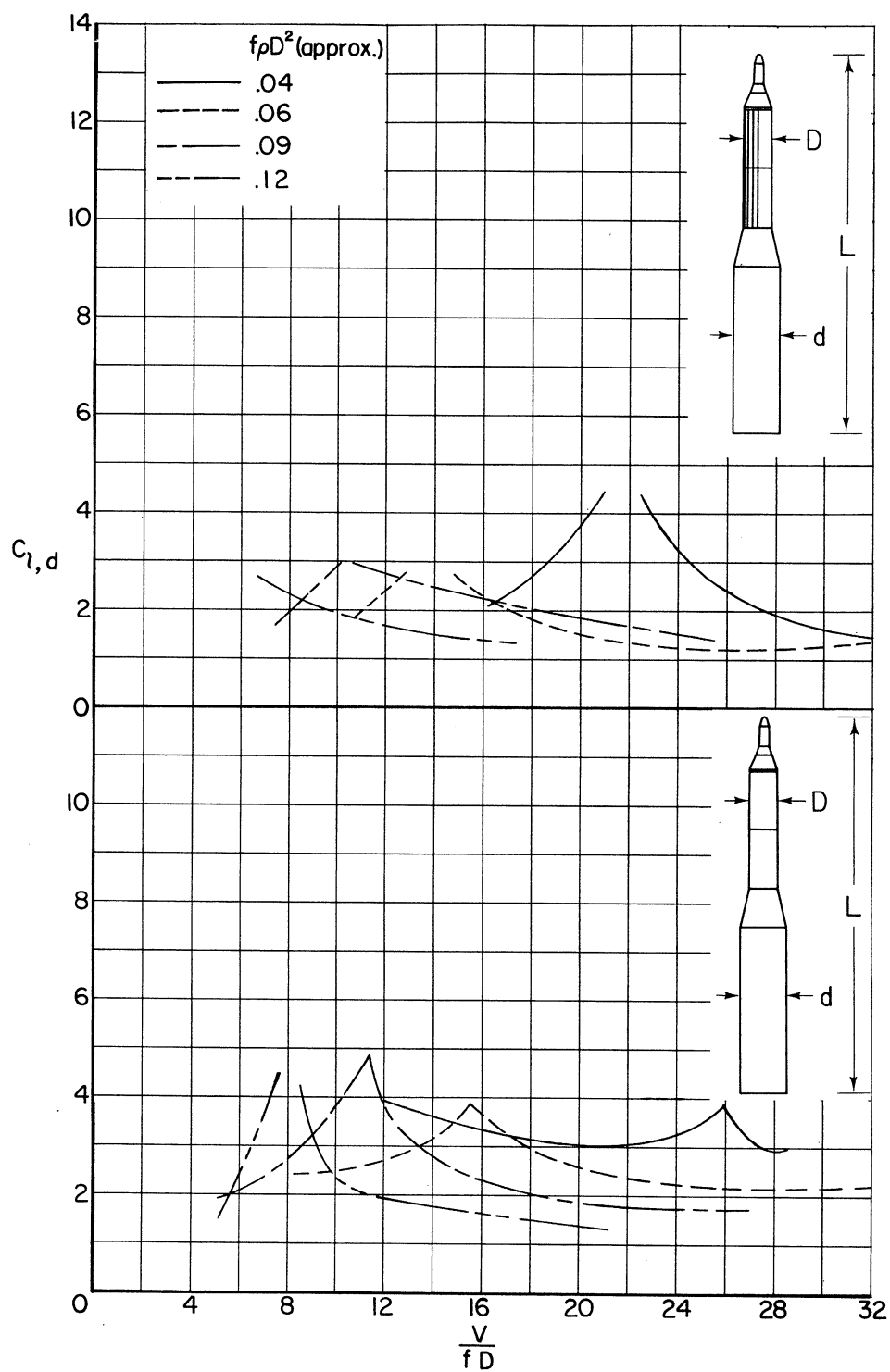
(a) Effect of $f_p D^2$ with and without tapes 0.00022D to 0.00036D thick; $D/d = 1$.

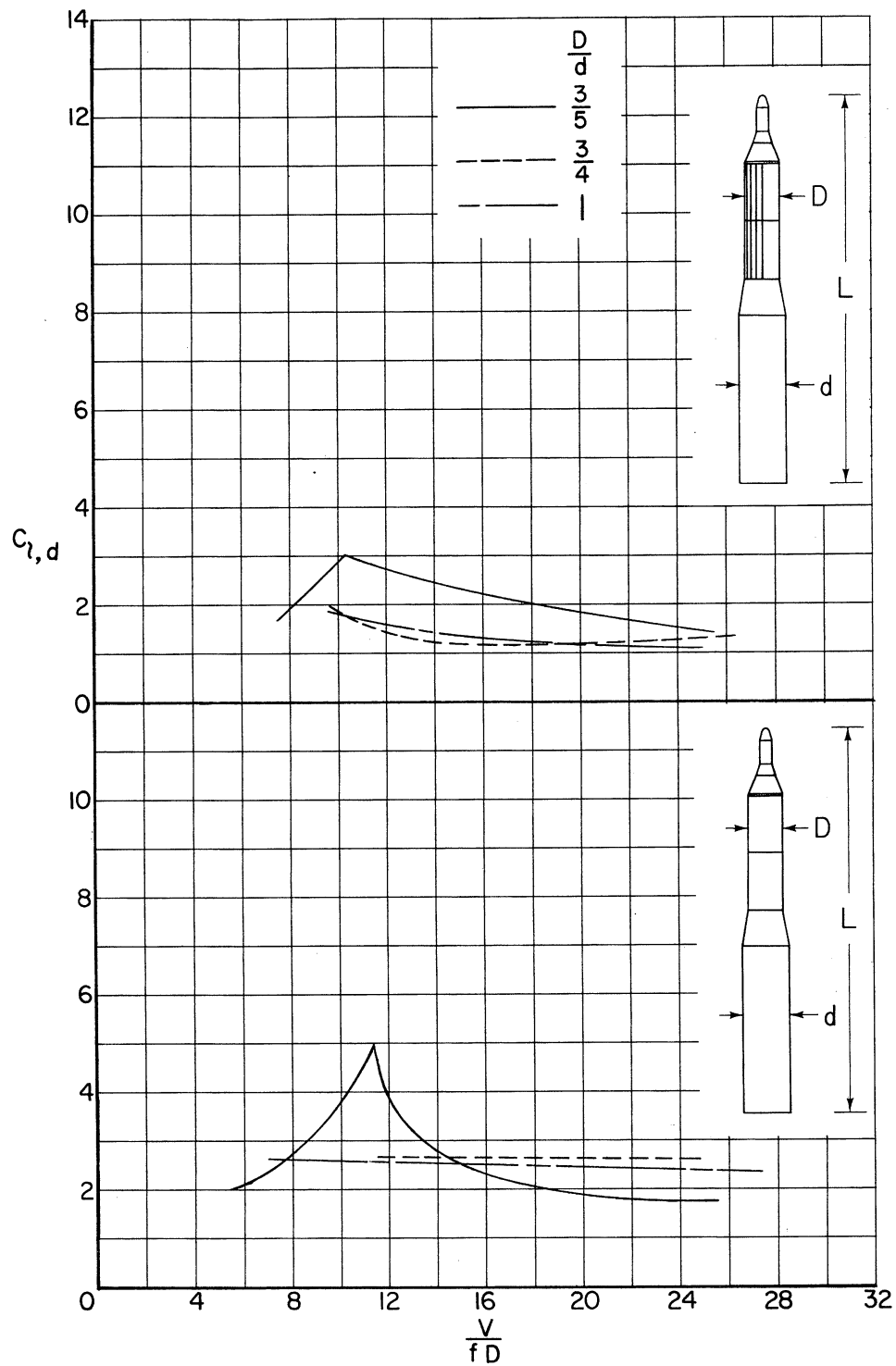
Figure 23.- Comparison of dynamic lateral moment characteristics of models with cone-cylinder nose.



(b) Effect of $f\rho D^2$ with and without tapes $0.00029D$ thick; $D/d = 3/4$.

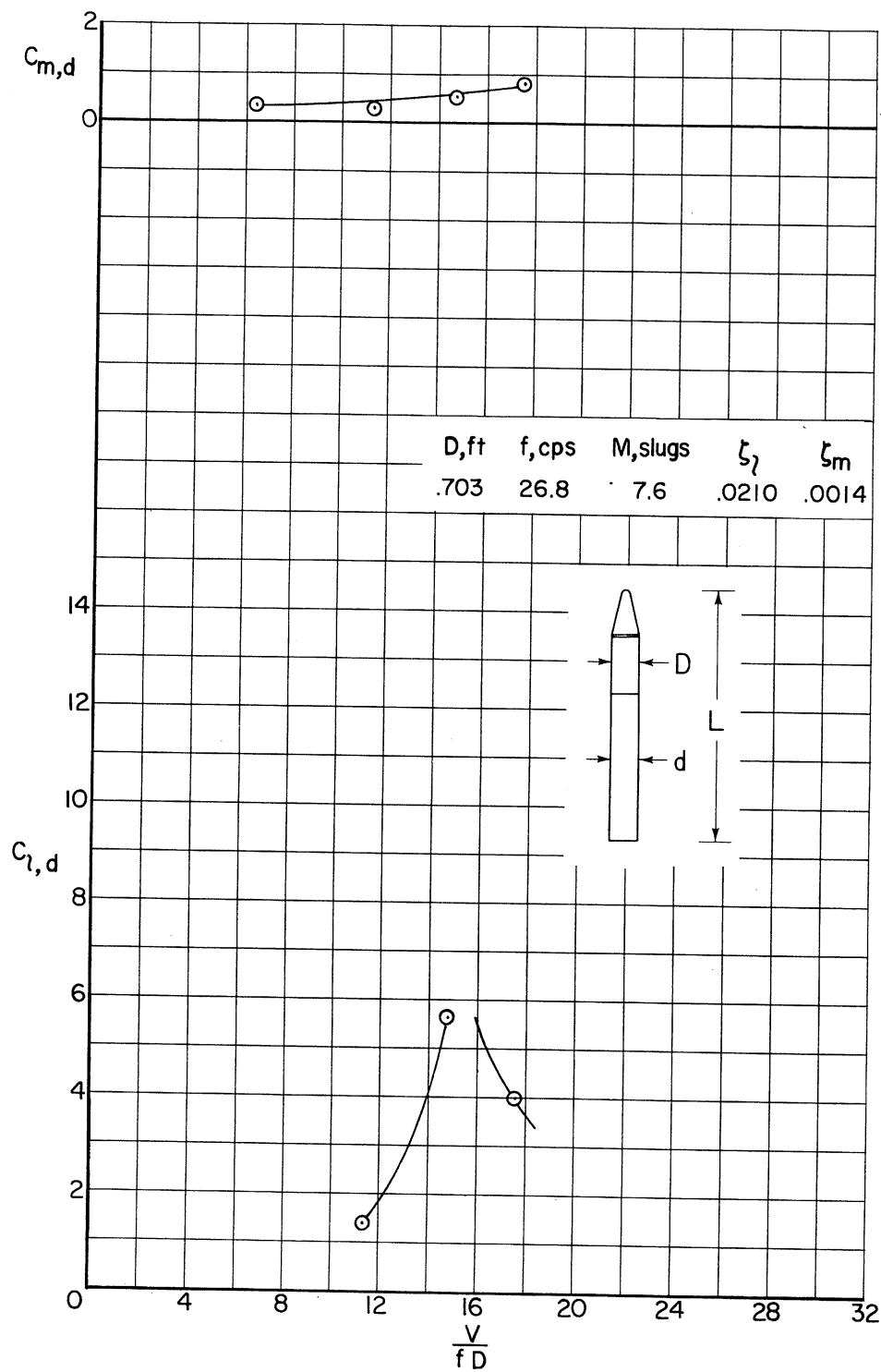
Figure 23.- Continued.





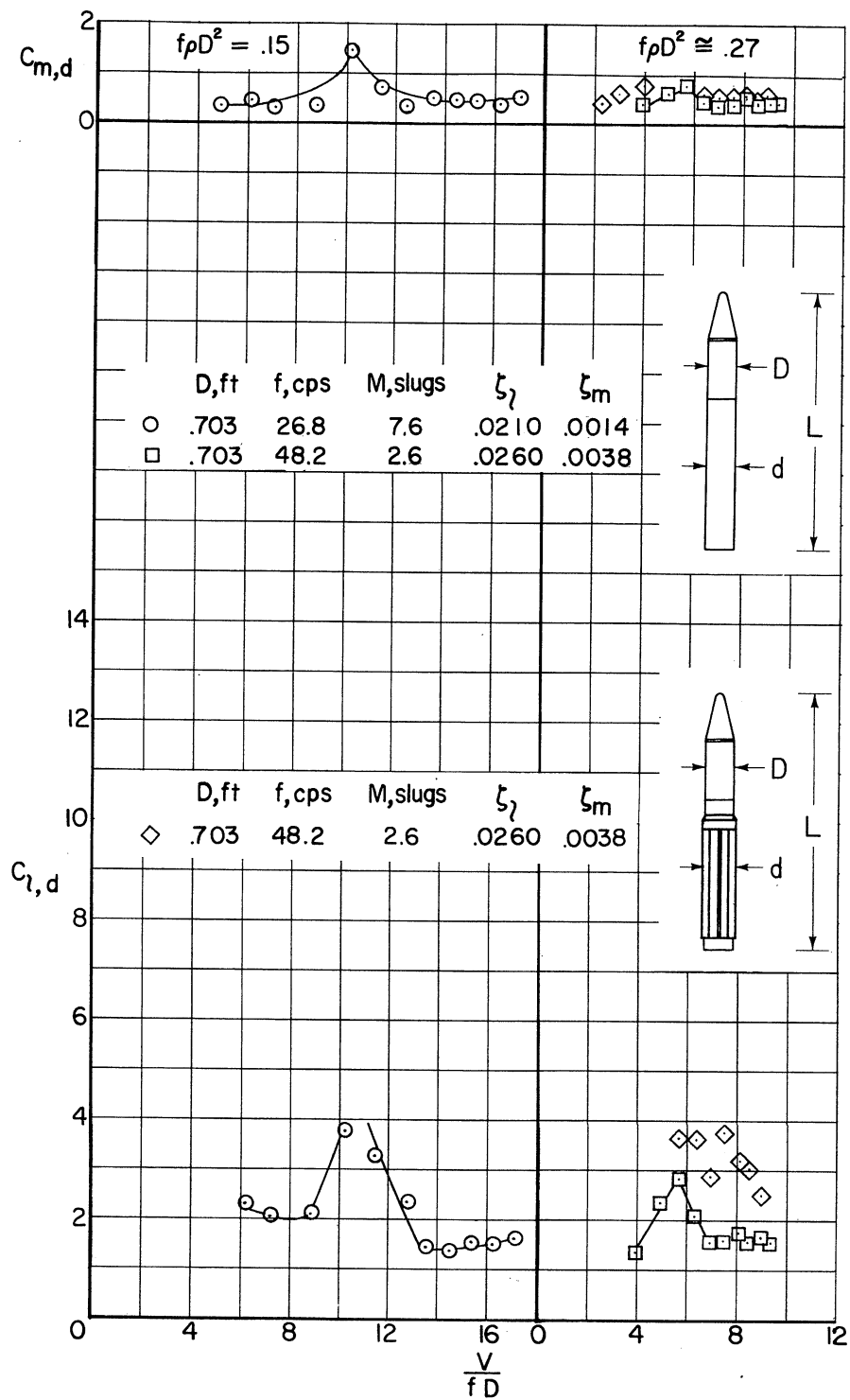
(d) Effect of stage-diameter ratio with and without tapes 0.00029D to 0.00036D thick; $L/d = 8.3$ to 10.4; $f_p D^2 = 0.09$.

Figure 23.- Concluded.



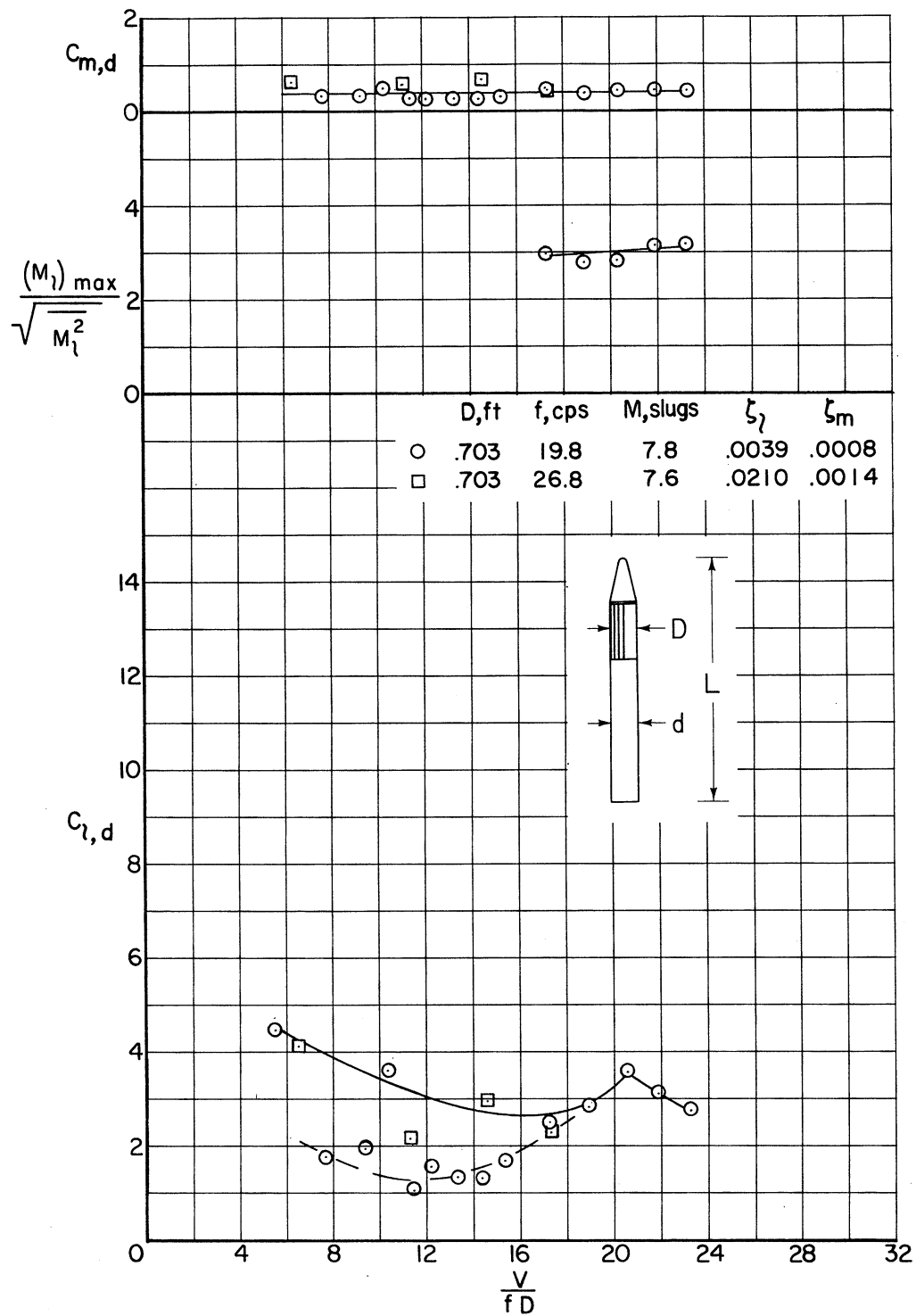
(a) Without roughness; $f_p D^2 = 0.09$, $D/d = 1$.

Figure 24.- Dynamic moment characteristics of models with blunted-cone nose; $L/D = 9.3$.



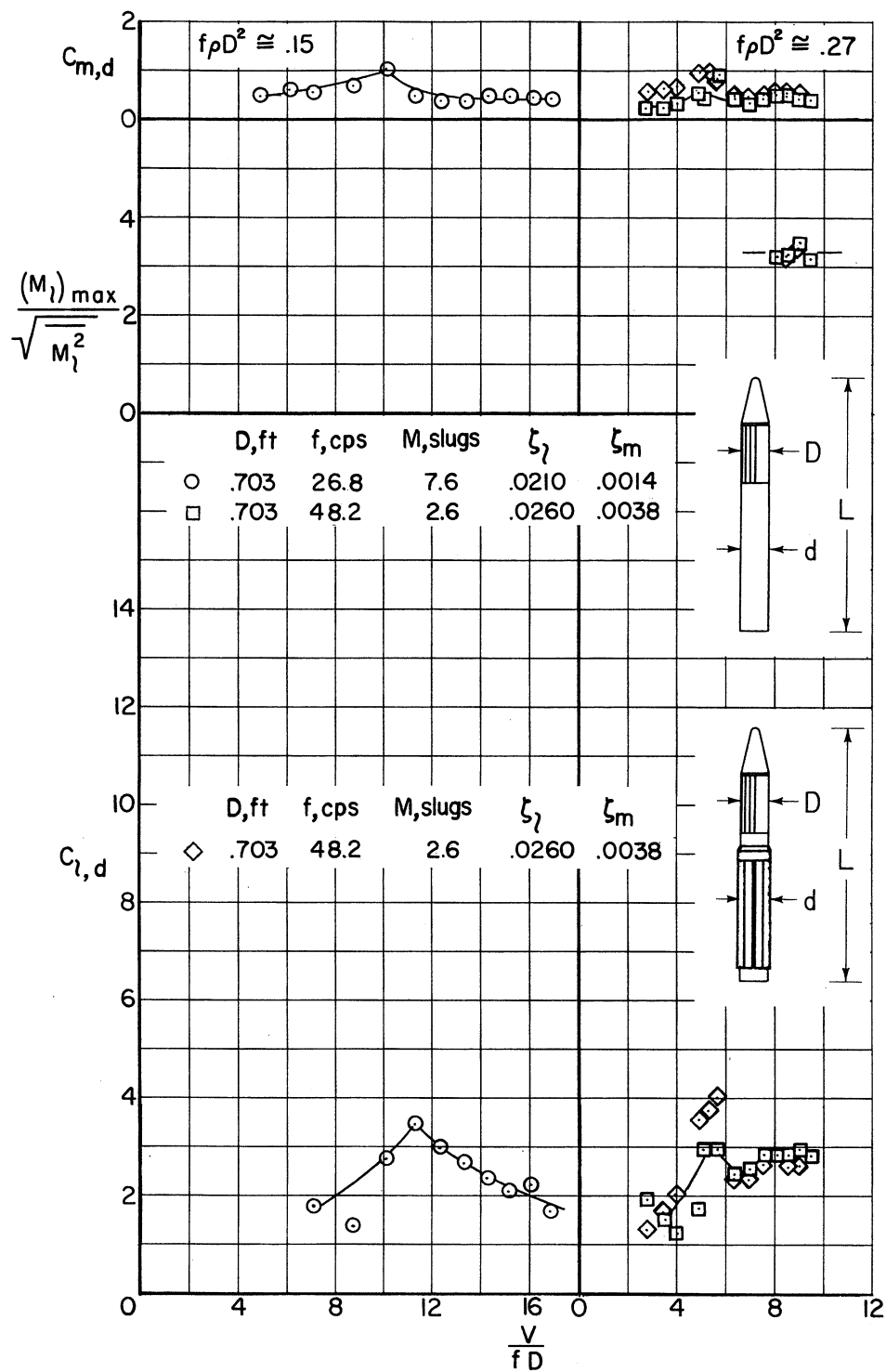
(b) Without roughness; $f\rho D^2 \approx 0.15, 0.27$; $D/d = 1$ or $6/7$.

Figure 24.- Continued.



(c) With tapes 0.00036D thick; $f_p D^2 = 0.09$; $D/d = 1$.

Figure 24.- Continued.



(d) With tapes 0.00036D thick; $f\rho D^2 \approx 0.15, 0.27$; $D/d = 1$ or $6/7$.

Figure 24.- Concluded.

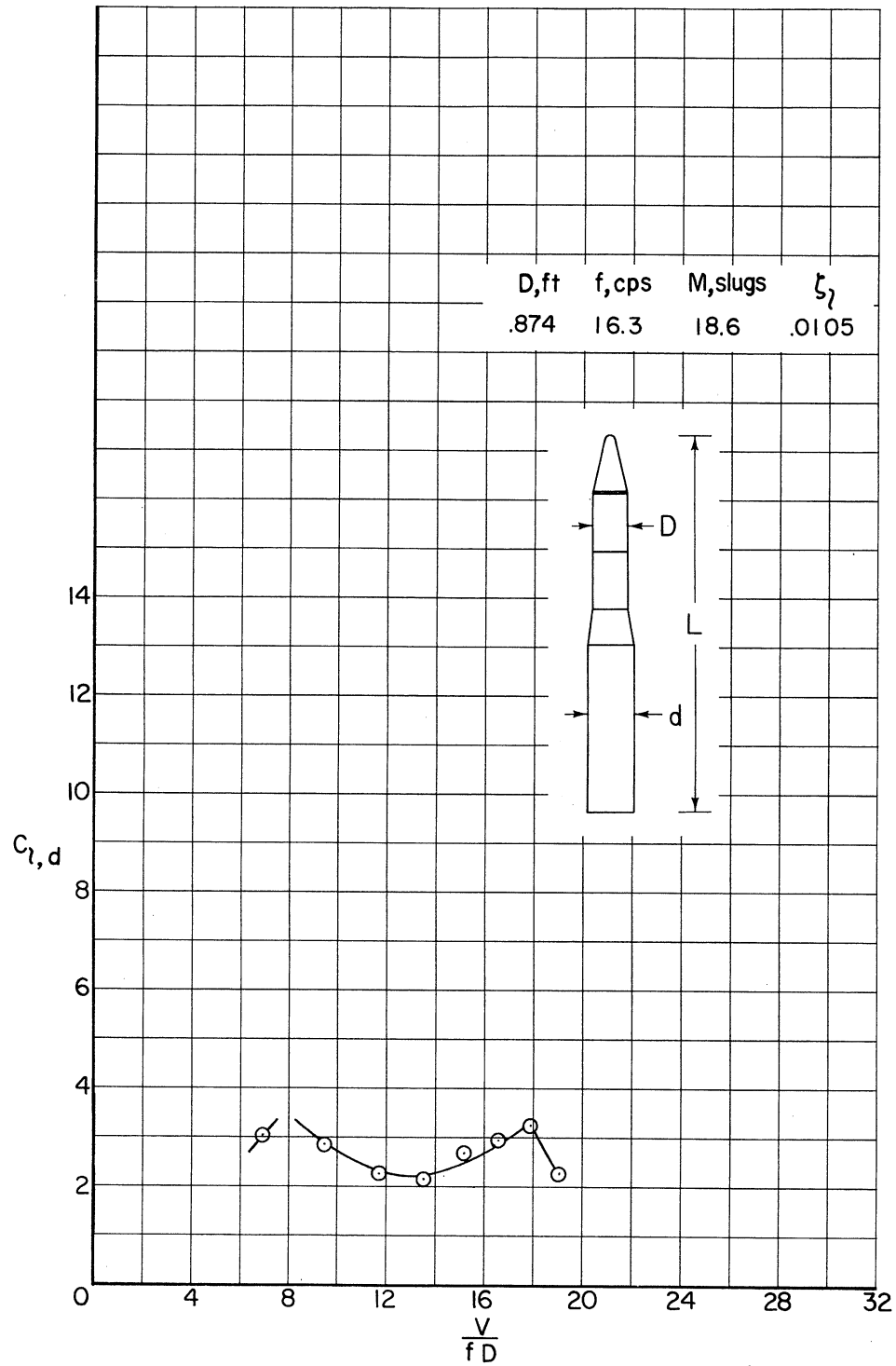
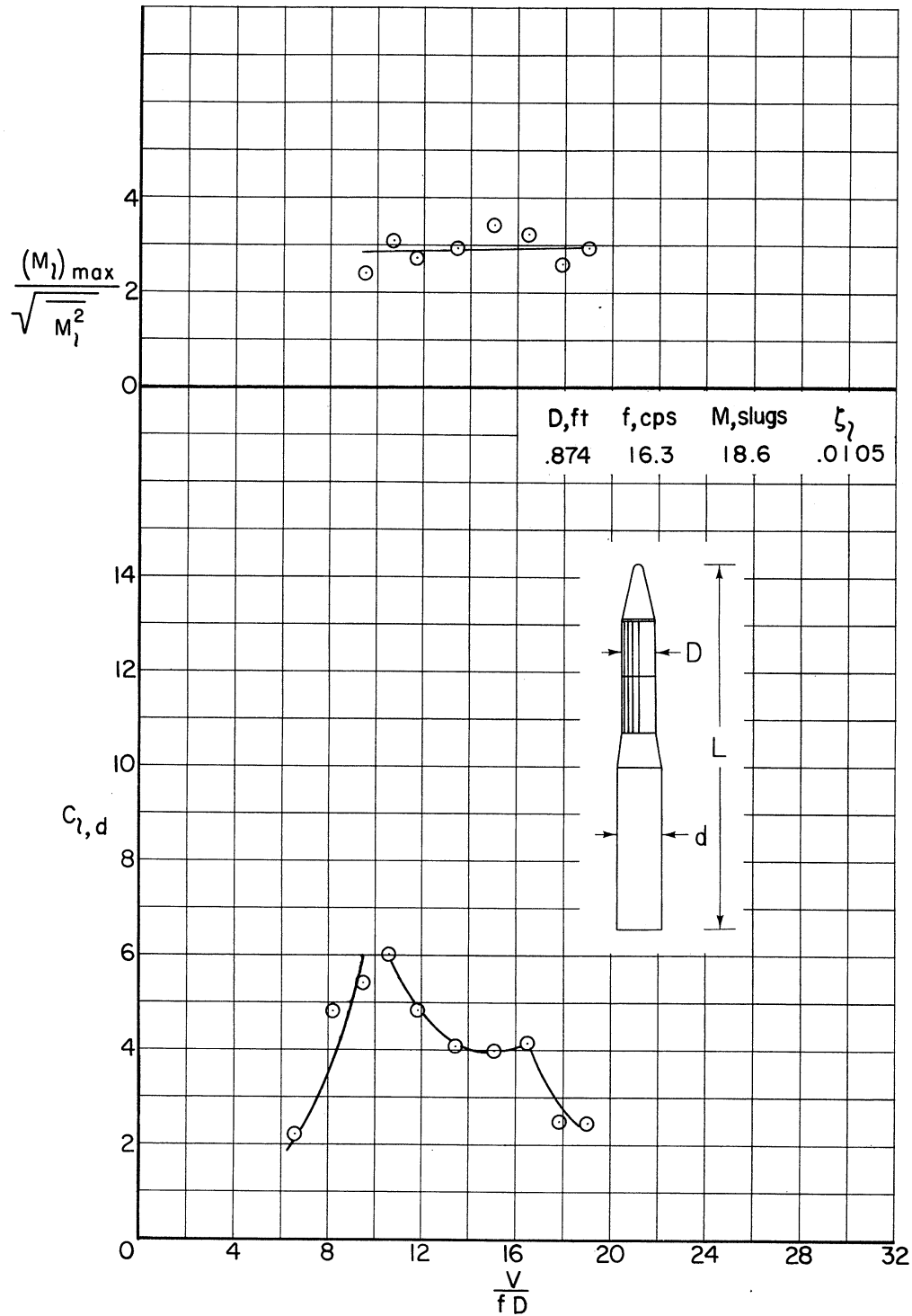
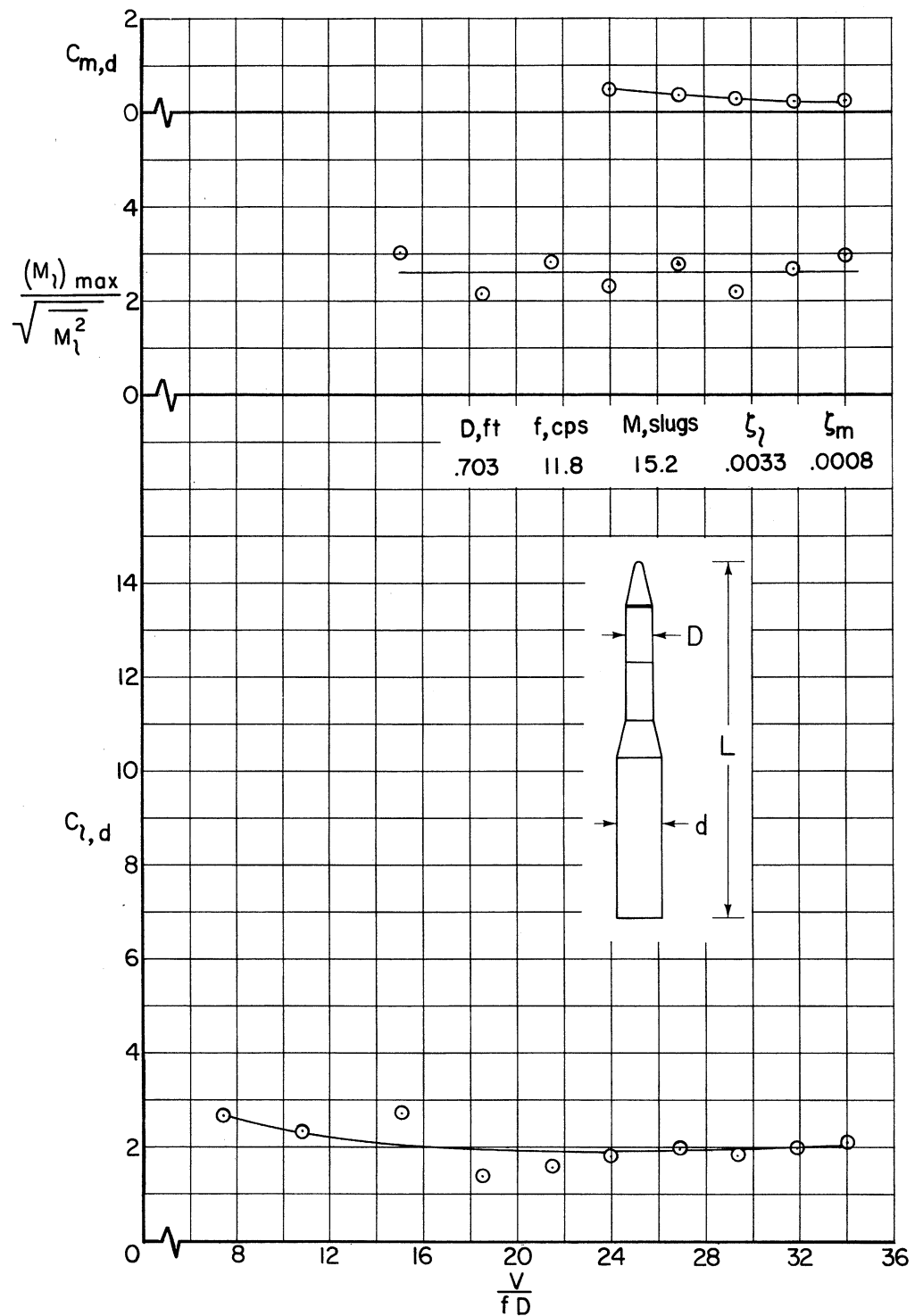


Figure 25.- Dynamic moment characteristics of models with the blunted-cone nose; $D/d = 3/4$; $L/D = 10.6$.



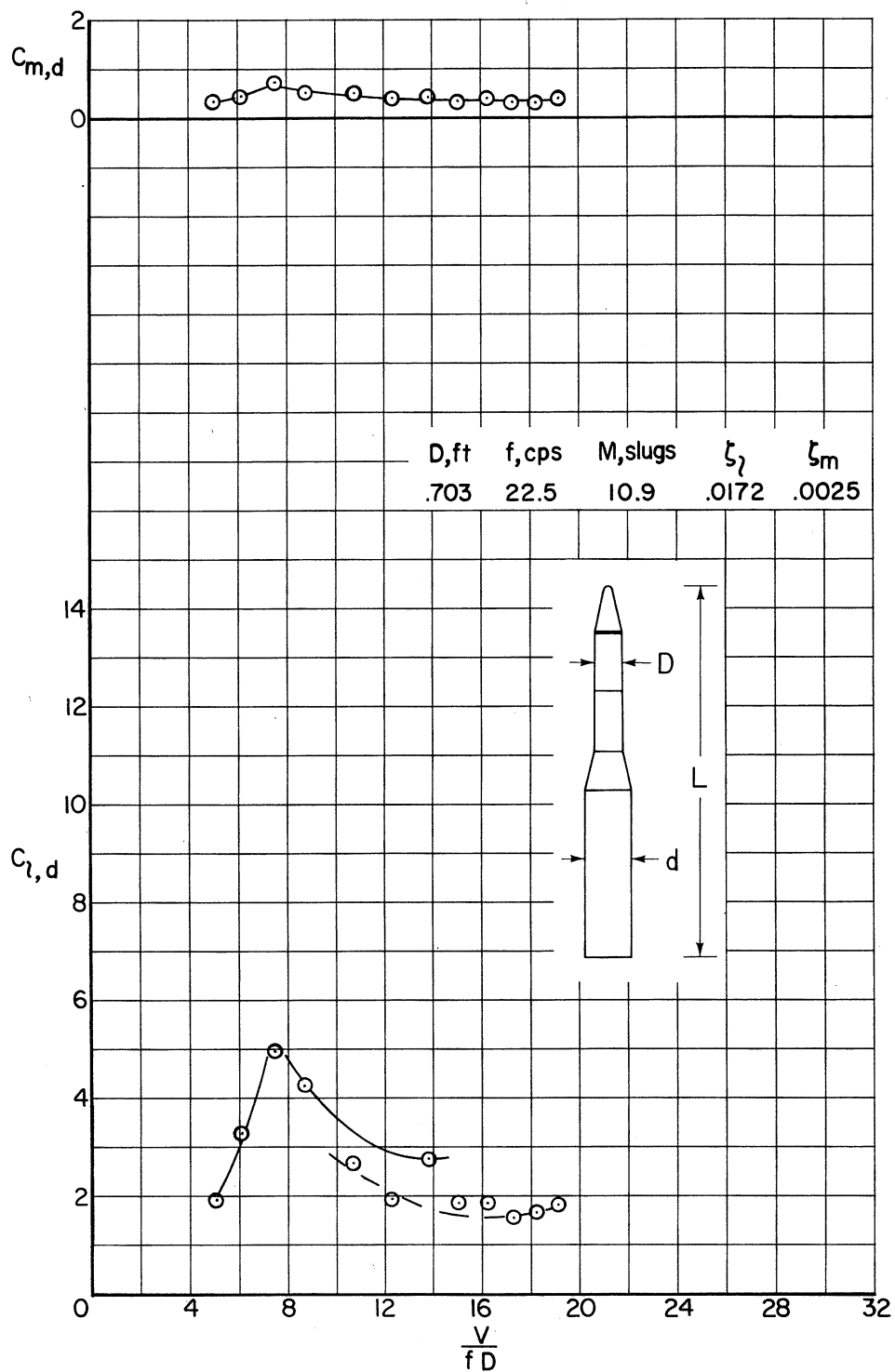
(b) With tapes 0.00029D thick; $f_p D^2 = 0.14$.

Figure 25.- Concluded.



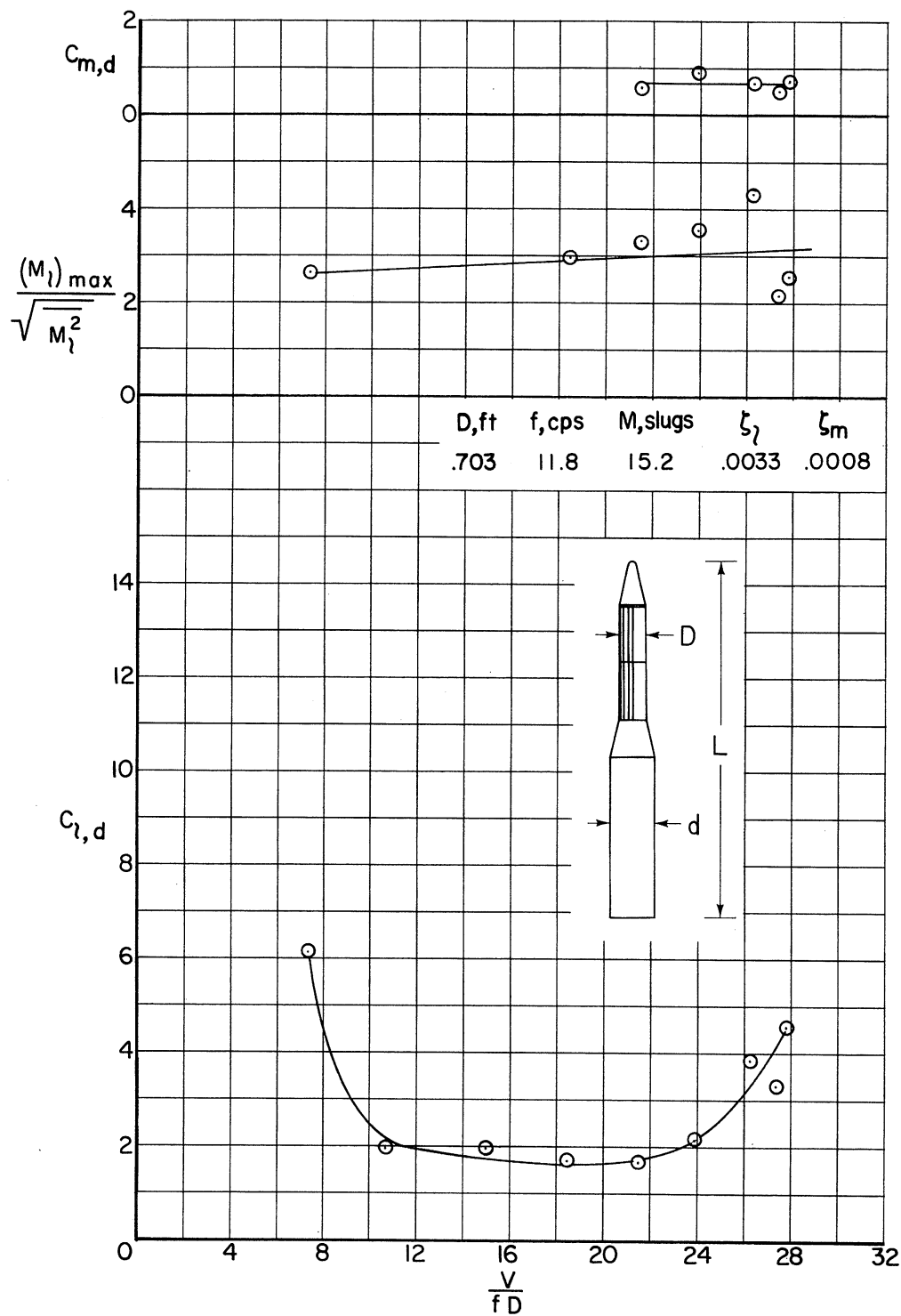
(a) Without roughness; $f_p D^2 = 0.06$.

Figure 26.- Dynamic moment characteristics of models with the blunted-cone nose; $D/d = 3/5$; $L/D = 13.5$.



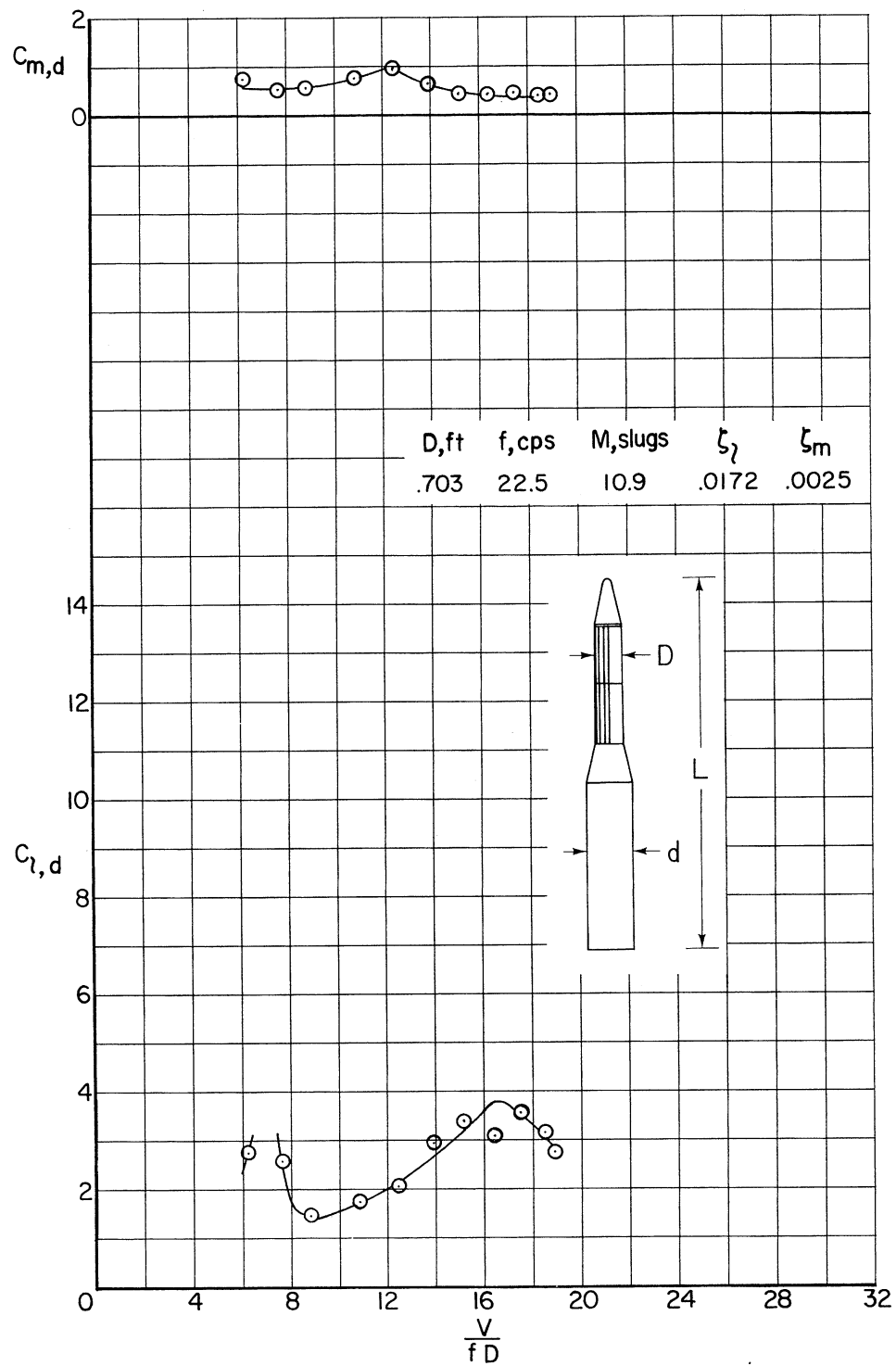
(b) Without roughness; $f_0 D^2 = 0.12$.

Figure 26.- Continued.



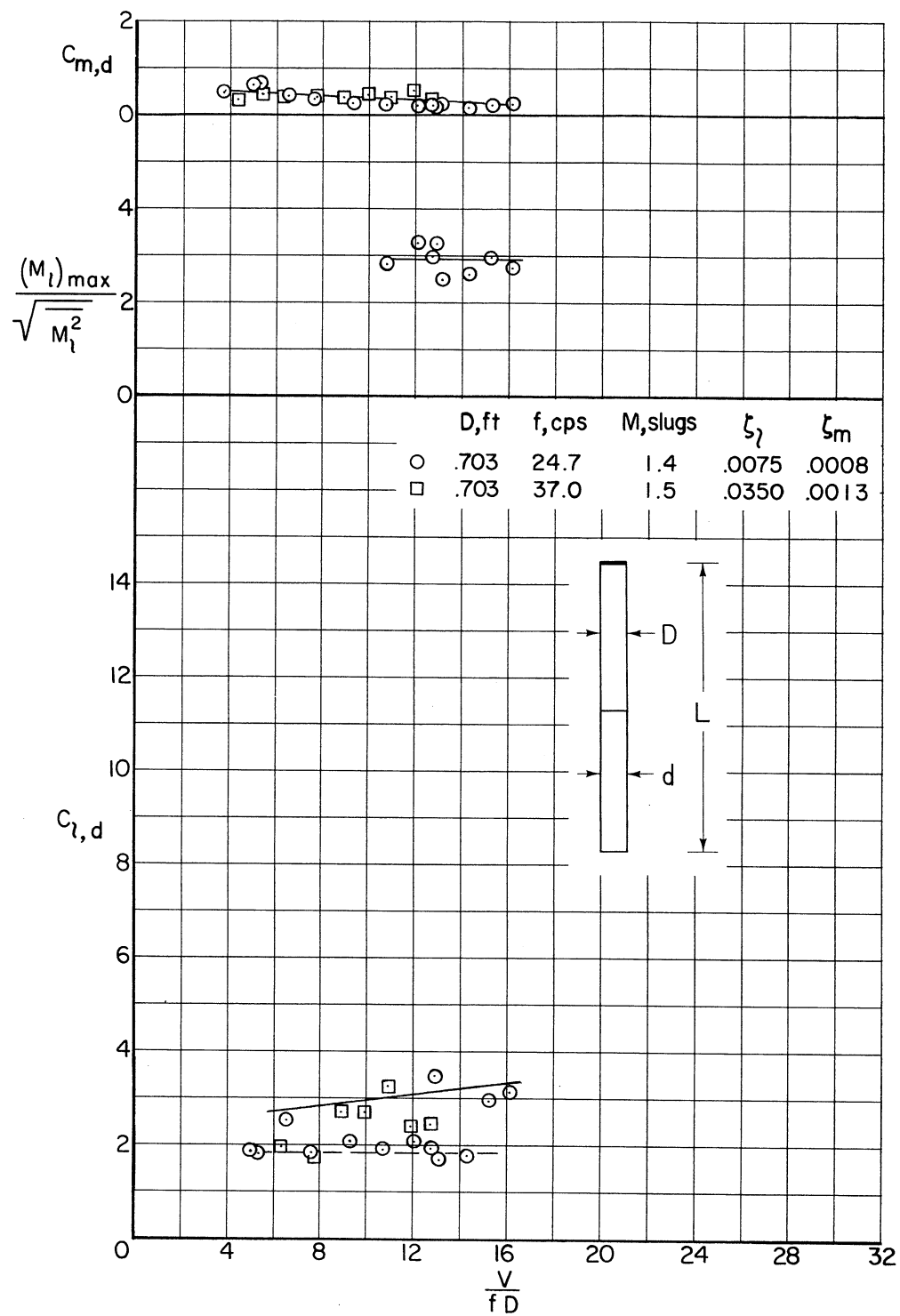
(c) With tapes 0.00036D thick; $f_0 D^2 = 0.06$.

Figure 26.- Continued.



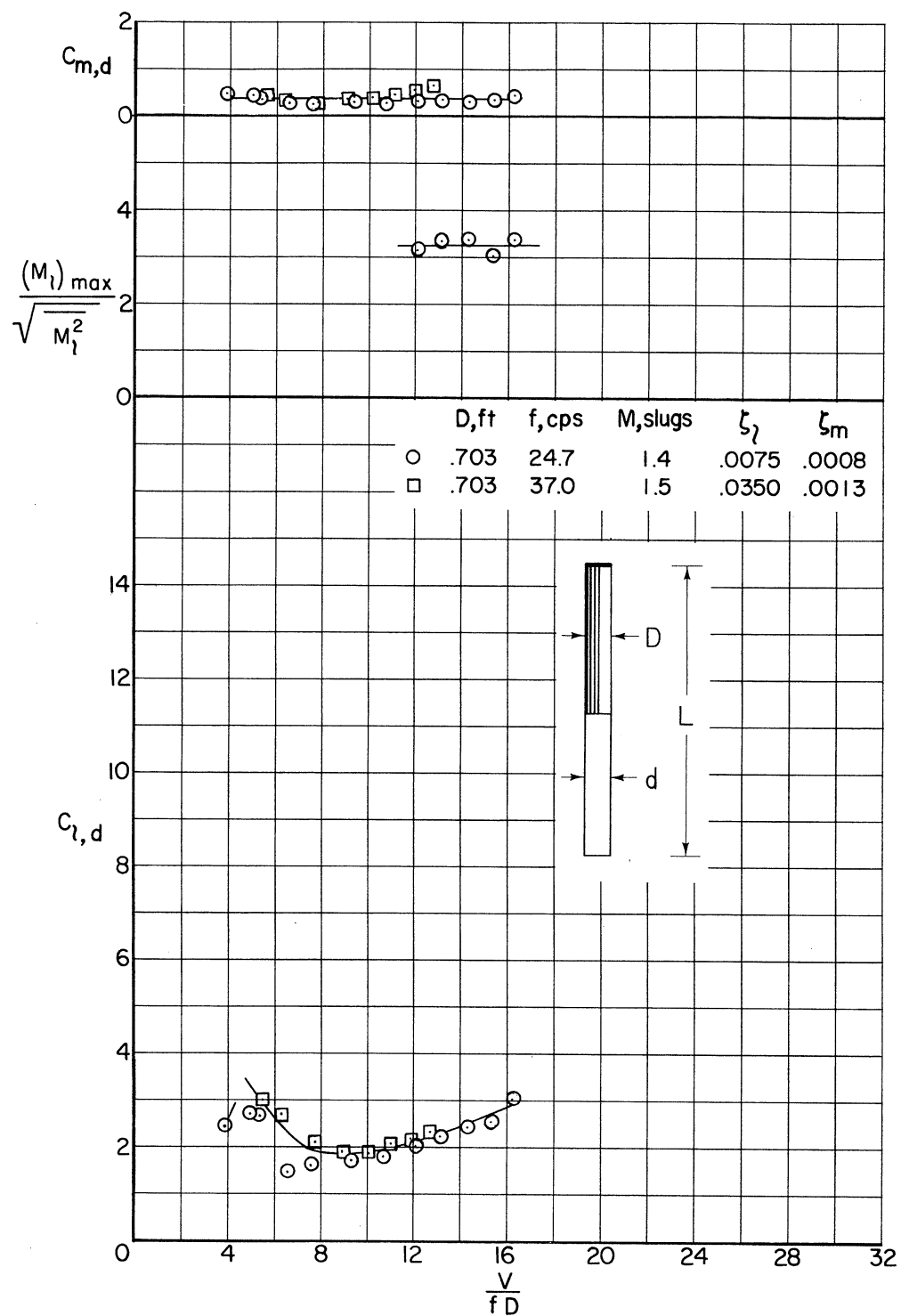
(d) With tapes $0.00036D$ thick; $f_0 D^2 = 0.12$.

Figure 26.- Concluded.



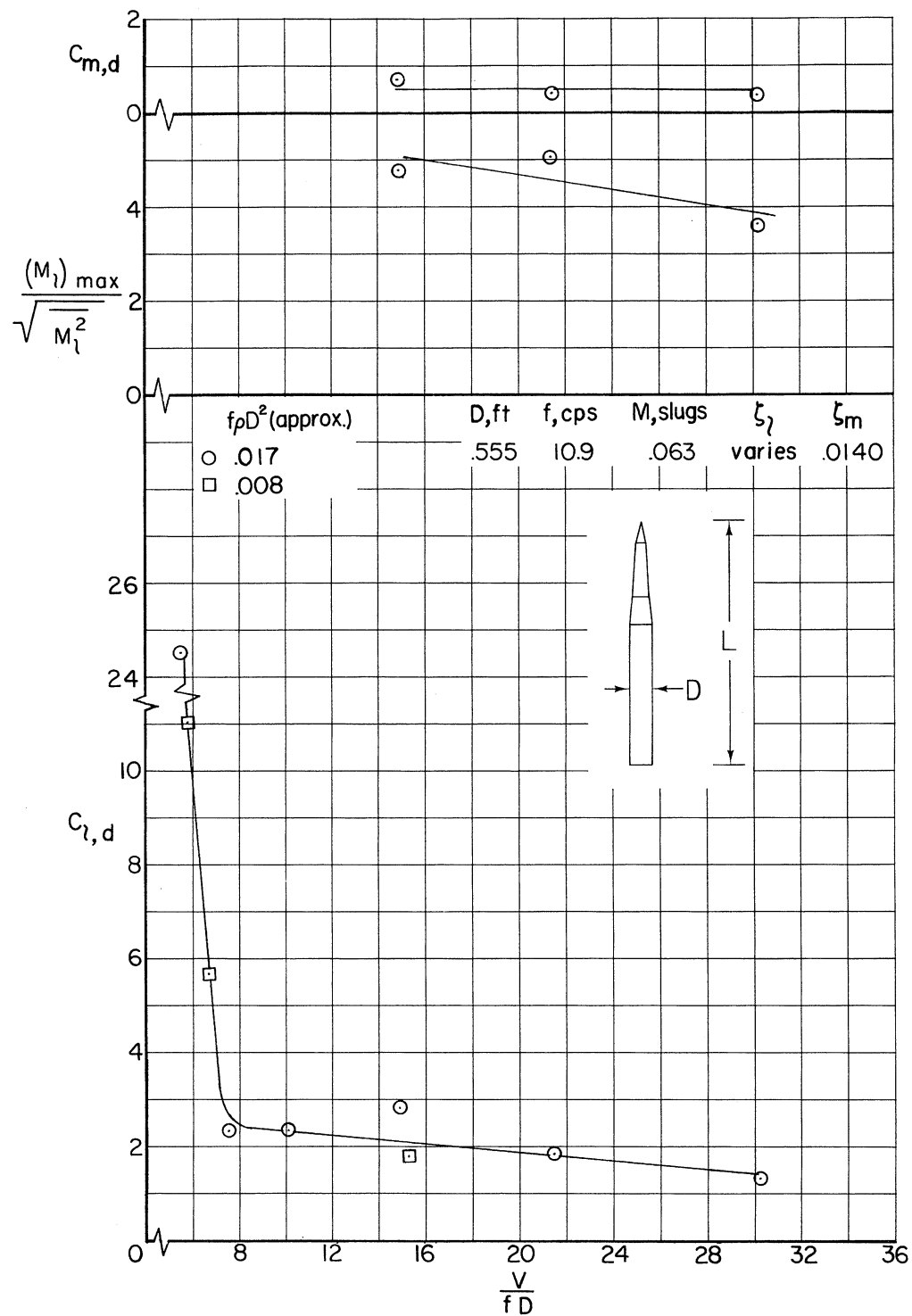
(a) Without roughness; $f\rho D^2 = 0.14$.

Figure 27.- Dynamic moment characteristics of the flat-face configuration;
 $D/d = 1$; $L/D = 11.1$.



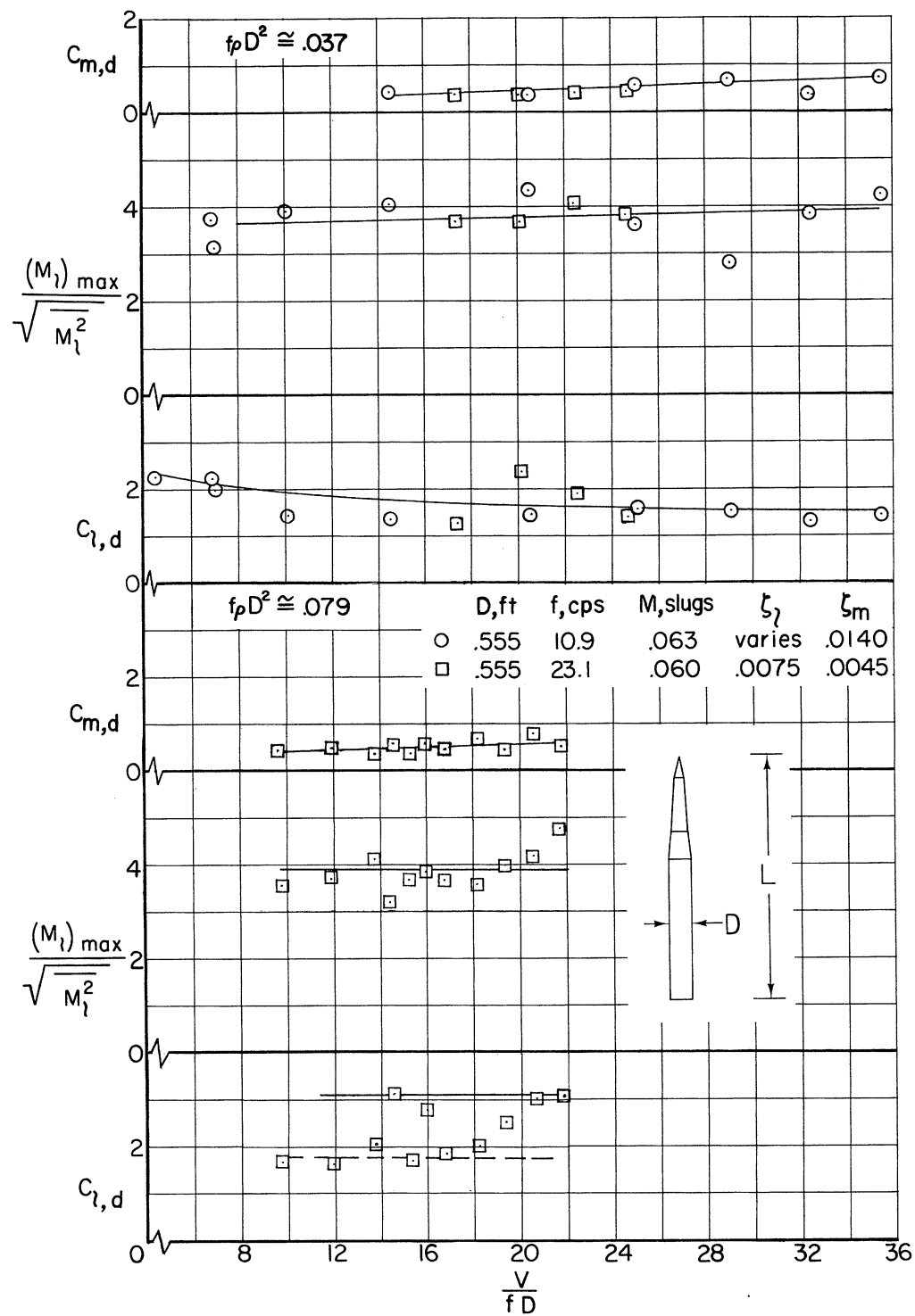
(b) With tapes 0.00036D thick; $f_0 D^2 = 0.14$.

Figure 27.- Concluded.



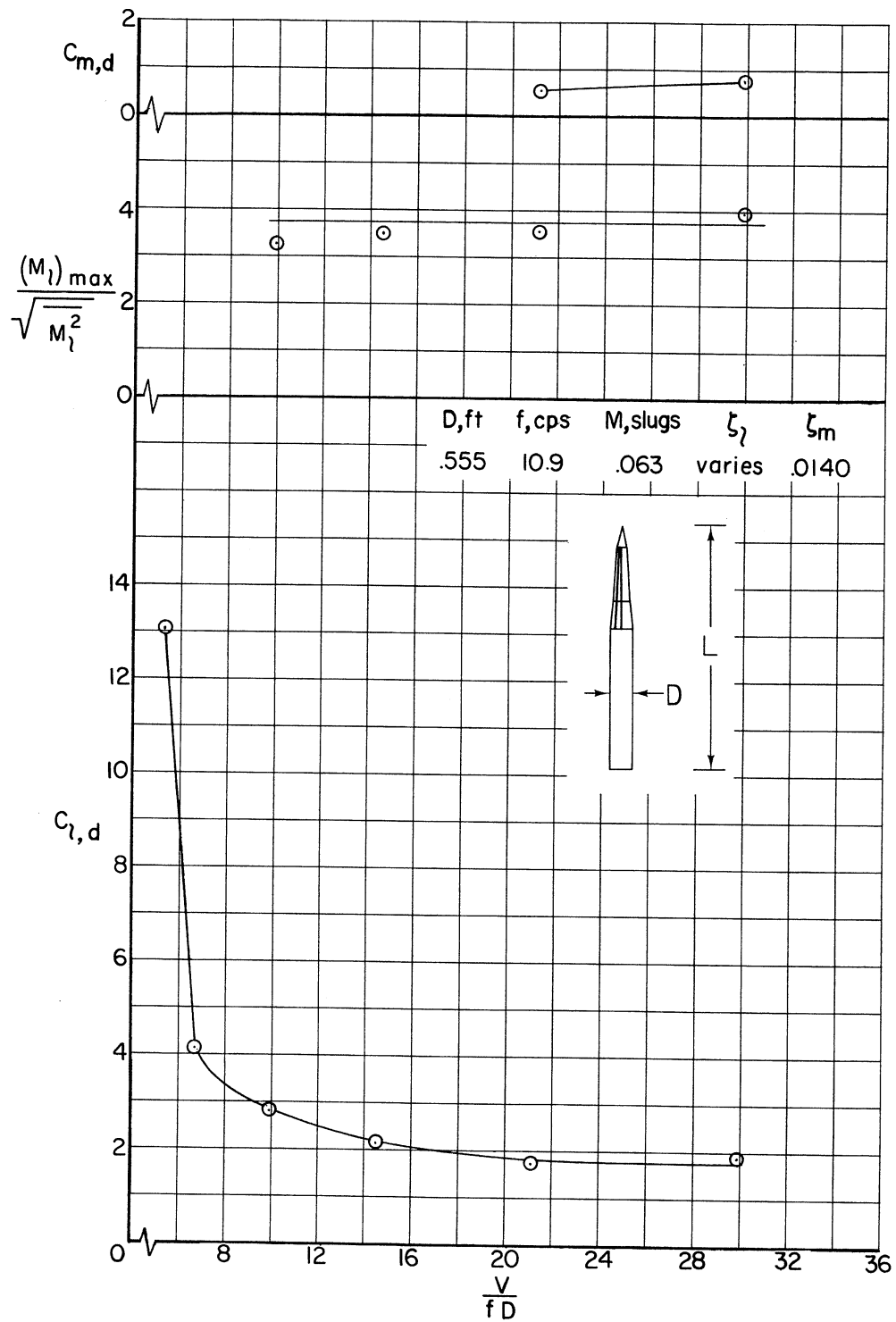
(a) Without appendages or roughness; $f_0 D^2 \approx 0.008, 0.017$.

Figure 28.- Dynamic moment characteristics of the model with the tapered upper stage; $L/D = 11.7$.



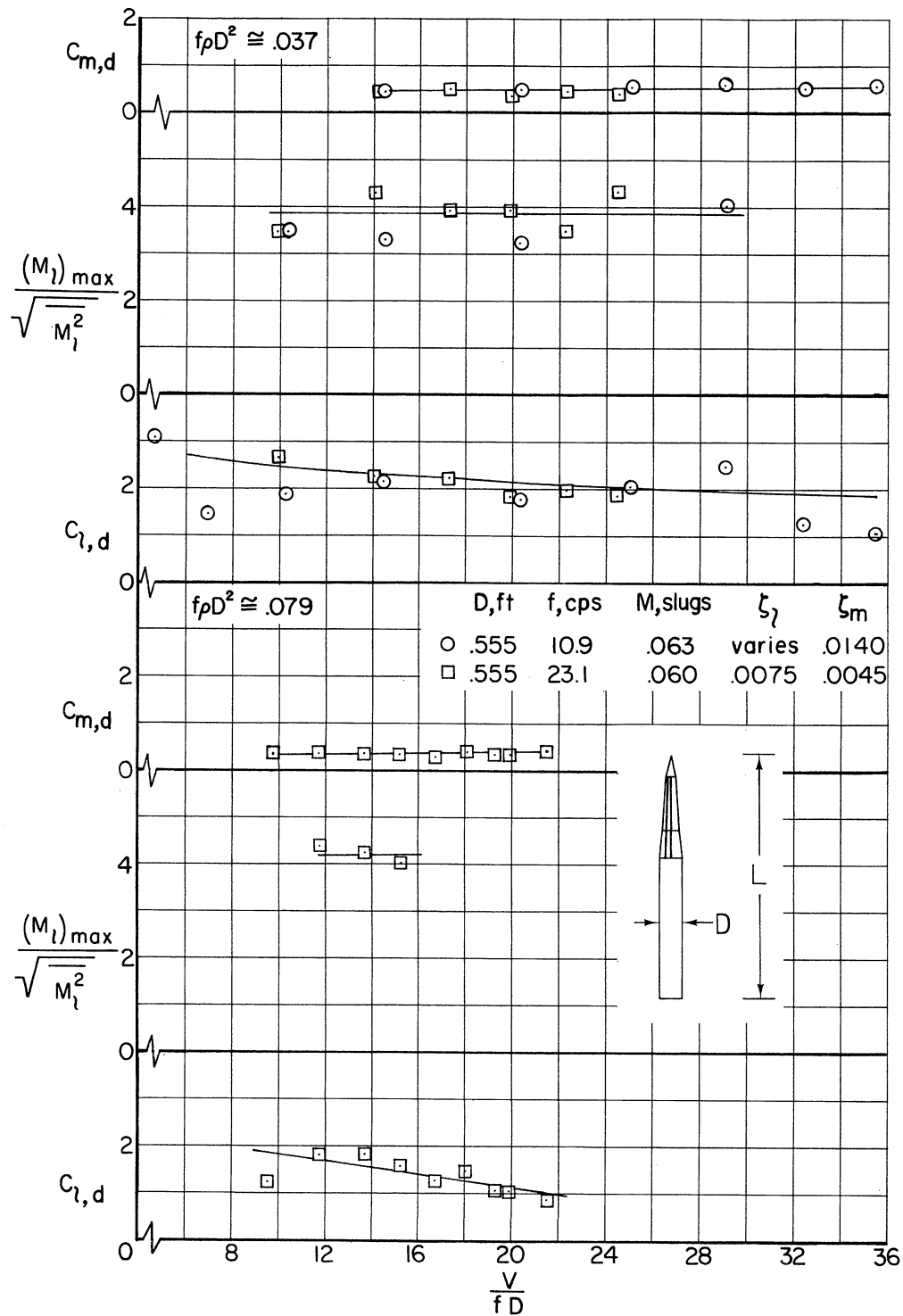
(b) Without appendages or roughness; $f_p D^2 \approx 0.037, 0.079$.

Figure 28.- Continued.



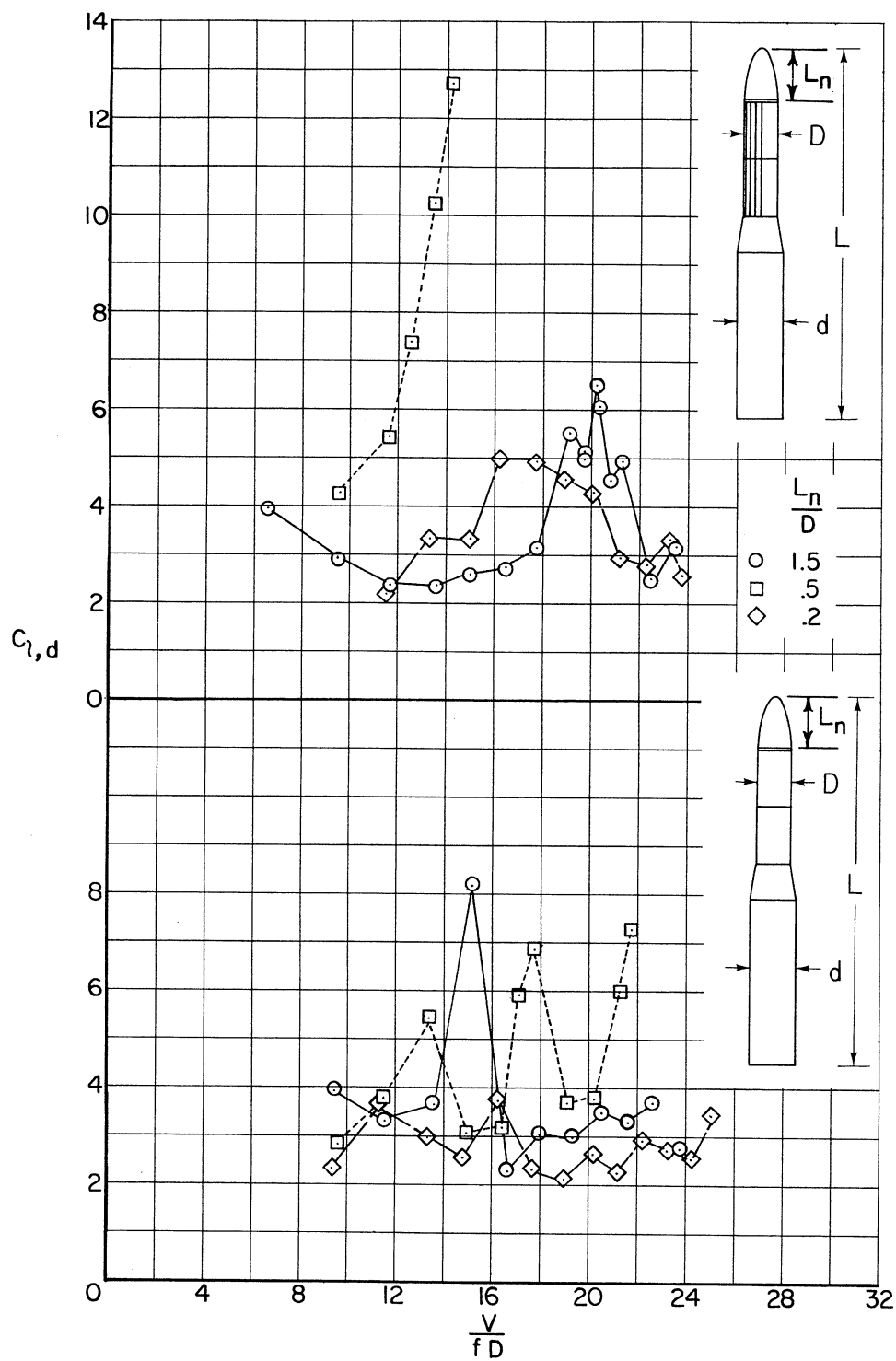
(c) Without appendages; with tapes 0.00045D thick; $f_0 D^2 = 0.017$.

Figure 28.- Continued.



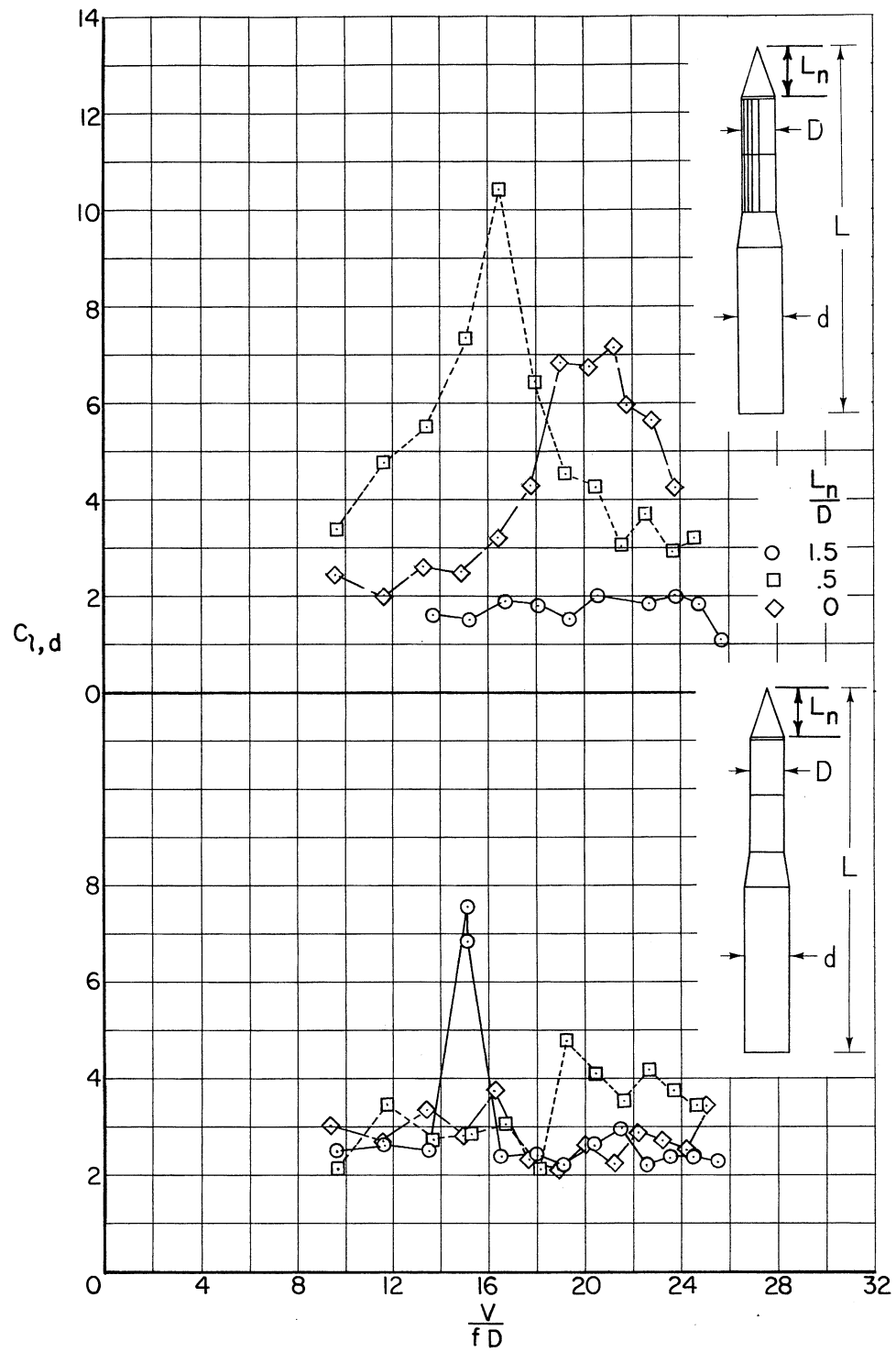
(d) Without appendages; with tapes $0.00045D$ thick; $f\rho D^2 \approx 0.037, 0.079$.

Figure 28.- Concluded.



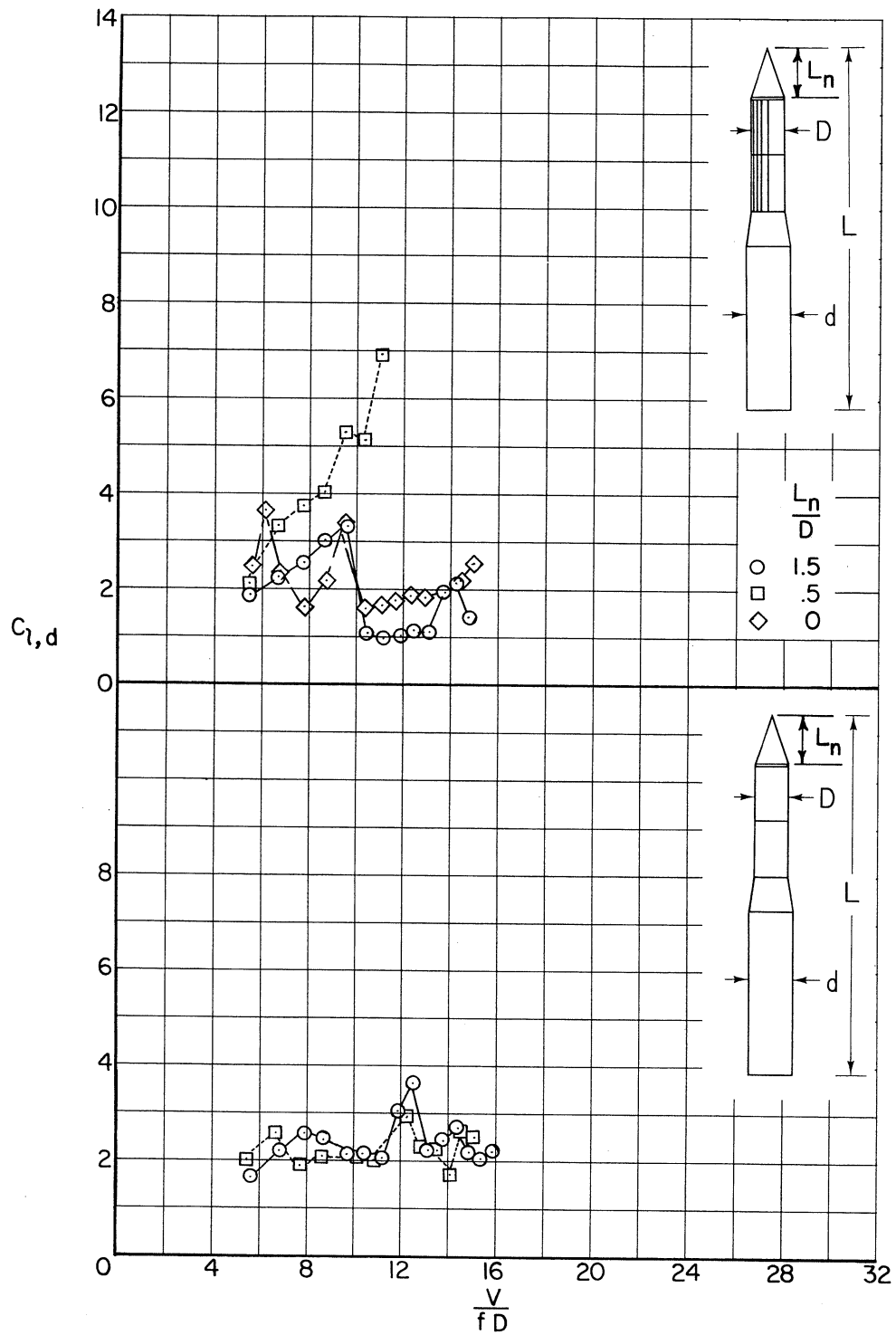
(a) Ellipses; $f_p D^2 = 0.09$.

Figure 29.- Effects of nose shape on the dynamic lateral moment characteristics of the models; $D/d = 3/4$; $L/D = 9$ to 11.



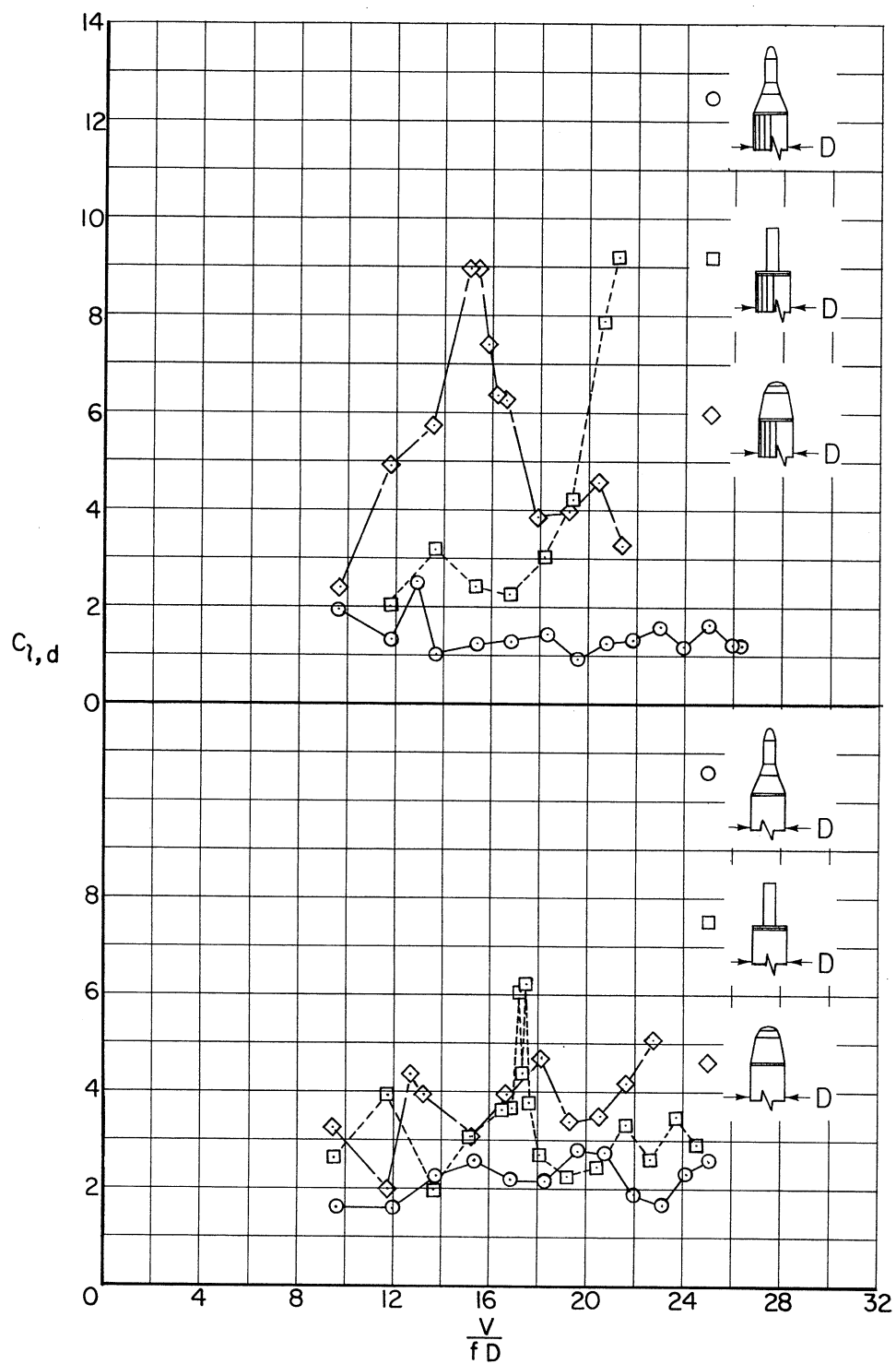
(b) Cones; $f_0 D^2 = 0.09$.

Figure 29.- Continued.



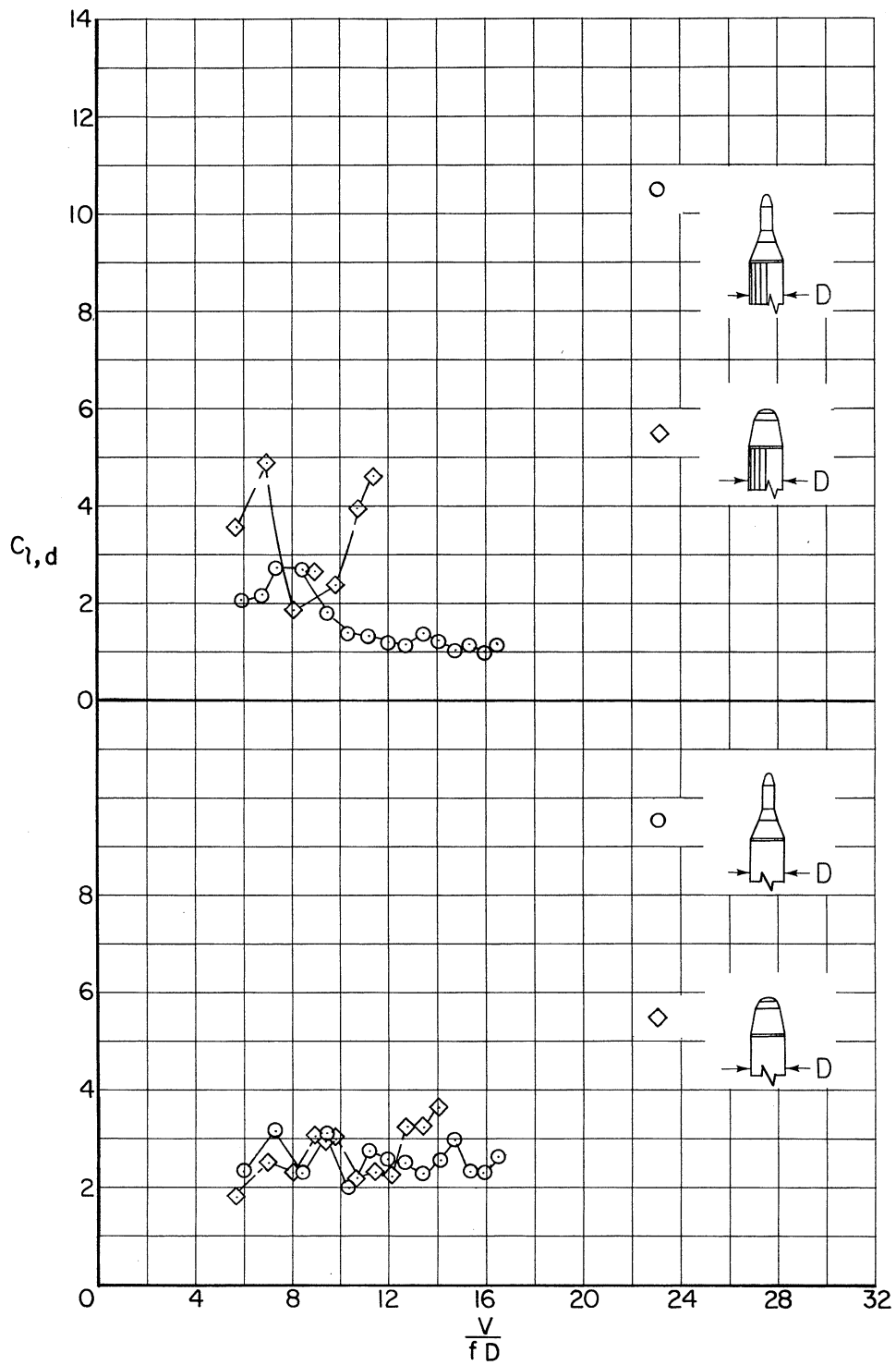
(c) Cones; $f_p D^2 = 0.16$.

Figure 29.- Continued.



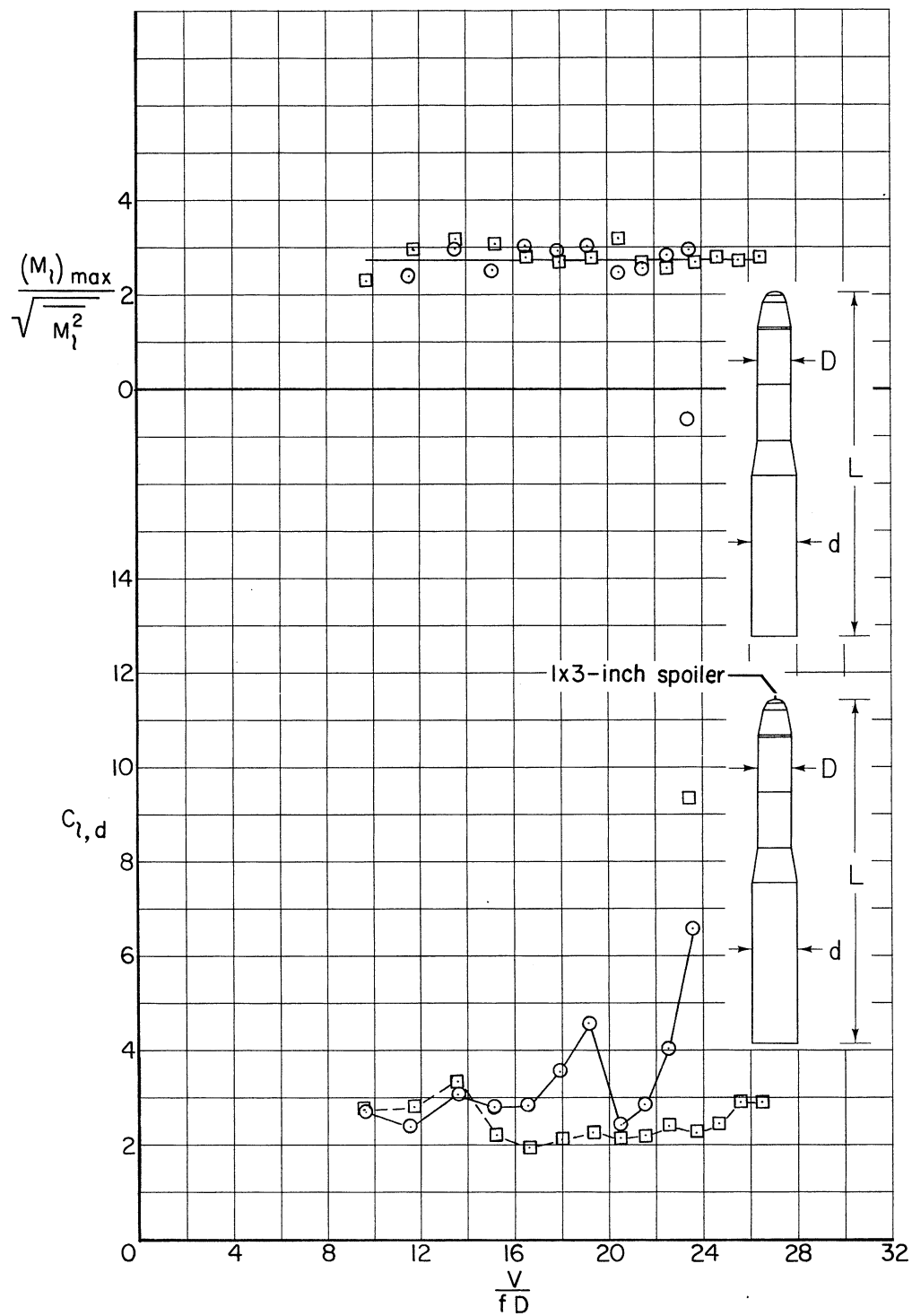
(d) Cylinder and cone combination; $f_0 D^2 = 0.09$.

Figure 29.- Continued.



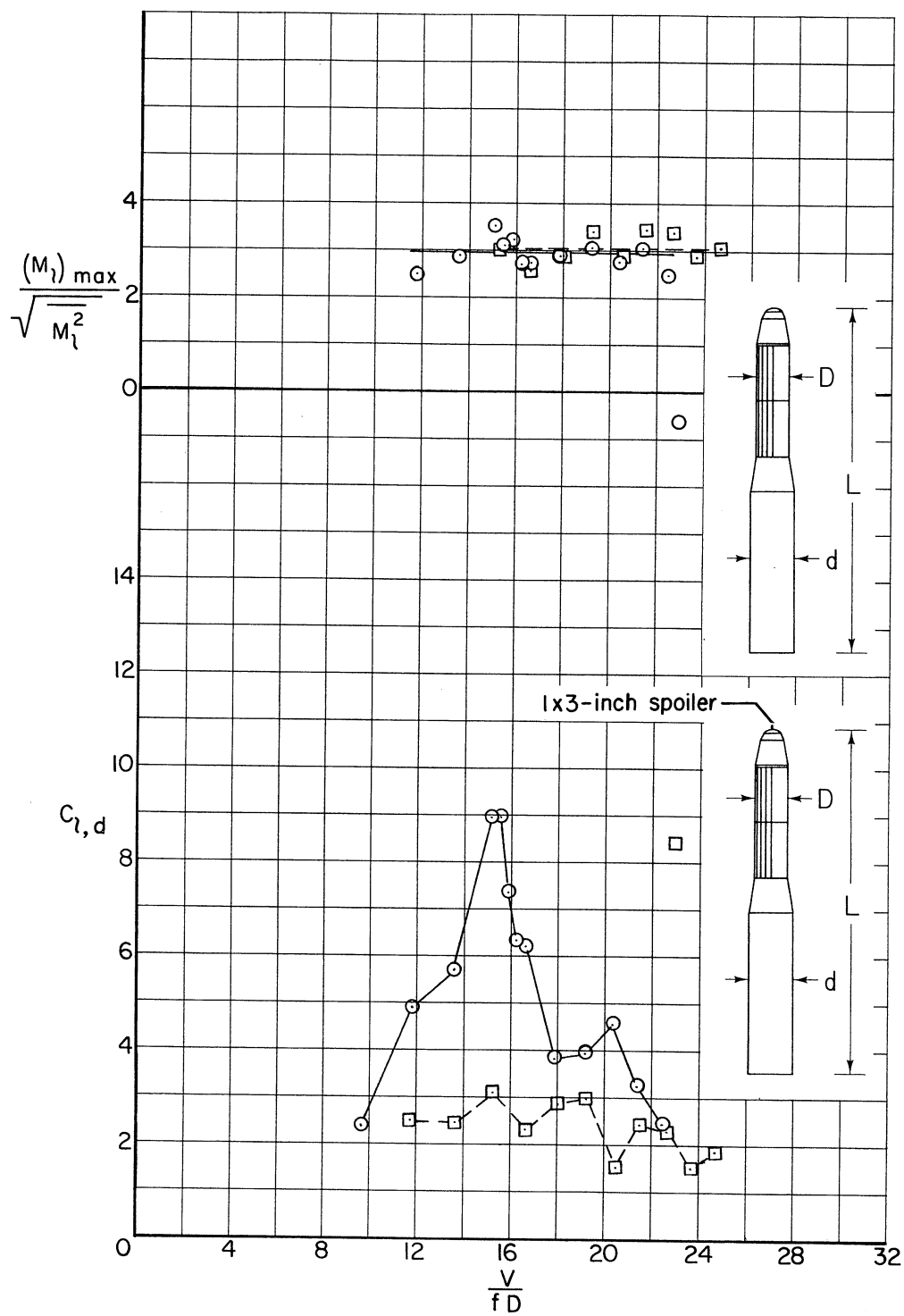
(e) Cylinder and cone combinations; $f_p D^2 = 0.15$.

Figure 29.- Concluded.



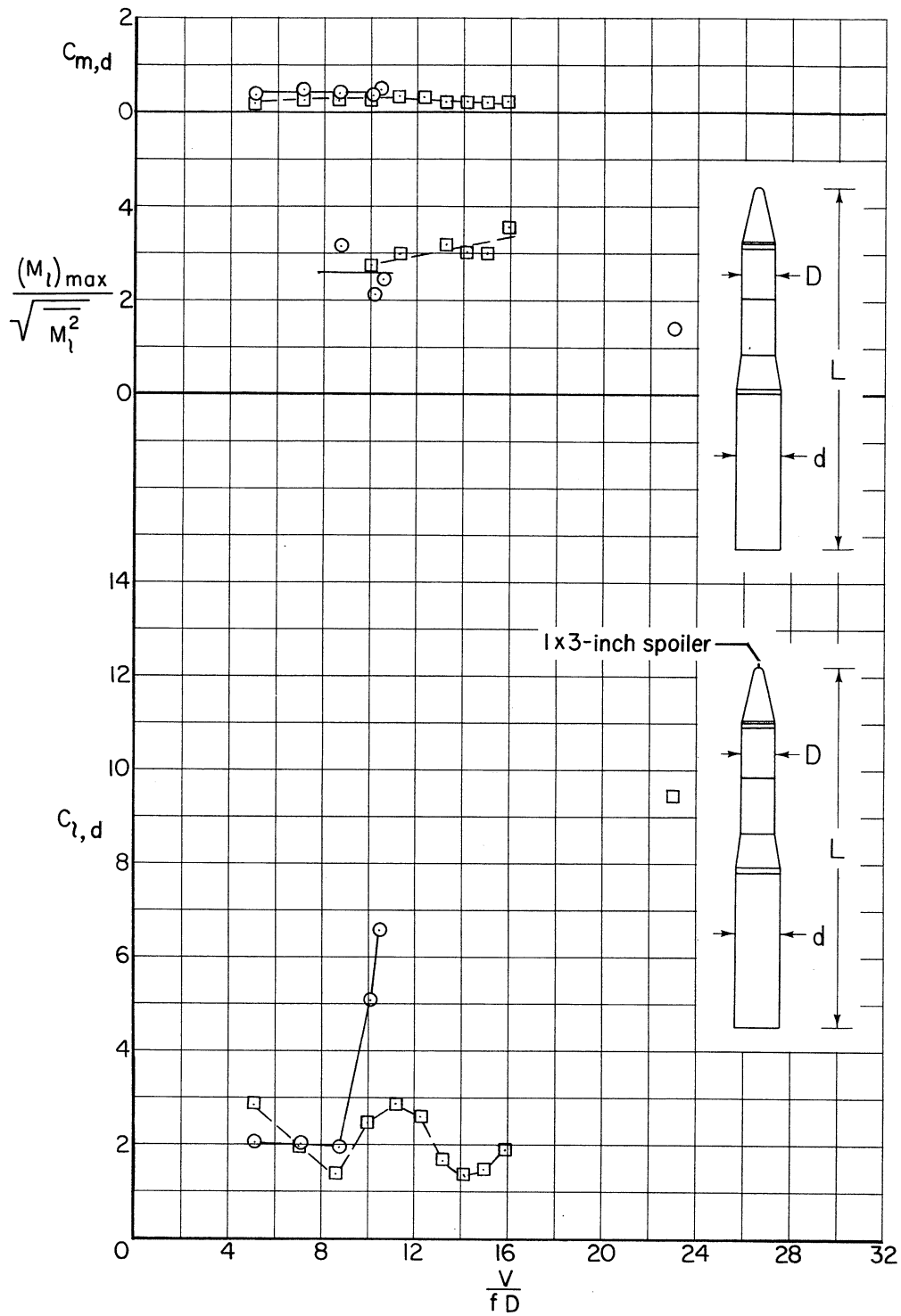
(a) Without roughness.

Figure 30.- Effects of a spoiler on the dynamic lateral moment characteristics of models with the double-cone nose; $D = 10.5$ inches; $D/d = 3/4$; $L/D = 10.0$; $f_p D^2 = 0.09$.



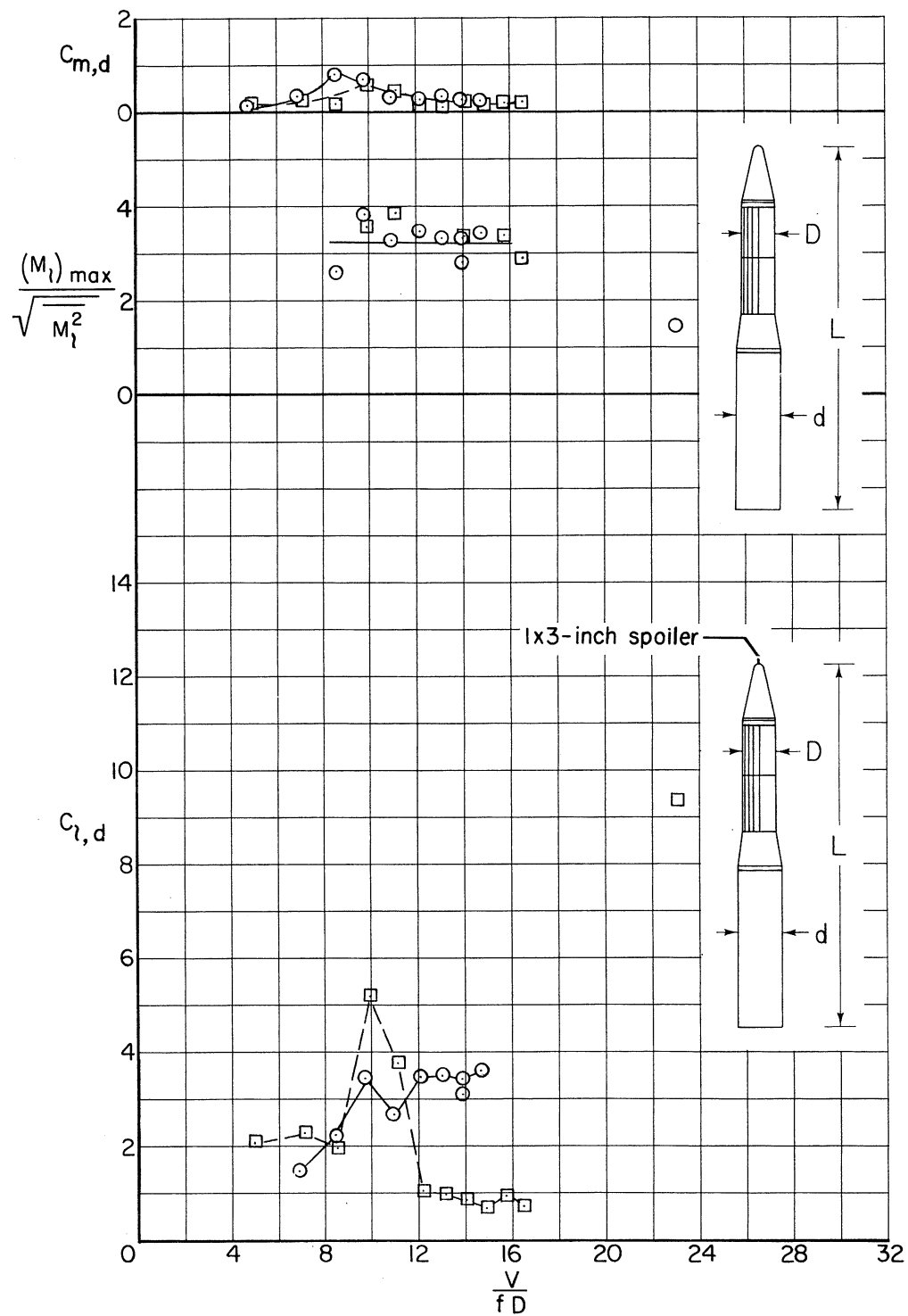
(b) With tapes 0.00029D thick.

Figure 30.- Concluded.



(a) Without roughness.

Figure 31.- Effects of a spoiler on the dynamic moment characteristics of models with the blunted-cone nose; pressure transducers at top of each stage; $D = 10.5$ inches; $D/d = 3/4$; $L/D = 10.6$; $f_0 D^2 = 0.14$.



(b) With tapes 0.00029D thick.

Figure 31.- Concluded.

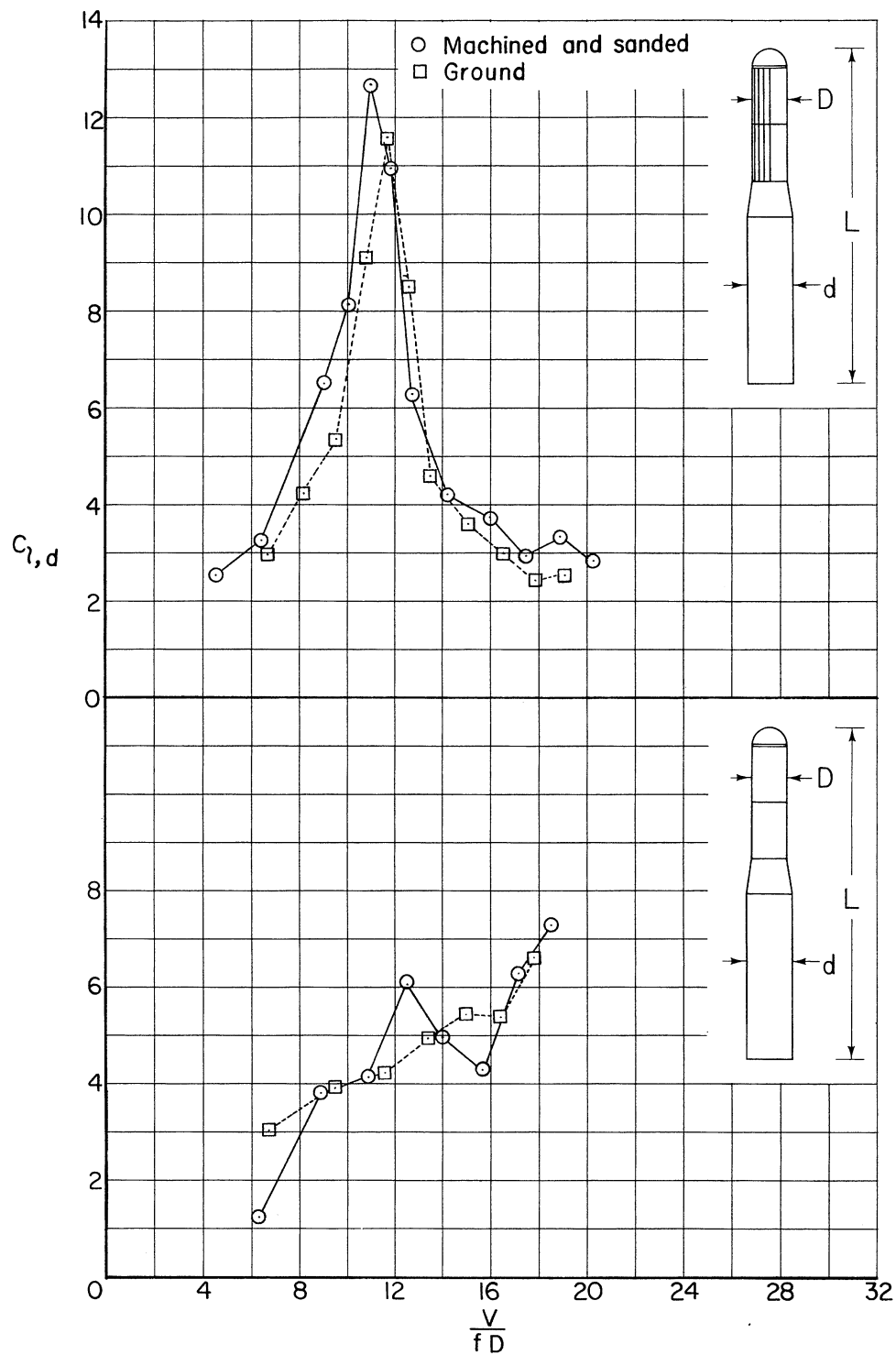
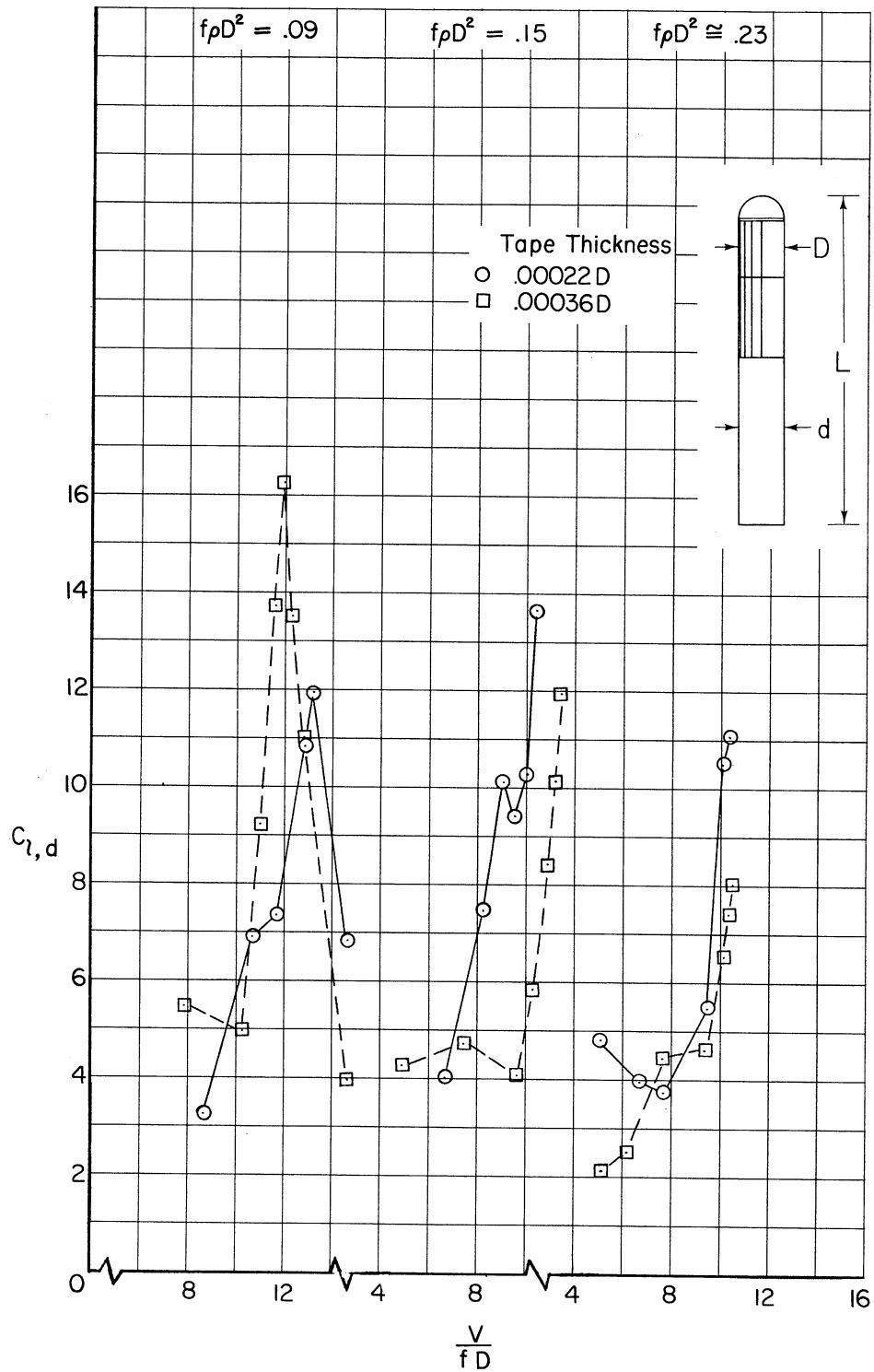
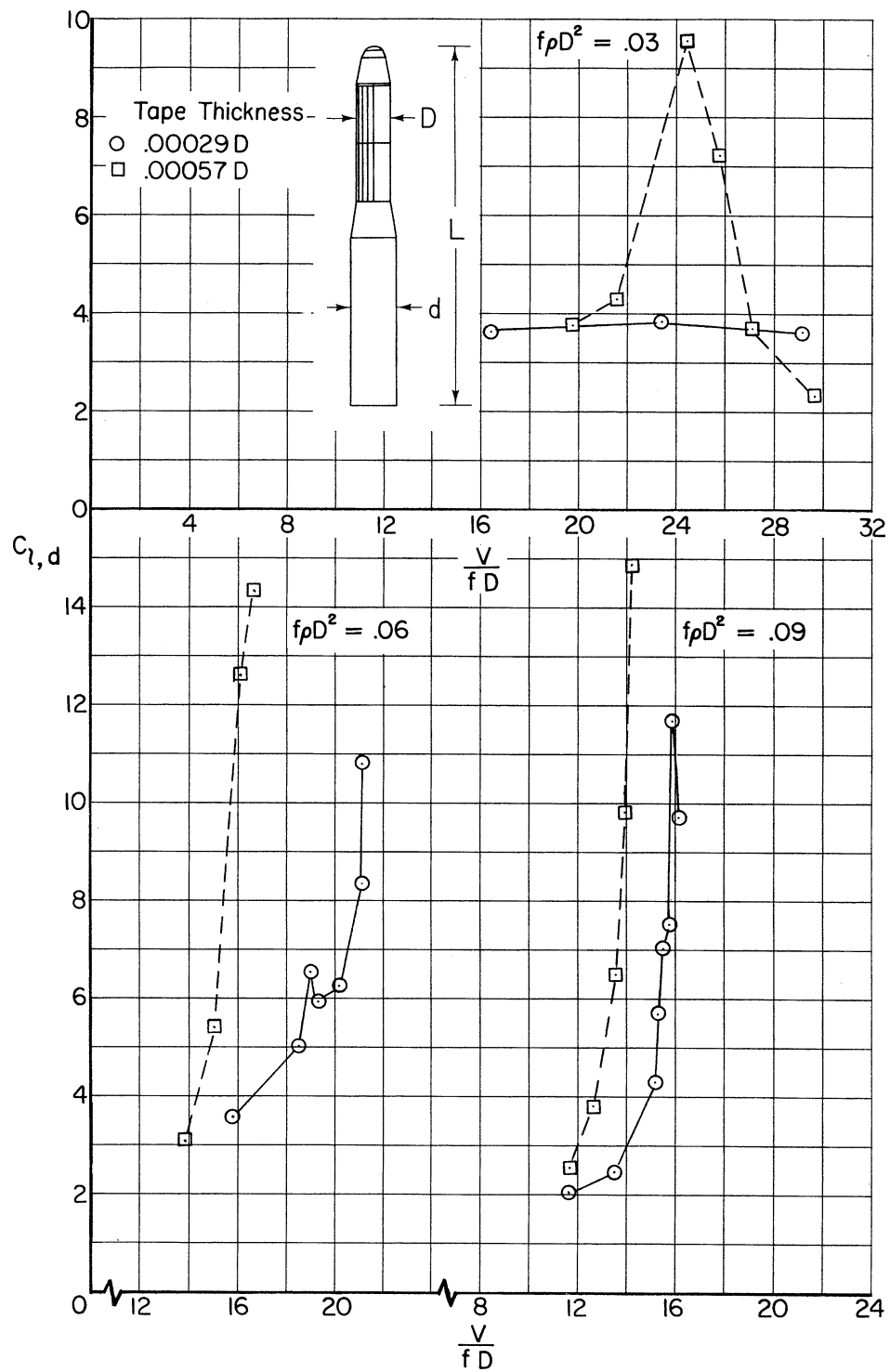


Figure 32.- Effects of surface finish on the dynamic lateral moment characteristics of the models with the hemisphere nose; $D/d = 3/4$; $L/D = 9.5$; $f\rho D^2 \approx 0.14$.



(a) $L/D = 7.3$; hemisphere nose.

Figure 33.- Effects of tape thickness on the dynamic lateral moment characteristics of the models.



(b) $D/d = 3/4$; $L/D = 10.0$; double-cone nose.

Figure 33.- Concluded.

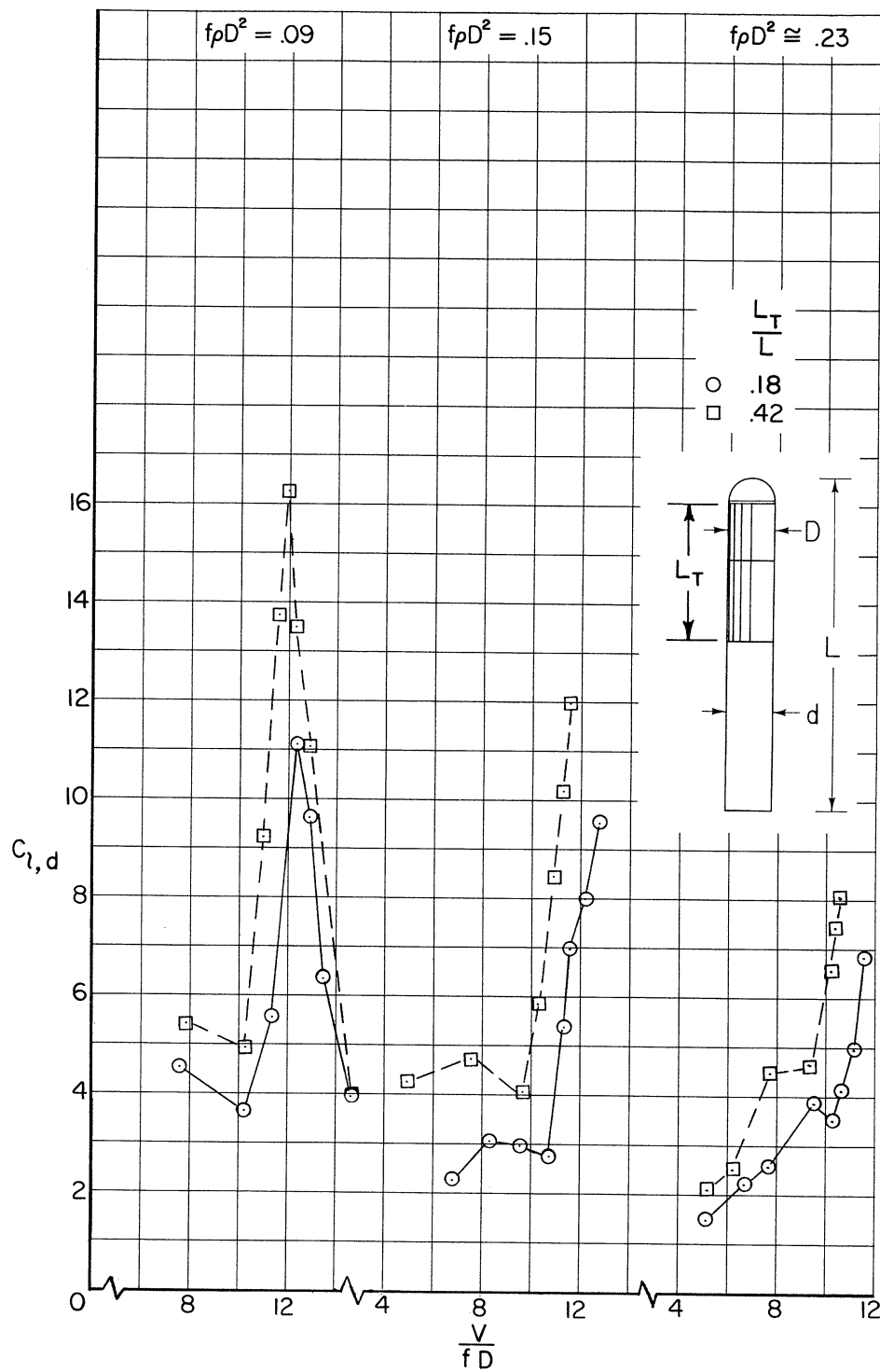
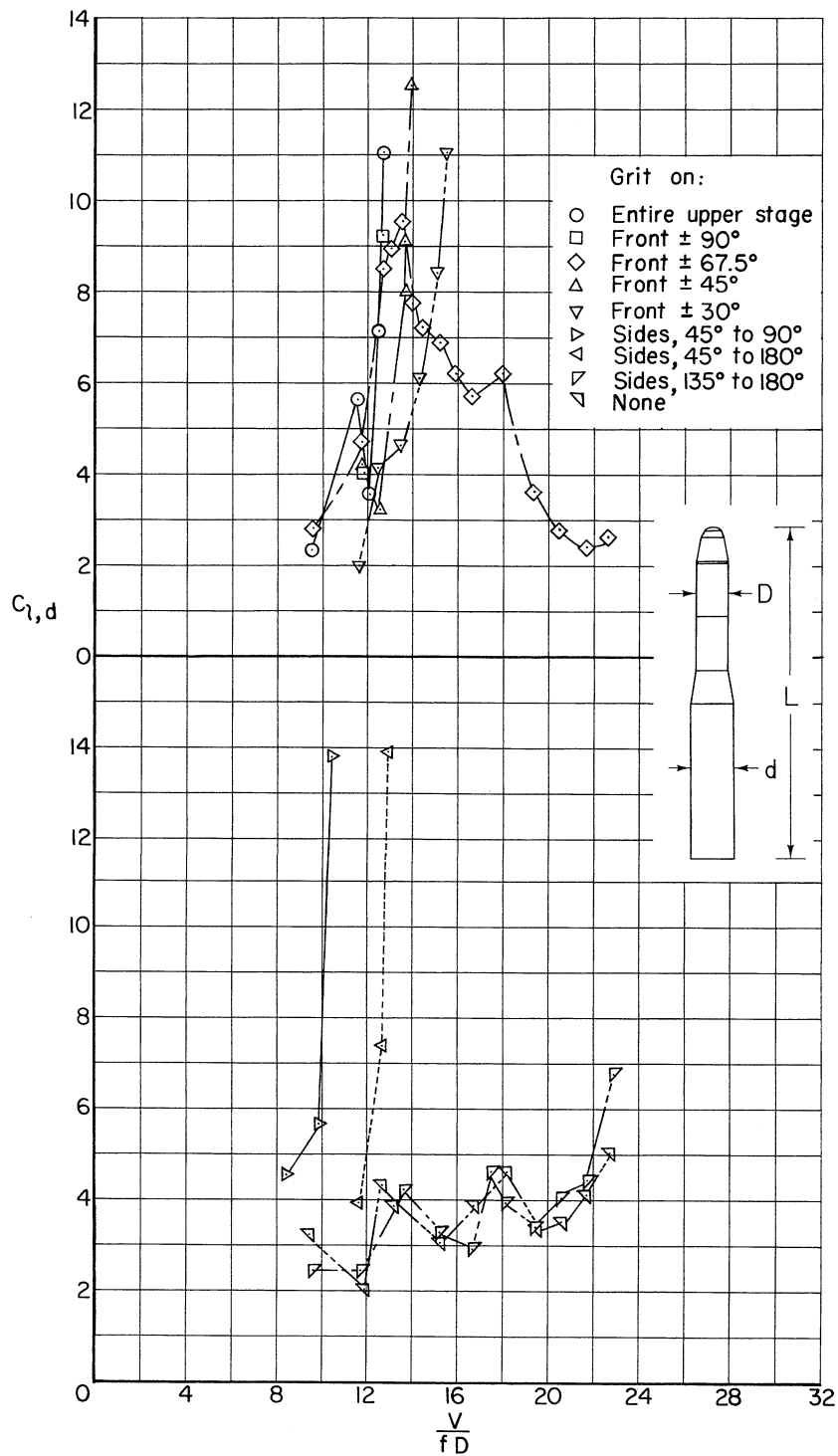
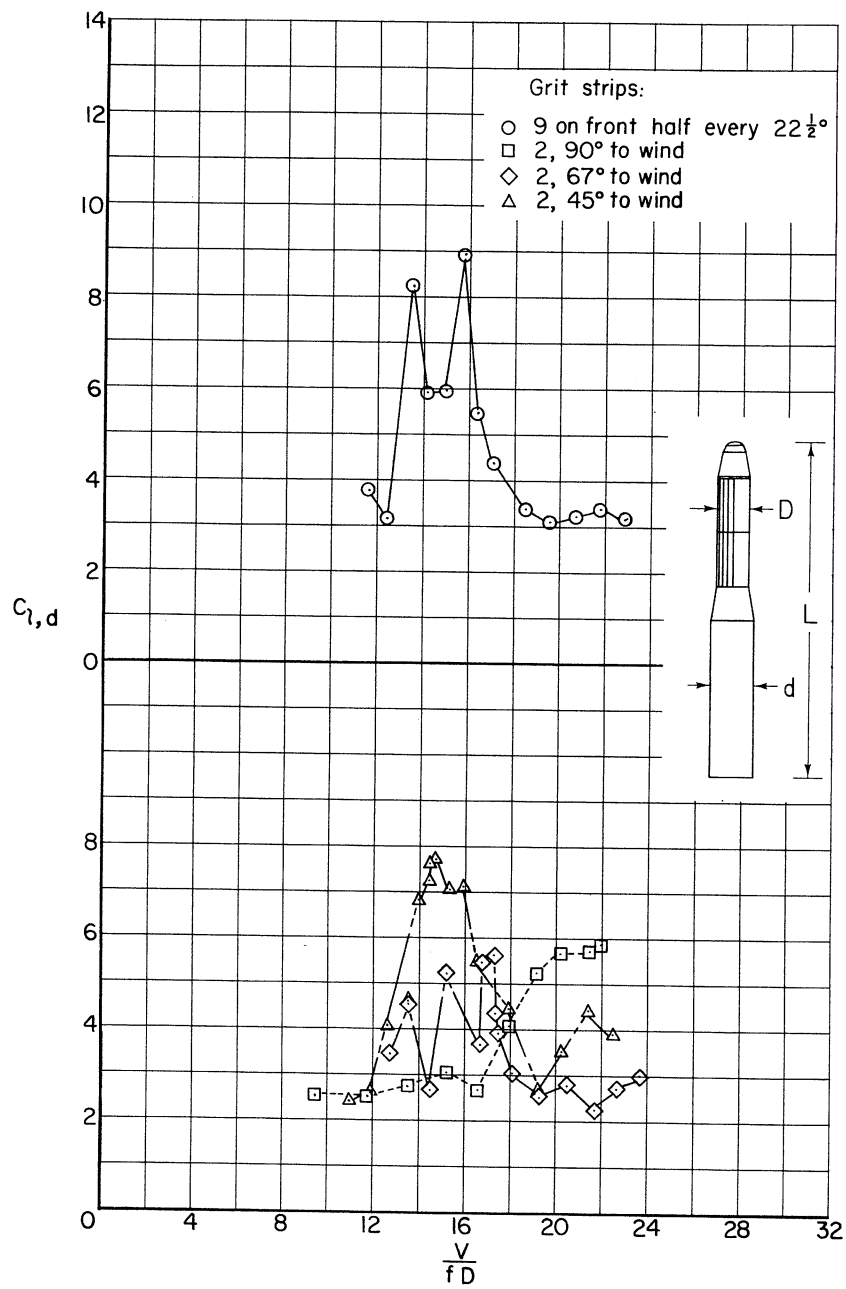


Figure 34.- Effects of tape length on the dynamic lateral moment characteristics of the models; $D/d = 1$; $L/D = 7.3$; hemisphere nose; tape $0.00036D$ thick.



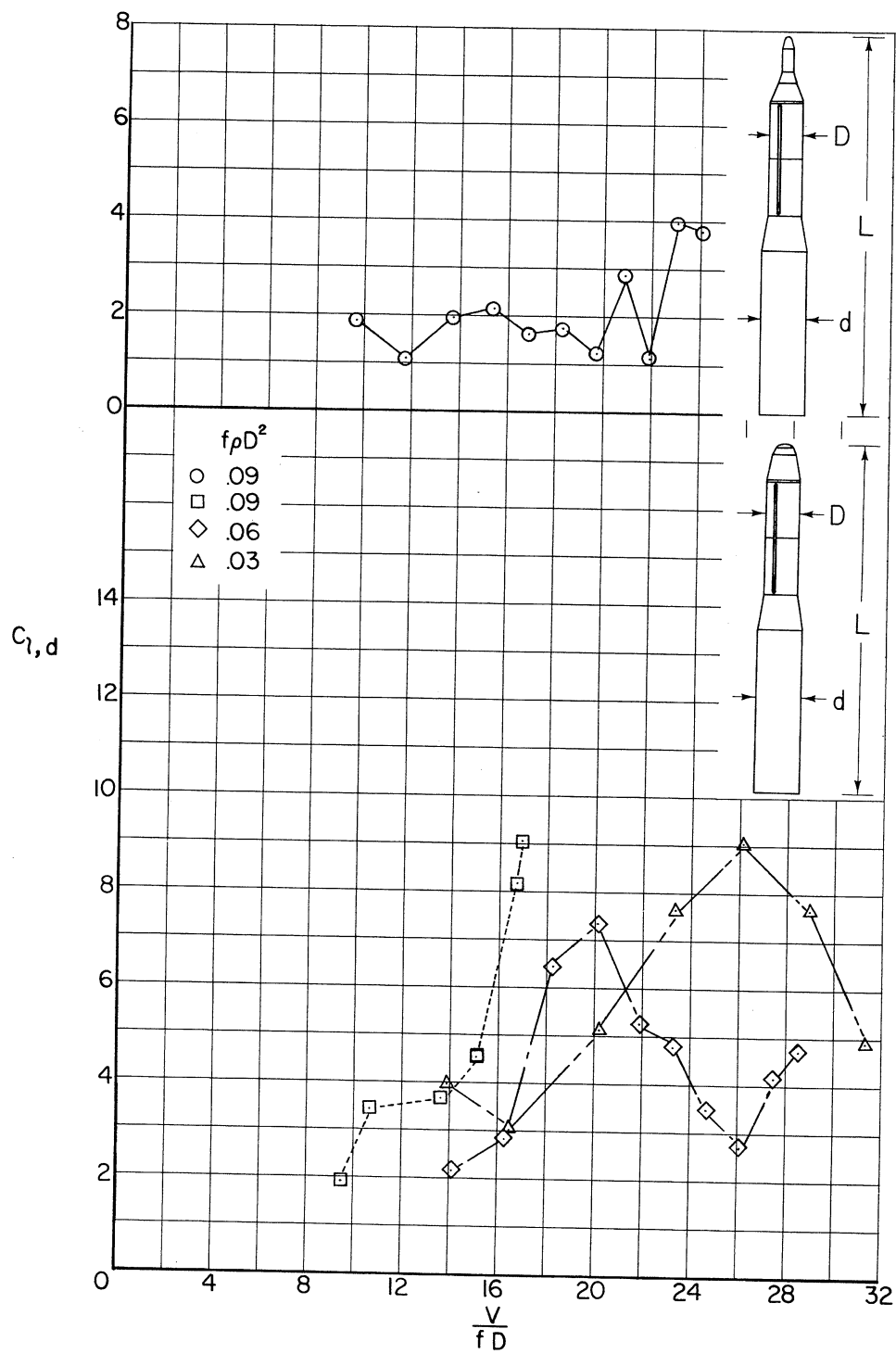
(a) Grit applied over areas.

Figure 35.- Effects of No. 280 carborundum particles on upper stage on the dynamic lateral moment characteristics of the models; $D = 10.5$ inches; $D/d = 3/4$; $L/D = 10.0$; double-cone nose; $f_p D^2 = 0.09$.



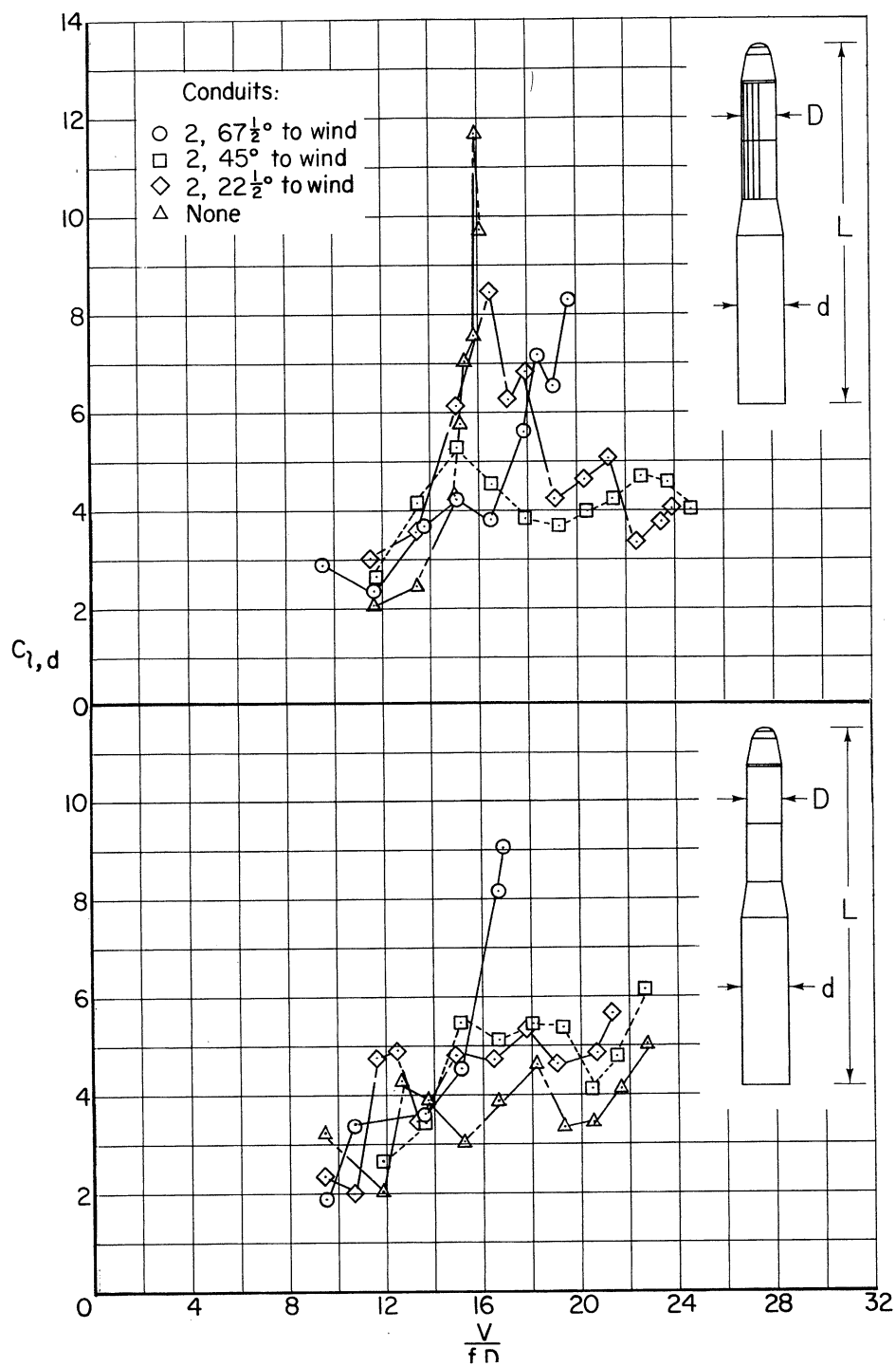
(b) Grit applied in vertical strips 1/2 inch wide.

Figure 35.- Concluded.



(b) Two conduits, $67\text{-}1/2^\circ$ to wind.

Figure 36.- Concluded.



(a) Conduits at various angular locations; $f_p D^2 = 0.09$.

Figure 36.- The dynamic lateral moment characteristics of the model with circular-arc conduits $1/2$ inch in radius, $1/4$ inch thick, and $7/8$ inch wide on the upper stage; $D = 10.5$ inches; $D/d = 3/4$; $L/D = 10.0$ to 10.9 .

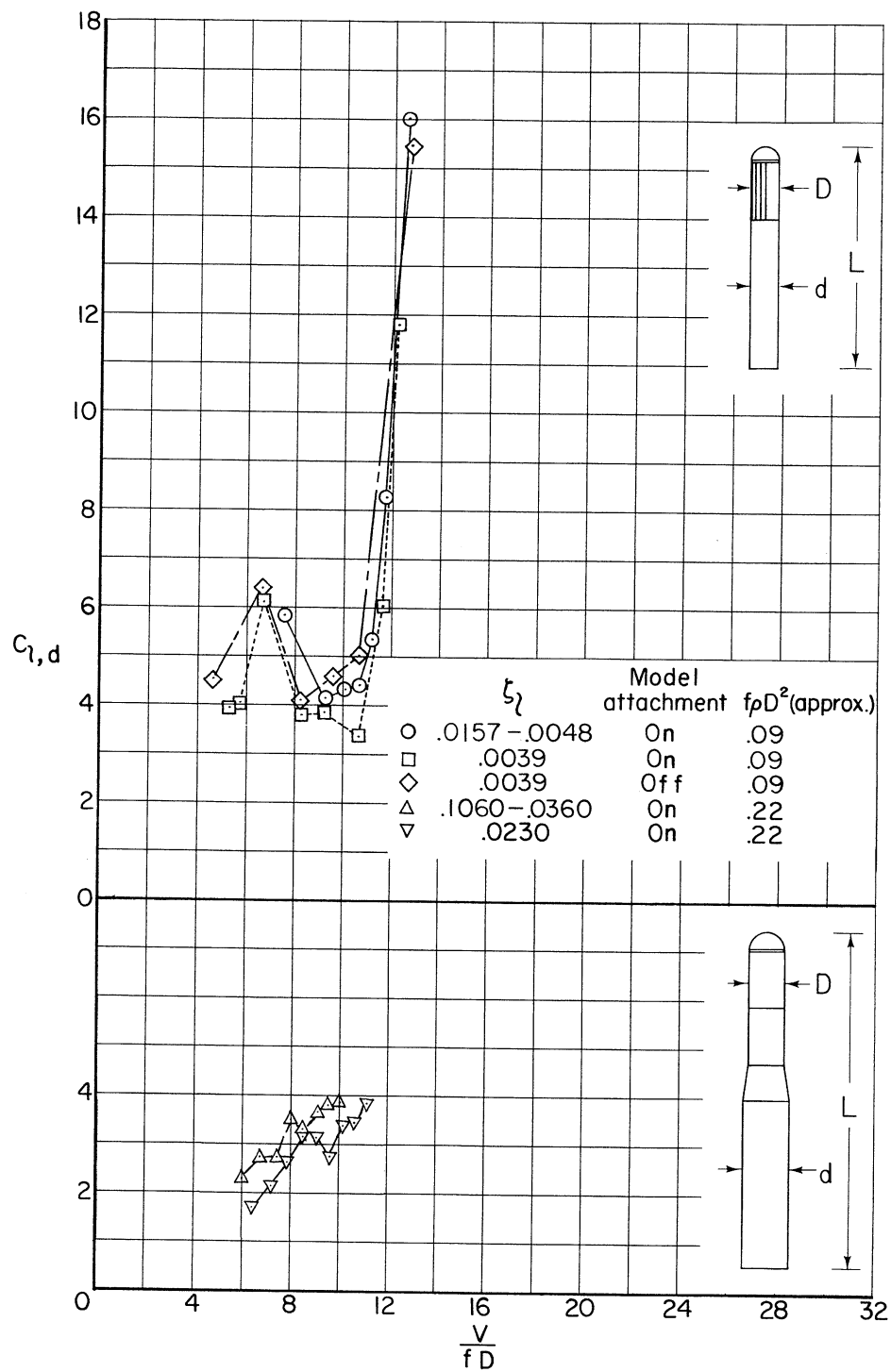


Figure 37.- Effects of friction damper on the dynamic lateral moment characteristics of the model.

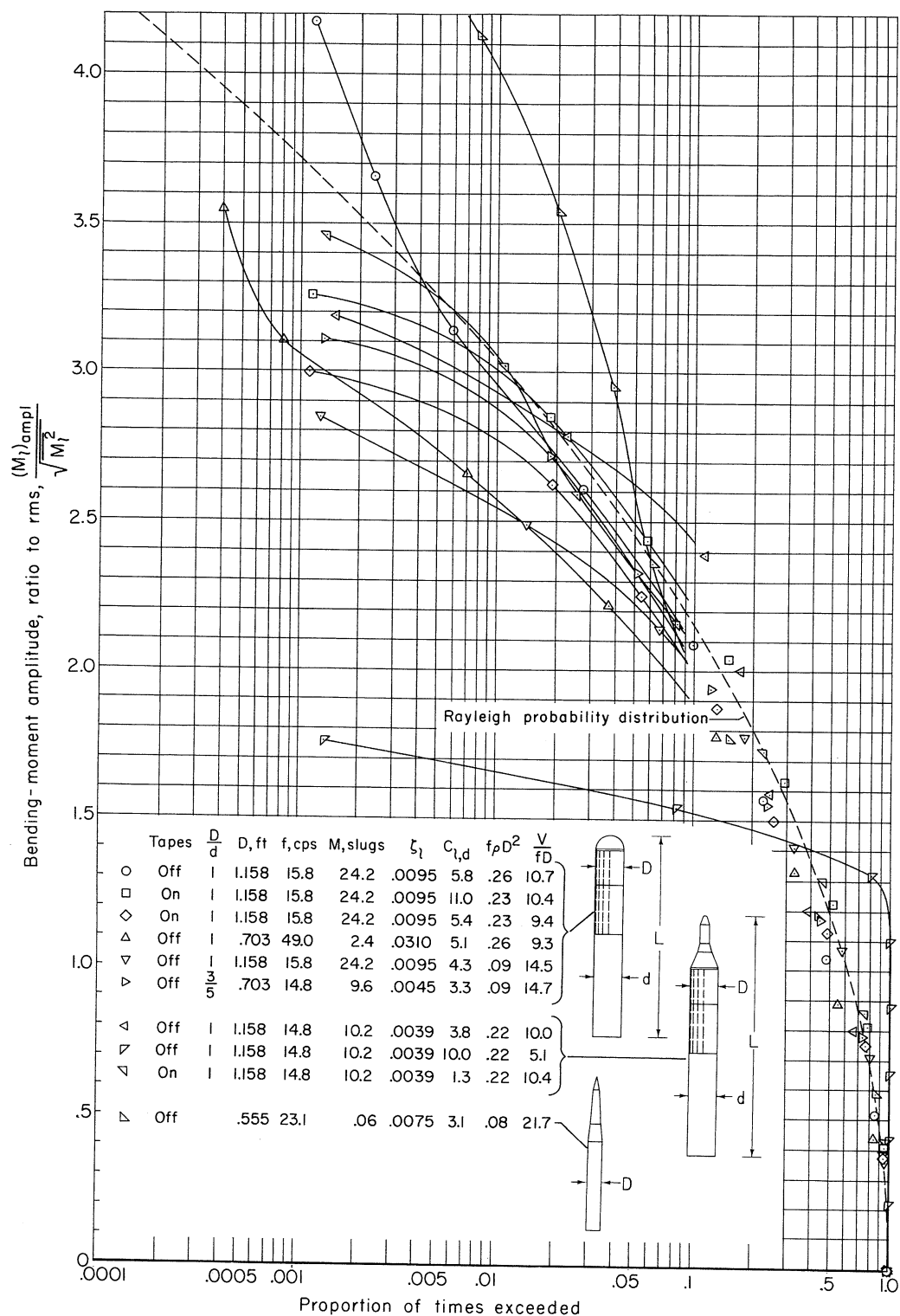
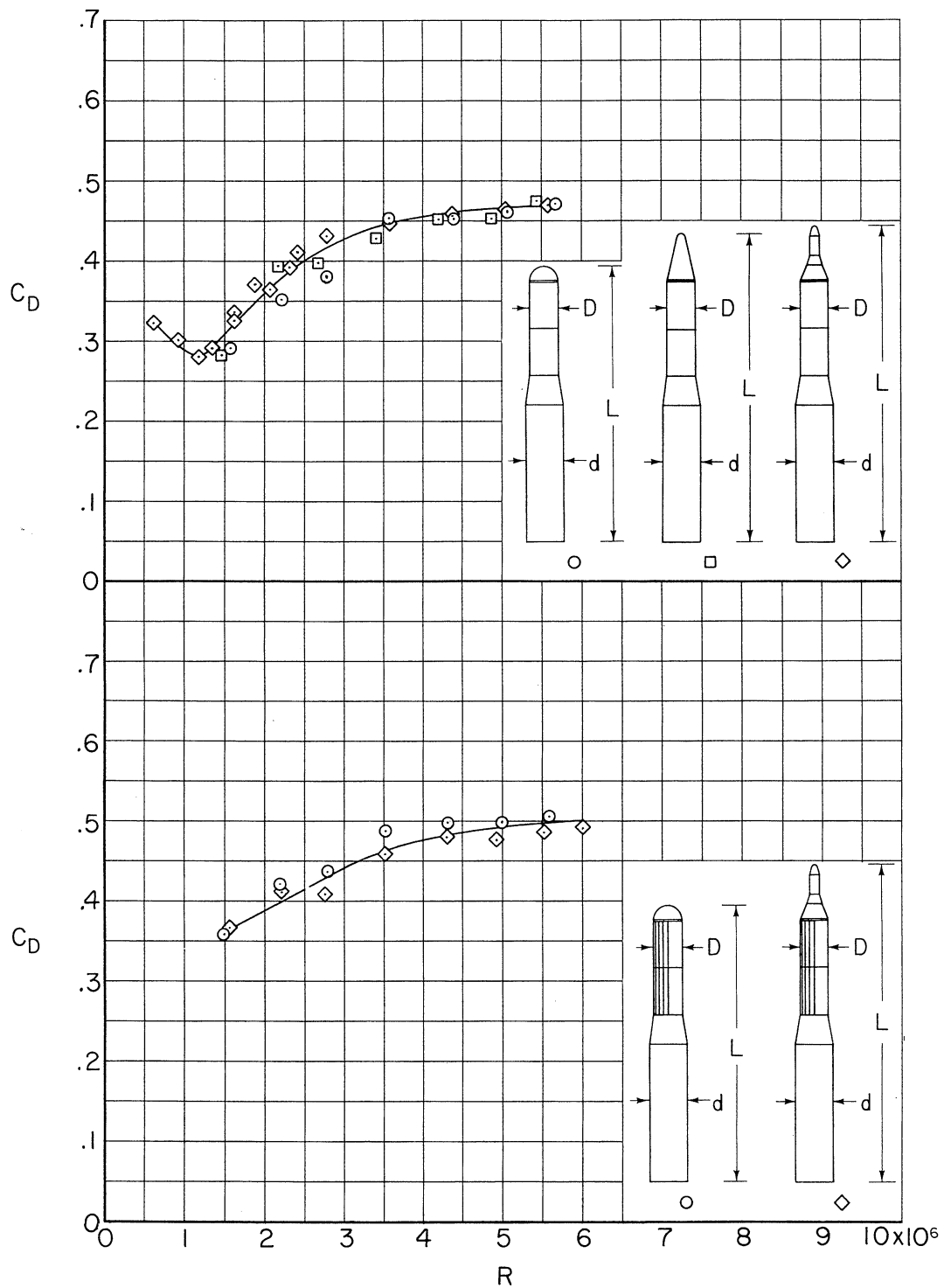
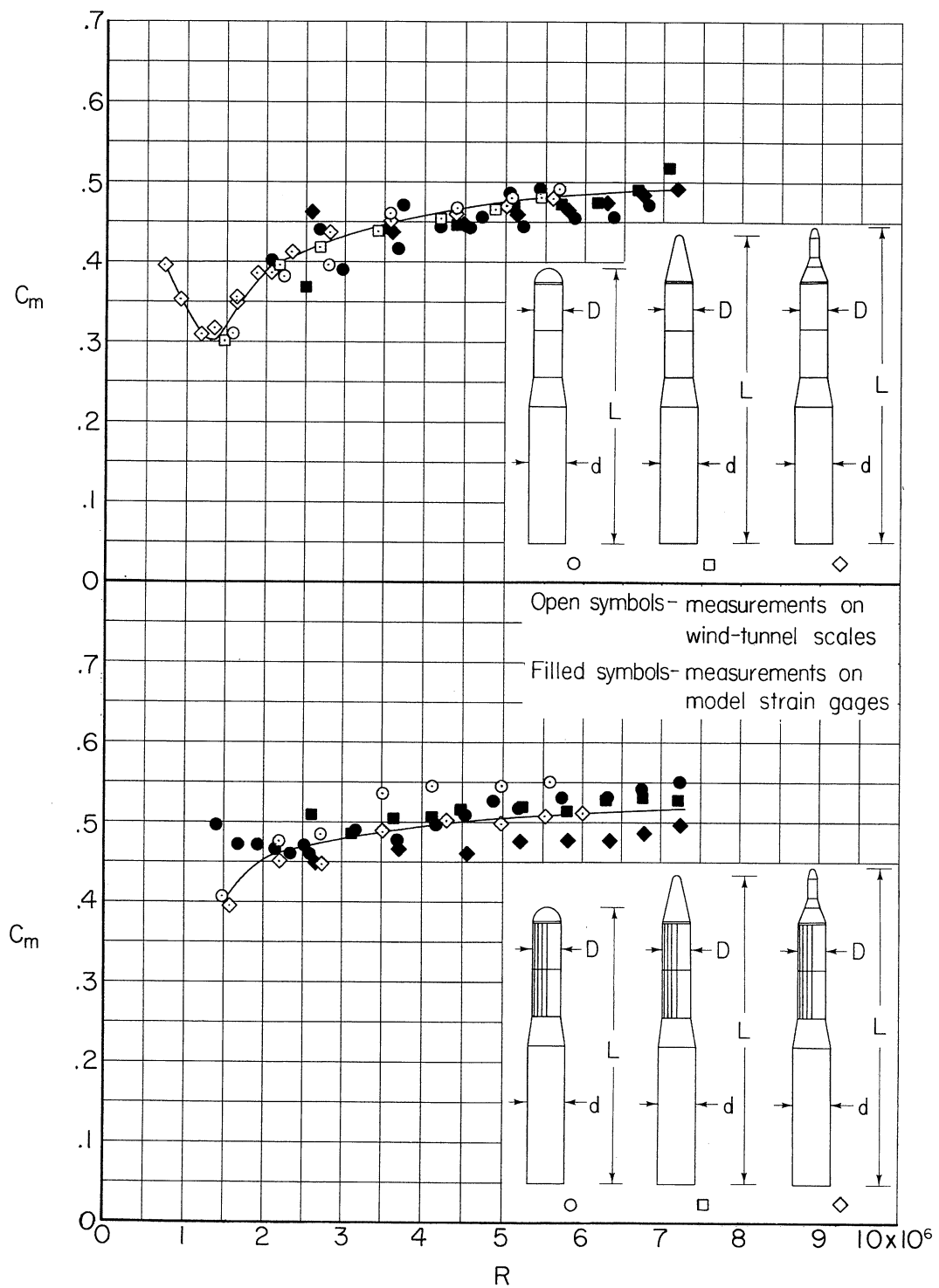


Figure 38.- Analysis of typical data samples showing the proportion of times that normalized bending-moment amplitude in the lateral direction exceeded nominal values; $L/d = 7.3$ to 8.6 .



(a) Drag coefficient.

Figure 39.- Typical steady-state dragwise force and moment characteristics of the models; $D/d = 3/4$; $L/D = 9.5$ to 10.9 .



(b) Dragwise moment coefficient.

Figure 39.- Concluded.

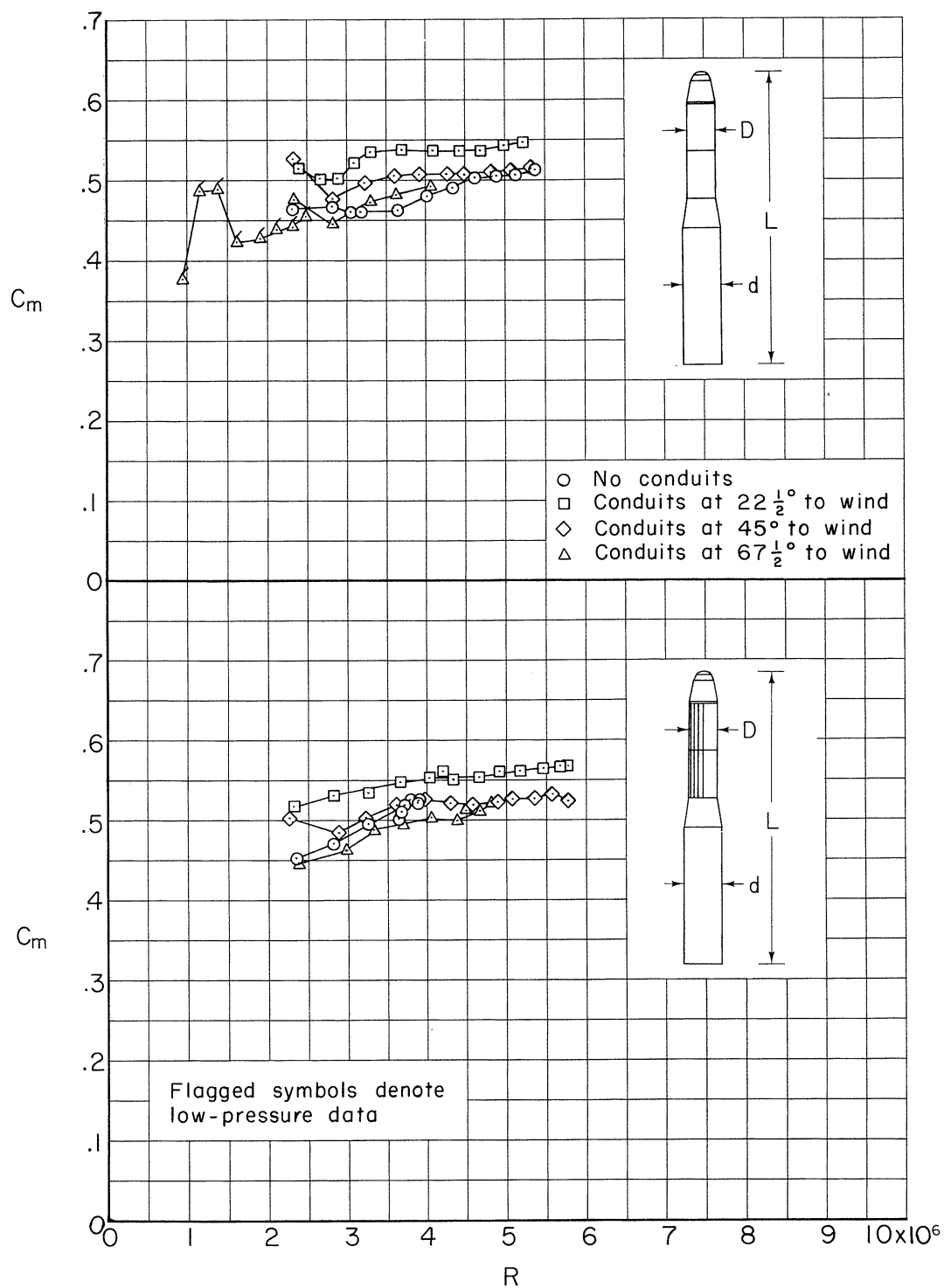


Figure 40.- The effect on the steady-state dragwise moment coefficients of circular-arc conduits 1/2 inch in radius, 1/4 inch thick, and 7/8 inch wide on the upper stage; $D = 10.5$ inches; $D/d = 3/4$; $L/D = 10.0$.

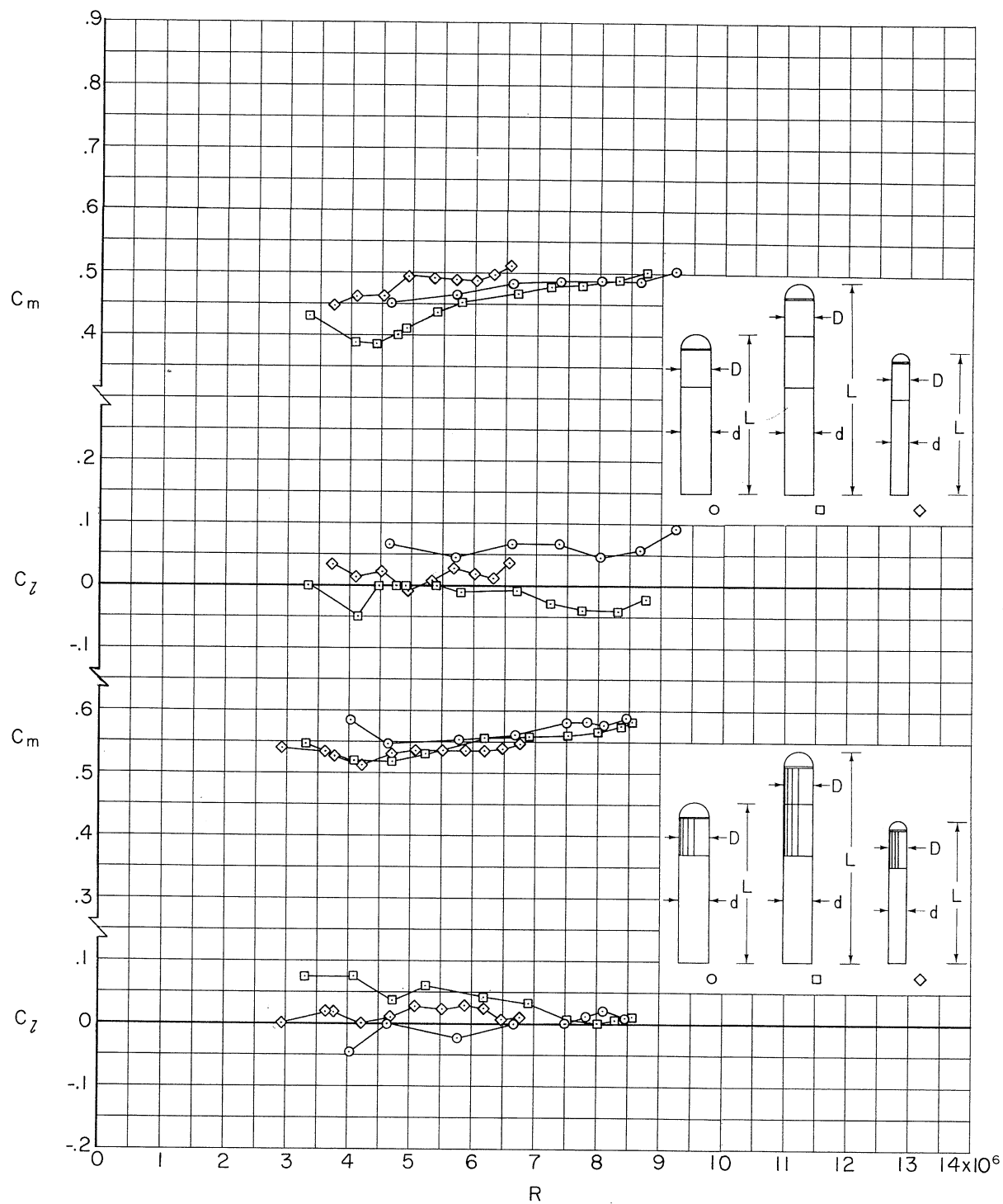
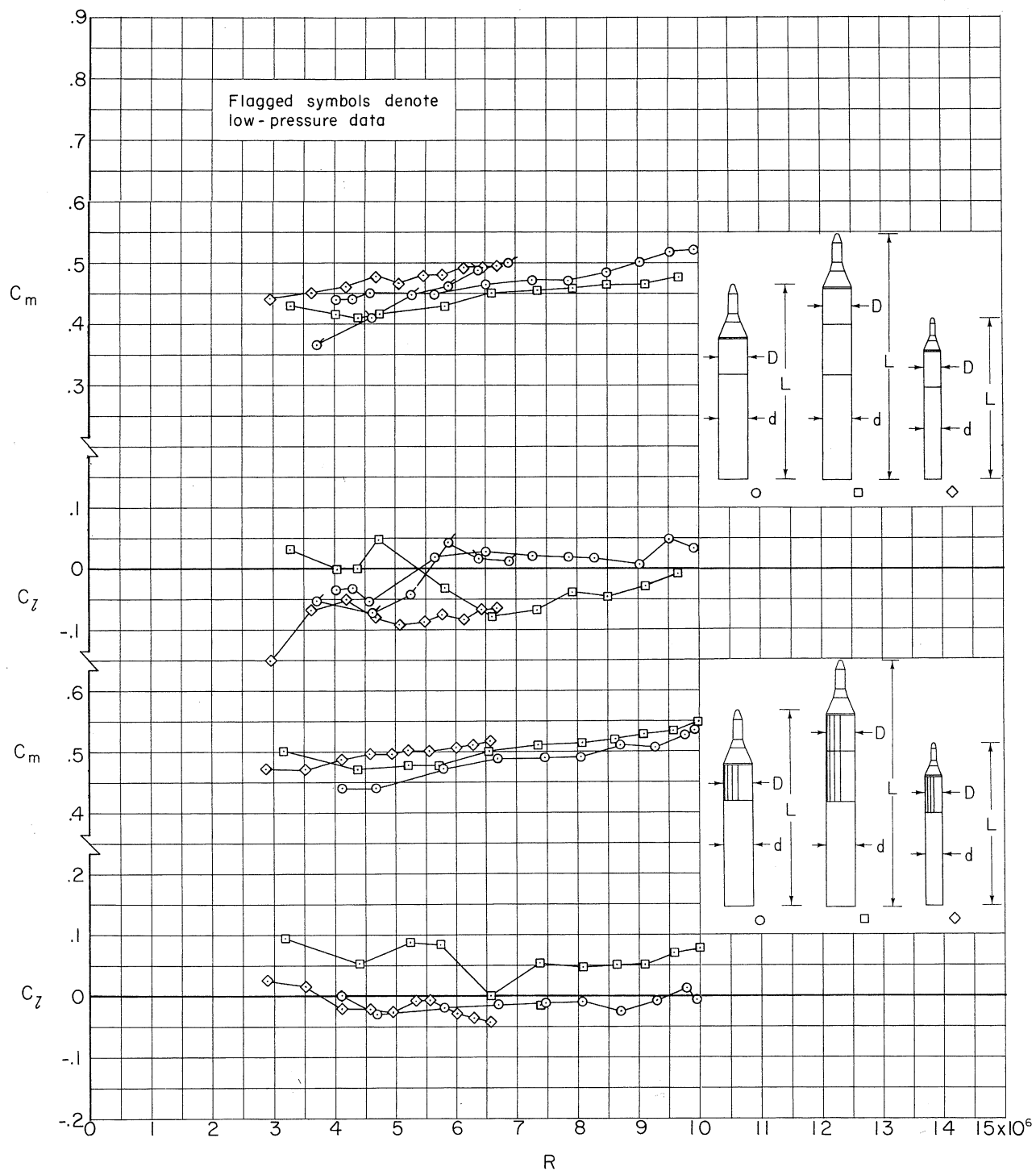


Figure 41.- The effect of fineness ratio and model scale on the steady-state moment coefficients of the models; $D = 1.158$ and 0.703 feet; $D/d = 1$.



(b) Cone-cylinder nose; $L/D = 6.9$ to 9.5 .

Figure 41.- Concluded.

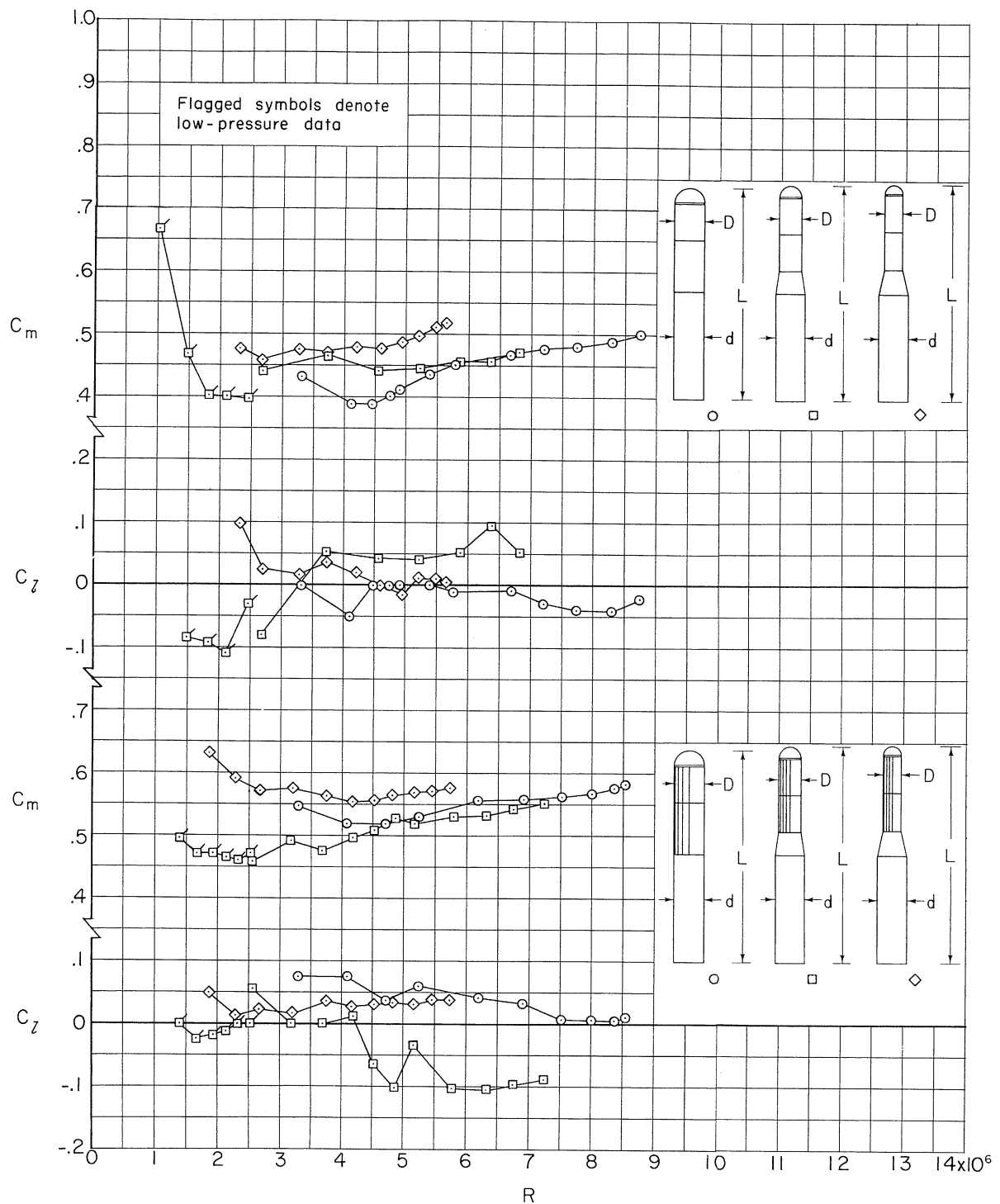


Figure 42.- The effects of stage-diameter ratio on the steady-state moment coefficients of the hemisphere-nose models; $D/d = 1, 3/4$, and $3/5$; $L/d = 7.2$ to 7.5 .

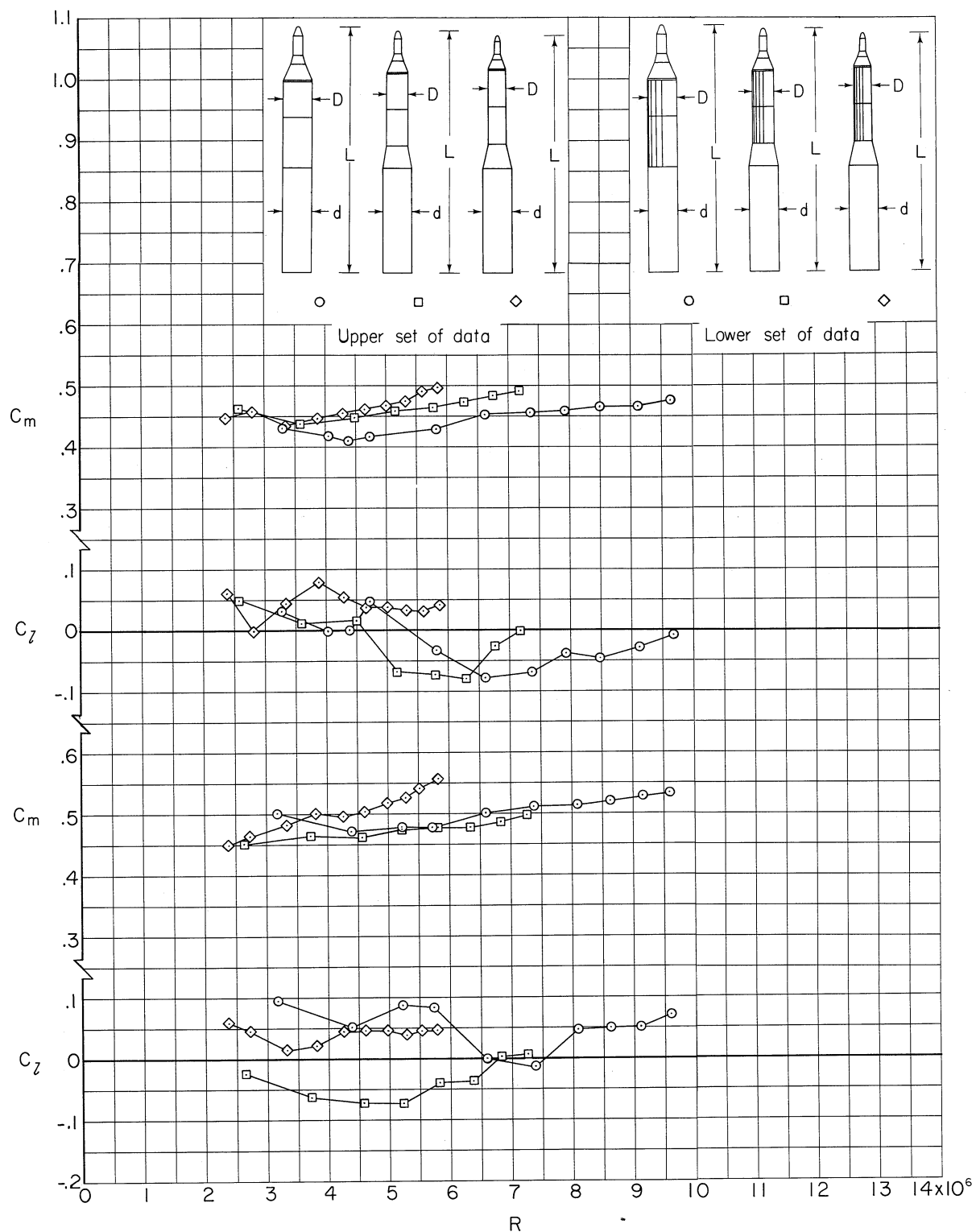
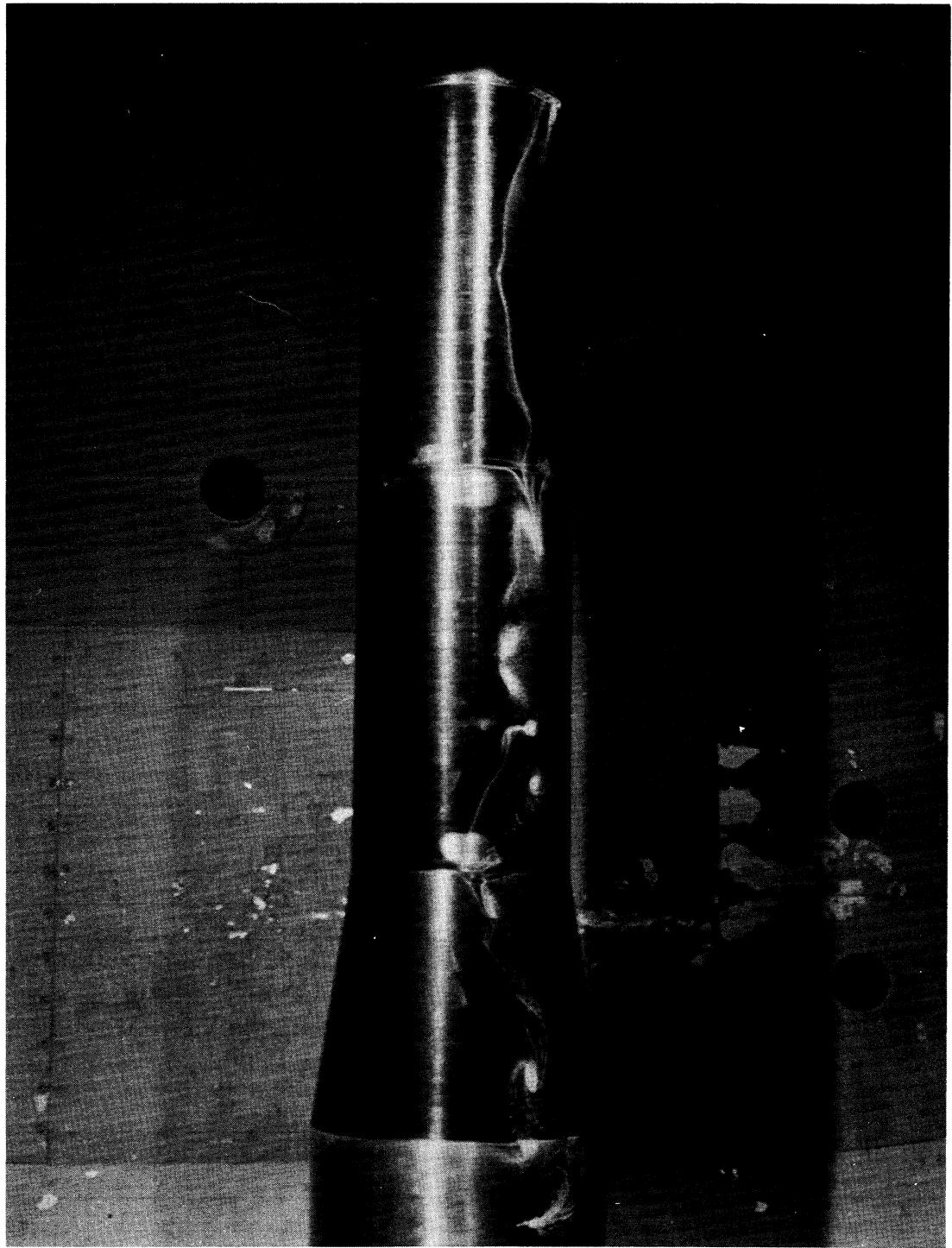
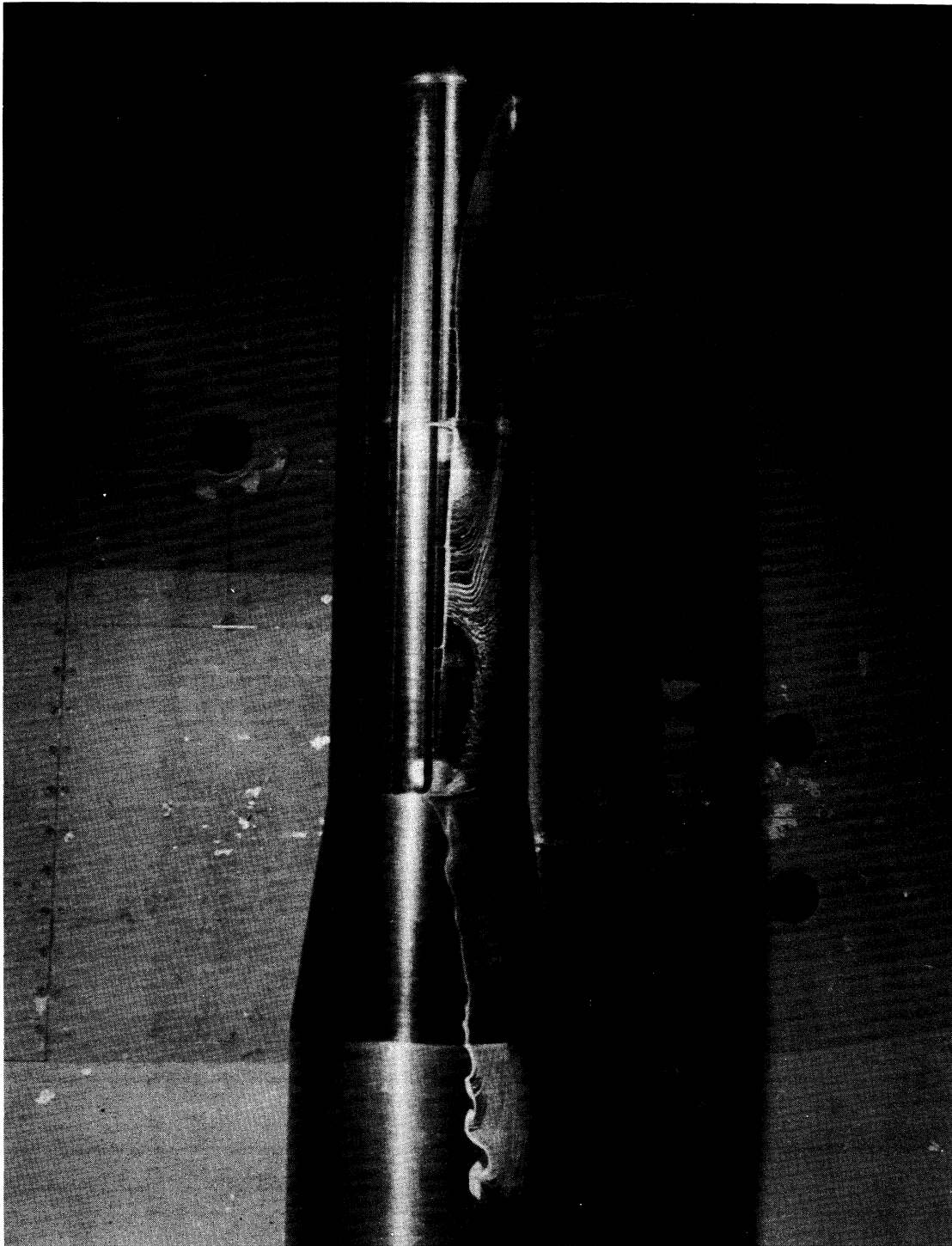


Figure 43.- The effects of stage-diameter ratio on the steady-state moment coefficients of the cone-cylinder nose models; $D/d = 1, 3/4$, and $3/5$; $L/d = 8.3$ to 8.6 .



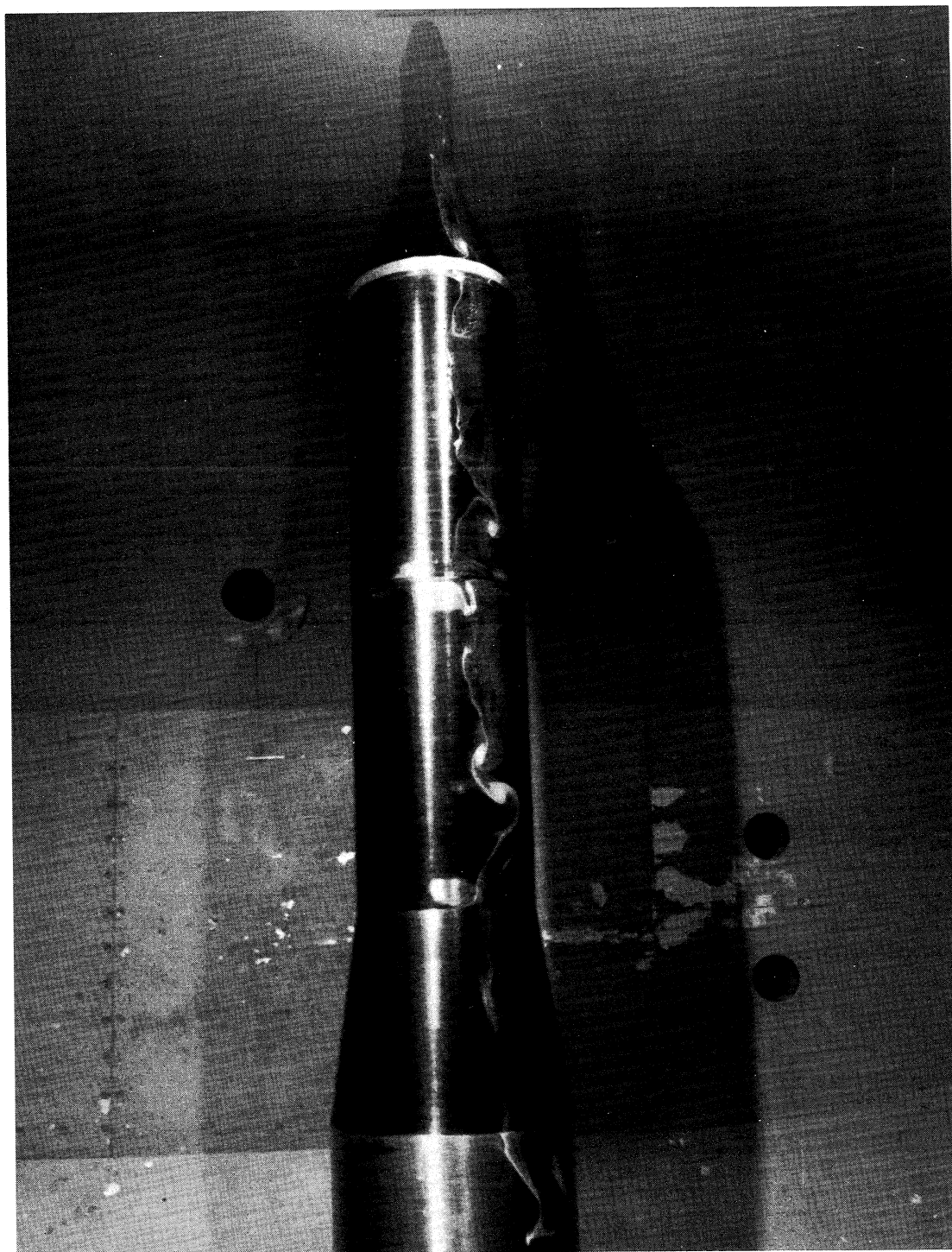
(a) Without roughness, with hemisphere nose.

Figure 44.- Photographs of the model in ultraviolet light with a fluorescent oil coating (air flow from left); $D/d = 3/4$; $R = 3.6$ million.



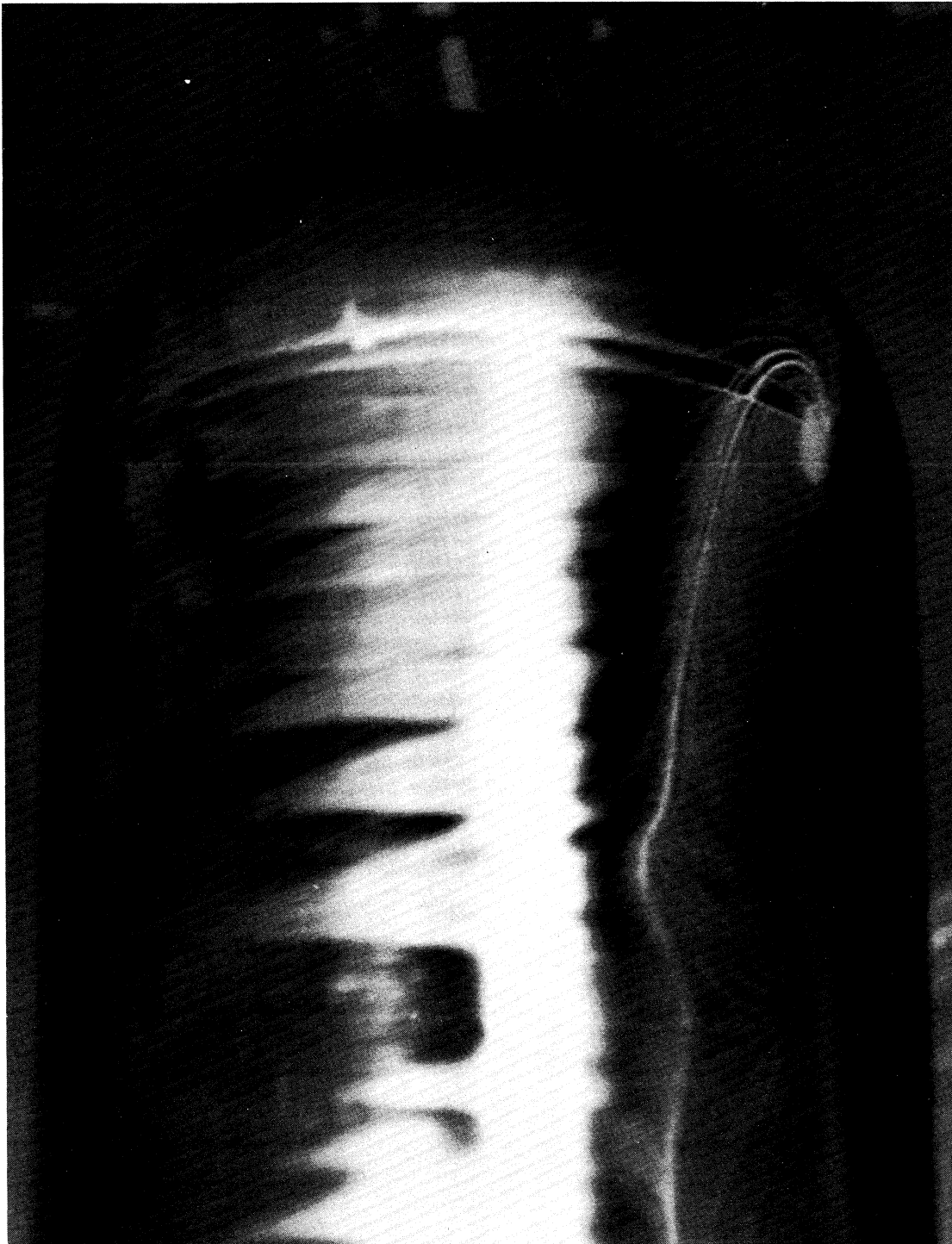
(b) With tapes 0.00029D thick and hemisphere nose.

Figure 44.- Continued.



(c) Without roughness, with cone-cylinder nose.

Figure 44.- Concluded.



(a) Without roughness, with hemisphere nose.

Figure 45.- Close-up photographs of the nose area of the models in ultraviolet light with a fluorescent oil coating (air flow from left); $D/d = 3/4$, $R = 3.6$ million.



(b) With tapes 0.00029D thick and hemisphere nose.

Figure 45.- Continued.



(c) Without roughness, with cone-cylinder nose.

Figure 45.- Continued.



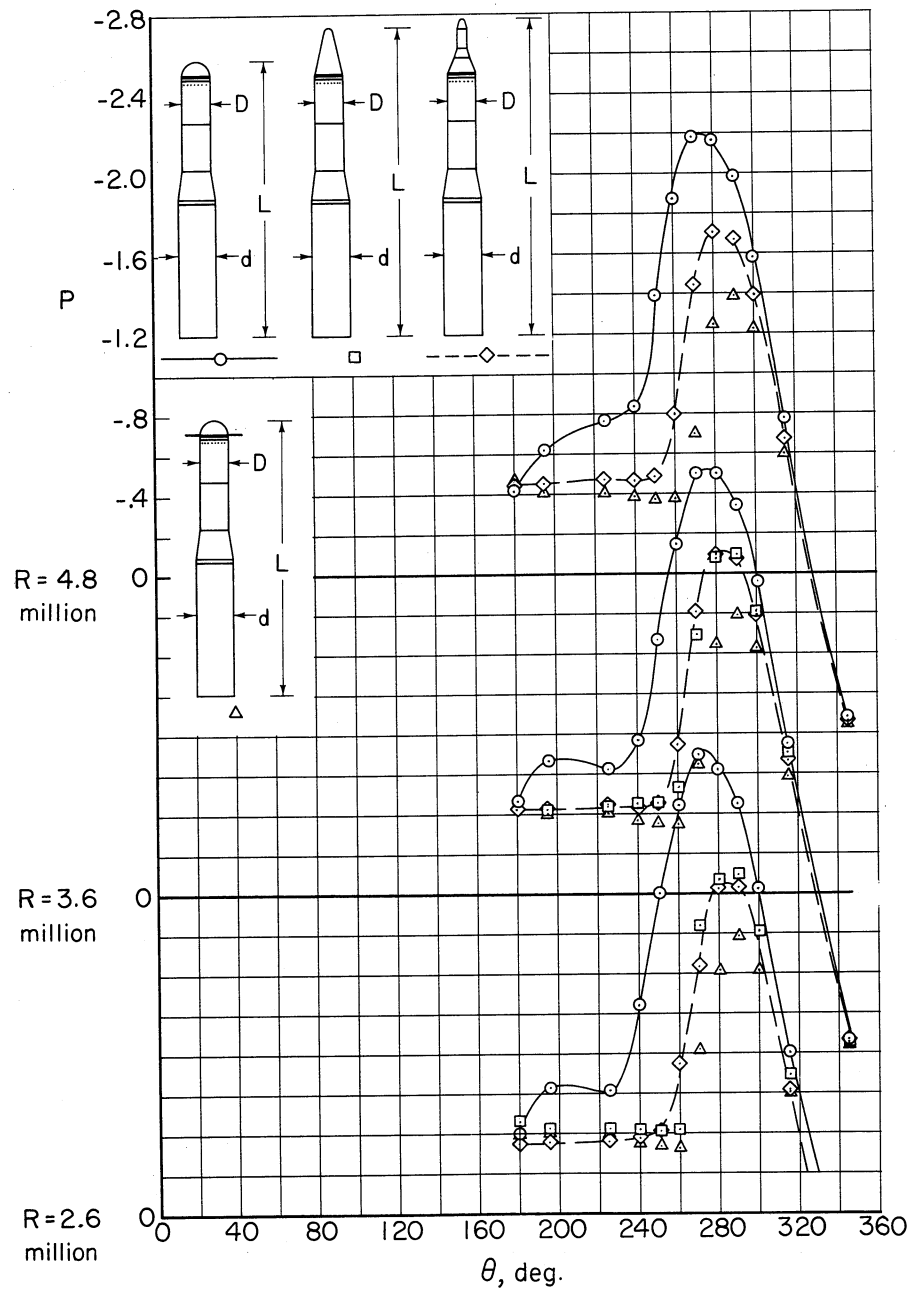
(d) With tapes 0.00029D thick and cone-cylinder nose.

Figure 45.- Continued.



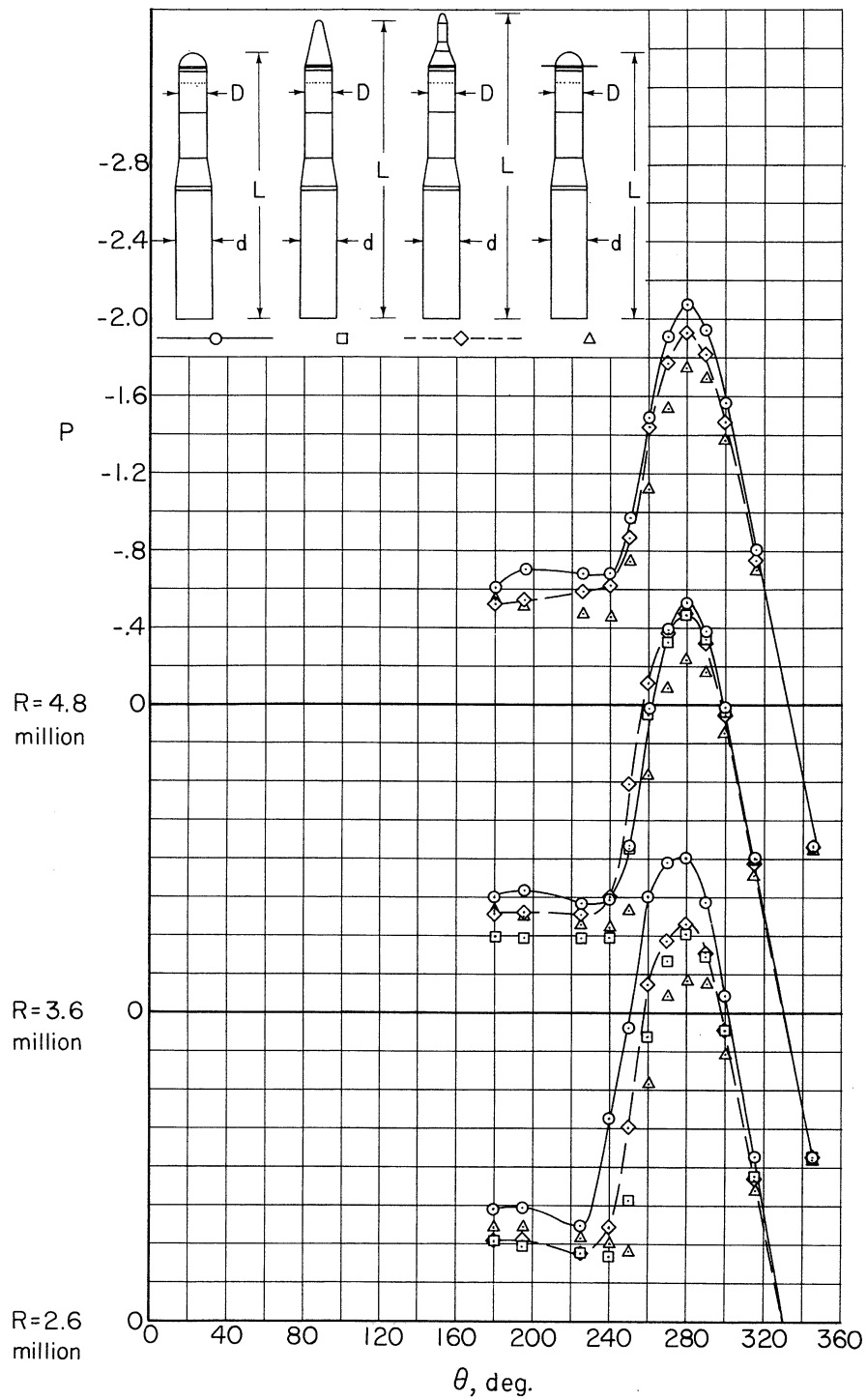
(e) Without roughness, with plate under hemisphere nose-plate concentric with upper stage and twice its diameter.

Figure 45.- Concluded.



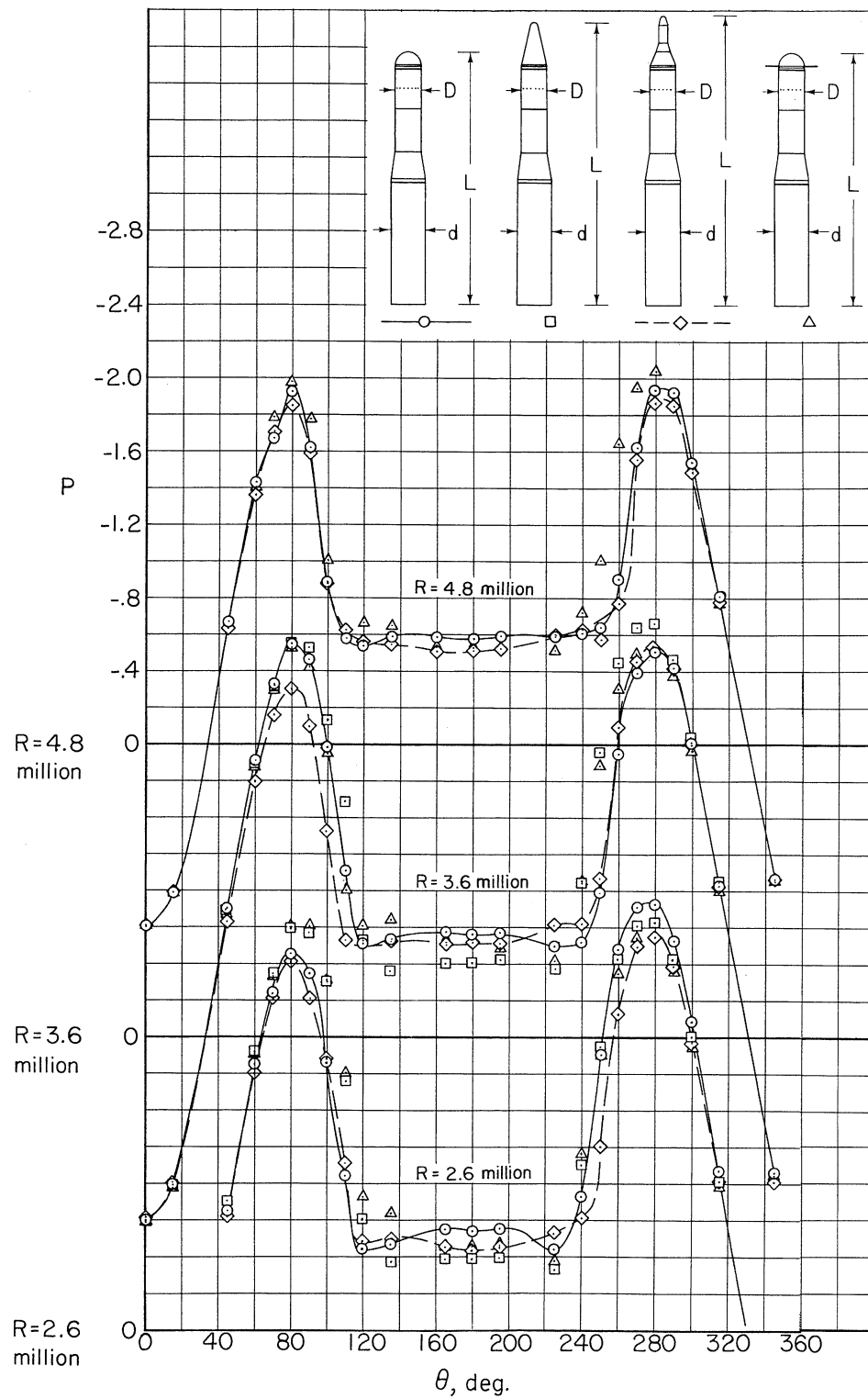
(a) Station B, 2.7 inches below the nose.

Figure 46.- Coefficients of static pressure measured at orifices in the model surface without roughness; plate diameter, $2D$, concentric with model; $D = 10.5$ inches; $D/d = 3/4$.



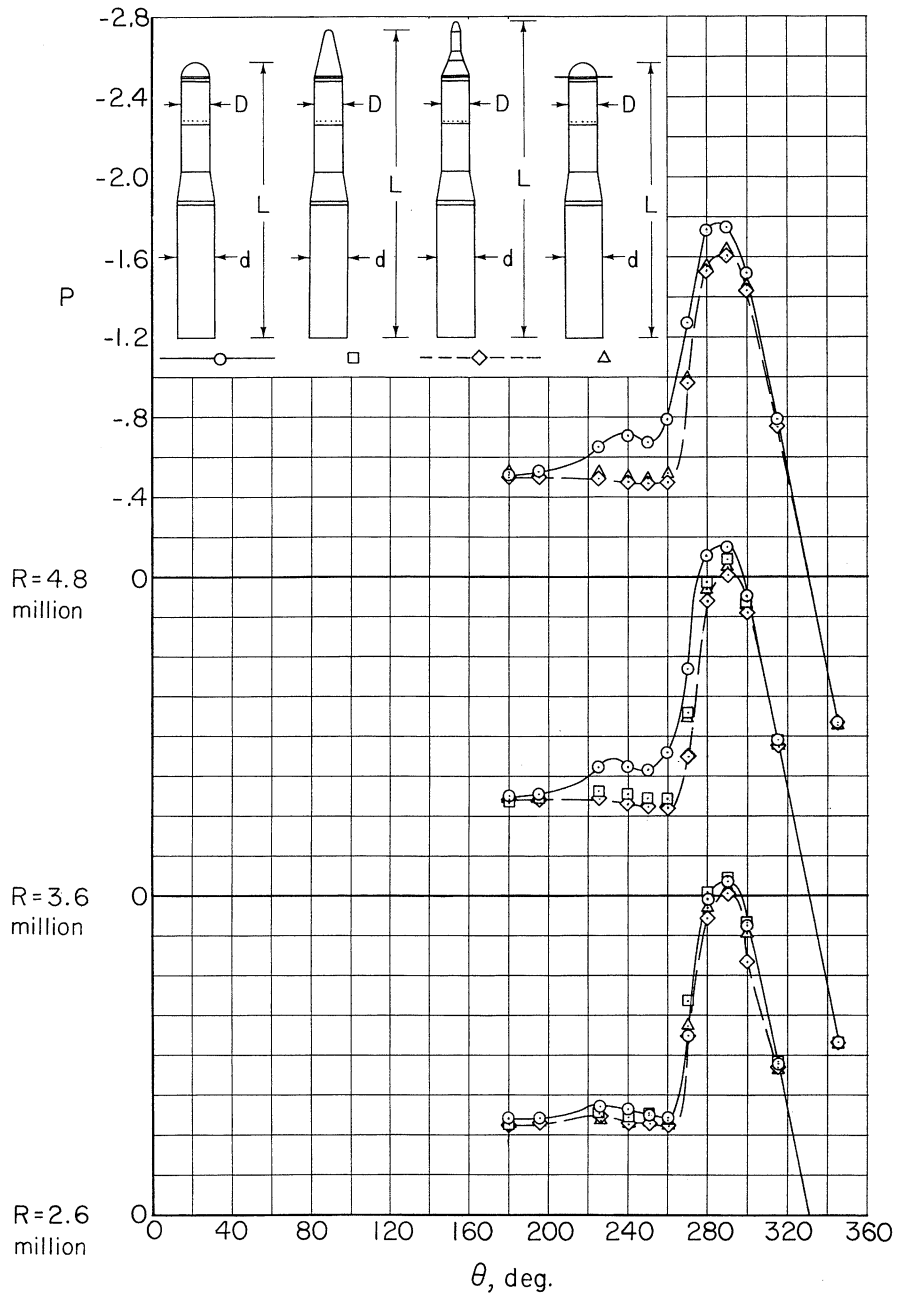
(b) Station C, 6.7 inches below the nose.

Figure 46.- Continued.



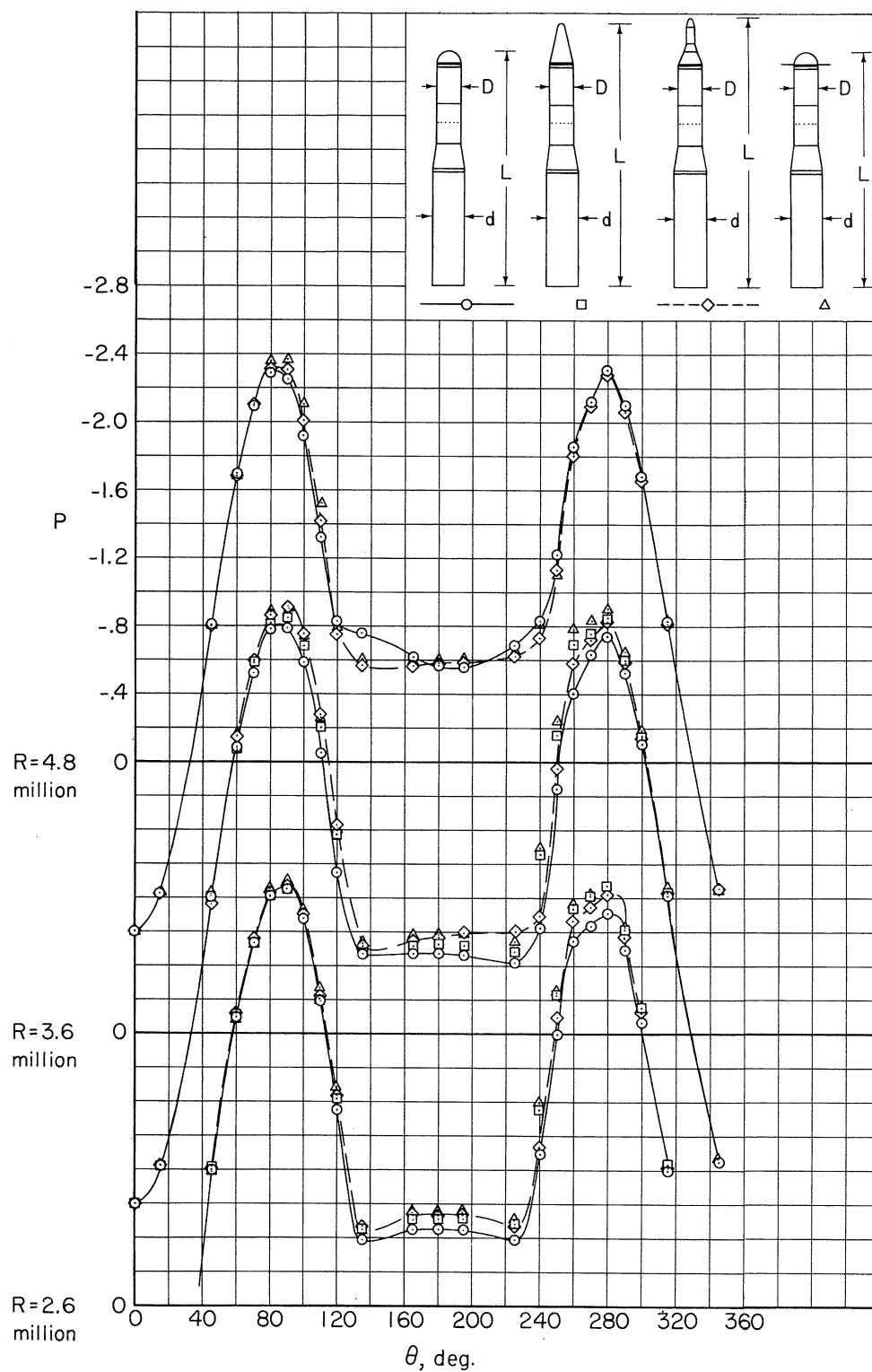
(c) Station D, 10.6 inches below the nose.

Figure 46.- Continued.



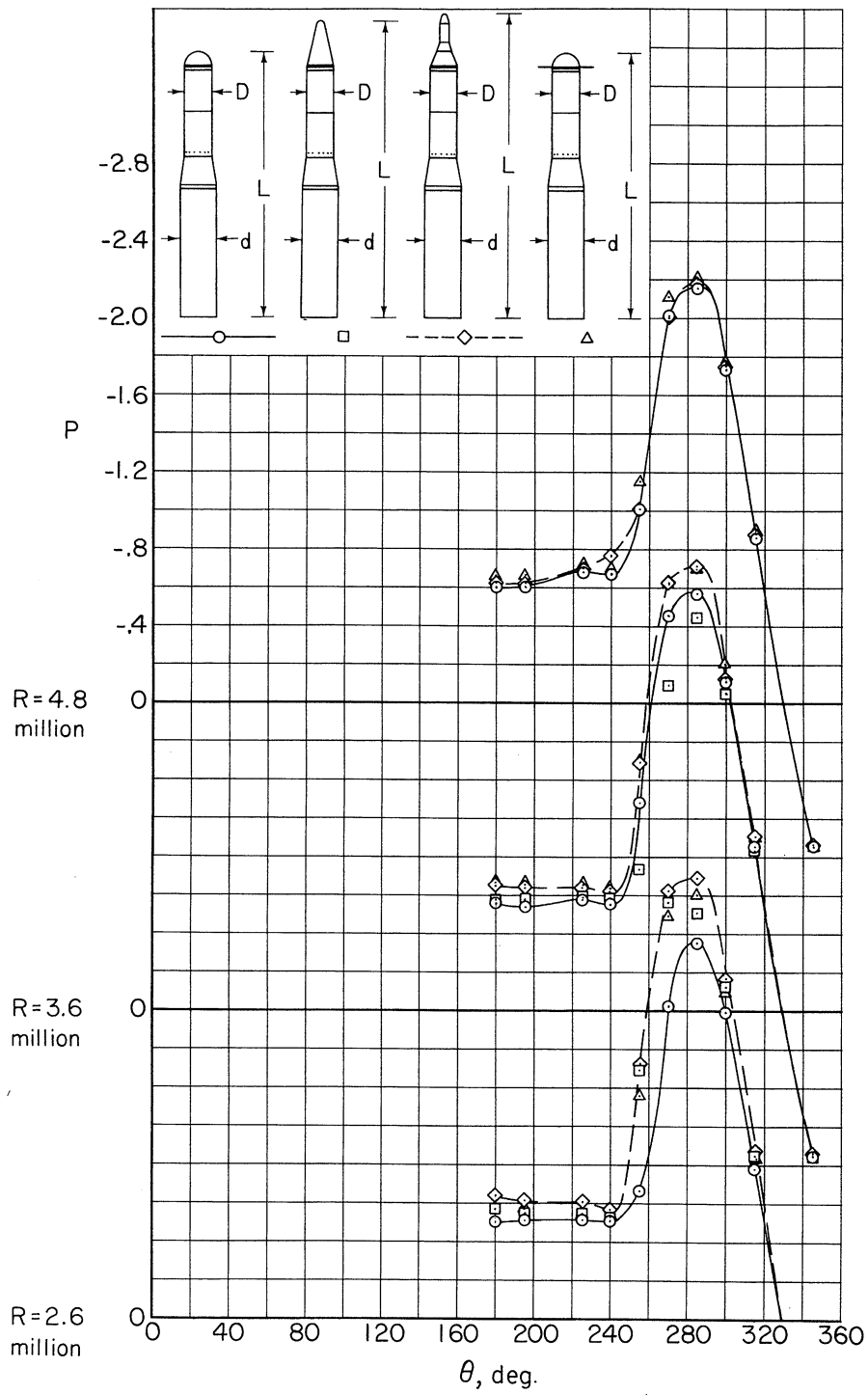
(d) Station E, 18.4 inches below the nose.

Figure 46.- Continued.



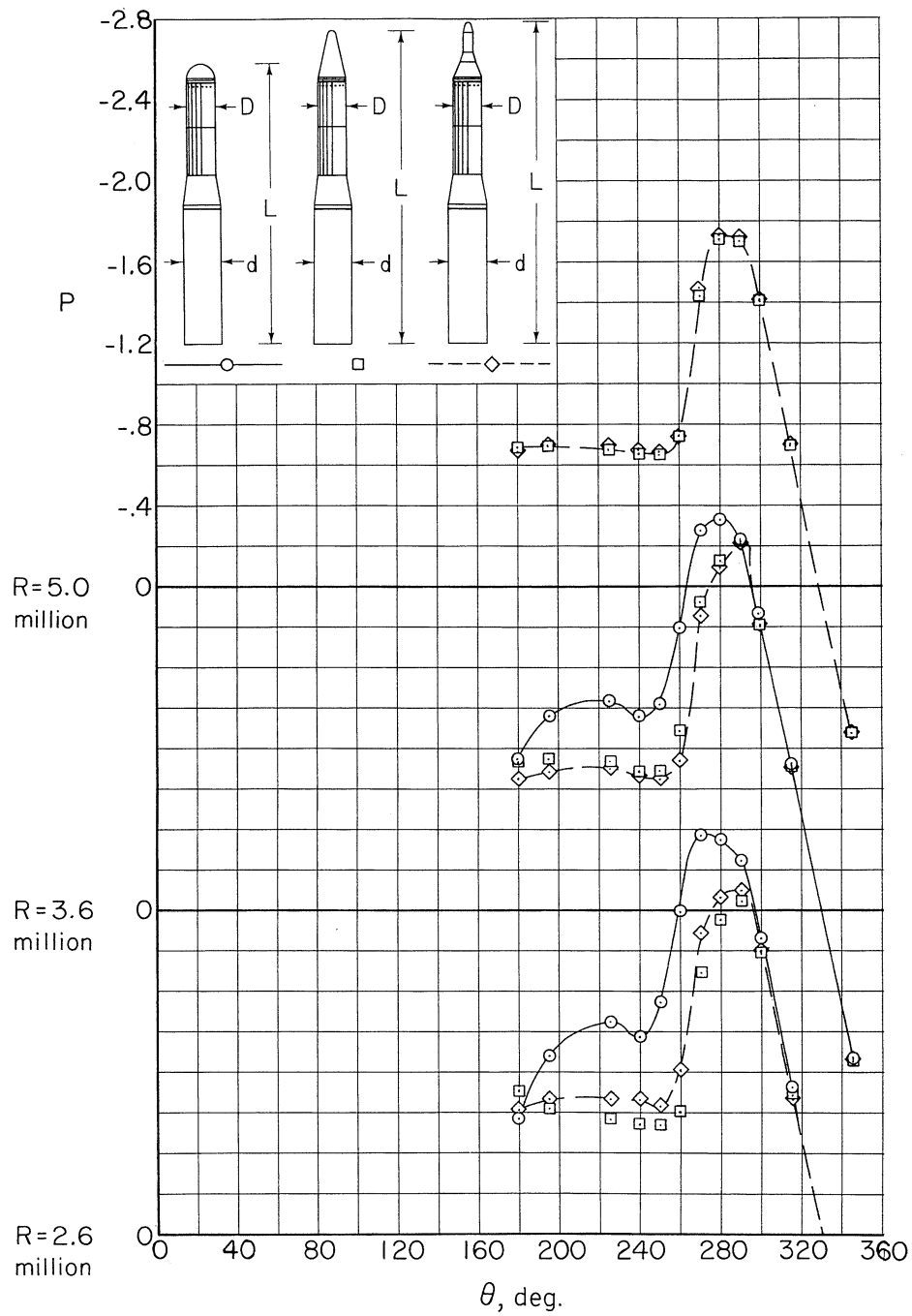
(e) Station G, 28.7 inches below the nose.

Figure 46.- Continued.



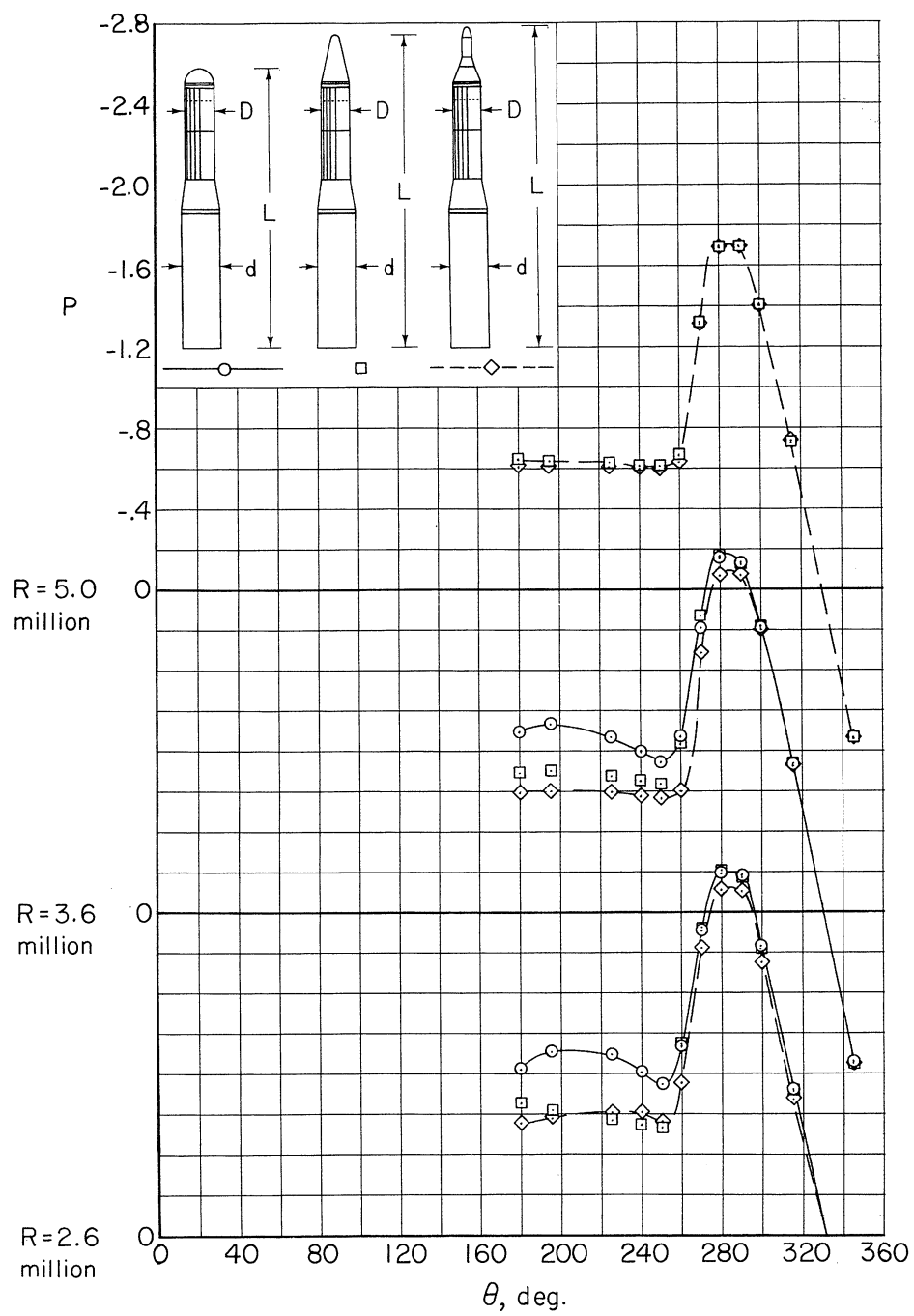
(f) Station H, 37.2 inches below the nose.

Figure 46.- Concluded.



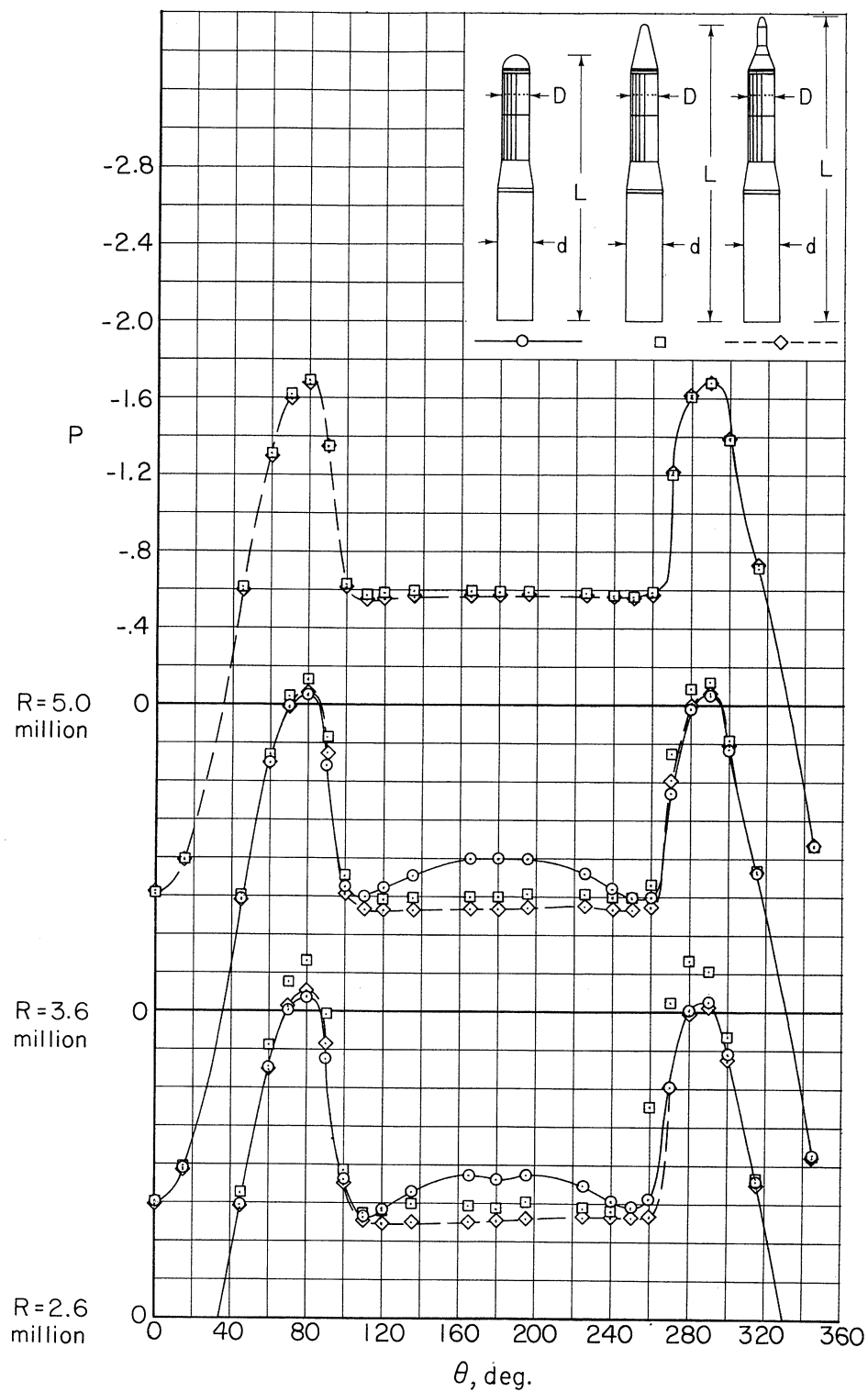
(a) Station B, 2.7 inches below the nose.

Figure 47.- Coefficients of static pressure measured at orifices in the model surface with tapes 0.00029D thick; $D = 10.5$ inches; $D/d = 3/4$.



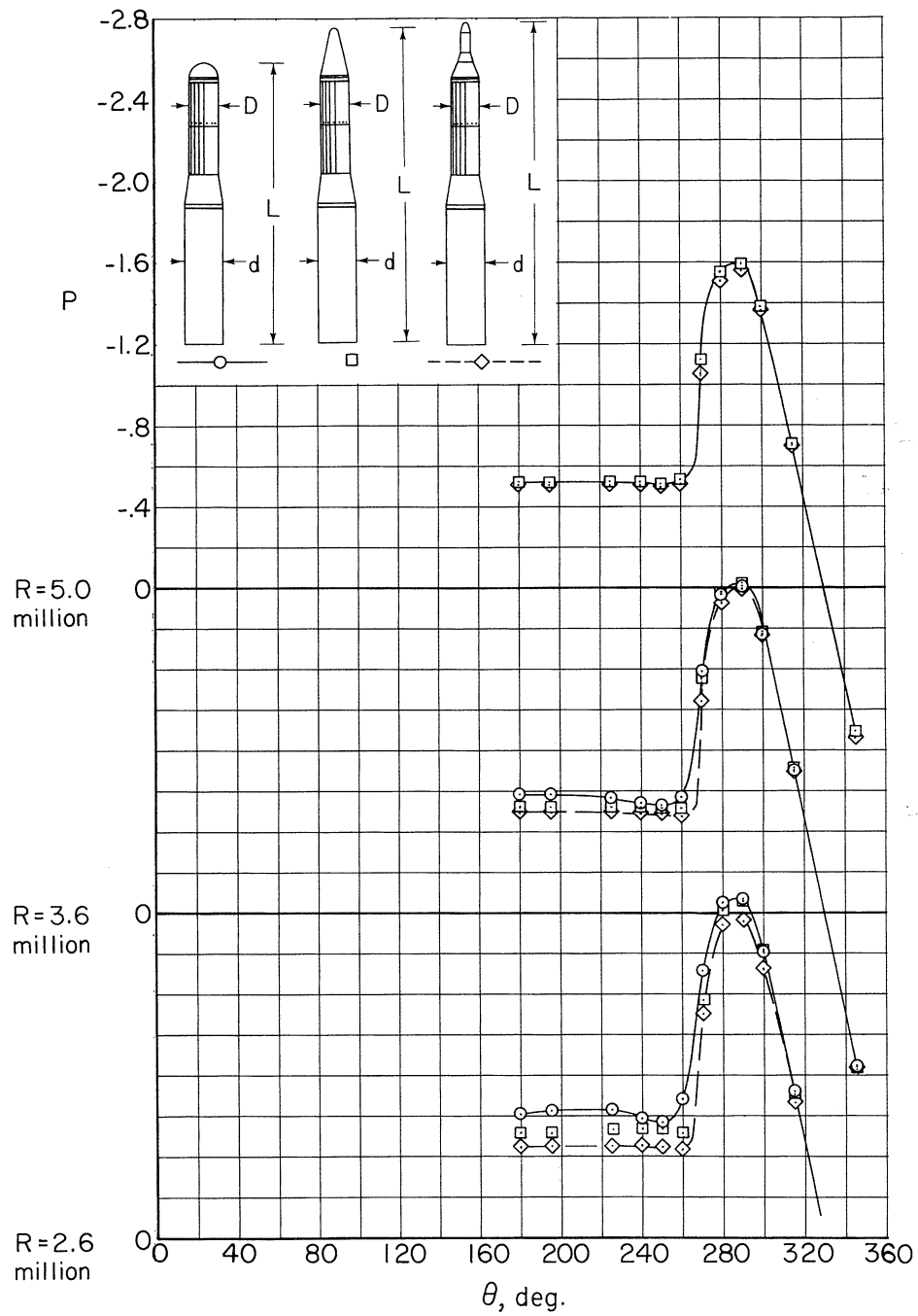
(b) Station C, 6.7 inches below the nose.

Figure 47.- Continued.



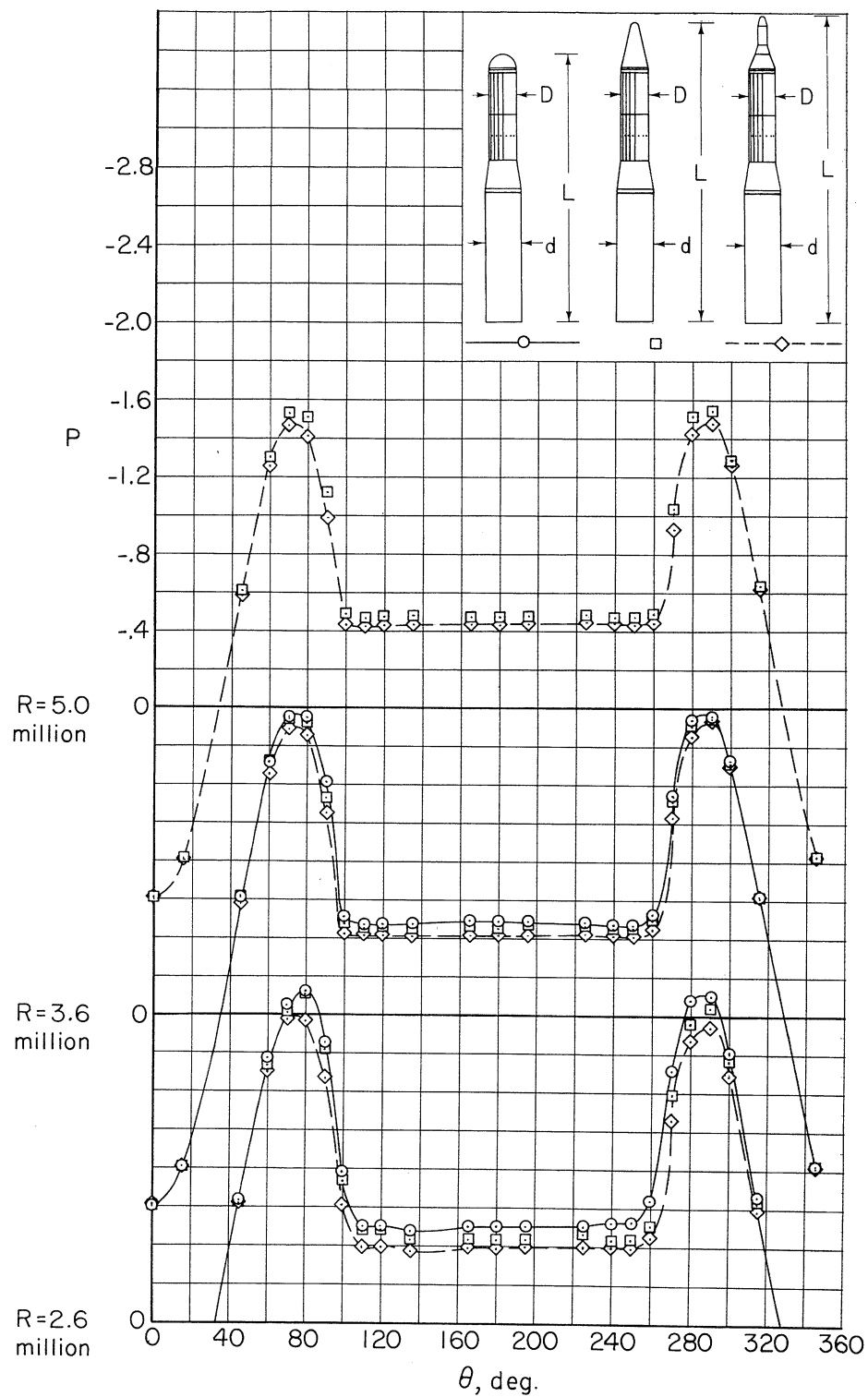
(c) Station D, 10.6 inches below the nose.

Figure 47.- Continued.



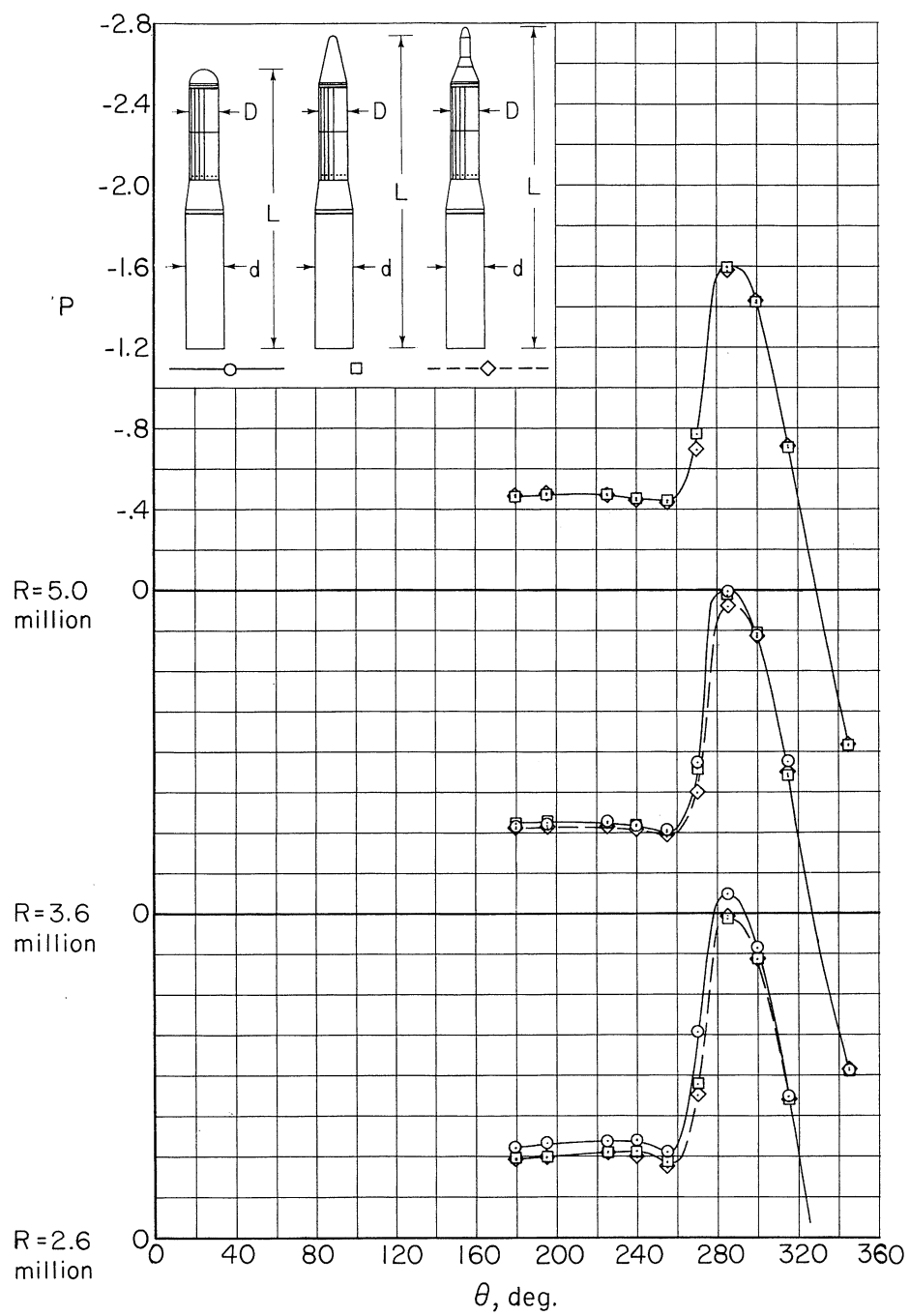
(d) Station E, 18.4 inches below the nose.

Figure 47.- Continued.



(e) Station G, 28.7 inches below the nose.

Figure 47.- Continued.



(f) Station H, 37.2 inches below the nose.

Figure 47.- Concluded.

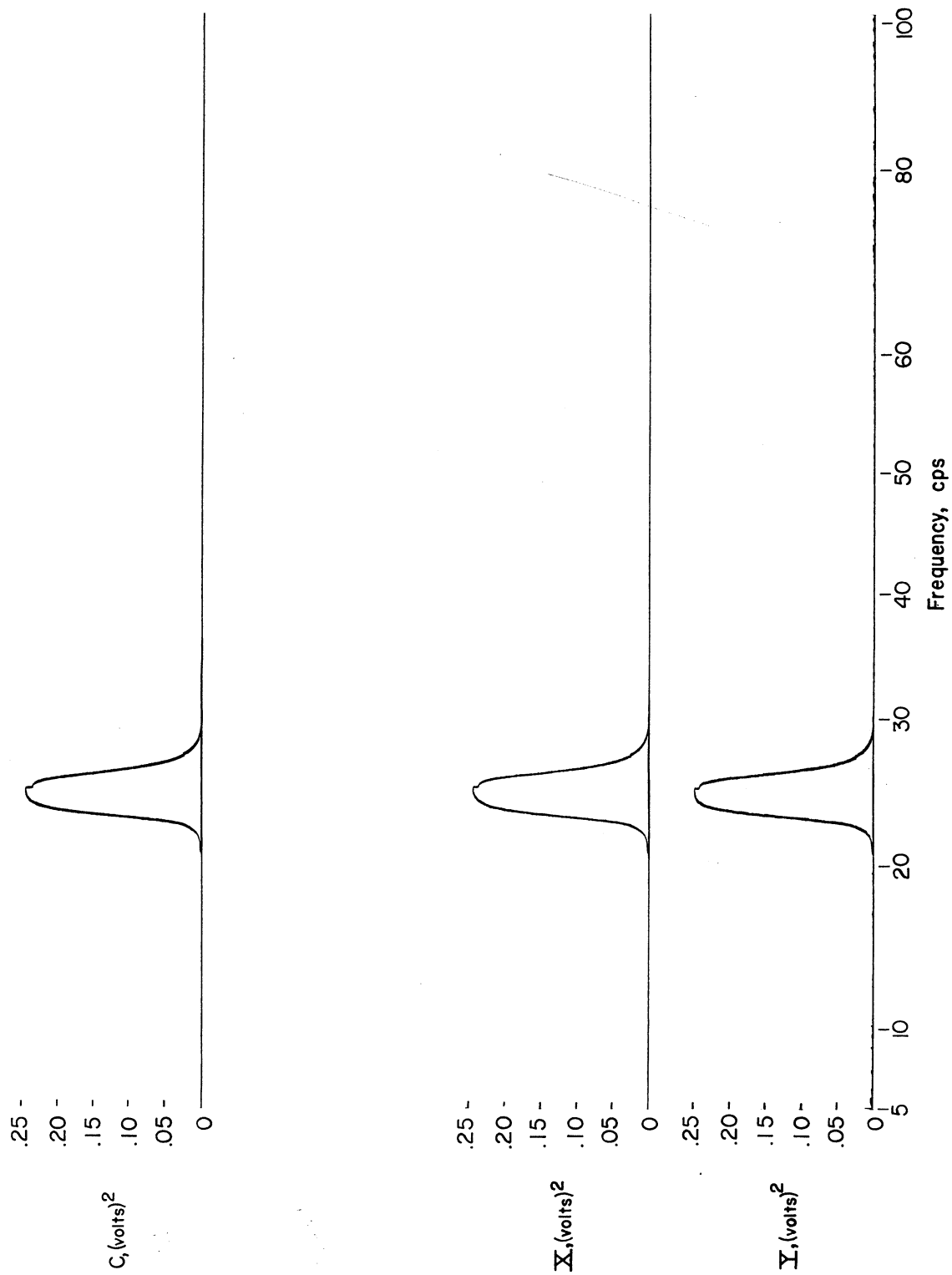
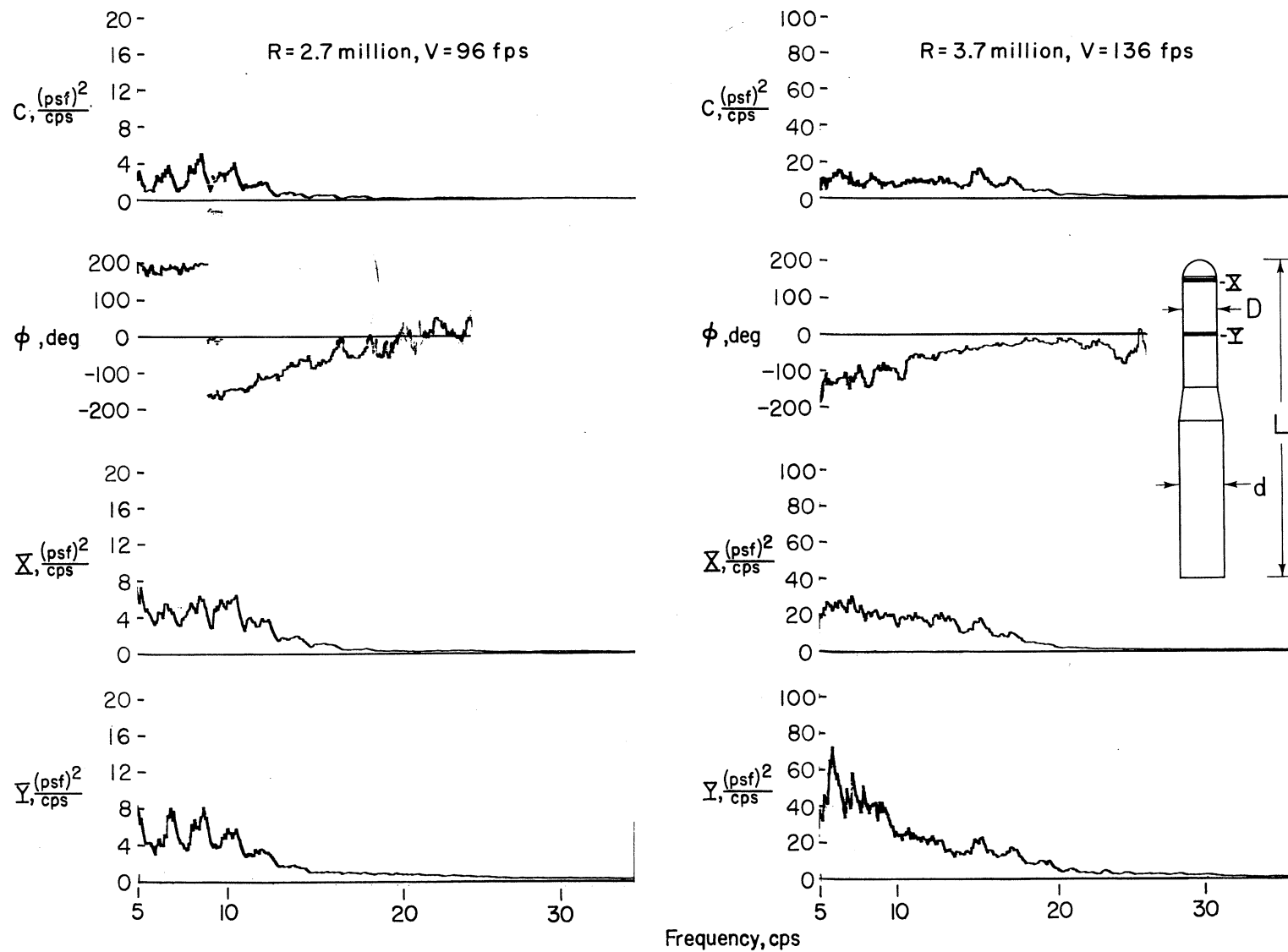
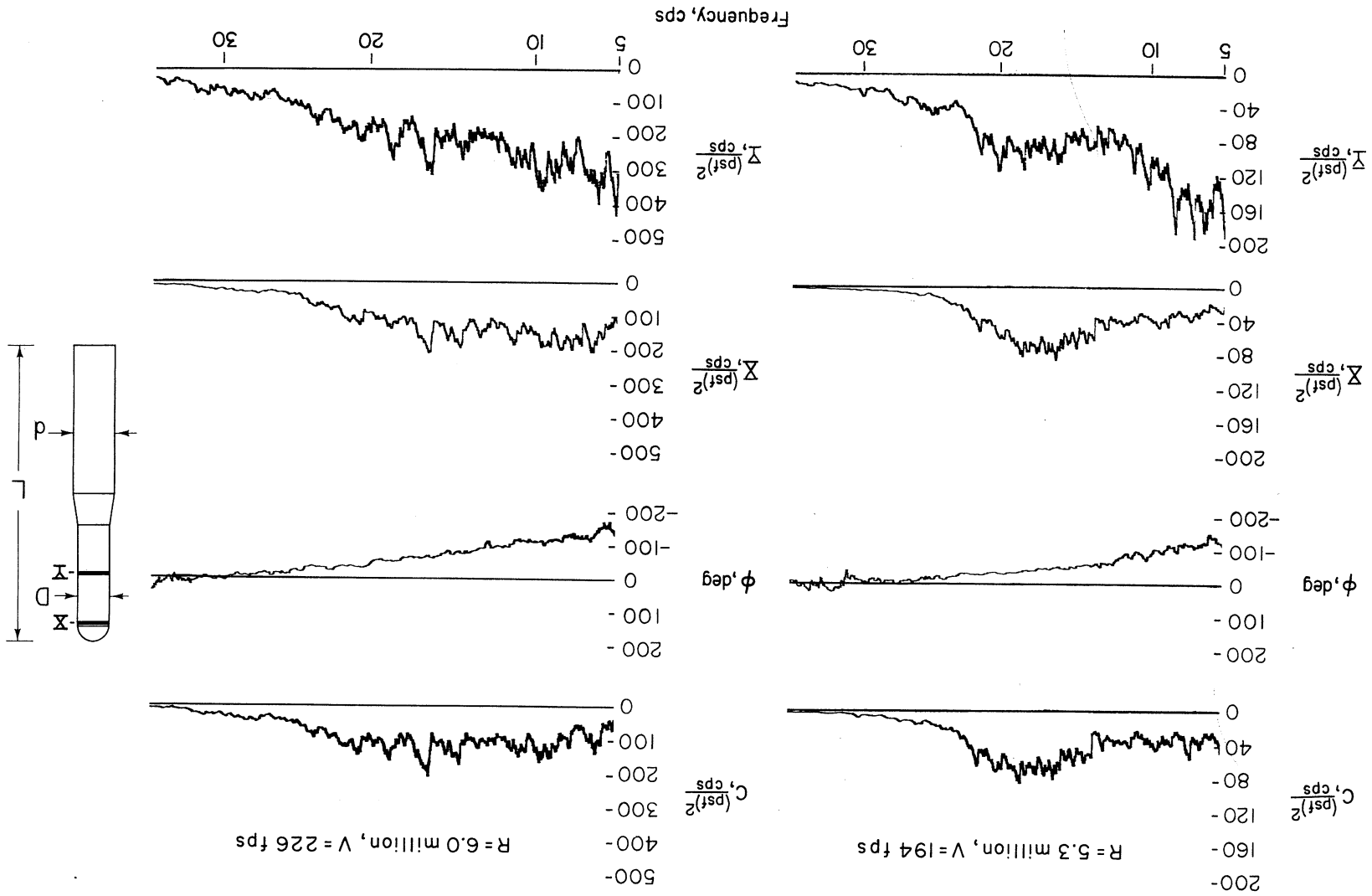


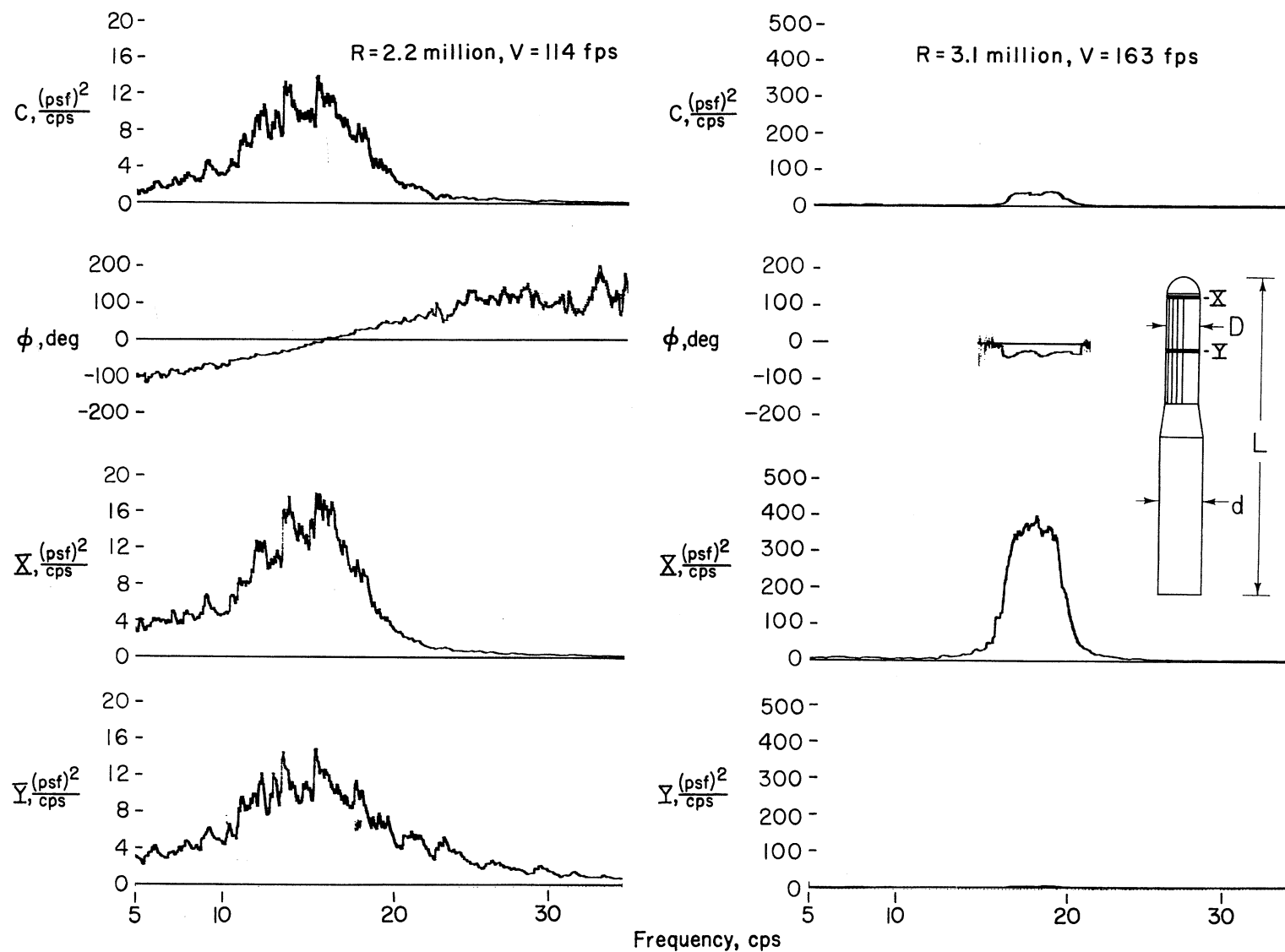
Figure 48.- Power spectra for sinusoidal inputs of 1/2-volt rms at 25 cps.



(a) $R = 2.7$ million; $V = 96$ fps; $R = 3.7$ million; $V = 136$ fps.

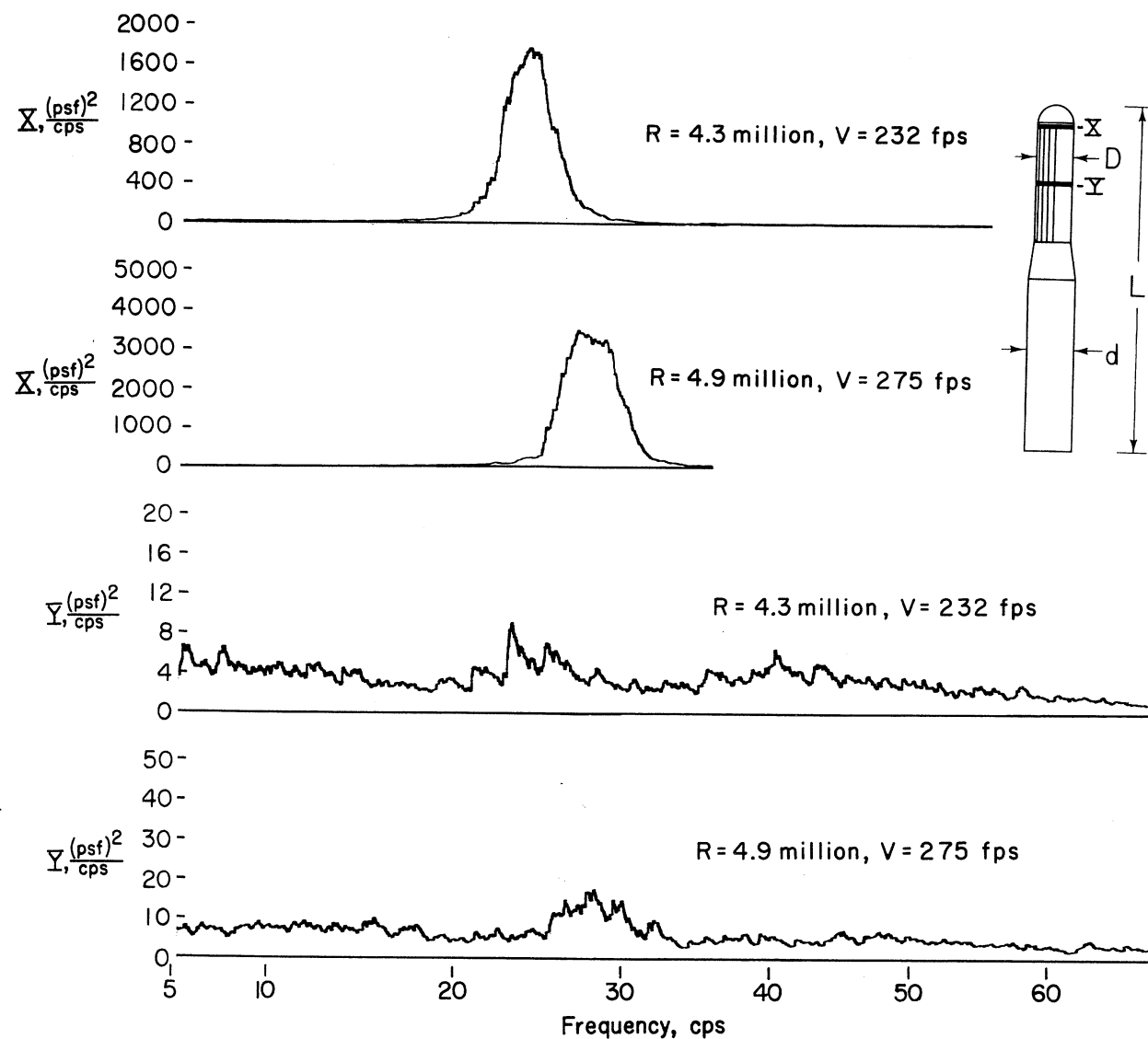
Figure 49.- Power spectra of the lateral-pressure fluctuations at stations A and F (fig. 7) of a model with hemisphere nose; f of model = 23 cps.





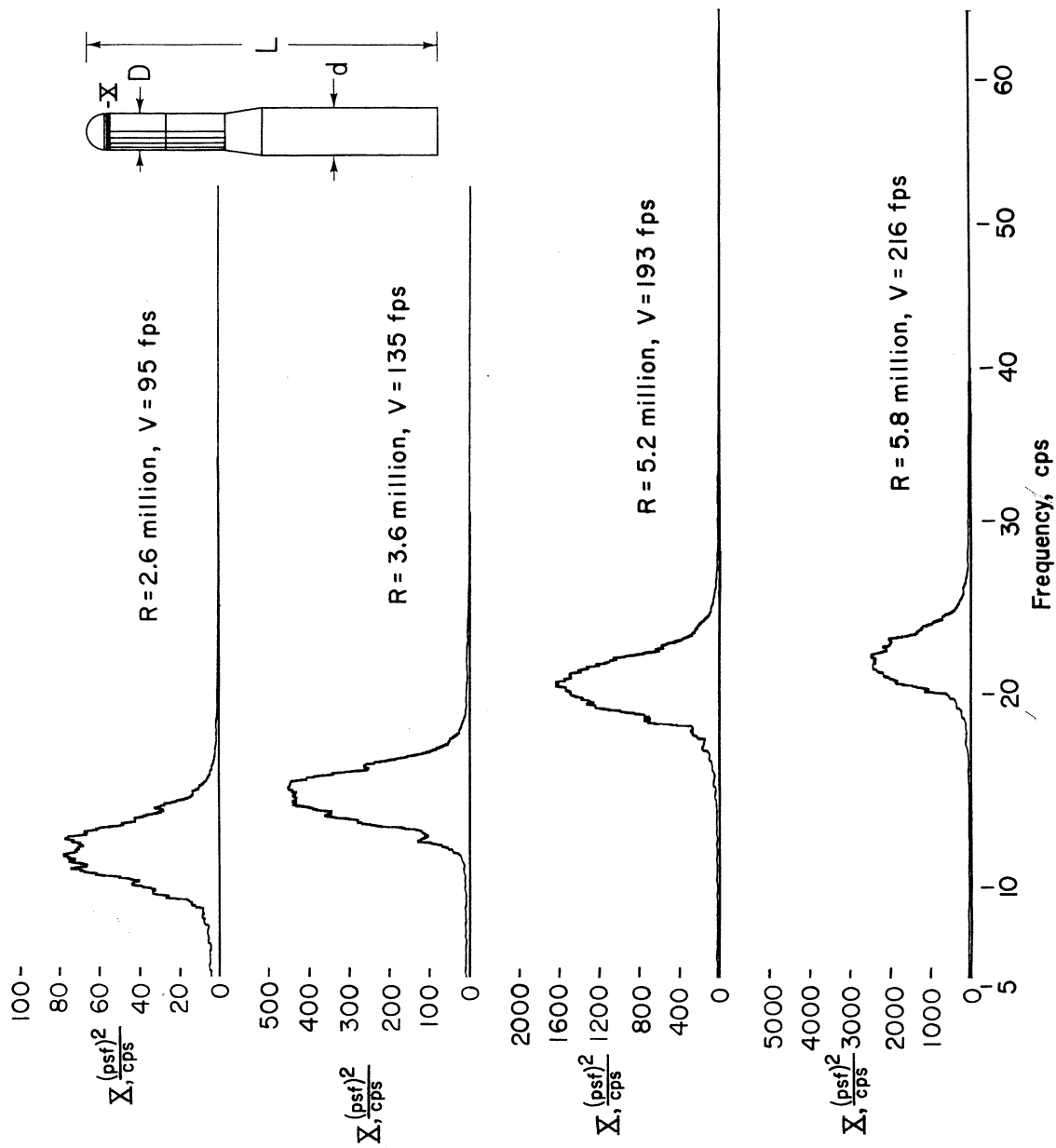
(a) $R = 2.2$ million, $V = 114$ fps; $R = 3.1$ million, $V = 163$ fps.

Figure 50.- Power spectra of the lateral-pressure fluctuations at stations A and F (fig. 7) of a model with hemisphere nose and with tapes 0.00029D thick; f of model = 23 cps.



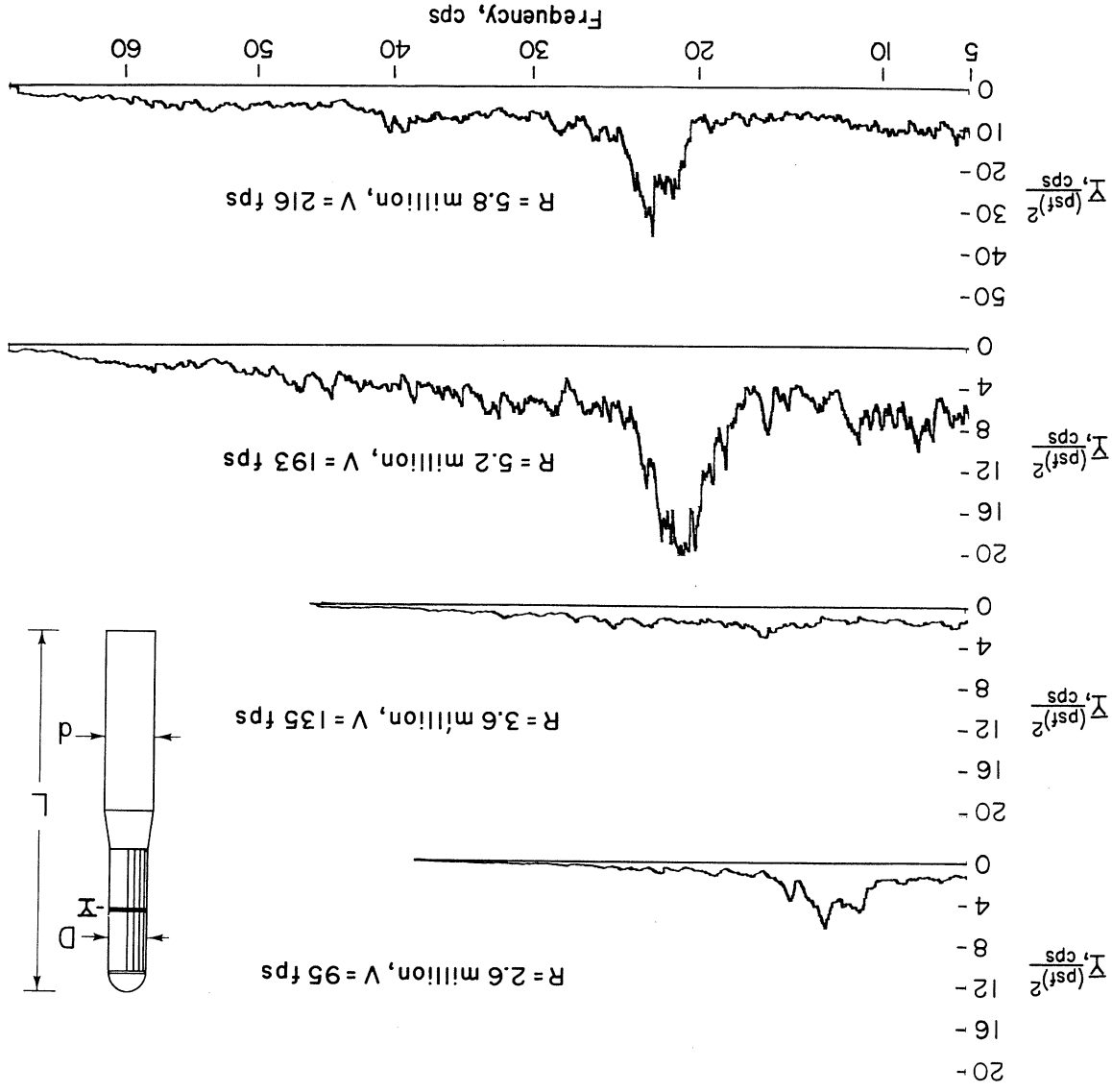
(b) $R = 4.3$ million, $V = 232$ fps; $R = 4.9$ million, $V = 275$ fps.

Figure 50.- Concluded.

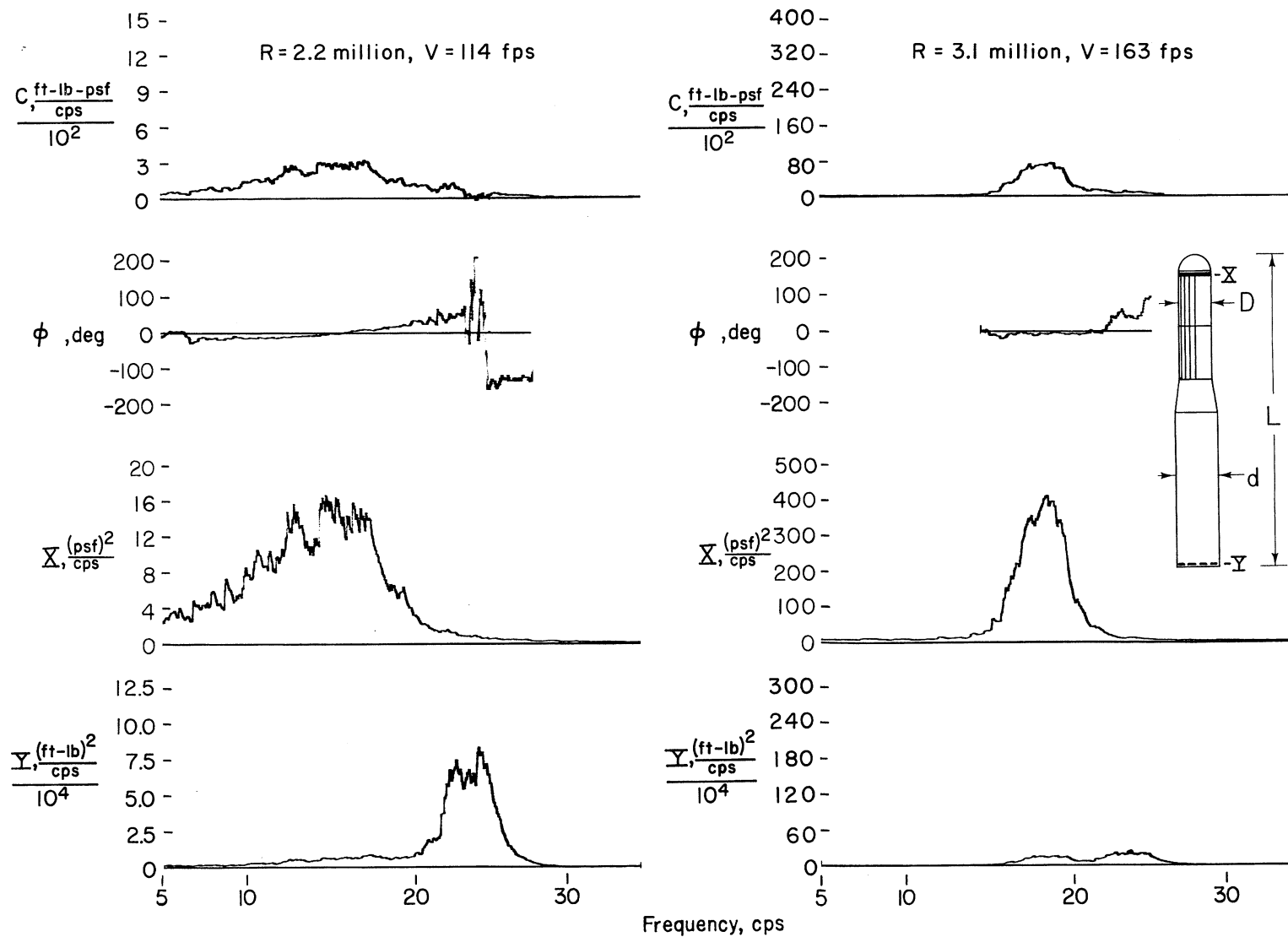


(a) Station A.

Figure 51.- Power spectra of the lateral-pressure fluctuations of a model (fig. 7) with hemisphere nose and with tapes 0.00029D thick; \$f\$ of model = 23 cps.

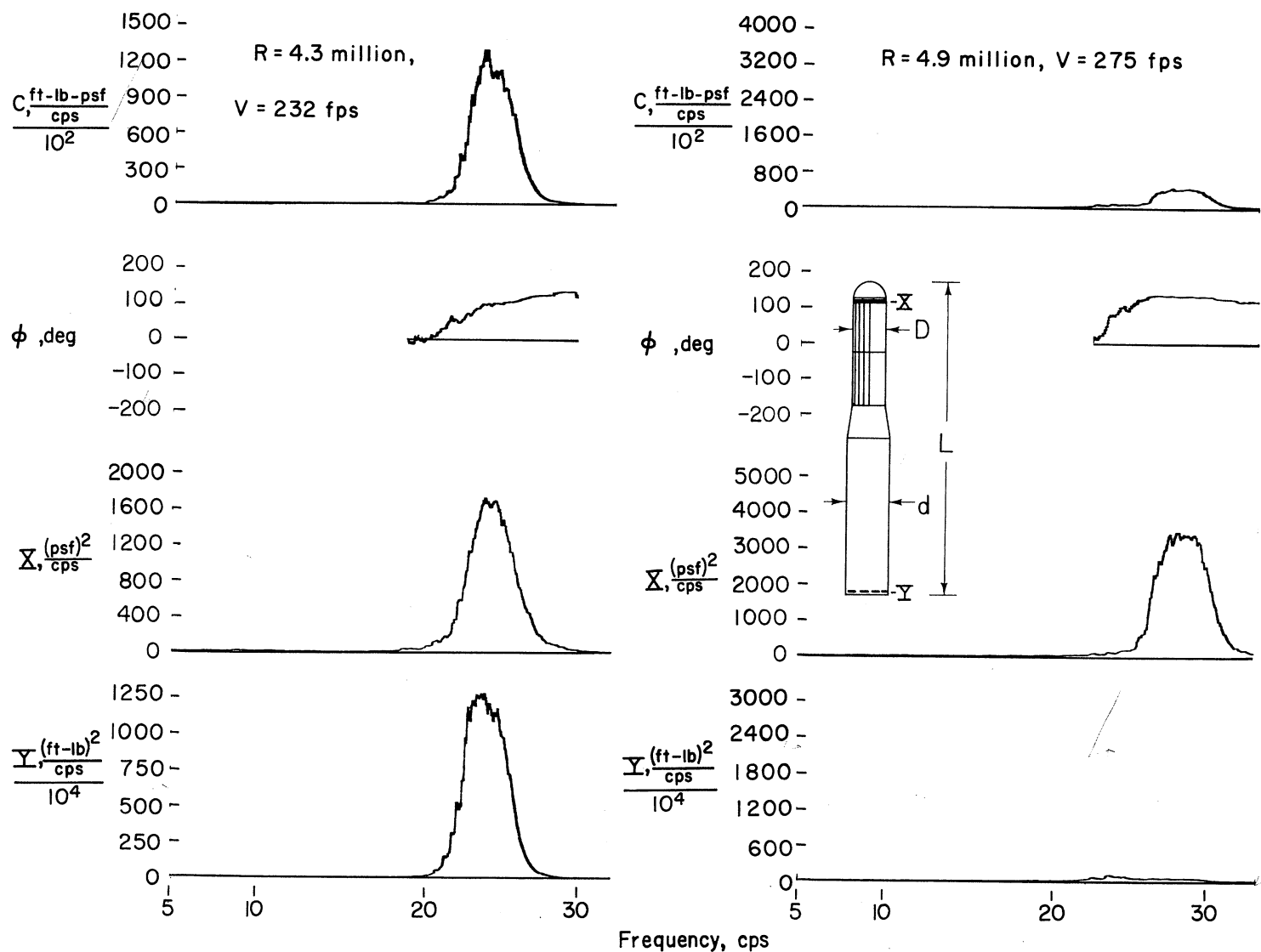


(b) Station F.
Figure 51. - Concluded.



(a) $R = 2.2$ million, $V = 114$ fps; $R = 3.1$ million, $V = 163$ fps.

Figure 52.- Power spectra of the lateral-pressure fluctuations at station A (fig. 7) and lateral bending-moment response of a model with hemisphere nose and with tapes 0.00029D thick; f of model = 23 cps.



(b) $R = 4.3$ million, $V = 232$ fps; $R = 4.9$ million, $V = 275$ fps.

Figure 52.- Concluded.

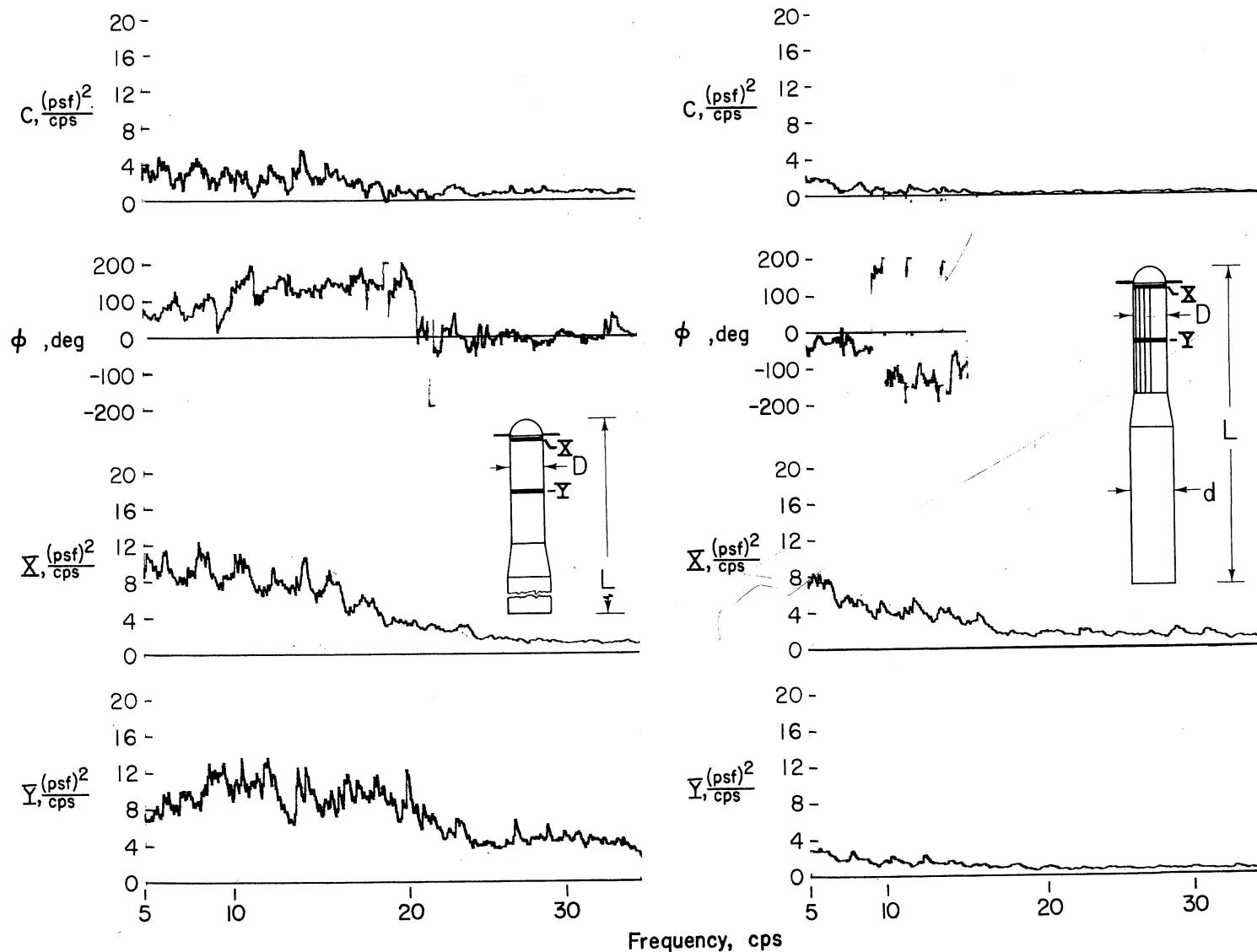


Figure 53.- Power spectra of the lateral-pressure fluctuations at stations A and F (fig. 7) of a model with hemisphere nose and a plate beneath the nose, with and without tapes 0.00029D thick; plate diameter, 2D, concentric with model; f of model = 23 cps; $R = 5.1$ million, $V = 194$ fps.

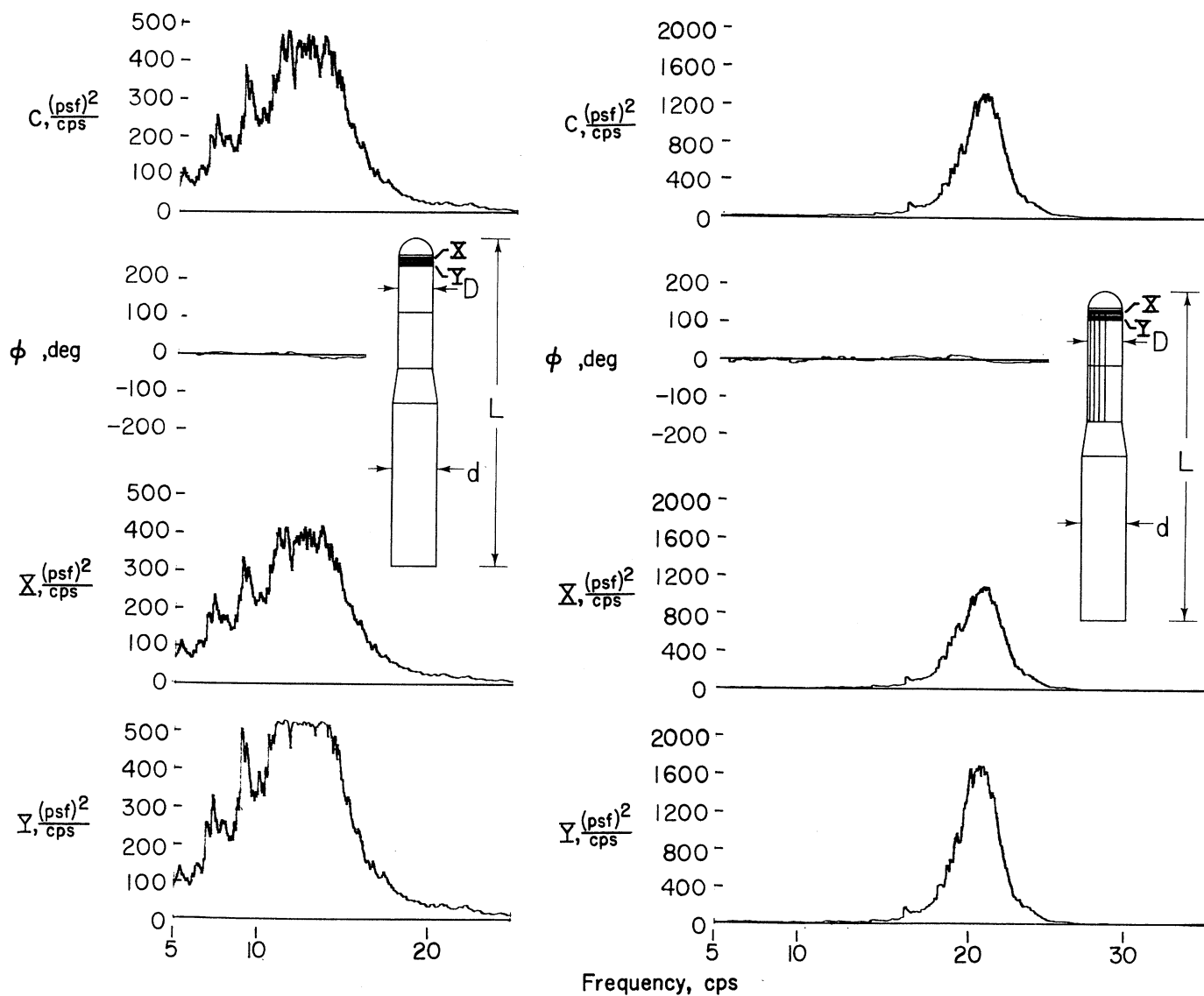


Figure 54.- Power spectra of the lateral-pressure fluctuations at and just beneath station A (fig. 7) of a model with hemisphere nose, with f of model = 23 cps; $R = 5.0$ million; $V = 193$ fps.

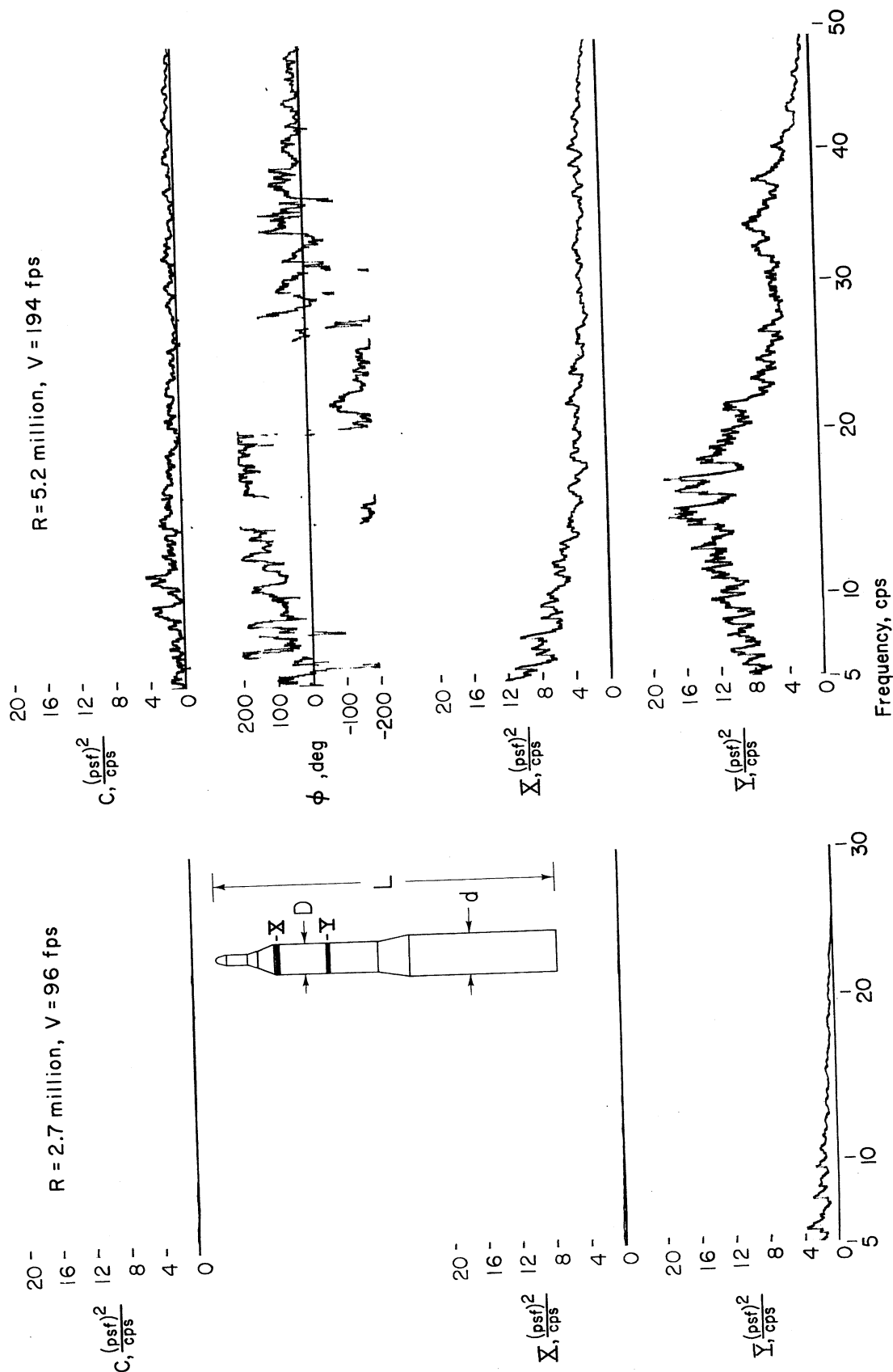


Figure 55.- Power spectra of the lateral-pressure fluctuations at stations A and F (fig. 7) of a model with cone-cylinder nose; f of model = 22 cps.

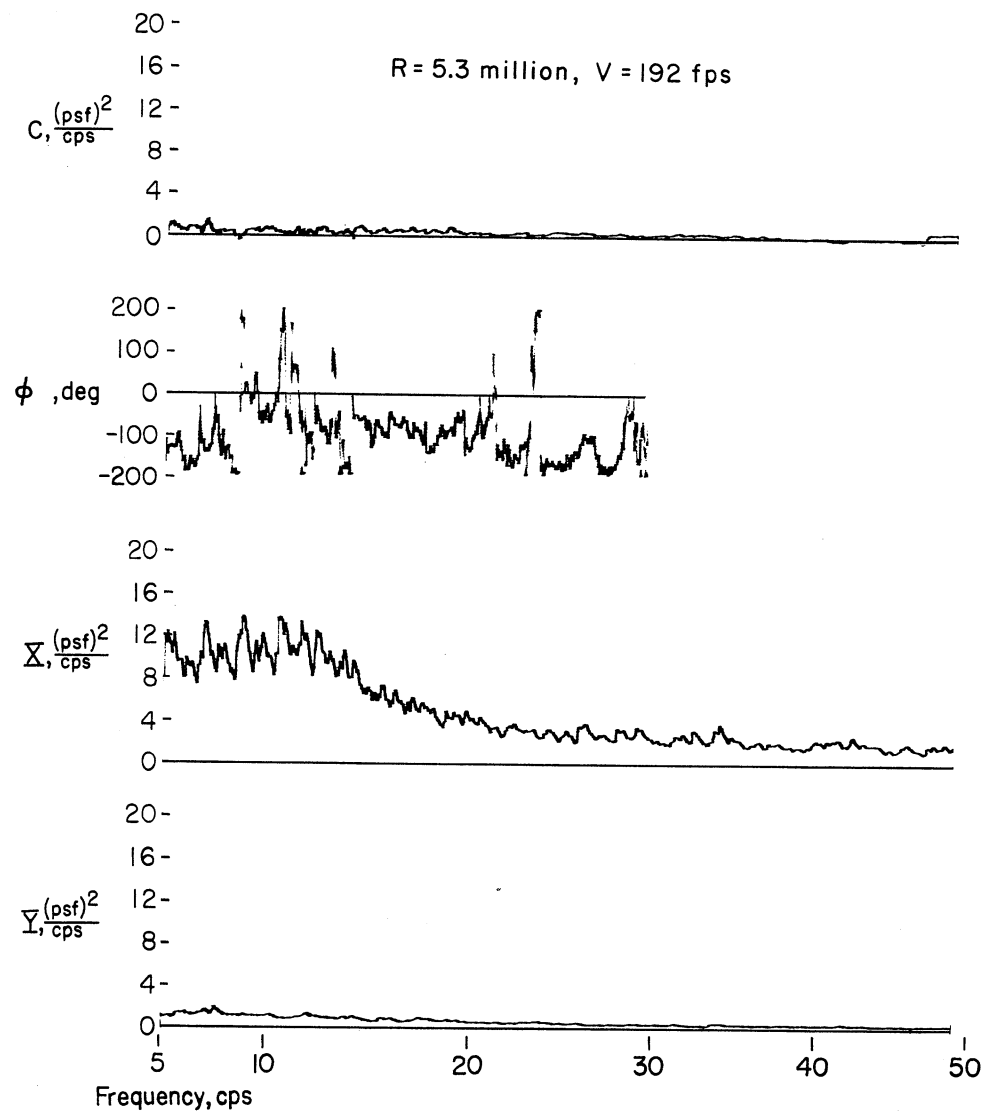
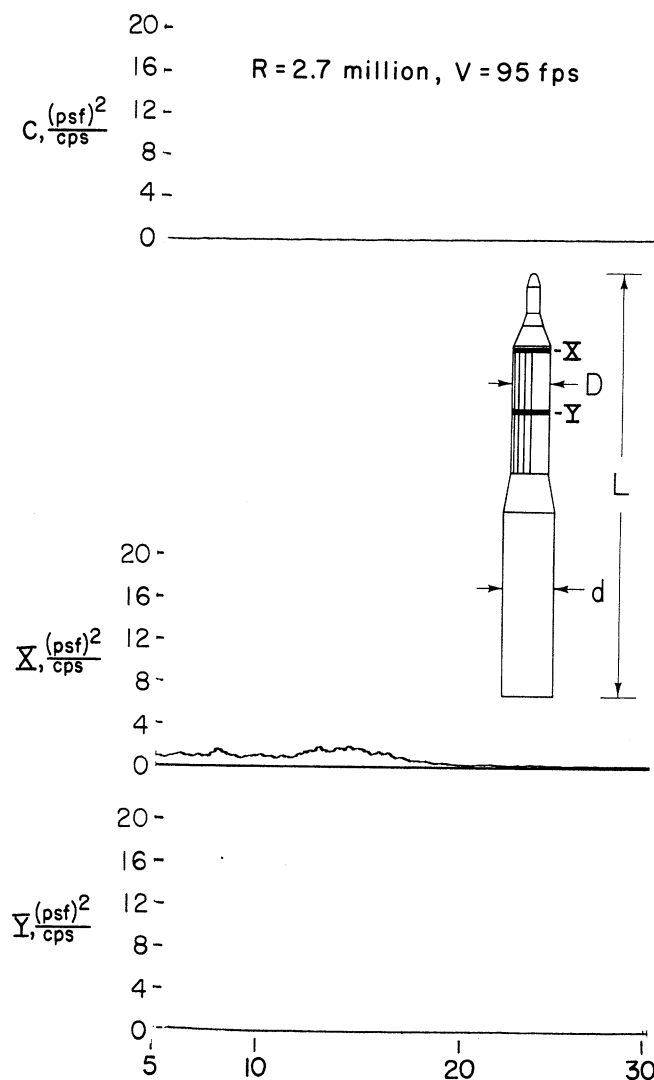
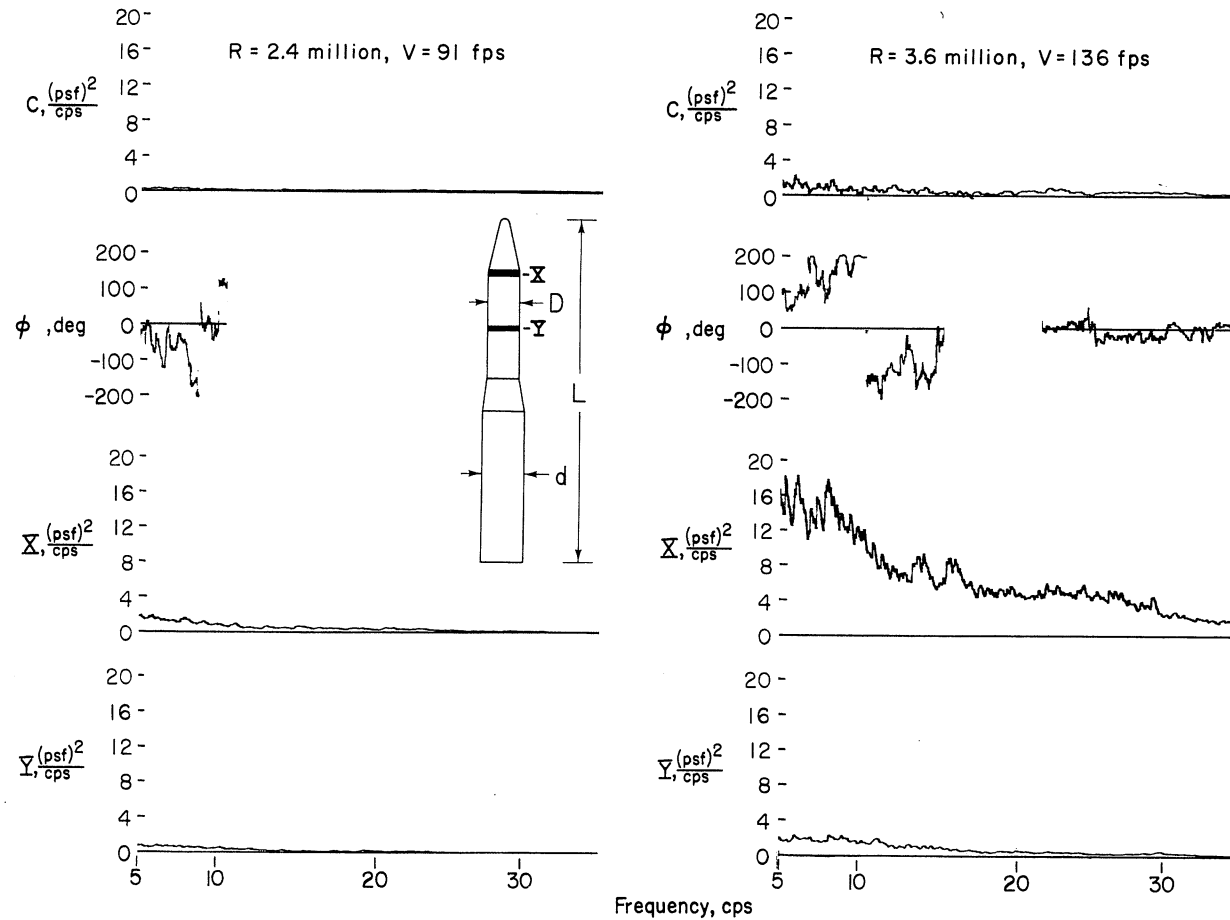
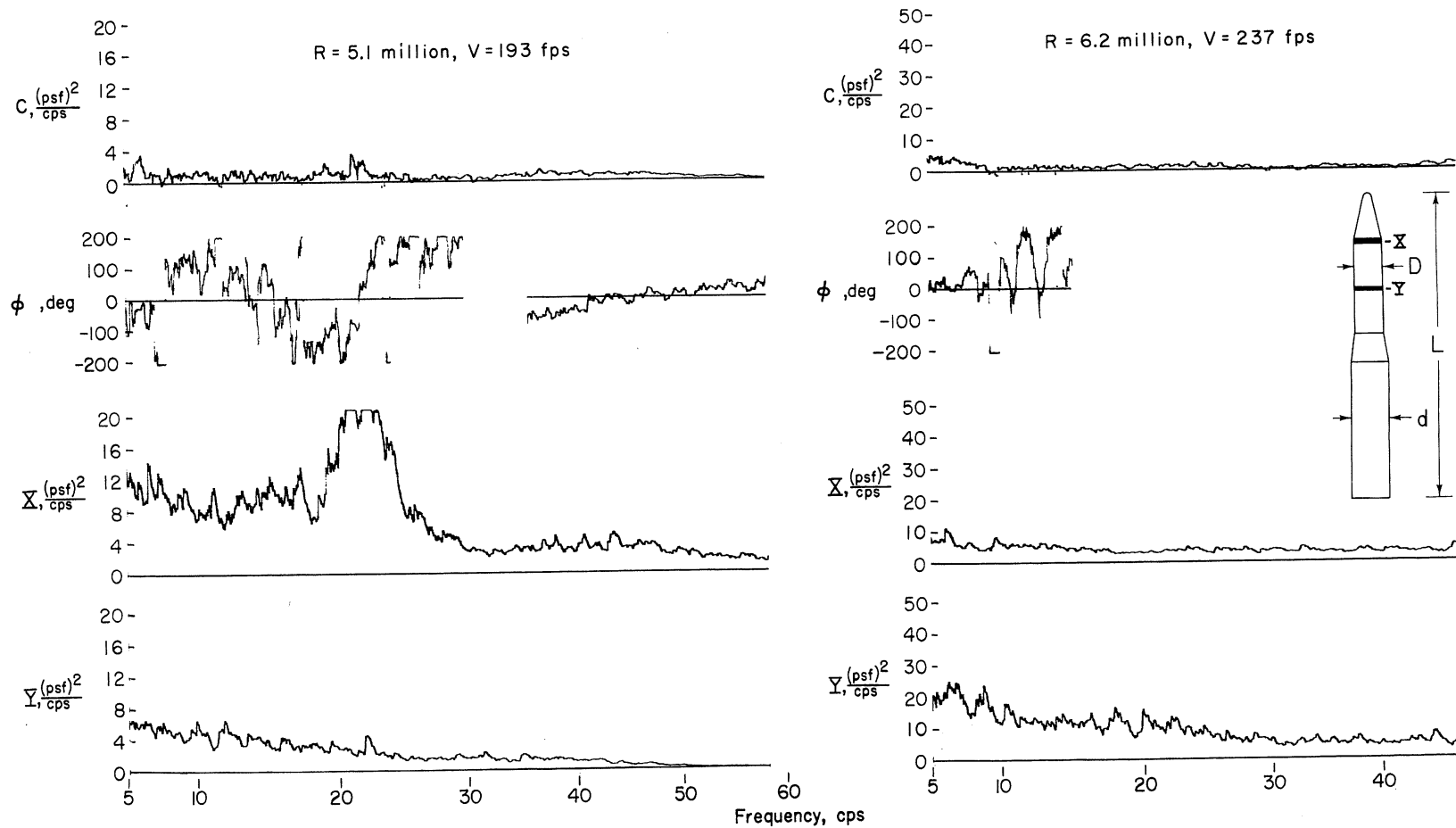


Figure 56.- Power spectra of the lateral-pressure fluctuations at stations A and F (fig. 7) of a model with cone-cylinder nose and with tapes 0.00029D thick; f of model = 22 cps.



(a) $R = 2.4$ million, $V = 91$ fps; $R = 3.6$ million, $V = 136$ fps.

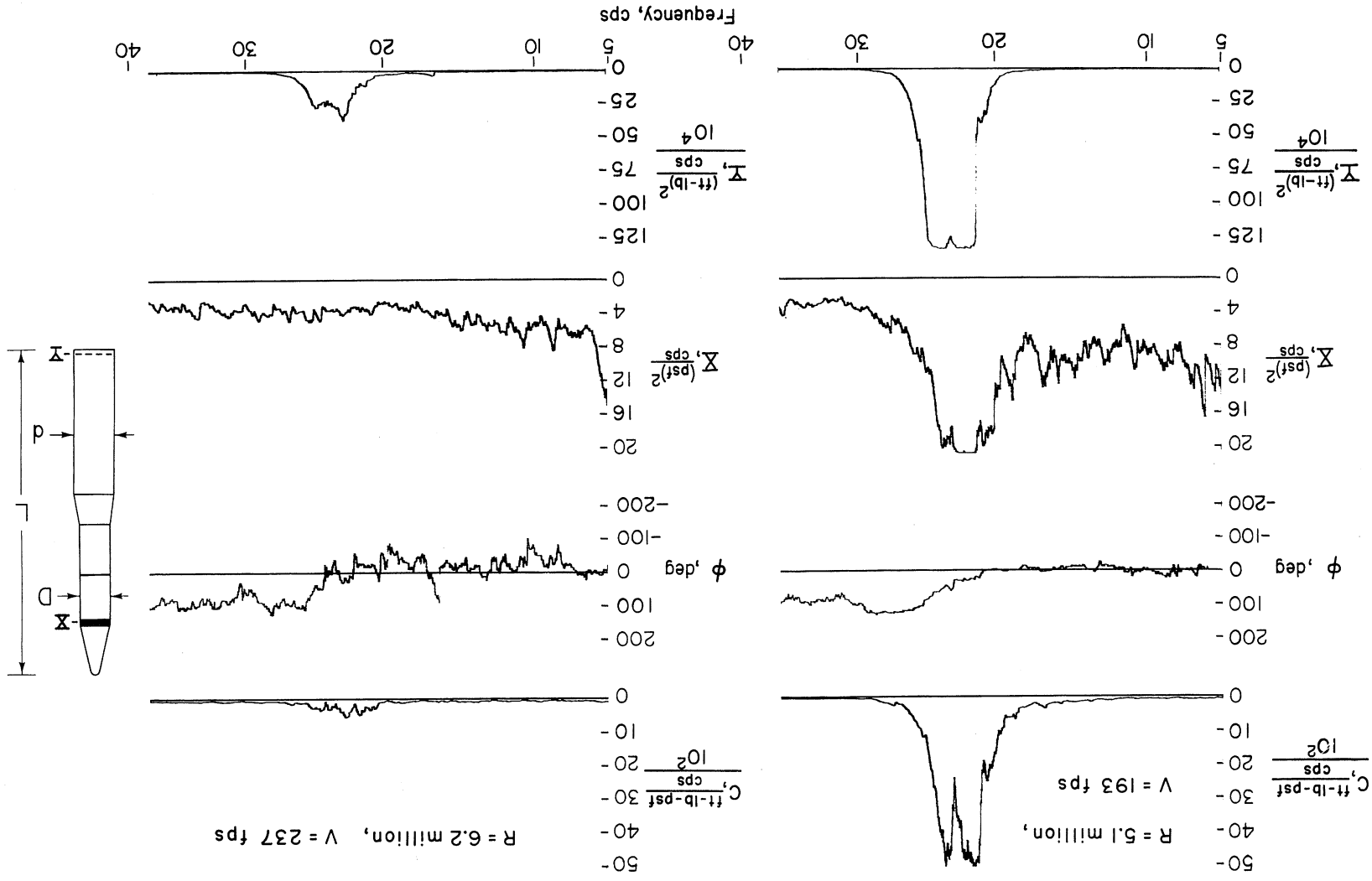
Figure 57.- Power spectra of the lateral-pressure fluctuations at stations A and F (fig. 7) of a model with blunted-cone nose; f of model = 23 cps.

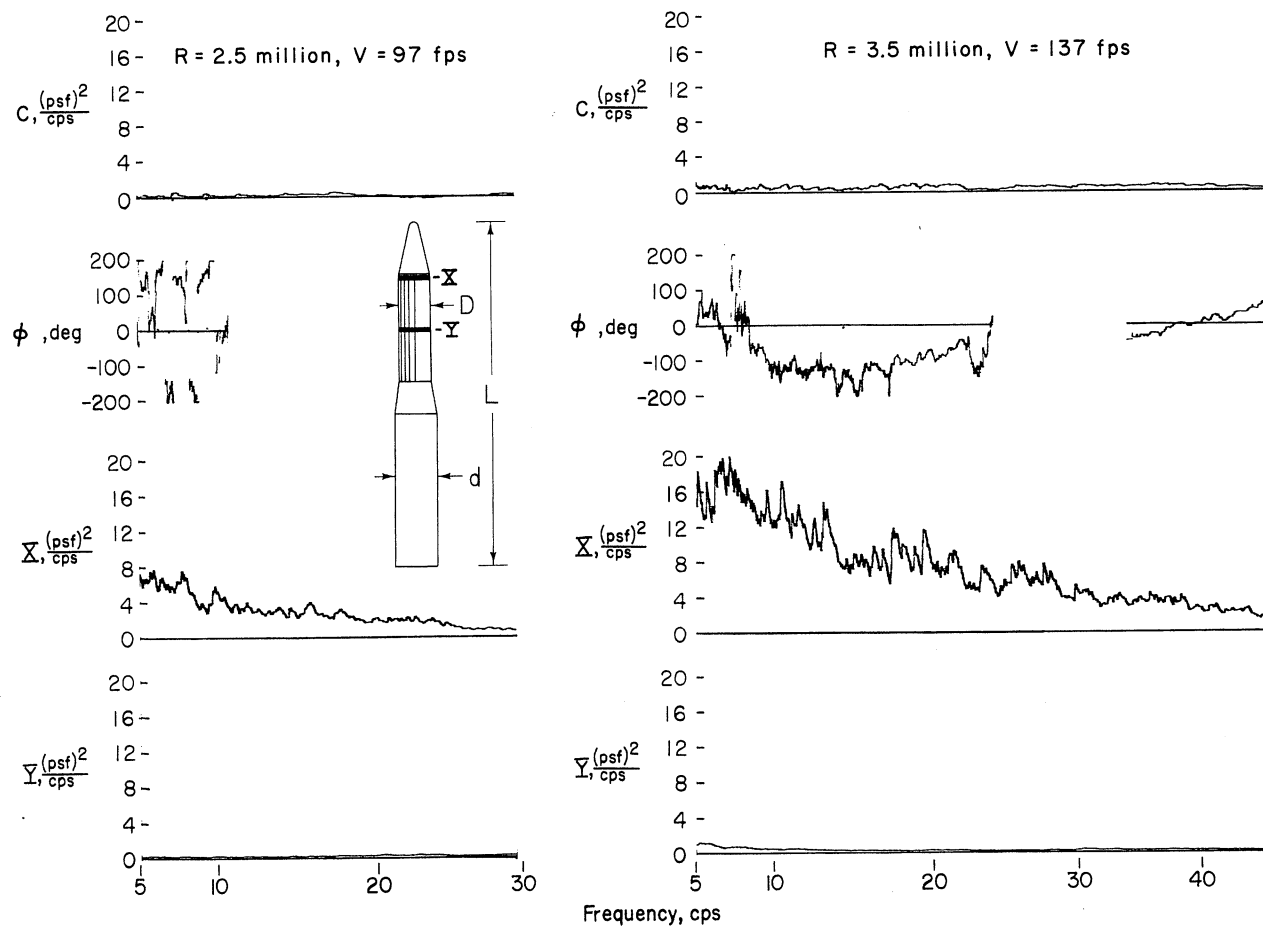


(b) $R = 5.1$ million, $V = 193$ fps; $R = 6.2$ million, $V = 237$ fps.

Figure 57.- Concluded.

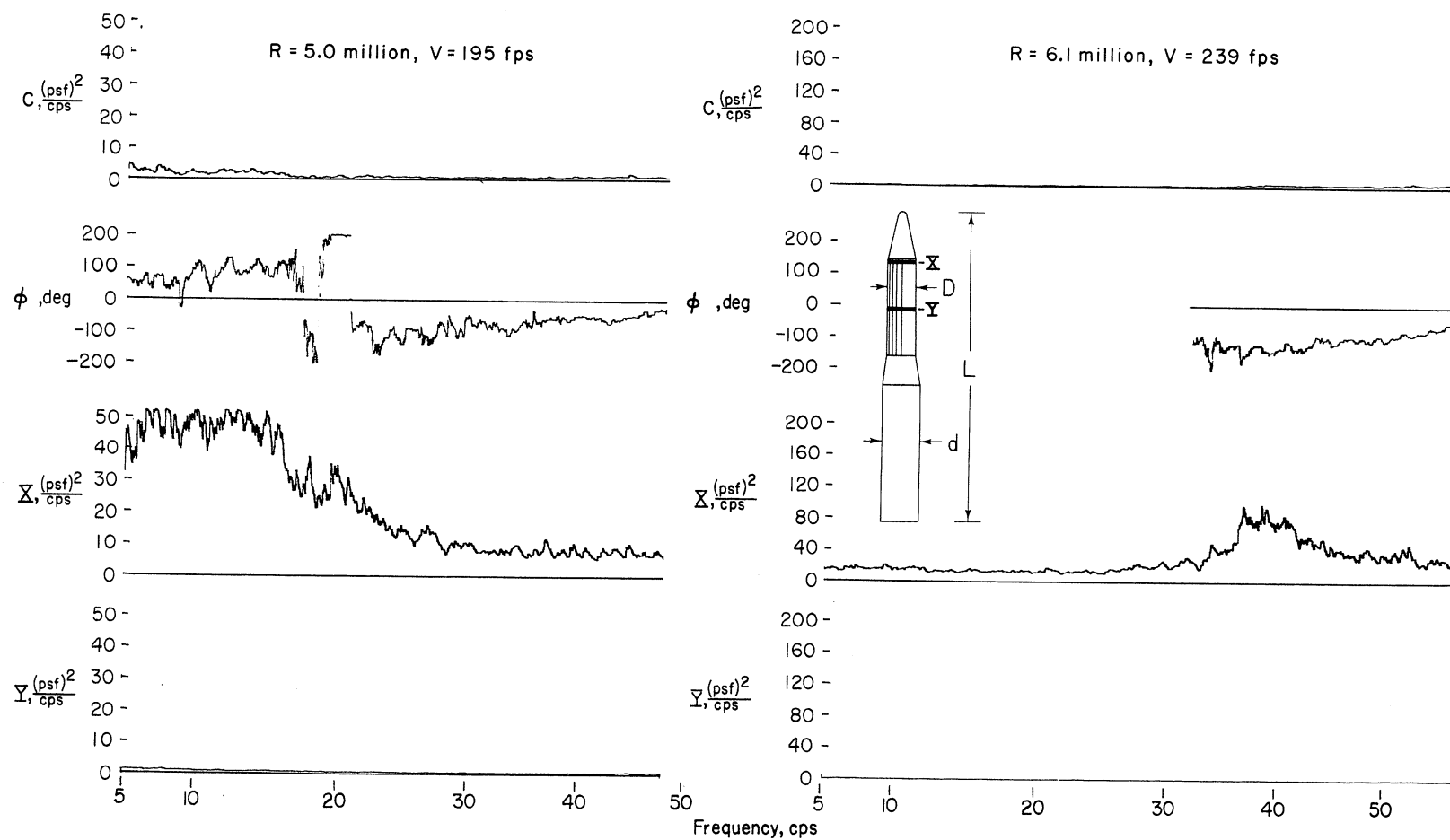
Figure 58. - Power spectra of the lateral-pressure fluctuations at station A (fig. 7) and lateral bending-moment response of a model with blunted-cone nose.





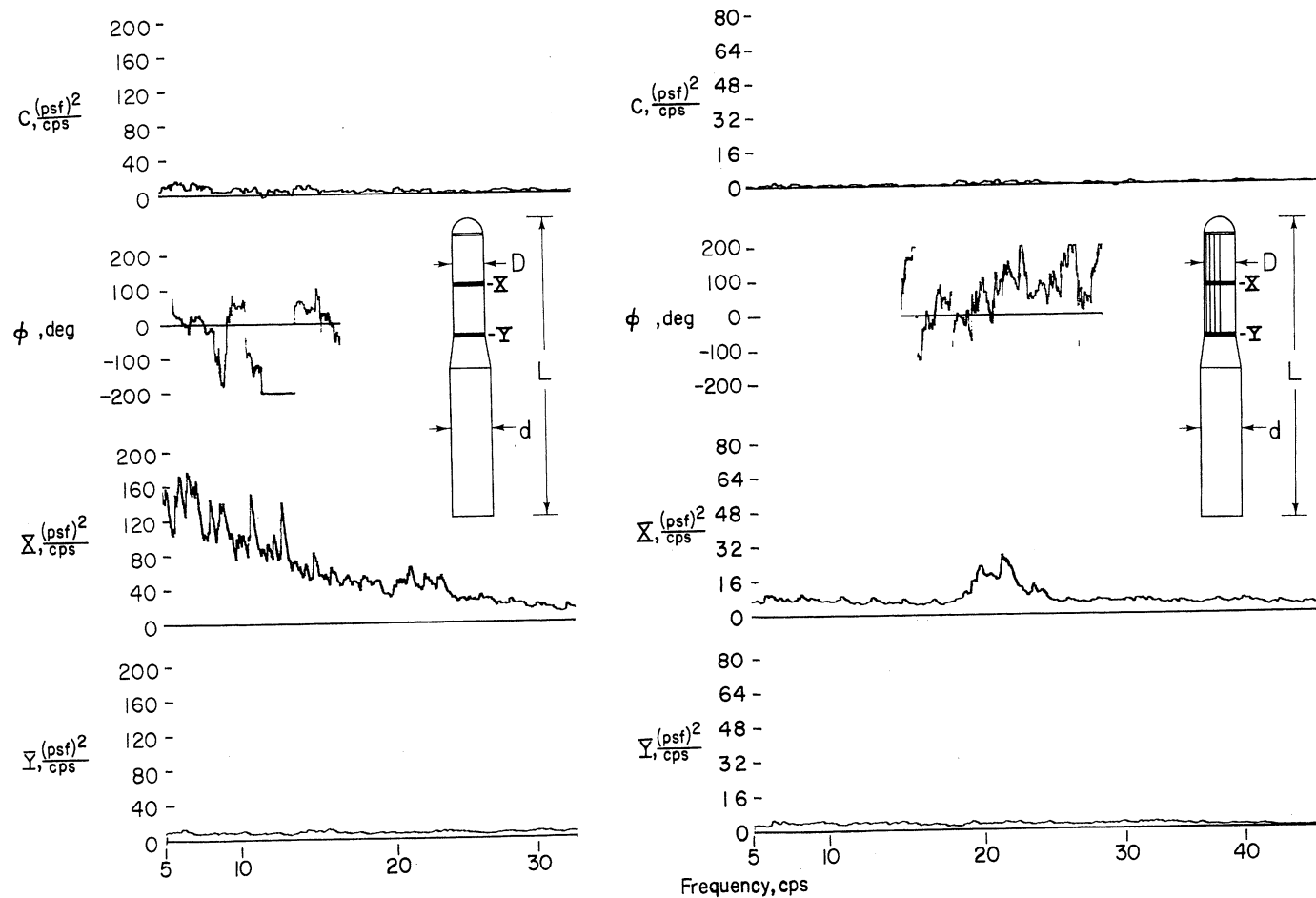
(a) $R = 2.5$ million, $V = 97$ fps; $R = 3.5$ million, $V = 137$ fps.

Figure 59.- Power spectra of the lateral-pressure fluctuations at stations A and F (fig. 7) of a model with blunted-cone nose and with tapes 0.00029D thick; f of model = 23 cps.



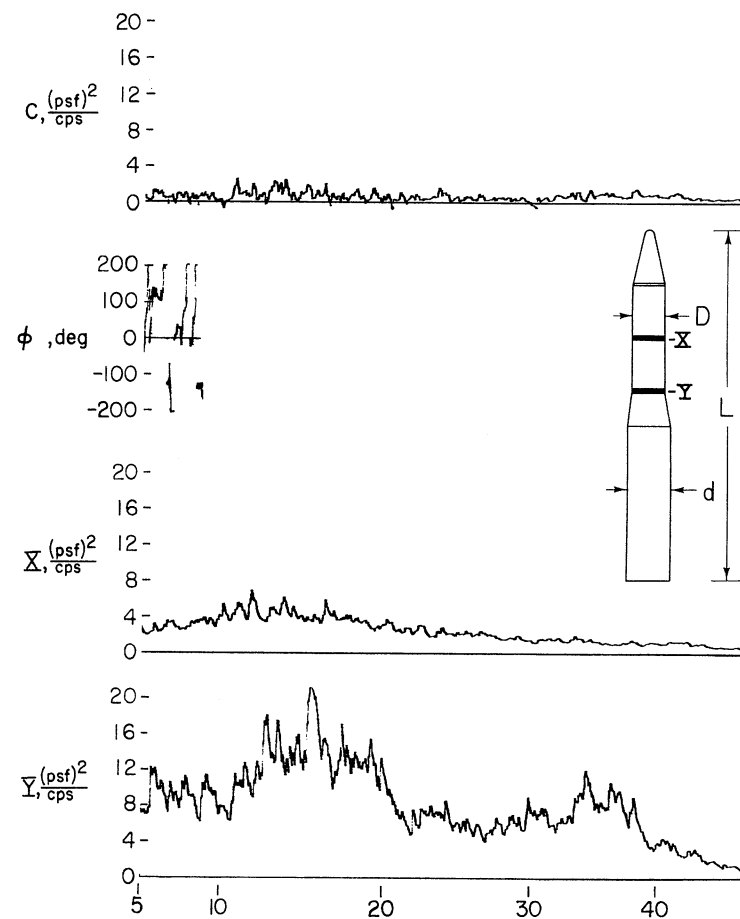
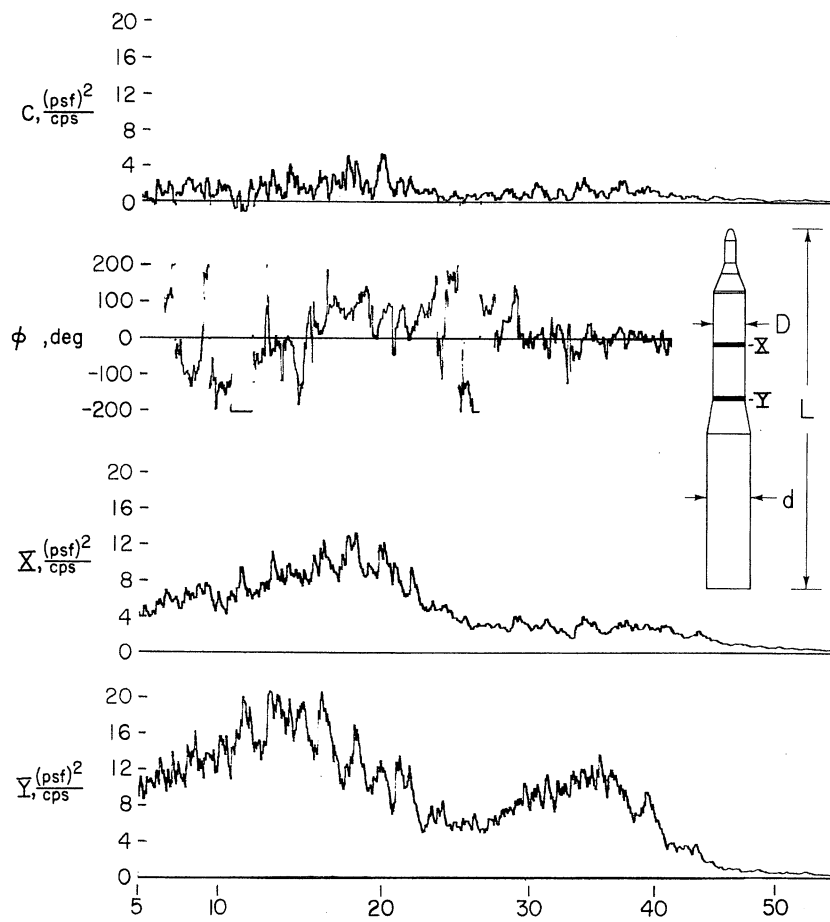
(b) $R = 5.0$ million, $V = 195$ fps; $R = 6.1$ million, $V = 239$ fps.

Figure 59.- Concluded.



(a) With hemisphere nose, with and without tapes 0.00029D thick.

Figure 60.- Power spectra of the lateral-pressure fluctuations at stations F and J (fig. 7); f of the model = 22 to 23 cps; $R = 5.0$ million; $V = 194$ fps.



Frequency, cps

(b) With cone-cylinder nose and with blunted-cone nose.

Figure 60.- Concluded.

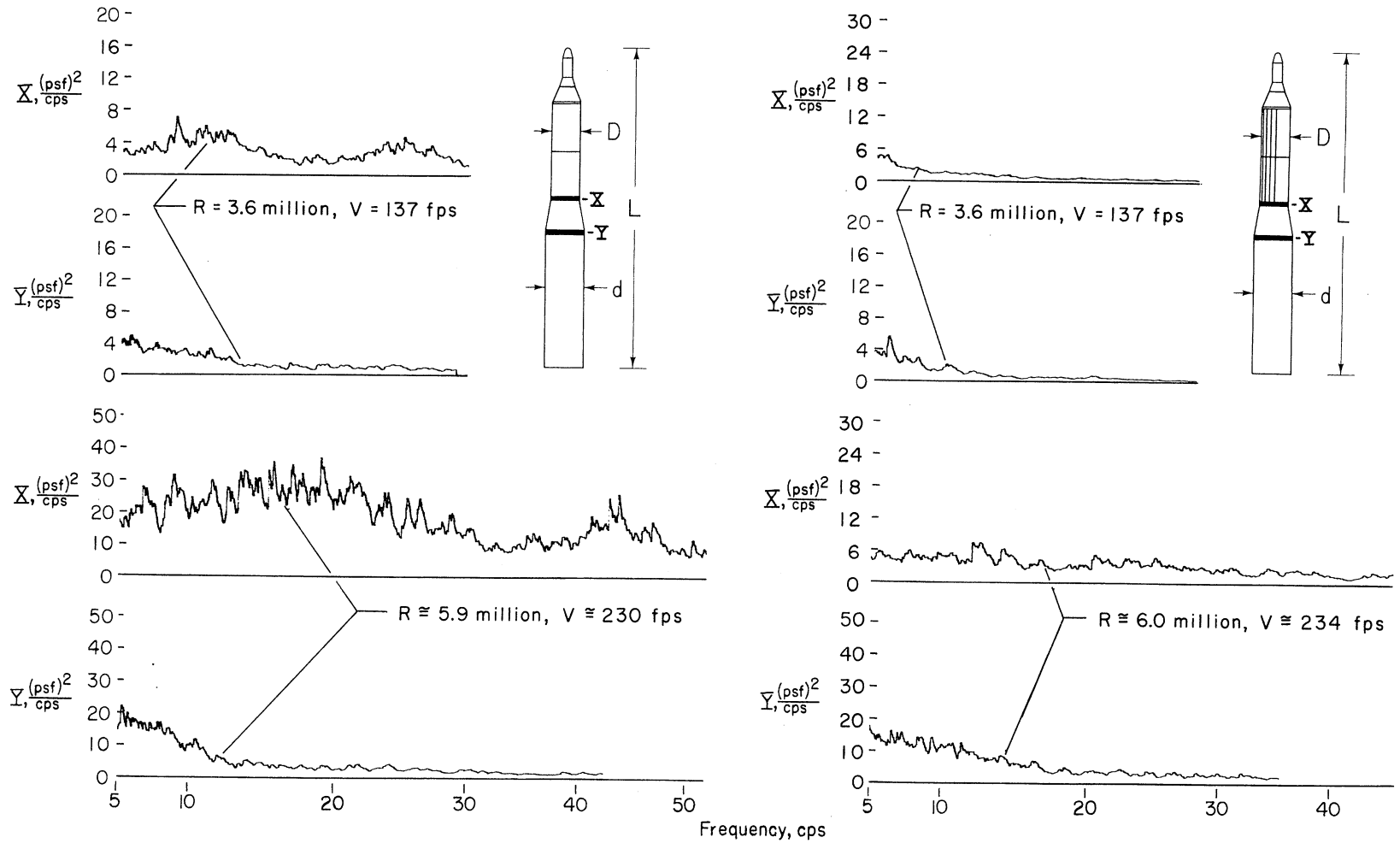
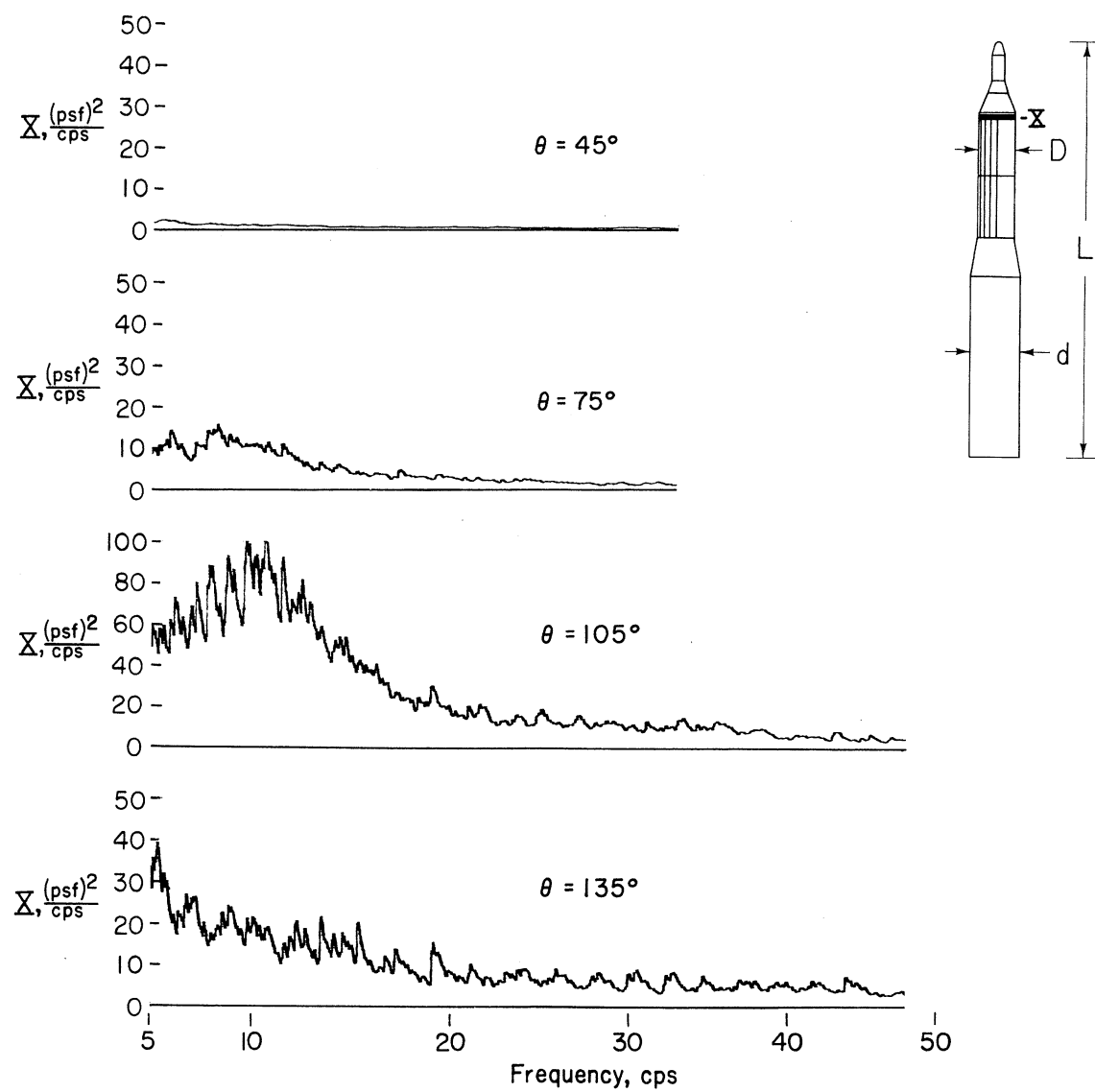
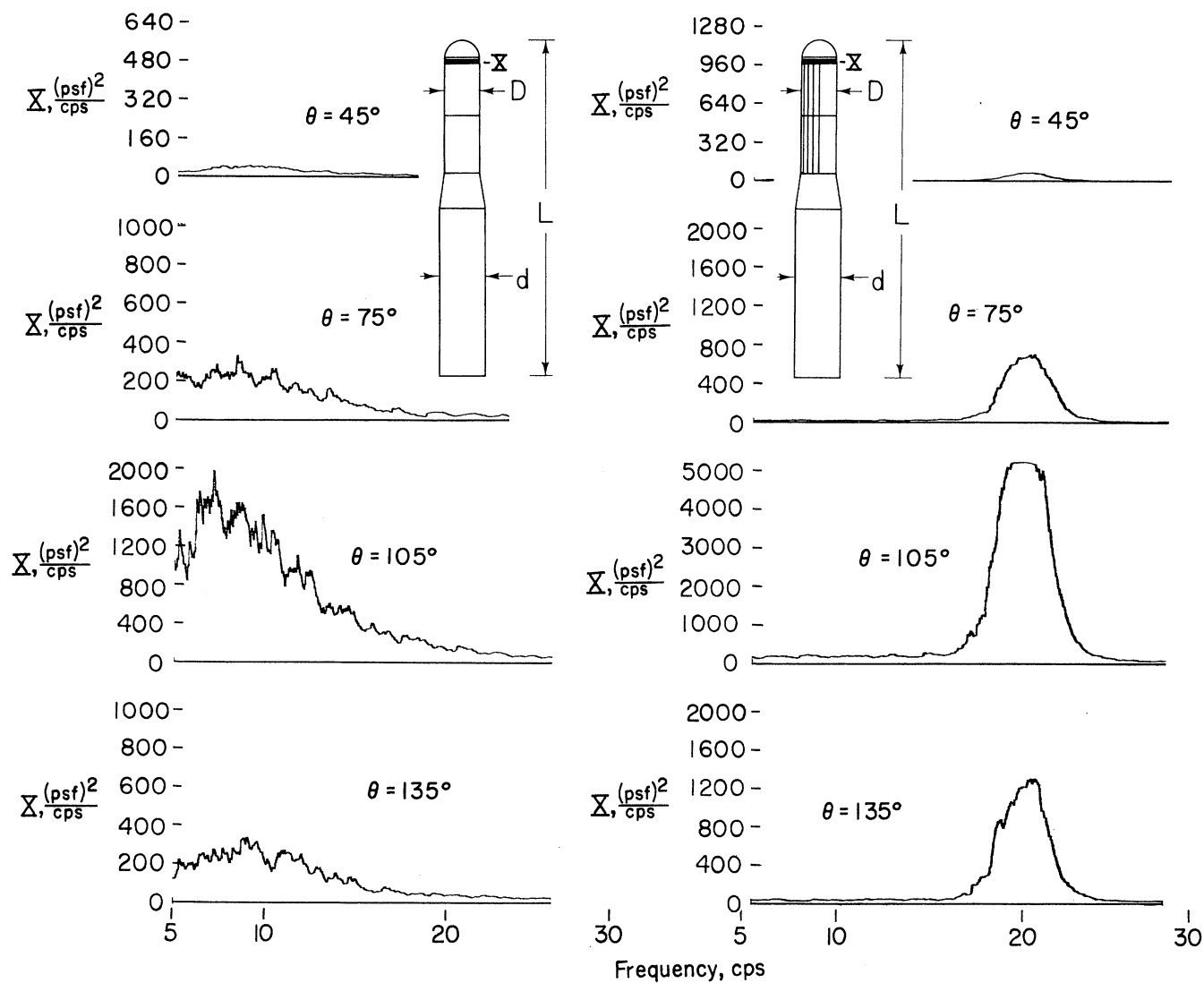


Figure 61.- Power spectra of the lateral-pressure fluctuations at stations J and K (fig. 7) of a model with cone-cylinder nose, with and without tapes 0.00029D thick.



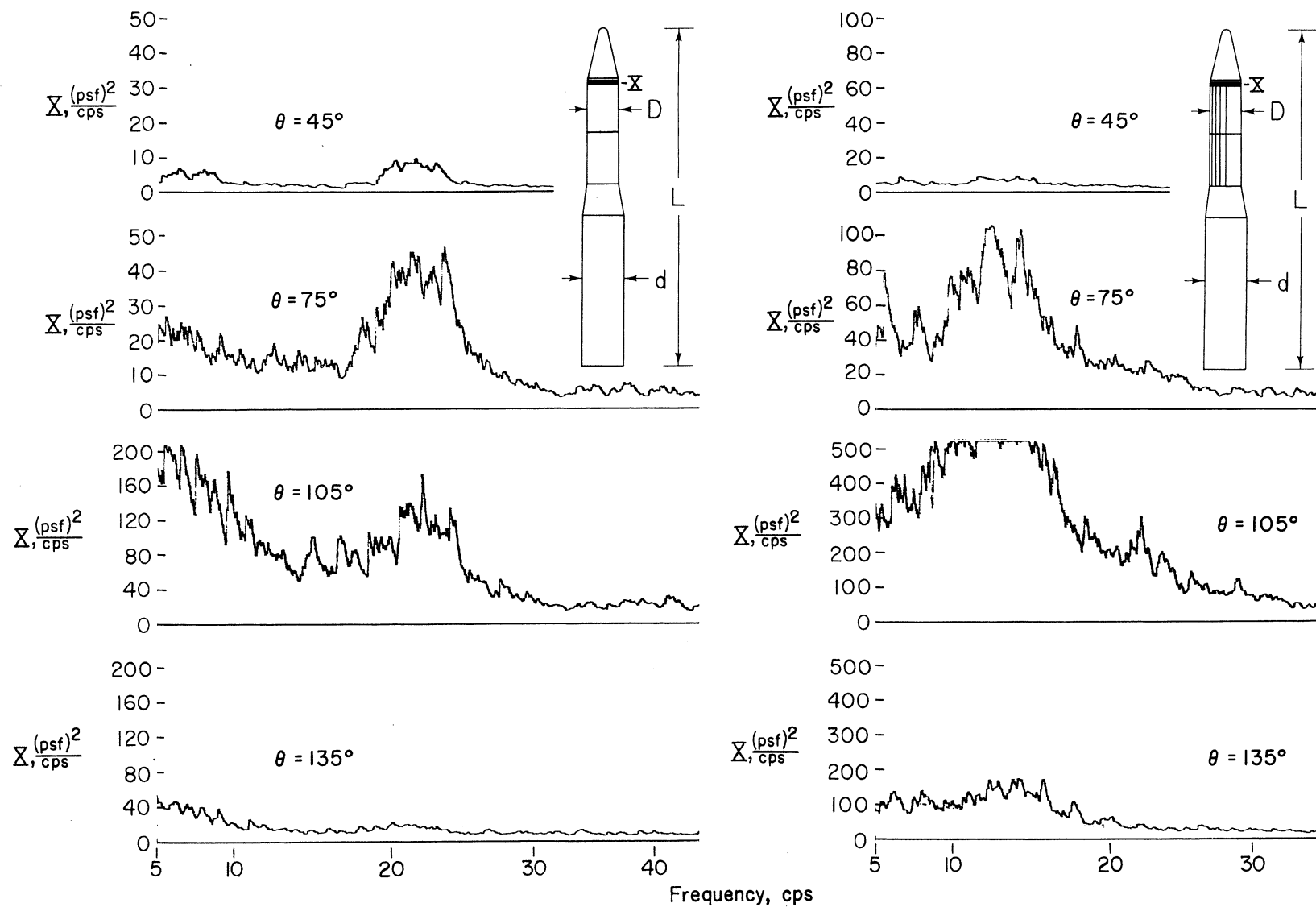
(b) With cone-cylinder nose and tapes 0.00029D thick.

Figure 62.- Continued.



(a) With hemisphere nose, with and without tapes 0.00029D thick.

Figure 62.- Power spectra of the pressure fluctuations on each pressure transducer at station A (fig. 7); $R = 5.1$ million; $V = 194$ fps.



(c) With blunted-cone nose, with and without tapes 0.00029D thick.

Figure 62.- Concluded.

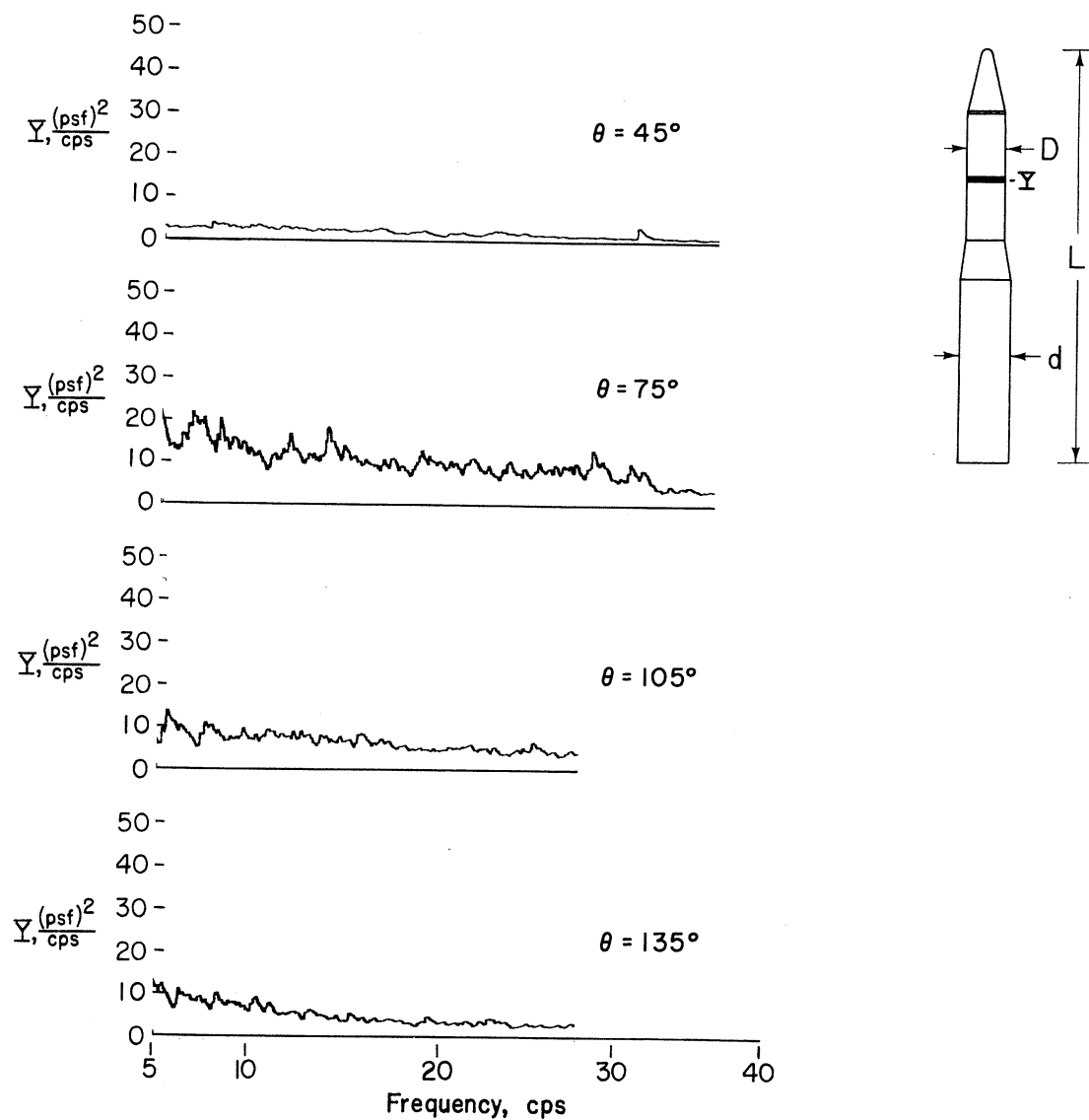
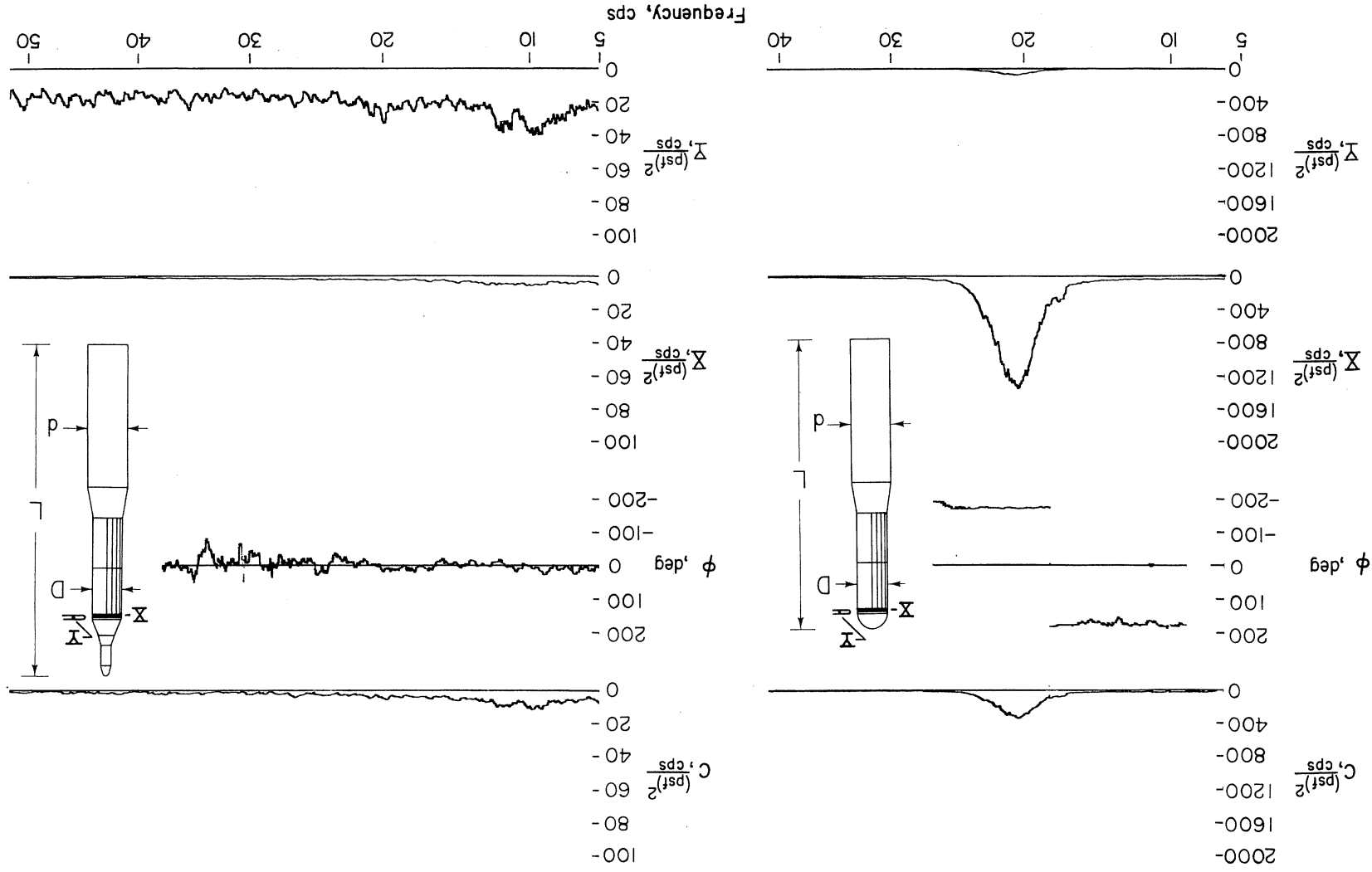


Figure 63.- Power spectra of the pressure fluctuations on each pressure transducer at station F (fig. 7) of a model with blunted-cone nose; $R = 5.1$ million; $V = 194$ fps.

Figure 64. - Power spectra of the lateral-pressure fluctuations at station A and R_3 , 6.5 inches behind station A (Fig. 7) of a model with tapes 0.00029D thick; $R = 5.3$ million; $V = 190$ fps.



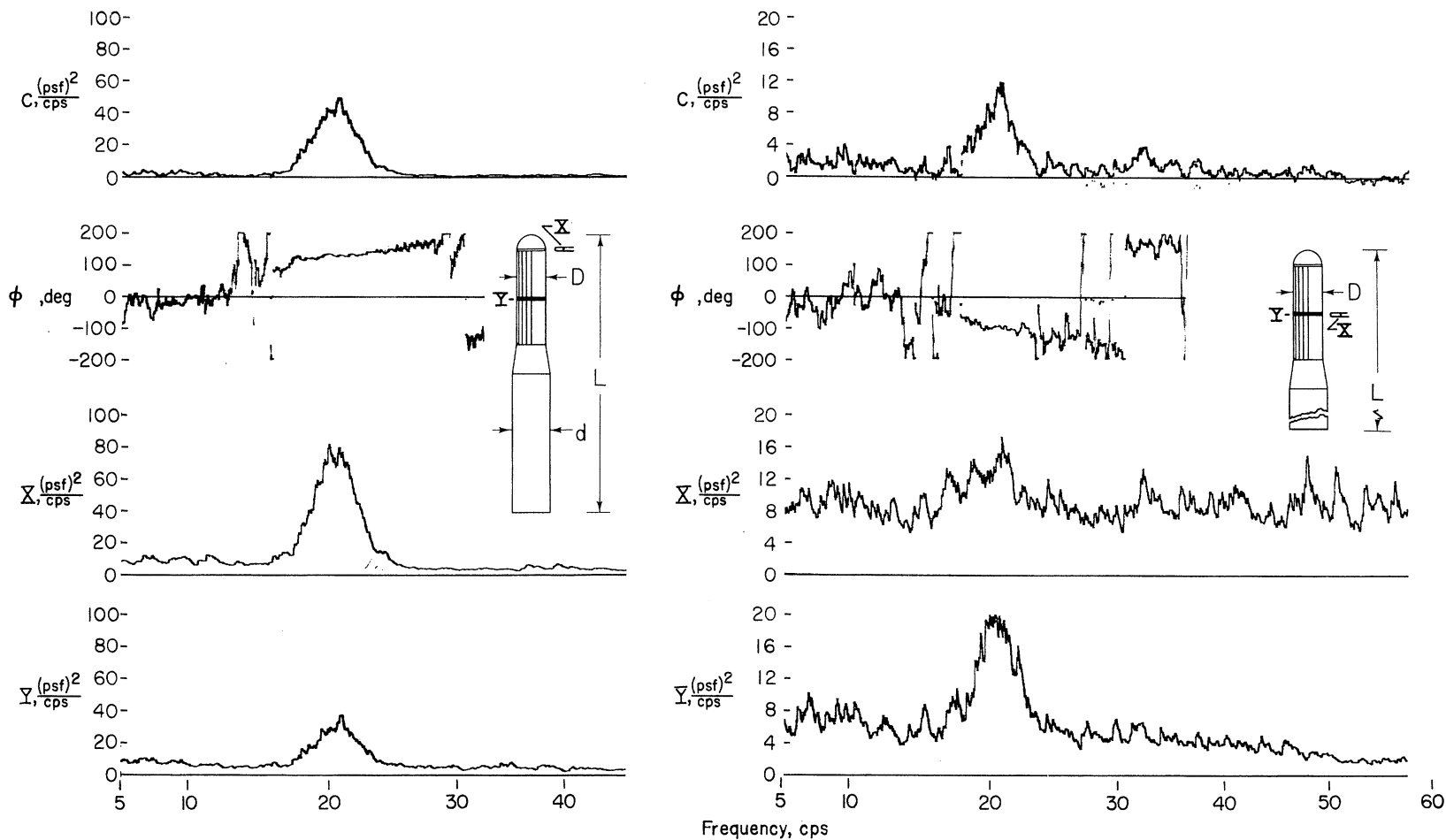
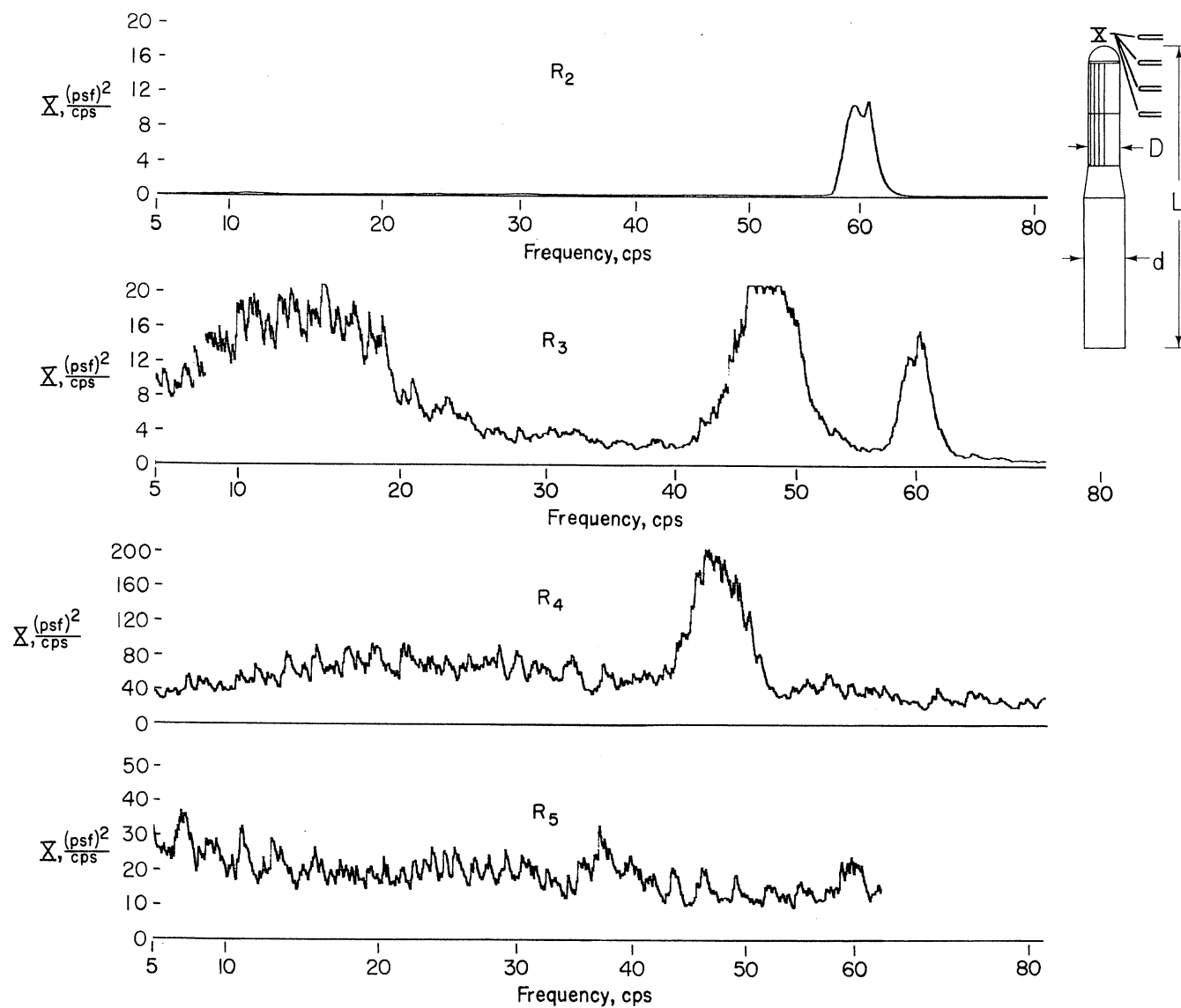
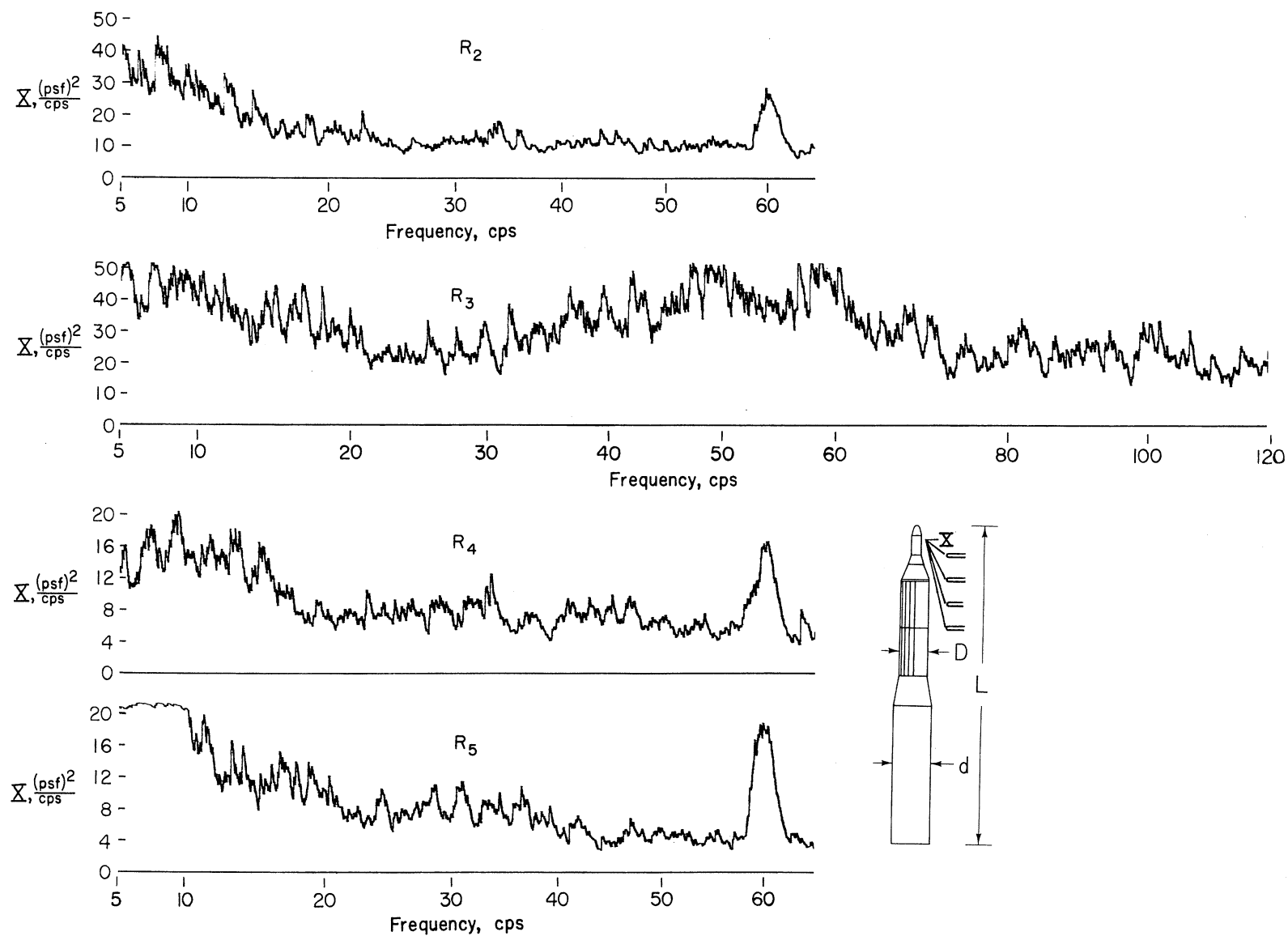


Figure 65.- Power spectra of the lateral-pressure fluctuations at station F (fig. 7) and at R_3 and R_5 , 6.5 inches behind the model with hemisphere nose and tapes 0.00029D thick; $R = 5.3$ million; $V = 192$ fps.



(a) With hemisphere nose; $R = 4.3$ million; $V = 233$ fps.

Figure 66.- Power spectra of the pressure fluctuations at the nose of the rake tubes (fig. 7) 6.5 inches behind the model with tapes 0.00029D thick.



(b) With cone-cylinder nose; $R = 5.3$ million; $V = 191$ fps.

Figure 66.- Concluded.

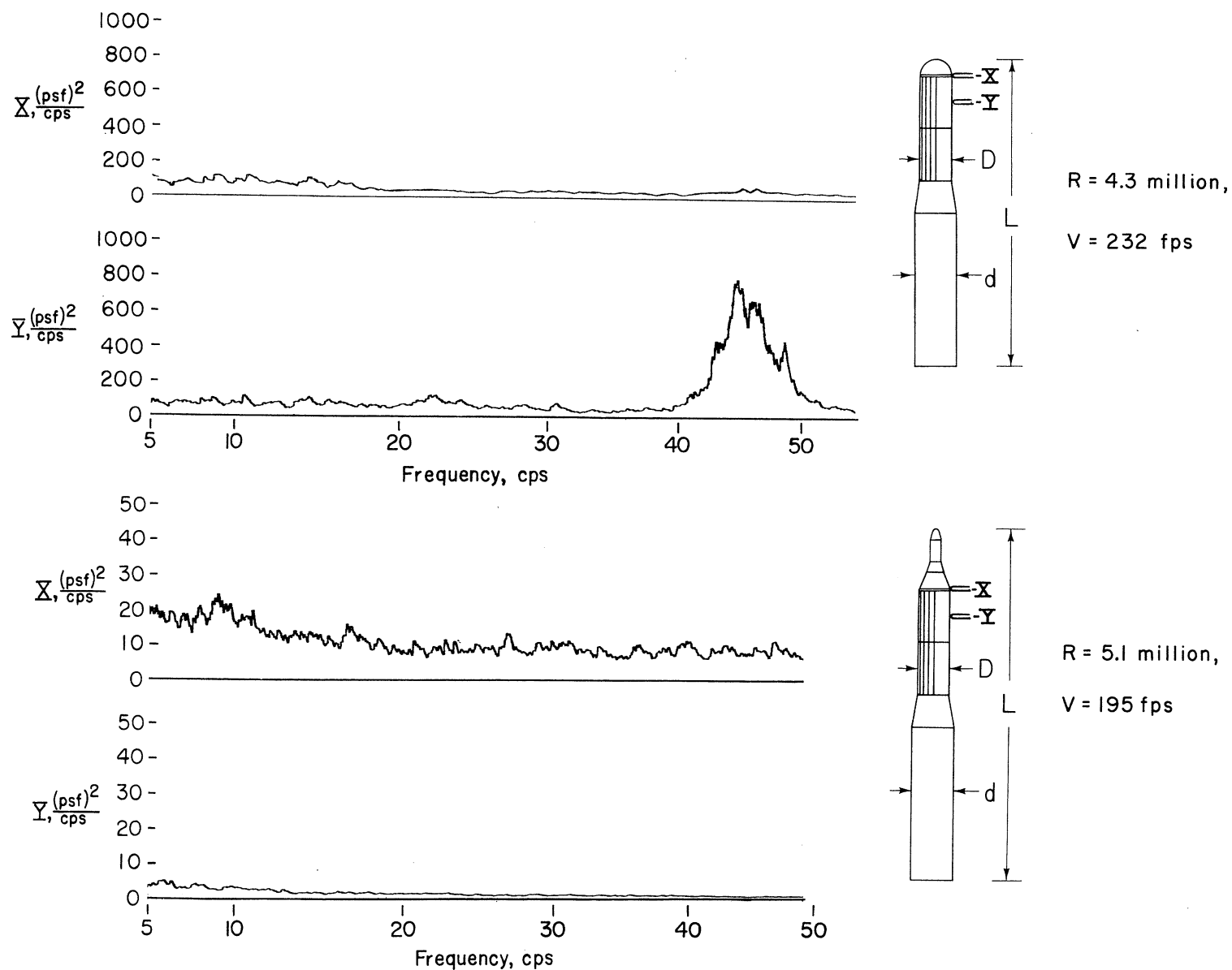


Figure 67.- Power spectra of the pressure fluctuations at the nose of the rake tubes R_3 and R_4 (fig. 7) 0.2 inch behind the model with tapes 0.00029D thick.

